Fouling layer formation by flocs in inside-out driven capillary ultrafiltration membranes

Von der Fakultät für Ingenieurwissenschaften, Abteilung Maschinenbau der
Universität Duisburg-Essen
zur Erlangung des akademischen Grades

DOKTOR-INGENIEUR

genehmigte Dissertation

von

André Lerch
aus
Düsseldorf

Referent: Prof. Dr.-Ing. habil. Rolf Gimbel
Korreferent: Prof. Dr.-Ing. Wolfgang Uhl
Korreferent: Prof. Dr. Anthony G. Fane
Tag der mündlichen Prüfung: 28.02.2008

Abstract

The interest in low pressure membrane filtration, i. e. micro- and ultrafiltration (MF and UF) increased rapidly in recent years, particularly due to the extremely high requirements for potable water quality with respect to hygiene aspects. However, some limiting factors exist, especially when applying MF or UF for the direct treatment of surface waters without any pretreatment. Particularly dissolved organic matter (DOM) can be very problematic due to the formation of hardly reversible and/or irreversible fouling layers and due to its general contribution in formation of disinfection by-products (DBP). To get these problems under control, different pretreatment processes are conceivable and available, whereas this work is focused on the hybrid process coagulation and UF. Coagulation is an established technology for the removal of DOM and, from an engineering perspective, can easily be combined with membrane processes.

To achieve an appropriate operation performance of hybrid process with respect to economic and procedural engineering aspects, it is necessary to understand what the limiting factors are, when they are of importance and how their effects may be avoided by design and the chosen operating parameters. The most important point in this respect is to understand how fouling layers are formed, because these layers will limit the efficiency of the entire process. Therefore, the objective of this work was to contribute to the understanding of formation of fouling layers by porous floc aggregates during filtration of coagulated raw waters in inside-out driven capillary UF membranes.

A computational fluid dynamics (CFD) model was developed for the description of the complete fluid flow field in inside-out driven UF capillaries of arbitrary cylindrical geometry, alignment and physical properties of the membrane and chosen operation condition. This was done by numerical calculations of the Navier-Stokes and continuity equations. Based on the fluid flow field, floc velocities and trajectories were derived by balancing the forces and torques acting on the flocs in the flow field. They were used to determine places of preferential floc deposition for flocs of different properties, considering floc volume concentration derived from numerical calculations of the convection and diffusion equation and the influence of the membrane wall.

Abstract

The models were coupled and eventually used to account for the growing fouling layer height and its influence on the resulting fluid flow field, floc volume distribution and floc trajectories, delivering a dynamic fouling layer formation over time. It was shown that the local resistance of the fouling layer increases at surface areas of preferential deposition, whereupon the fluid rather flows through uncoated or less coated areas. Hence, fouling layer formation over time and eventually clogging behaviour for longer filtration times could be investigated theoretically for different cylindrical capillary geometries, alignments, operation conditions and physical properties of the flocs and the membrane.

New aspects could be derived qualitatively to understand the formation of fouling layers by porous floc aggregates in inside-out driven capillary membranes from which recommendations for appropriate operation conditions were concluded. Under these are, e. g. top-down dead-end or cross-flow operation for the filtration of flocs, ballasted with micro sand.

Acknowledgements

This work was created during my activities as a research assistant at the Universität Duisburg-Essen, Institute for Energy- and Environmental Engineering, Process Engineering/Water Technology, at the IWW Rheinisch-Westfälisches Institut für Wasserforschung gGmbH in Mülheim a. d. Ruhr (IWW Water Center) and at the Technische Universität Dresden (TU Dresden), Institute of Urban Water Management, Chair of Water Supply Engineering.

A work such as this cannot be completed without assistance, and I am deeply indebted to the following people for their help throughout the project. In particular, I am profoundly indebted to my doctoral advisor Prof. Dr. Rolf Gimbel. He always was interested in my work, supported my research activities and gave me the necessary freedom to tap new topics at the university and the IWW Water Center. He has decisively promoted my work by his critical suggestions and by sharing his philosophy of plausibility checks of colourful CFD figures.

I am deeply grateful to Prof. Dr. Wolfgang Uhl from the Institute of Urban Water Management, Chair of Water Supply Engineering at the TU Dresden for not being an examiner evaluating my dissertation only, but for supporting me and my research activities during the last years in Dresden. He always was interested in my work and gave valuable and critical advice and especially free time if necessary to bring this work to a successful end. I am really looking forward to our future collaboration.

Further, I am very grateful to Prof. Dr. Anthony G. (Tony) Fane from the UNESCO Centre for Membrane Science and Technology, University of New South Wales, Australia, for being my second examiner and for his critical contributions and suggestions when evaluating my dissertation.

Gratitude is expressed to all my former and current research teammates at the Universität Duisburg-Essen, the IWW water center and the TU Dresden. They let me participate in a lot of research experience, theoretical knowledge and practical know-how. Especially, I would like to thank for the invaluable discussions with Dr. Georg Hagmeyer, Dr. Ralph Hobby, Dr. Achim Mälzer, Dr. Andreas Nahrstedt, Andreas Palinski and Dr. Stefan Panglisch. Now its my part to support younger researchers

and students as well. I hope I can be as good. Furthermore, the excellent working atmospheres in Duisburg, Mülheim a. d. Ruhr and Dresden could not have been created without all the other staff members in the laboratory, technical centre and administration. I could always rely on their support. My sincere thanks to Dr. Markus Gerlach, who can be made somehow responsible for this thesis too. He awoke my interest in water treatment processes and research in particular by sharing his enthusiasm of his own work on the role of humic substances in bank filtration when supervising me in my first research project.

I would like to gratefully thank all students who have written their research, project or diploma theses in my group. My deepest gratitude goes to Christina Neuhaus, who was working as my student assistant in Duisburg. Her support, diligence, correctness and friendship was highly appreciated all the time. Thank you for this so much! I am deeply grateful to Kristina Wachholz, who has produced an excellent piece of work in designing and setting up the test unit for single capillaries in her project thesis. I regret that, due to time restrictions, it was not possible to do more experiments on it.

Thanks to the staff of COMSOL Multiphysics and the members of the COMSOL_ Users yahoo! group, in particular Roland Martin, Dan Smith, Akos Tota, Dr. Andreas Wilde and Prof. Dr. Will Zimmerman, for their support and invaluable discussions.

And last, but not least, thanks goes to my immediate family and friends who have been an important and indispensable source of spiritual support. Special thanks to my friend Dr. Sandra Rosenberger for discussing and proof-reading the thesis, providing me with valuable comments and giving it a better structure, which was certainly not that easy considering my writing style.

Especially, this thesis had not been written without the endless support, great encouragement, tolerance, patience and understanding of my dearly beloved wife Alexandra and our son Wesley. They gave me love and inspiration all the time, especially when I needed it most. Wesley taught me that playing ‘bamm’ with him, i. e. football, is definitely much more interesting than just modelling the trajectory of the kicked ball. Thanks for this mate!

Content

1 Introduction

1.1 Problem description and objectives

Potable water treatment of surface waters involves most commonly the removal of particulate and dissolved matter by combinations of coagulation, flocculation, sedimentation or flotation and filtration processes along with disinfection prior distribution of the finished water. Hence, filtration processes for particle removal are the basic part of the multi barrier principle in potable water treatment, conventionally in form of granular multi media depths filters.

Even though filtration by granular media filters can produce high quality water, the process generally represents a probabilistic rather than an absolute barrier and consequently, pathogens can still pass through the filters and may pose a health risk, especially if anthropogenic influenced surface waters are to be treated. Disinfection processes provide an additional measure of public health protection by inactivating these pathogens. However, some microorganisms like parasites, such as *Cryptosporidium* or *Giardia* or their resistant dormant bodies *oocysts* and *cysts* respectively, are resistant to common processes of potable water disinfection using chlorine, chlorine dioxide or ultraviolet (UV) irradiation. These disinfection processes will be ineffective not only in the control of parasites but also where viral and bacterial agents are present in particles of faecal origin. Furthermore, potable water regulations have established maximum contaminant levels for disinfection by-products (DBP) that may create incentive for water utilities to minimise the application of some disinfectants. As a result of the concern over chlorine-resistant microorganisms and DBP formation, the potable water industry is increasingly utilising alternative treatment technologies in effort to balance the often-competing objectives of disinfection and DBP control. One such alternative technology that has gained broad acceptance is membrane filtration.

Although the use of membrane processes has increased rapidly in recent years, the application of membranes for water treatment extends back several decades. Reverse osmosis (RO) membranes have been used for desalination of water since the 1960s, with more widespread use of nanofiltration (NF) for softening and removal

of total organic carbon (TOC) dating to the late 1980s. The commercialisation of backwashable capillary microfiltration (MF) and ultrafiltration (UF) processes for the removal of particulate matter, i. e. turbidity and microorganisms, in the early 1990s has had the most profound impact on the use, acceptance and regulation of all types of membrane processes for potable water treatment. MF and UF can be used to retain particulate matter and are therefore able to retain bacteria and parasites, like *Escherichia coli*, *Giardia cysts* or *Cryptosporidium*, which have been in discussion worldwide due to public health issues, accompanied by recent outbreaks of waterborne diseases as e. g. in Walkerton, Ontario, (HUCK ET AL. (2001)) and North Battleford, Saskatchewan (STIRLING ET AL. (2001)) in a row with others (CRAUN (1979) and CRAUN ET AL. (1998)). Since then, membranes in potable and industrial water production, in recycling and reuse have emerged as a cost competitive and viable alternative to conventional methods due to a dramatic decrease in membrane filtration costs as a result of innovations in membrane manufacturing and process conditions (BOERLAGE (2001), GIMBEL AND HAGMEYER (2003), PANGLISCH ET AL. (2004)). This is reflected for instance in the exponential increase of the production capacity of low pressure membranes (MF/UF) plants installed worldwide (LERCH ET AL. (2005B)). Especially the interest in UF increased due to the extremely high water quality with respect to hygienically relevant parameters. Compared to conventional treatment processes, UF provides two main advantages. First, UF is a complete barrier against all kind of microorganisms and particles, integrity presumed, and second, the filtrate quality is independent of raw water quality regarding colloidal and particulate matter. Further advantages are for instance the possibility of fully automatic operation, compact system design with efficient space utilisation and flexibility in system enlargements, modernisations and new installations.

However, one limiting factor in membrane filtration is fouling. Generally, fouling can be defined as the gradual accumulation of water components, i. e. foulants or/and scalants, on the membrane surface or within the porous membrane structure that inhibits the passage of water, see chapter 2.1.5. Particularly dissolved organic matter (DOM) like humic substances can cause severe problems due to formation of hardly reversible or even irreversible fouling layers on the membrane surface. In order to target these problems and to utilise the advantages of membrane filtration, hybrid processes were developed and established, see chapter 2.2. The hybrid process

considered in this work is the combination of coagulation and membrane filtration. To achieve an appropriate operation performance of coagulation and MF/UF with respect to economic and procedural engineering aspects, it is necessary to understand what the limiting factors are, when they are of importance and how their effects may be avoided by design and chosen operating parameters. The main factor limiting performance considered here is the increase of transmembrane pressure (TMP) necessary to maintain constant flux operation due to fouling layer formation during filtration of coagulated raw waters with inside-out driven capillary membranes. Hence, the objective of this work is to answer the following questions:

- How are fouling layers formed by porous floc aggregates?
- What are the main influencing parameters?
- What are the appropriate operation conditions?

The approach is to develop a model based on finite element method (FEM) and computational fluid dynamics (CFD) models for the description of the flow field in inside-out driven membrane capillaries and on models for floc transport and deposition. The developed model will then be used to describe and predict at least qualitatively the loss in permeability as function of the floc and membrane properties and the chosen operating conditions.

1.2 Description of the work procedure

PANGLISCH (2001) showed that solid particles with a size smaller than a certain limiting diameter will settle homogeneously on the surface along the total length of a capillary driven in dead-end and inside-out mode. Larger particles occupy preferential places and do not deposit until they are at a certain distance from the inlet. If the particle is larger than a so called „plug forming diameter“, then it is transported to the dead-end which may cause complete clogging of the capillary. Thus, while filtering particle suspensions it comes to the formation of zones of different composition, porosity and thickness.

In principle, the described fouling layer formation is applicable for the filtration of floc suspensions too. Flocs are always thought of being aggregates consisting of iron or

aluminium hydroxide with embedded primary particles and colloids, being rigid and ideally spherical and of constant shape, but reveal basic floc properties such as inner porosity, low density and low zeta potential. However, in contrast to the work of PANGLISCH (2001) the homogeneous distribution on the membrane surface and the preferential deposition of smaller and mid sized particles will decrease or vanish, depending on coagulation efficiency of those particles. For smaller and mid sized primary particles it applies that they are embedded into the formed flocs in significant number during coagulation. It is hypothesised, depending on operational as on geometrical boundary conditions, porous flocs formed behave like solid particles of similar hydraulic size and are transported likewise to the dead-end of the capillary. The consequence is that smaller and mid size particles are transported also more deeply into the capillary by the flocs as they would actually do due to their own size and density. This hypothesis will be confirmed with following work steps:

- Modelling of the complete flow field for inside-out driven membrane capillaries of arbitrary cylindrical geometries and membrane operation conditions like cross-flow or dead-end in CFD. This will be done by numerical calculations of the Navier-Stokes and continuity equations for stationary and transient flows.
- Modelling the floc volume concentration distribution for inside-out driven membrane capillaries of arbitrary geometries and membrane operation conditions by numerical calculations of the convection and diffusion equation, based on the modelled flow field and parallel calculated floc velocities.
- Modelling of floc trajectories and velocities by balancing the forces and torques acting on the flocs under the previously modelled flow field and parallel modelled concentration distribution, considering arbitrary floc properties like porosity, density, size and surface charge etc.
- Derivation and discussion of fouling layer formation under consideration of the derived transport and deposition behaviour.
- Examination and discussion of the theoretical model results by experimental investigations.
- Description and discussion of the engineering and scientific relevance.

2 State of the art

2.1 Membrane processes in potable water treatment

2.1.1 Mechanisms

Membrane processes have been subject to a considerable strong increased technical development in recent decades and are nowadays established in different areas like potable water and wastewater treatment, chemistry -, environmental- and medical technology. They became irreplaceable for blood cleaning and are nearly unrivalled for the concentration of proteins, for the production of beverages and seawater desalination for instance. MULDER (1991) characterised membrane processes by the use of a membrane to accomplish a particular separation of components. Herein, the membrane itself can be considered as a permselective barrier between two phases, transporting one component more readily than others because of differences in physical and/or chemical properties between the membrane and the permeating components. This transport through the membrane takes place due to driving forces, i. e. concentration c, pressure p, temperature T or electrical potential E (chemical or electro-chemical respectively), acting on the individual components in the feed (see Figure 2.1).

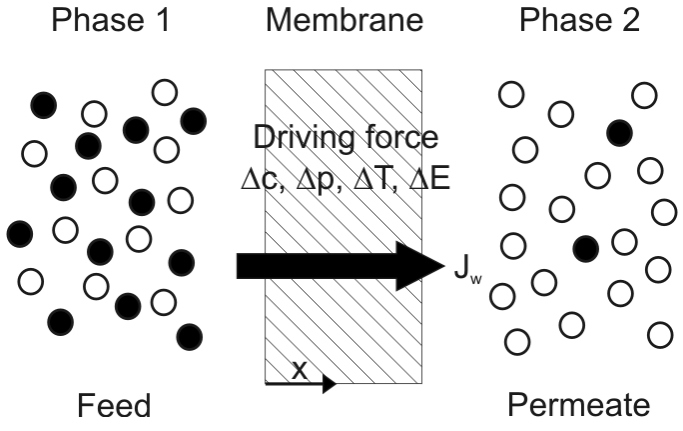

Figure 2.1: Schematic representation of a two phase system separated by a membrane (adapted from MULDER (1991))

The permeation rate, the so called permeate or filtrate flux J denotes the flow through the membrane and is generally reported as the fluid volume flowing through the

membrane per unit surface area of the membrane and time. Hence, permeate or filtrate flux has the dimension of velocity (m/s), often expressed as (L/m²/h).

The proportionality between the flux and the driving force is presented by MULDER (1991) with the general phenomenological equation

$$J_i = - A \frac{dX}{dx}, \qquad \textbf{Equation 2.1}$$

where A is called the phenomenological coefficient and (dX/dx) the driving force, expressed as the gradient of X along a coordinate x perpendicular to the transport barrier (compare Figure 2.1). Regarding a pure water flux through a membrane or more generally through a porous medium, Equation 2.1 delivers the Darcy law

$$J_W = \vec{u} = - \frac{k}{\eta} \nabla p . \qquad \textbf{Equation 2.2}$$

Herein, $\vec{u}$ denotes the velocity vector of the fluid flow, η denotes the dynamic fluid viscosity and p the applied driving force, here pressure or geodetic height respectively. The permeability coefficient k of the porous media is a measure of the ability of the material, here the membrane, to transmit fluids.

According to MELIN AND RAUTENBACH (2004), membranes can be characterised on the one hand by size or molar mass of the biggest component in the feed still able to pass the membrane and on the other hand by the acting driving force, the separation mechanism (size exclusion (sieving) and sorption and diffusion) or by the state of aggregation of feed and permeate (liquid or gaseous). The membrane filtration process discussed in this work is described in its simplest form as a pressure driven separation process, primarily through a size-exclusion mechanism which utilises the membrane as a sieve to retain suspended components from the liquid feed, producing a solid-free liquid filtrate.

2.1.2 Classification of membrane processes

According to the characterisation of a membrane filtration process given above, the common membrane technologies applied in the field of potable water treatment are

microfiltration (MF), ultrafiltration (UF), nanofiltration (NF) and reverse osmosis (RO). Figure 2.2 illustrates schematically the areas of application covered by membrane processes and indicates their abilities to retain certain water components according to their approximate pore size given in nanometer (nm) or molecular weight (Dalton, Da) respectively. Furthermore, Figure 2.2 indicates the ability of the different membrane technologies to remove drinking water pathogens, i. e. viruses, bacteria and parasites, which are of special interest in the potable water industry due to public health concerns and risks.

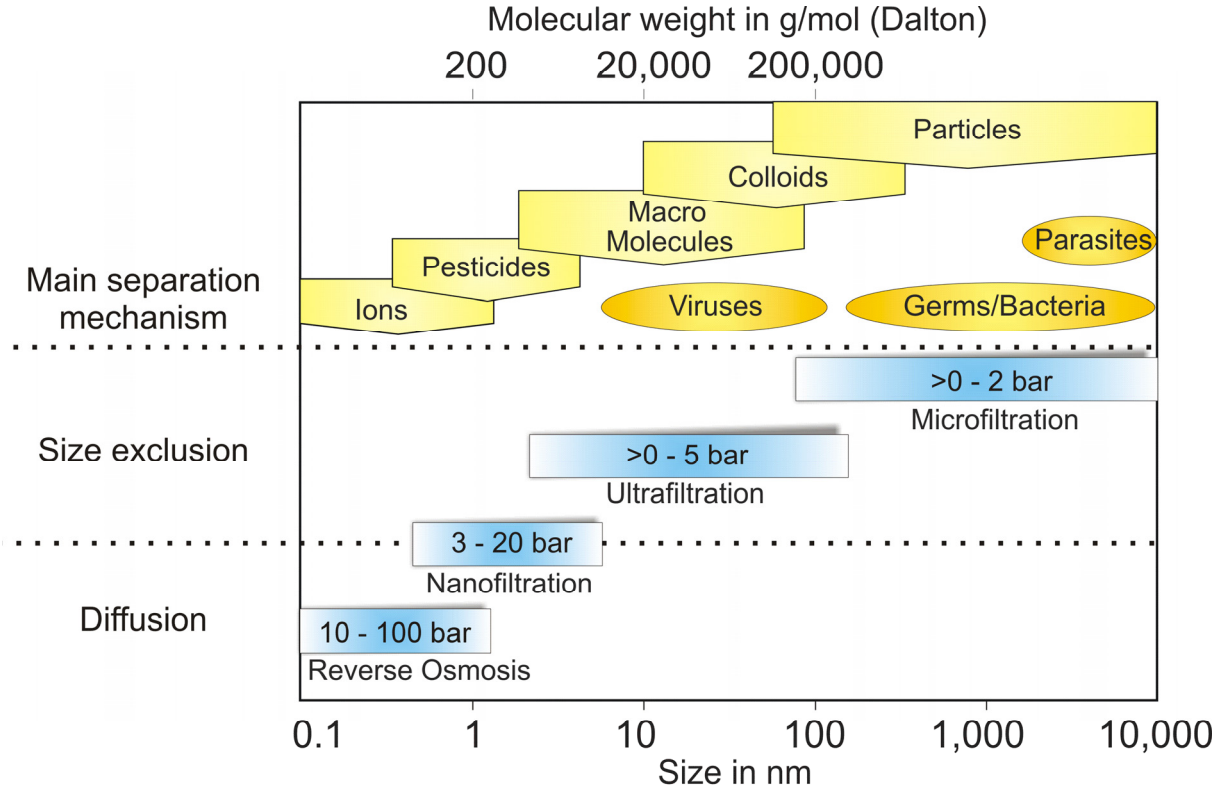

Figure 2.2: Schematic areas of application for pressure- or vacuum driven membrane processes with respect to the size of water components to be retained (adapted from PANGLISCH (2001) and SMITH (2003))

All represented membrane processes use pressure as the driving force but can be divided by the main separation mechanism applied, as indicated on the left hand side in Figure 2.2. In each case the separation of dissolved and particulate substances is due to physical mechanisms. Consequently, there is no chemical change of the water components in membrane filtration processes. However, by exceeding the solubility equilibrium of individual components in the feed water, agglomeration, precipitation or crystallisation may occur. Depending on the membrane processes with their

different mass transport mechanisms, different resistances opposed by the membrane, i. e. hydraulic resistance for convective mass transport and/or osmotic pressure for diffusive mass transport, have to be overcome by the applied transmembrane pressure (TMP) necessary to operate the membrane process. Furthermore, operation and raw water condition etc. influence the TMP. Typical applied TMP are indicated as pressure ranges in Figure 2.2 for each membrane technology.

The membranes used in UF and MF are exclusively porous membranes. Whether particulate matter will be retained by the membrane depends particularly on its size and structure relative to the size and structure of the membrane pores, i. e. the retention is based on size exclusion. Contrary to the dense membranes of RO a primarily convective mass transport takes place in the porous membranes of UF and MF. Pore size and pore size distribution of the membrane used determine the retention characteristics. Pore size distribution will vary according to the membrane material and manufacturing process. When a pore size is stated, it can be presented as either nominal, i. e. the average pore size, or absolute, i. e. the maximum pore size, usually in terms of microns (µm). MF membranes are generally considered to have a nominal pore size in the range of 0.1 to 0.2 µm, although there are exceptions, as MF membranes with pore sizes of up to 10 µm are available on the market. A typical MF water flux is about 150 L/m²/h or higher with an applied TMP up to 2 bar. Figure 2.2 indicates that MF can be used to retain particulate matter to great extent and that it is even able to retain bacteria and parasites. However, UF provides more reliability and safety when it comes to retention of colloids and viruses to the greatest possible extent. For UF, pore sizes generally range from 0.1 down to 0.05 µm or less, decreasing to an extent at which the concept of a discernable ‘pore’ becomes inappropriate. Though, in terms of pore size, the lower cut off for UF membranes is approximately about 5 nm. Because tight UF membranes have the ability to retain larger organic macromolecules, they have historically been characterised by the molecular weight cut off (MWCO, expressed in Daltons) rather than by a particular pore size. MWCO is a measure of the retention characteristic of a membrane in terms of atomic weight (or mass) rather than size, determined by the retention of at least 90% of a specific compound with a certain molecular weight. Thus, UF membranes specified by MWCO are presumed to act as a barrier to

compounds of molecules with a molecular weight exceeding the stated MWCO. Typical MWCO levels for UF range from 300 to 500,000 Da, with most membranes used for potable water treatment at approximately 100,000 Da (USEPA (2003)). UF usually excites fluxes of 40 to 100 L/m²/h at a TMP up to 5 bar.

2.1.3 Membrane materials, structure and modules

2.1.3.1 General remarks

There are a number of different types of membrane materials, modules, and associated systems that are utilised in pressure driven membrane processes. While several different types of membrane modules may be employed for any single membrane filtration technology, each class of membrane technology is typically associated with only one type of membrane module. This is in general, MF and UF use mainly tubular and capillary membrane modules, and NF and RO use mainly spiral-wound membrane modules. This chapter will give a brief overview and descriptions on MF and UF membranes, as well as the materials from which the membranes are made and the systems into which they are configured. However, explanation will mainly be given for capillary, organic UF and MF membranes, driven in inside-out mode, since these kinds of membranes were used in the experimental and theoretical part of this thesis. Further detailed descriptions and additional information about other materials, modules and processes etc. can be found in CHERYAN (1998), MELIN AND RAUTENBACH (2004) and MULDER (1991)

2.1.3.2 Membrane materials

Only synthetic membranes are employed in water treatment processes. They can be made from a large number of different materials, which can be divided further into the groups of organic and inorganic membranes. The material properties of the membrane may significantly impact the design and operation of the filtration system. Its selection is crucial in deciding the membranes porosity and pore size distribution, as it is essentially an intrinsic property of the polymer selected (MULDER (1991)) and also determines the mechanical and surface properties of the membrane. The polymers used in MF are not inevitably the same as used in UF due to differences in the applied production techniques for polymeric membranes. Commonly used

polymers in MF are polycarbonate (PC), polysulphone (PS), polyvinylidene fluoride (PVDF), polypropylene (PP) and polytetrafluoroethylene (PTFE). Organic UF membranes are mainly prepared by a phase inversion process and may also be constructed from a wide variety of materials, including cellulose acetate (CA), PVDF, polyacrylonitrile (PAN), PS, polyethersulfone (PES), polyimide (PI) and aliphatic polyamide (PA). Ceramic MF and UF membranes are based mainly on the materials alumina (Al_2O_3), titania (TiO_2) and zirconia (ZrO_2). Each of these materials used in MF and UF membrane production has different properties with respect to surface charge, degree of hydrophobicity, pH and oxidant tolerance, strength and flexibility. Some properties of membranes used in potable water treatment are shown in the appendix, Table A.1.

2.1.3.3 Membrane structure

The selection of the membranes, either polymeric or ceramic, in reference to their structure is closely associated with its separation mechanism and therefore with its application to be used in. Two types of membranes can be distinguished by the structure of the cross sectional area of the membrane wall. This structure is used to describe the level of uniformity throughout this area, i. e. symmetric and asymmetric. MF and UF membranes usually are either symmetric or integral asymmetric membranes. Symmetric membranes (porous or homogeneous) are roughly about 10 to 200 µm thick. The resistance to mass transfer is hence determined by the total membrane thickness. Asymmetric membranes are more or less about the same thickness but there is a change in density of the membrane material across the cross sectional area and the resistance to mass transfer is linked to the resistance of the top or active layer. In some asymmetric membranes the porous structure gradually increases in porosity from the feed to the permeate side of the membrane. They can be subdivided further into integral asymmetric, i. e. from a single (polymeric) material or blend, and composite asymmetric, i. e. composed from different (polymeric) materials or blends. Figure 2.3 shows exemplarily some scanning electron microscopy (SEM) pictures of integral asymmetric membrane wall cross sections.

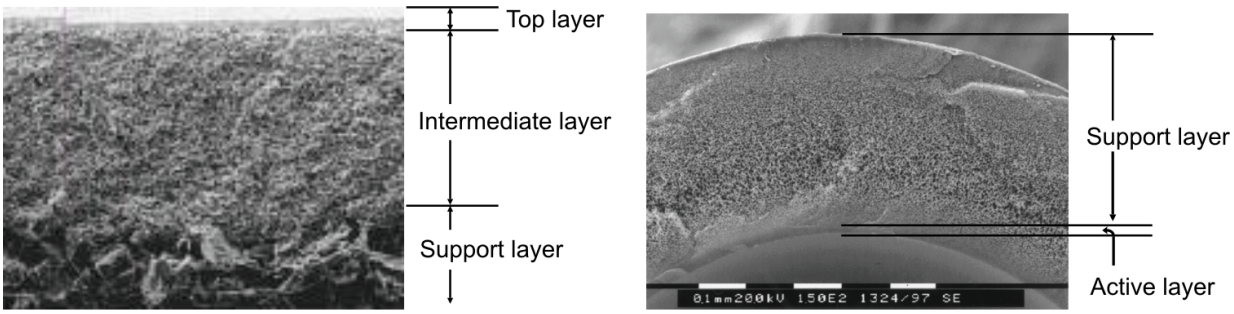

MF Al_2O_3 ceramic membrane
(NGK Insulators, LTD.)

UF PES capillary membrane
(UFC M5, Company X-Flow B.V.)

Figure 2.3: Exemplary SEM pictures of membrane wall cross sections (adapted from PANGLISCH (2001) and BENKHALA ET AL. (1995))

2.1.3.4 Membrane modules

Basically, membranes are manufactured in two configurations: flat or tubular, and then configured into one of several different types of membrane modules. Tubular membranes are used in hollow fibre, capillary and tubular modules. Most capillary modules used are manufactured to accommodate porous MF or UF membranes. They are comprised of capillaries which are long (1 – 1.5 m) and very narrow (0.5 – 5 mm) tubes, being constructed of any of the various membrane materials and structures described above. The capillaries are bundled together and one or both free ends of the capillaries are potted with agents such as epoxy resins, polyurethanes or silicone rubber and encased in a pressure vessel or into some other housings, e. g. inserts or cartridges. A typical commercially available capillary module may consist of several hundred to over 10,000 capillaries and packing densities of about 600 – 1,200 m²/m³ are obtained (MULDER (1991)).

Capillary membrane modules may be operated in either “inside-out” or “outside-in” mode. In inside-out mode, the feed water usually enters the capillary lumen at one or both fronts of the module and is filtered radially through the capillary membrane wall. The filtrate is collected from outside of the capillaries in the module and exits through an outlet at the centre or the end(s) of the pressure vessel, compare Figure 2.4. During backwashing, the flow direction of the filtrate is reversed; i. e. the filtrate is pressed through the membrane capillary into the direction of the active layer and hence detaches the accumulated components from the membrane surface. This concept is used by a multiplicity of the membrane manufacturers, e. g. Infilco

Degremont, Inc. (Aquasource™), inge AG (Dizzer), Koch Membrane Systems Inc. (ROMICON®), Microdyn-Nadir GmbH (MOLPURE® and MOLSEP®), and NMT with X-Flow B.V. (AquaFlex™).

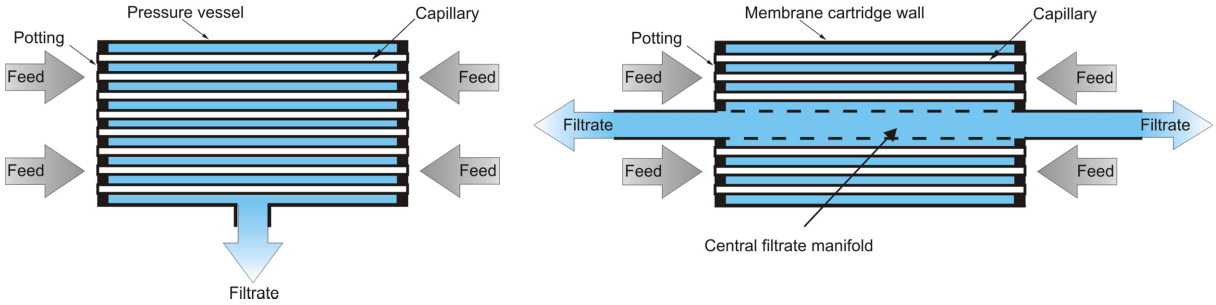

Figure 2.4: Schematic drawing of inside-out operated modules applied in MF/UF with exits through an outlet at the centre (left) or the end(s) (right) of the pressure vessel

Another alternative inside-out operation concept possesses many similarities to the one mentioned above and is known as the XIGA™ concept (BLUME ET AL. (1997)). Differences can be found only in the filtrate extraction method, since the filtrate is collected in a central filtrate manifold in the axis of the module (see Figure 2.4 right hand side). One or more of these cartridges can be placed in pressure vessels that are independent of the module itself, similar to spiral-wound modules used in RO and NF. Some manufacturers, e. g. Infilco Degremont, Inc. (Aquasource™), Hydranautics Corp. (HYDRAcap®) and Koch Membrane Systems Inc. (PMPW™ and TARGA®), offer modules with only one cartridge, where special end caps, which include feed inlet and retentate or backwash water as well as filtrate outlets, are fitted to the front sides of the cartridge. Differences in modules and cartridges are drawn by the manufacturers in the alignment, in diameter and length, in the used fittings, end caps and adaptors for the integration of the module or cartridge into installed systems and of course in the used capillary membranes. Modules and cartridges are typically mounted vertically, although horizontal mounting may also be utilised.

2.1.4 Hydraulic configuration

The simplest hydraulic configuration, i. e. the operation mode a membrane module can be driven in, is the dead-end mode, which often is also called deposition mode. Here, all feed water is forced through the membrane, which implies that the rejected

components of the feed are accumulated (deposited) at the membrane surface in a so called fouling layer along the capillary. Furthermore, dead-end mode implies that there is one point in the capillary where the longitudinal velocity of the feed water flow through the capillary becomes zero. If the feed water enters the capillary only from one side, this point will be on the opposite end of the capillary. If the feed water enters the capillary from both sides, e. g. in membrane cartridges applied in the XIGA^{TM} concept, this point will be somewhere within the capillary length, depending on inlet pressure on both sides of the capillary and membrane resistance. However, even if there is a feed water flow tangential to the membrane surface inside the capillary, the velocity is much smaller than in cross-flow mode, which will be described next.

In cross-flow mode, which is also often called suspension mode, the feed flows tangential to the membrane surface inside the capillary with the inlet feed water flow entering the module at a certain composition. In both configurations the feed composition inside the module changes, i. e. gets more concentrated as a function of distance in the module. The feed flow will be separated in cross-flow mode into two: a filtrate and a retentate flow. Common cross-flow velocities of the retentate flow at the outlet of the capillary applied in potable water and wastewater treatment are in the range of 1 – 6 m/s (KOLLBACH ET AL. (1997)). Both, cross-flow and dead-end mode are illustrated schematically in Figure 2.5.

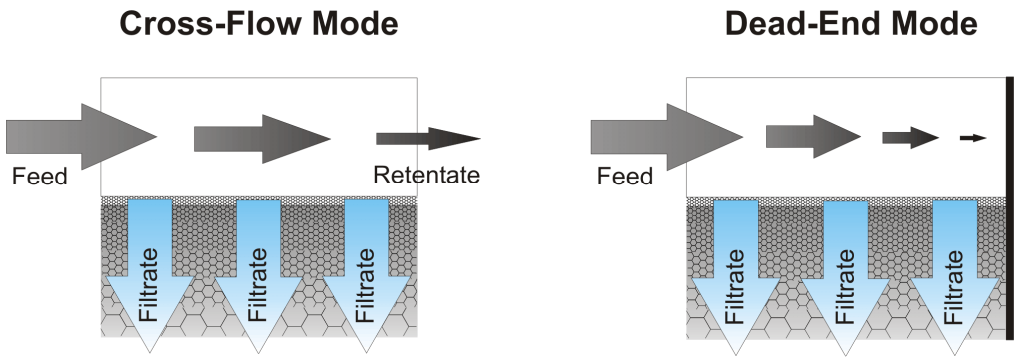

Figure 2.5: Schematic drawing of the two basic hydraulic configurations applied in MF/UF

Dead-end configurations are often used in potable water treatment due to the considerable lower energy consumption compared to cross-flow systems. Here, the higher energy consumption is due to the pressure drop on the feed side in the

capillary, aroused by the necessary cross-flow velocity. The energy demand of dead-end operated processes is in the range of about 0.1 – 0.5 kWh/m³$_{Filtrate}$ (MELIN AND RAUTENBACH (2004), PANGLISCH ET AL. (1997)), which is much lower than in cross-flow operated processes with about 1 – 7 kWh/m³$_{Filtrate}$ (MELIN AND RAUTENBACH (2004), KOLLBACH ET AL. (1997)). However, with increasing content of solids in the feed water, dead-end operation becomes more and more inappropriate because of the higher risk to clog the capillaries, or membrane module respectively, and because of the loss of filtrate due to distinct higher backwashing frequencies, which themselves consume high amounts of energy.

Capillary membrane filtration systems are designed and constructed in one or more discrete water production units, also called racks, trains or skids. A unit consists of a number of membrane modules that share feed and filtrate valving, and the individual units can usually be isolated from the rest of the system for testing, cleaning or repair. A functional diagram of a typical pressure driven capillary membrane filtration system is shown in Figure 2.6.

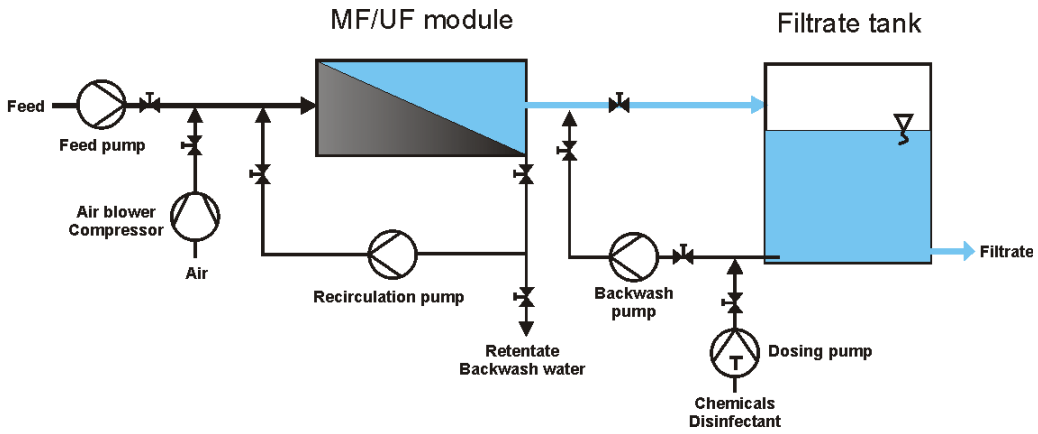

Figure 2.6: Functional diagram of a pressure driven MF/UF module

In the example shown, the system can be operated in dead-end or cross-flow hydraulic configuration, with and without recirculation of the retentate, depending on the valve settings.

2.1.5 Operation of membrane processes

Generally, the permeability P of a porous system is defined as the volume flow $\dot{V}$ per unit system area A and unit driving force, here the pressure difference Δp with:

$$P = \frac{\dot{V}}{A \cdot \Delta p} \qquad \textbf{Equation 2.3}$$

If the porous system is a UF or MF membrane, then the permeability of the membrane P_M is defined as the fluid flow $\dot{V}$ per unit membrane surface area A_M – which delivers the filtrate flux J - and transmembrane pressure difference TMP. Hence, permeability is also often called specific flux and is calculated as shown in Equation 2.4 with:

$$P_M = \frac{J}{TMP} = \frac{\dot{V}}{A_M \cdot TMP}. \qquad \textbf{Equation 2.4}$$

According to Darcy's law, compare Equation 2.2, P_M is inversely proportional to the dynamic viscosity of the fluid η and the total resistance R_{Tot} acting against the transport of fluid through the membrane as shown in the following Equation 2.5:

$$P_M = \frac{1}{\eta \cdot R_{Tot}}. \qquad \textbf{Equation 2.5}$$

The TMP can be calculated according to its hydraulic configuration, which, in cross-flow mode, is the arithmetic mean of the inlet and outlet pressure p_{in} and p_{out} minus the filtrate pressure, commonly called the backpressure $p_{Filtrate}$ as:

$$TMP = \frac{p_{in} + p_{out}}{2} - p_{Filtrate}. \qquad \textbf{Equation 2.6}$$

In dead-end mode the TMP is generally approximated by use of Equation 2.6. Here, it is assumed that the outlet pressure p_{out} at the dead-end of the capillary equals the inlet pressure p_{in}, which is in fact not true, even for clean membranes. This is because the pressure along the membrane surface and at the dead-end of the capillary depends significantly on membrane resistance and on length and inner diameter of the capillary and therefore varies more or less, see also chapter 3.5.1.

The resistance acting in opposition to the driving force, inhibiting the transport of water across the membrane, can be generally quantified according to the resistance

in series model. The model divides the total resistance R_{Tot} into two components: the intrinsic resistance of the membrane R_M and the resistance attributed to the coating layer R_{CL} due to fouling. Generally, fouling can be defined as the gradual accumulation of water components, i. e. foulants and/or scalants, on the membrane surface or within the porous membrane structure that inhibits the passage of water, resulting in an increased necessary pressure difference to let the water pass the membrane. Depending on kind of water components three types of fouling can be distinguished, i. e. organic fouling, colloidal particulate fouling, scaling due to crystal growth and biological fouling. Usually all types may occur during membrane filtration of surface waters and combinations of them are possible and probable.

To account for concentration polarisation, which is the gradual increase in concentration of accumulated substances at the membrane surface forming a boundary layer, an additional resistance term R_{CP} can be added to the total resistance equation as:

$$R_{Tot} = R_M + R_{CL} + R_{CP}, \qquad \textbf{Equation 2.7}$$

where R_{CP} is a function of operating parameters and physical properties. At low pressures, the R_{CP} term will be small compared to R_M and R_{CL}. At high pressures, the resistance of the boundary layer will increase and the R_{CP} term will be relatively large. R_M and R_{CP} should remain constant under constant operating conditions, the latter one after a given period of time when steady-state conditions are established. The increase in fouling during operation and the decrease in fouling as a result of backwashing and chemical cleaning causes R_{CL} to fluctuate. R_M can be experimentally determined by measuring the filtrate flux of pure water at constant TMP and temperature, hence at constant dynamic viscosity, and applying a known membrane area. With Equation 2.4 and Equation 2.5 the membrane resistance of the clean membrane can then be calculated with:

$$R_M = \frac{A_M \cdot TMP}{\eta \cdot \dot{V}}. \qquad \textbf{Equation 2.8}$$

The pure water flux as a measure of hydraulic permeability of the clean membrane depends on temperature. This temperature dependency equals the dependency of

the dynamic water viscosity on temperature. Hence, the membrane resistance itself is not significantly temperature dependent. Generally, the membrane permeability is normalised on a reference temperature, typically 20°C, for the purpose of monitoring the system productivity independent of changes in water temperature:

$$P_M^{20°C} = P_M \frac{\eta}{\eta^{20°C}} . \qquad \textbf{Equation 2.9}$$

The dynamic fluid viscosity η of the filtrate as a function of temperature T can be approximately expressed by following polynomial Equation 2.10:

$$\eta = (17.9098 - 0.6003 \cdot T + 0.01299 \cdot T^2 - 0.000134 \cdot T^3) * 0.0001, \qquad \textbf{Equation 2.10}$$

whereas the dynamic viscosity η of the filtrate at 20°C is approximately $\eta^{20°C} = 1 \cdot 10^{-3}$ kg/m/s. The given polynomial Equation 2.10 was derived by regression of listed values in VEREIN DEUTSCHER INGENIEURE (1988) and PERRY ET AL. (1984). It is important to note that the normalised permeability or flux does not represent an actual operating condition. This term simply represents what the flux or permeability would be at 20°C for a certain TMP and total membrane resistance R_{Tot}. Thus, changes in the value of flux during course of normal operation are indicative of changes in pressure and/or total resistance due to fouling and not temperature. While filtering the feed water, foulants are retained and accumulated, causing the fouling or cake layer build up on the membrane surface. The consequences of fouling in dead-end and cross-flow systems are shown schematically in Figure 2.7. In dead-end filtration the cake grows with time and, consequently, the flux decreases with time at constant TMP. Though, in practise it is more usual to have a constant flux operation and an increasing TMP over time due to the fouling layer growth as considered in this work. In relation to dead-end, flux decline is relatively smaller with cross-flow filtration and can be controlled and adjusted by proper module choice and cross-flow velocity, i. e. the velocity of the retentate flow when it leaves the capillary. But, an increased cross-flow velocity leads to an increased energy consumption due to the associated high pressure drop on the feed side of the membrane.

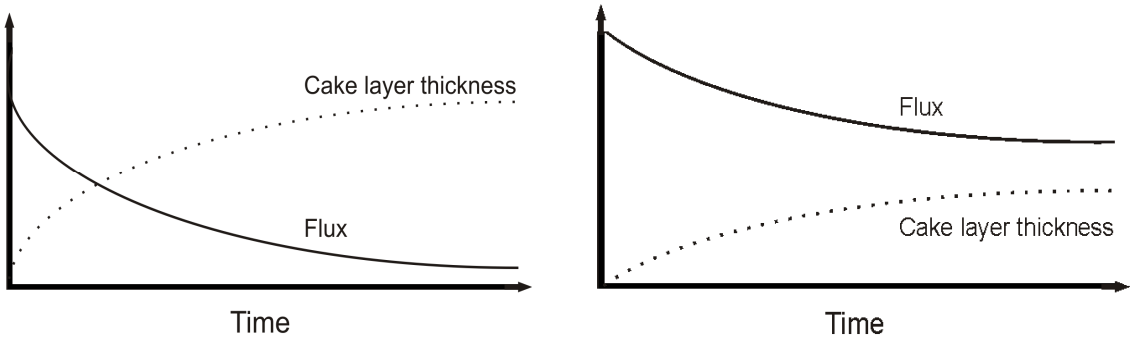

Figure 2.7: Flux decline (arbitrary scale) in dead-end (left) and cross-flow (right) operation and cake-layer build-up at constant TMP (arbitrary scale), (adapted from CHERYAN (1998) and MULDER (1991))

Typically, the accumulated foulants are removed by periodic mechanical cleaning procedures, usually conventional backwashing. This means in inside-out operated systems the filtrate is pressed from the outside to the inside of the capillary. Figure 2.8 shows the effect of backwashing and chemical cleanings schematically.

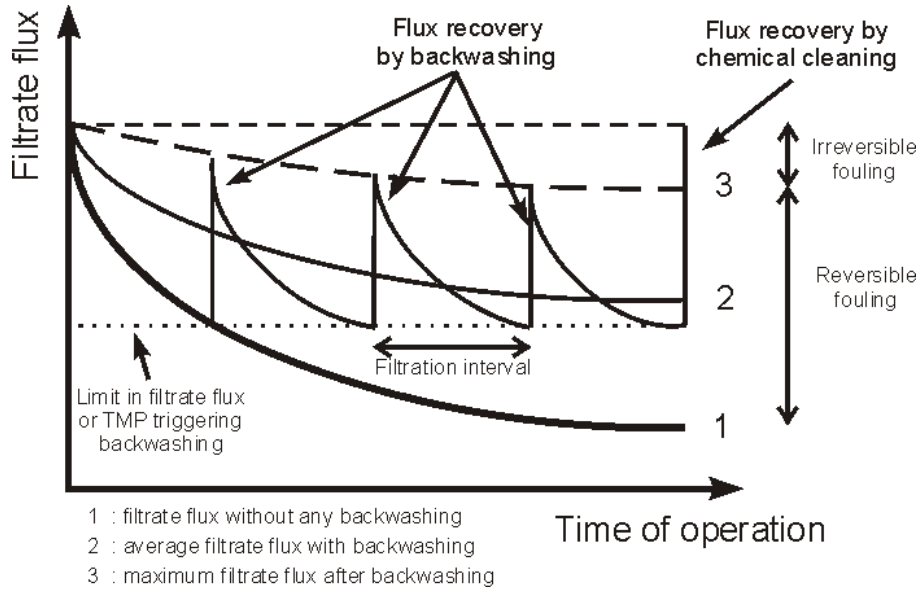

Figure 2.8: Effect of backwashing and chemical cleaning on filtrate flux (adapted from PANGLISCH (2001))

Reversible fouling layers can be removed by conventional backwashing, whereas irreversible fouling layers need a chemical cleaning. With each filtration interval the rate of irreversible fouling increases, i. e. the maximum filtrate flux after conventional backwashing decreases. At a certain limiting point, which may be reached after weeks or months of operation, a chemical cleaning has to be performed to achieve

the desired filtration flux again. This shows that the rate of irreversible fouling is not only a function of the feed water quality and operation conditions but also a function of the quality of the conventional backwashing procedure. A chemical cleaning which may be performed in-situ, i. e. cleaning in place (CIP) usually recovers the initial state of the filtration performance of the system completely but can be labour and chemical intensive and causes longer production downtimes. Chemicals used for chemical cleanings are often different cleaning solutions, oxidants like sodium hypochlorite, hydrogen peroxide as well as citric acid, hydrochloric acid, sulphuric acid or sodium hydroxide. Often, a conventional backwashing procedure is enhanced by dosing chemicals into the filtrate flow during backwashing, followed by soaking of the membrane with the chemical-dose water for some minutes before the chemicals are flushed out by an additional conventional backwashing. This kind of backwashing procedure is called chemical enhanced backwashing (CEB) and is usually performed fully automated several times per week of operation. Chemicals used are usually acids and bases like citric acid, hydrochloric acid, sulphuric acid or sodium hydroxide.

A further improvement of conventional backwashing efficiency may be achieved by use of a so called forward flush. Here, the capillaries are cleaned by flushing water, which may be feed water or filtrate, along the membrane surface. For inside-out operated processes it could be shown that the high shear forces achieved by forward flushing could be used to increase flux recovery (GIMBEL ET AL. (1996), FUTSELAAR AND WEIJENBERG (1998), FUTSELAAR ET AL. (1998)). If the modules are mounted vertically, this effect can be further improved by applying a two phase-flow, i. e. adding air to the flushing water flow (FUTSELAAR AND WEIJENBERG (1998), FUTSELAAR ET AL. (1998), POSPÍSIL ET AL. (2004)). But, the efficiency of an air-flush strongly depends on the diameter of the tubes; hence the air flush is best used in tubular membrane modules (VERBERK (2005)).

2.2 Hybrid membrane processes

In water, natural organic matter (NOM) is a complex mixture of particulate and dissolved components of both inorganic and organic origin that varies from one source to another (HOWE ET AL. (2002), WONG ET AL. (2002) and LEEUWEN ET AL. (2002)). NOM is a heterogeneous mixture with wide ranges in molecular weight (MW)

and functional groups (phenolic, hydroxyl, carbonyl groups and carboxylic acid). In water it is formed by autochthonous input such as algae and allochthonous input such as terrestrial and vegetative debris (ZULARISAMA ET AL. (2006)). Among these components, dissolved organic matter (DOM) is found to have the most detrimental effect on membrane performance as it can result in the formation of hardly reversible and/or irreversible fouling layers on the membrane surface and/or within the membrane pores (see chapter 2.1.3.2) due to direct adsorption onto the membrane material. DOM is a ubiquitous constituent in natural waters and is generally comprised of humic substances: polysaccharides, amino acids, proteins, fatty acids, phenols, carboxylic acids, quinines, lignins, carbohydrates, alcohols, resins, and inorganic compounds such as silica, alumino-silicates, iron, aluminium, suspended solids and microorganisms (bacteria and fungi) (ZULARISAMA ET AL. (2006)). Retention of DOM by porous membranes is generally determined by its molecular weight and structure, charge density and hydrophobicity. Furthermore, specific solution parameters including pH-value, ionic strength and presence of other solutes such as calcium and additionally membrane characteristics including hydrophobicity, charge and surface morphology play a decisive role (SCHÄFER (1999), HOWE (2001)). Hence, clear statements of retention efficiencies of DOM cannot be found in literature and published results vary strongly and are mainly given from the quantitative point of view. For instance, HOWE (2001) and HOWE AND CLARK (2002) showed that the majority of DOM does not foul MF and UF membranes and identified small colloidal matter as the primary foulant, as did CARROLL ET AL. (2000) and FAN ET AL. (2001) for instance. GRAY ET AL. (2004) showed for different raw waters that the hydrophobic components were the major foulant for the one and the hydrophilics for the other water. Yet, a good review is presented in the work of HOWE (2001) and AMY (2007), considering all aspects mentioned above.

As a result of degraded operation performance caused by NOM fouling layers, membrane processes can not be driven economically caused by a necessary increase of the backwash frequency and intensity, i. e. duration of backwashing or use of chemical enhanced backwashes (CEB) for example. Beside the retention of NOM additional interrelated treatment aims may arise depending on raw water quality. Those aims might be the reduction of colour, odour and trace organic compounds and cannot be solved by UF or MF alone. To get those challenging

problems and treatment tasks under control but still being able utilising the advantages of membrane filtration as treatment step, hybrid processes were developed and established.

Generally, hybrid processes are combinations of two or more separately and usually independently working processes like filtration, coagulation, sedimentation or adsorption. The feature of a hybrid process is that both processes already represent independent solutions, but develop additional new desired characteristics by their combination. Nevertheless, the terminology hybrid membrane process is often used in literature for the combination with different pre-treatment steps too. Depending on raw water quality, processes integrated with membrane processes in water treatment are most often such as coagulation/flocculation, sometimes followed by sedimentation, flotation or rapid sand filtration prior membrane filtration, often adsorption on powdered activated carbon, on particulate iron oxides or on ion exchange resins, but also biofiltration, oxidation and softening. The hybrid process considered in this work consists of the combination of coagulation and membrane filtration due to the increasing interest as outlined in Figure 2.9, illustrating the exponential development of production capacity and number of plants applying coagulation prior membrane filtration for the production of potable water, mainly from surface waters, until 2005. About 14 % of worldwide installed MF/UF plants are used in combination with coagulation and produce about 22 % of the total potable water produced by MF/UF plants, whereas the biggest plant is located in the Chestnut Avenue Water Works (Chestnut, Singapore) with a production capacity of 11,375 m³/h (JANSON ET AL. (2006)).

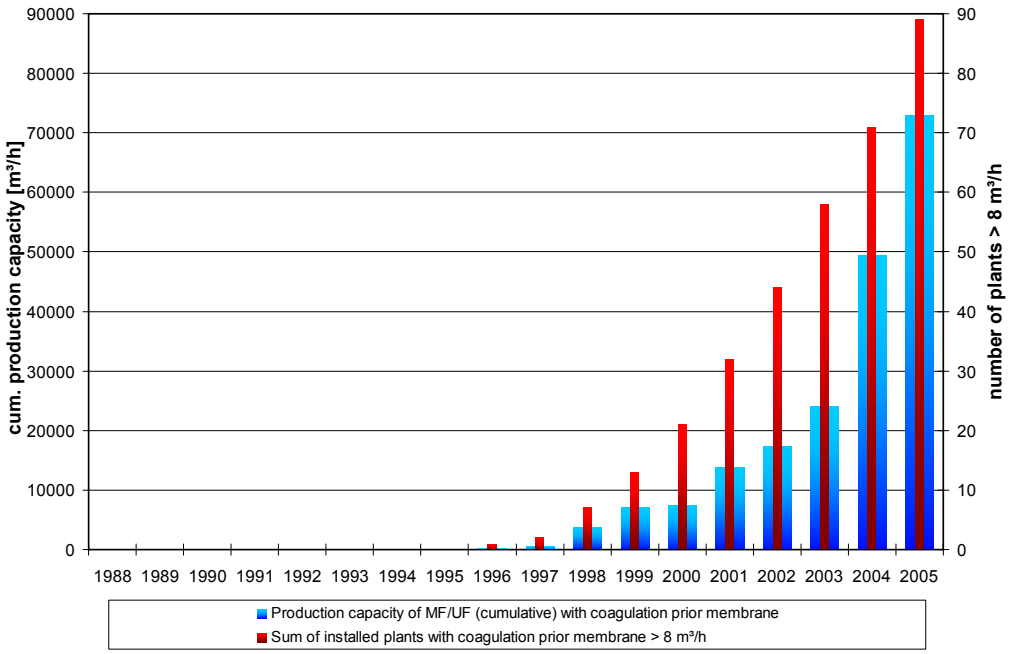

Figure 2.9: Cumulative production capacity (worldwide) and number of installed MF/UF plants > 8 m³/h with coagulation/flocculation prior membrane filtration (*Sources: Memcor, NMT, Pall, Zenon; 2005)

Dosing coagulants at adjusted coagulation pH-values into the raw water stream can be of high advantage for the upstream membrane process in terms of flux improvement and fouling reduction. This could be shown by several authors, for instance CARROLL ET AL. (2000), HOWE (2001), HAGMEYER ET AL. (2001), GUIGUI ET AL. (2002), LERCH ET AL. (2003), HAGMEYER ET AL. (2003), PIKKARAINEN ET AL. (2004), VAN LEEUWEN ET AL. (2005), LERCH ET AL. (2005B), JUNG ET AL. (2006), KABSCH-KORBUTOWICZ (2006), and CHEN ET AL. (2007) and references therein.

The intention of the process combination is that dispersed colloids, particles and other inorganic and/or organic water contaminants in stable suspension, may be transmuted into a preferable form for retention in the subsequent membrane step by dosing a suitable coagulant at certain coagulation conditions. Especially organic colloids such as humic substances and polysaccharides should be embedded into the formed flocs and retained by the subsequent membrane filtration step. As a result, those contaminants can neither adsorb onto nor interact otherwise with the membranes surface directly and therefore do not contribute to organic fouling. Instead they will be eliminated extensively from the membrane surface together with the flocs using an optimised backwashing procedure. Further, the flocs will build

highly permeable fouling layers, giving less resistance to fluid flow than layers build from smaller particles and colloids (LAHOUSSINE-TURCAUD ET AL. (1992), LEE ET AL. (2000), HOWE AND CLARK (2002), NGUYEN AND RIPPERGER (2002), KENNEDY ET AL. (2002), NGUYEN (2004), CHO ET AL. (2006)). Thus, performance will be improved and an economical process is possible, even if high coagulant dosages are necessary due to high contaminant loads. Especially for new installations or modernisation of water works it is a promising and cost-efficient alternative. Moreover, coagulation can be performed and optimised within the hybrid process as 'enhanced coagulation', whereas the term enhanced coagulation refers to the process of improved removal of disinfection by-product precursors (USEPA - DBPR (1999)). Hence, beside the advantage of achieving stable operation conditions, the hybrid process coagulation and membrane filtration will lead to an increased retention of NOM.

2.3 Modelling

Investigations on colloidal and particulate fouling were performed by several authors, e. g. PORTER (1972B), PORTER (1972A), GREEN AND BELFORT (1980), ALTENA AND BELFORT (1984), BELFORT AND NAGATA (1985), DREW ET AL. (1991), considering first more basic or simplifying models. The main emphasis here was usually set on calculating particle trajectories based on the thin-film or gel polarisation model, i. e. balancing filtration drag and a (solute) back-diffusive flow described by the 1st Fickian law for mass transport, combined with inertia induced lateral migration of matter, which was first observed by SEGRÉ AND SILBERBERG (1962A), SEGRÉ AND SILBERBERG (1962B) and investigated theoretically by KARNIS ET AL. (1966), COX AND BRENNER (1968), HO AND LEAL (1974) and VASSEUR AND COX (1976). The authors assumed that non-hydrodynamic forces between the particles and the surface are negligible. Further, the authors considered cross-flow filtration only, but different geometries like ducts, capillaries, tubes and/or channels with one or two permeable walls, non-interacting particles in the free solution, i. e. diluted suspensions at some distance from the membrane wall and filtrate flux being constant and independent of the axial coordinate. The used description of the velocity profiles for laminar flow in porous ducts was often based on the work of BERMAN (1953) and YUAN AND FINKELSTEIN (1956), whereas the used boundary condition at the boundary between the permeable wall and the free fluid was first presented by BEAVERS AND JOSEPH (1967).

A good review of research related to steady, single phase, two dimensional, isothermal, incompressible and internal laminar flow in porous walls, considering different flow regimes, boundary conditions and geometries was given by CHELLAM ET AL. (1995). FANE ET AL. (1982) postulated an alternative or additional mechanism for larger solids, founded on shear-induced transport or scour of the polarised layer by tangentially flowing feed suspensions. The model based on the analogy between suspension flow across a filter cake and the motion of a sediment-laden stream over a layer of settled sediment. DAVIS AND LEIGHTON (1987) introduced the shear-induced hydrodynamic diffusion mechanism to describe the lateral migration of particles away from the porous wall as the layer is sheared. At steady state, the effective particle diffusion within the layer is balanced by the convective flux of particles toward the porous wall due to the fluid flow into the wall. Though, FANE (1984) could show for stirred, i. e. cross-flow, and unstirred, i. e. dead-end filtration experiments that if the mechanisms are considered as simultaneous, a minimum in flux across porous membranes could be found at some particle diameter. Also WIESNER ET AL. (1989) and LAHOUSSINE-TURCAUD ET AL. (1990) showed that the minimum in particle transport with respect to particle size should result in a preferential deposition of particles of a certain diameter that correspond to this minimum. Their experiments showed further that the removal of submicron materials, i. e. colloidal organics and inorganics, by coagulation to form larger flocs may improve the performance of membrane filtration units. The maximum floc size was found for cross-flow and dead-end batch experiments when the zeta potential of the flocculated suspension was near zero. However, interactions between the coagulant and the membrane were not considered. Later, CHELLAM AND WIESNER (1992) extended the theory developed by ALTENA AND BELFORT (1984) to include the effects of sedimentation, London-van der Waals attraction, double layer repulsion and added mass of entrained fluid. However, these effects were discussed even earlier, e. g. by HUNG AND TIEN (1976), but not introduced as significant effects into the models, as it was done afterwards by several authors, e. g. SONG AND ELIMELECH (1995), ALTMANN AND RIPPERGER (1997), HARMANT AND AIMAR (1996), BACCHIN ET AL. (1995), PANGLISCH (2001) and NGUYEN (2004).

It becomes clear that accurate modelling of flow and particle or floc trajectories leading to deposition and fouling layer formation in pressure driven membrane processes is inhibited by the complex couplings in the flow equations along with any

added effect of variable particle, floc and membrane properties. Due to the rapid computer development in the last decade, accompanied with improved computational capacity, increasingly more complex computations can be accomplished nowadays. While models of fluid flow in porous ducts, particle deposition and fouling with varying degrees of complexity have been developed as described above, reports of the use of CFD have only recently appeared. For instance, WILEY AND FLETCHER (2002) and WILEY AND FLETCHER (2003) developed a general CFD model of concentration polarisation and fluid flow in pressure driven membrane processes, which has been tested and validated against semi-analytical solutions and shown to perform correctly from quantitative and qualitative perspective. They stated that one advantage of CFD models is that they contain specific equations for the cases to be investigated, but that they can be readily modified to encompass any combination of variations in the parameters of interest. Another model was published by KROMKAMP ET AL. (2005), who developed a model for suspension flow and concentration polarisation in cross-flow MF with shear induced diffusion as back-transport mechanism. Here, a more realistic approach was found to be especially significant for the calculation of the fouling layer profile at the beginning and the end of the membrane. A good prediction of a three-dimensional CFD model for calculating the flux through a cross-flow driven MF was presented by RAHIMI ET AL. (2005). Even here, the results and validation with laboratory experiments showed that flux predictions were more accurate in comparison with simple models. BACCHIN ET AL. (2006B) published the results of a CFD model accounting for colloidal phase transition leading to the formation of a deposit from the accumulated concentration polarisation phase in cross-flow MF. The model was used to determine the critical flux, predicting filtration conditions where particle accumulation occurs or where it is avoided. The predicted values were about 4 times larger than observed experimentally. This discrepancy was explained by heterogeneities of the membrane material which effected the local permeate flux and was not embedded into the CFD code. Even if such reports have only recently appeared, CFD is arising more and more interest and is increasingly applied also in other fields in water research (DO-QUANG ET AL. (2000), SCHWINGE ET AL. (2004), RANADE AND KUMAR (2006), SUBRAMANIA ET AL. (2006), KOUTSOU ET AL. (2007)).

3 Theoretical considerations and modelling

3.1 Velocity and concentration profiles in capillaries with permeable walls

3.1.1 Verification of the flow regime and start-up length

The axial flow regime inside the porous capillary is assumed to be laminar according to the general accepted transition between laminar and turbulent flow in a non-porous tube at a critical Reynold number $Re \leq 2300$. Additionally, BELFORT AND NAGATA (1985) found that the onset of turbulence was delayed to critical Reynold numbers of about $Re \leq 4000$ for flows in porous tubes when compared to flows in non-porous tubes. The capillary Reynold number Re_C can be calculated as shown in Equation 3.1:

$$Re_C = \frac{v \cdot d_C}{\nu}, \qquad \textbf{Equation 3.1}$$

where v denotes the axial fluid flow velocity, d_C denotes the capillary diameter and ν denotes the kinematic fluid viscosity. For the largest considered capillary diameter of 5 mm the critical Re number will be exceeded at an average axial flow velocity of about 0.8 m/s and at about 8.0 m/s for the smallest capillary diameter of 0.5 mm. Figure A.1 in the appendix illustrates calculated capillary Re numbers for porous tubes for different capillary diameters vs. the average axial flow velocity in the capillary lumen at a temperature T = 20°C. For example, in dead-end operation mode driven 1 m long capillaries with a capillary diameter of 0.5 mm could thus theoretically be operated in laminar flow regime up to a flux of about 3600 L/m²/h in porous capillaries as shown in Figure 3.1. The shown values are quite far from reality for dead-end driven UF and even MF membrane systems. Considering a common flux of up to 100 L/m²/h for a dead-end driven UF capillary of 1 m in length at T = 20°C, an average axial flow velocity up to 0.25 m/s is achieved depending on the capillary diameter. Hence, the capillaries will always reveal laminar flow as indicated in Figure A.2. Therefore, a laminar flow regime inside the capillary lumen will be considered throughout this work.

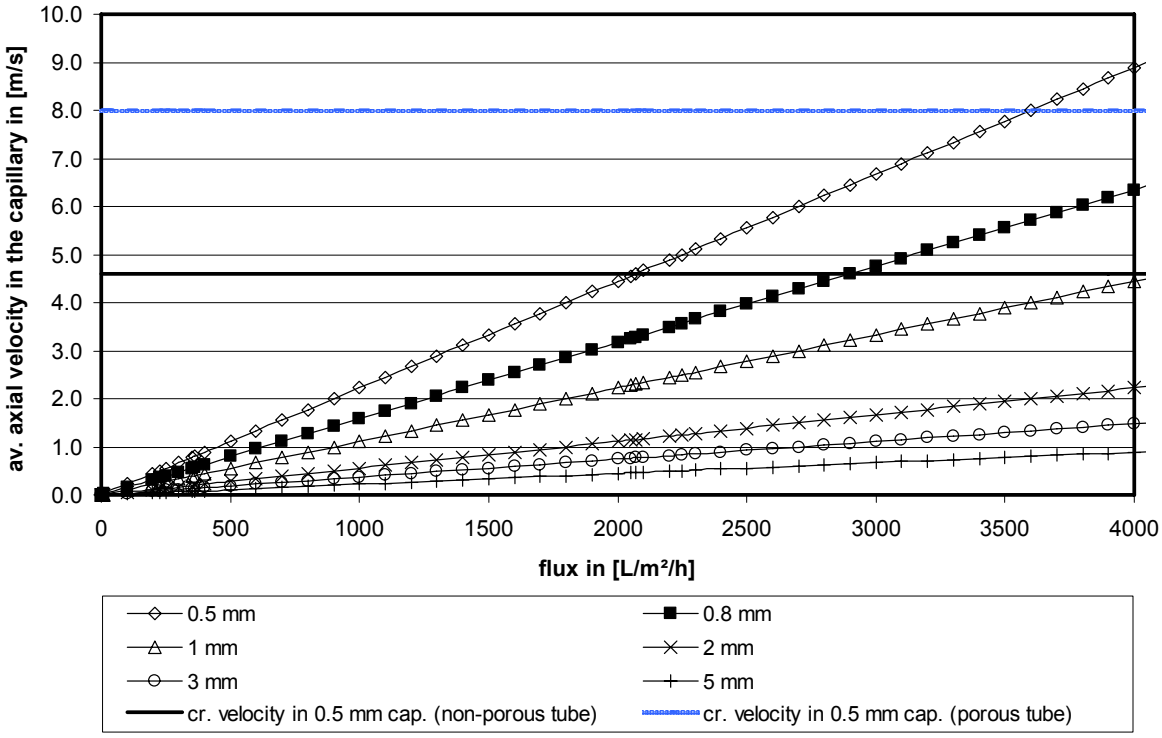

Figure 3.1: Average axial flow velocity in the capillary lumen vs. flux for capillaries of 1 m in length for different capillary diameters

However, when the fluid flows into one of the numerous of capillaries in a membrane module at one front side, the velocity of the flow at the capillary inlet can be regarded as constant over the whole single capillary diameter, because the capillary diameter will be very much smaller than the module diameter. Then, after the fluid entered the capillary, a laminar flow profile will be developed immediately in it. Hence a so called start up length for the development of the complete laminar flow profile in the capillary has to be considered theoretically. HÄNEL (1992) presented an estimated start up length with:

$$l_{su} = 0.03 \cdot Re_C \cdot d_C . \qquad \textbf{Equation 3.2}$$

Relating l_{su} to the capillary length l_C = 1 m delivers Figure 3.2 for different capillary diameters and common operative Re numbers in logarithmic scale. In case of capillaries operated with fluxes generally smaller than 100 L/m²/h, which corresponds to an inlet Reynolds number of about $Re_C \leq 111$, the start up length was calculated to be shorter than 0.23 % of the total capillary length for capillaries with a diameter of d_C = 0.8 mm. For the largest capillary diameter of d_C = 5 mm, this start up length was

calculated to be shorter than 1.67 %. Hence, a capillary of 1 m in length will show a start up length of about 0.23 cm for capillaries with 0.8 mm and 1.67 cm for capillaries with 5 mm in diameter respectively.

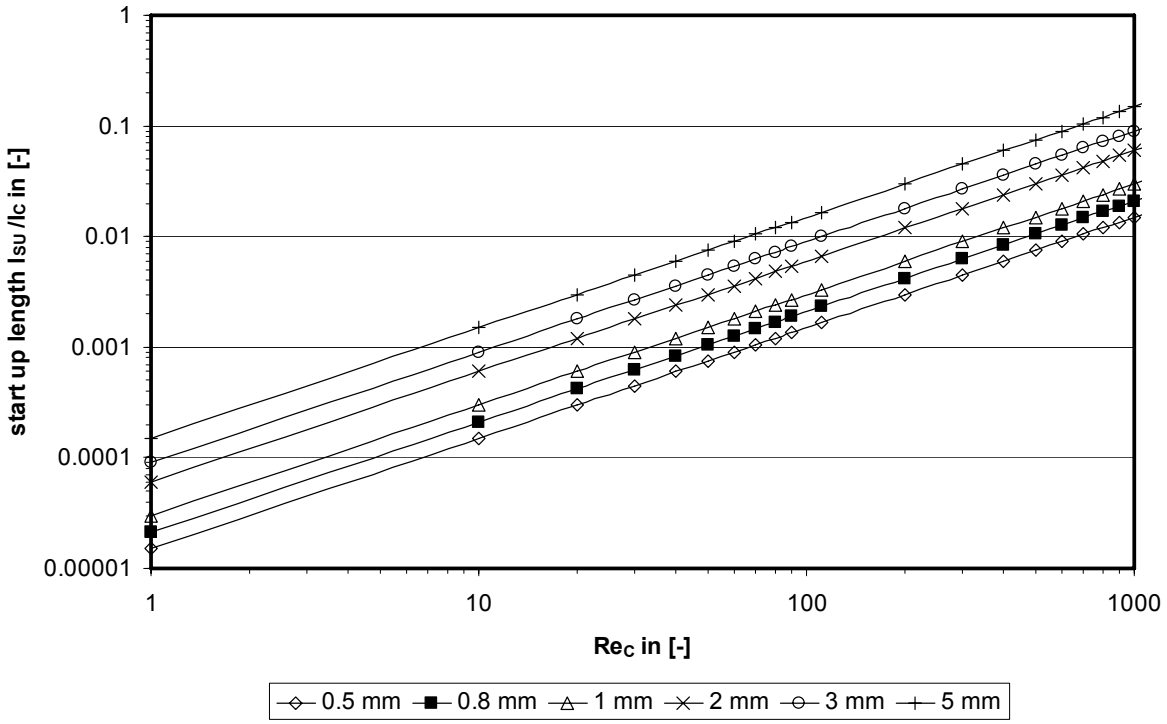

Figure 3.2: Start up length l_{su}/l_C vs. Re_C number for different capillary diameters logarithmic scale

All capillaries used in the experimental part of this work were potted at the capillary inlet over a length of about 1 to 3 cm, similar to capillaries in membrane modules. Here, the flow in the potting represents a real Poiseuille pipe flow. Due to this, a complete developed laminar flow profile can usually be assumed when the fluid enters the part of the capillaries where filtration occurs. However, the developed model can cope with both, developed and undeveloped laminar flow profiles.

3.1.2 The Navier-Stokes equations for laminar flow

Fundamental solutions for the hydrodynamics of flow through a membrane capillary with porous walls start from the Navier-Stokes (NS) equations which for a constant property fluid of density ρ and kinematic viscosity ν in presence of an external volume force F reads in vectorial notation (BIRD ET AL. (2002)):

$$\frac{\partial \vec{u}}{\partial t} + (\vec{u} \cdot \nabla)\vec{u} = \vec{F} + \nu \Delta \vec{u} - \frac{1}{\rho}\nabla p \,. \qquad \textbf{Equation 3.3}$$

Here, $\vec{u}$ denotes the velocity vector, $\vec{F}$ the external force vector (such as gravity), p the pressure and t the time. Together with appropriate boundary conditions and the mass conservation law, also known as the equation of continuity, as:

$$\nabla \cdot \vec{u} = 0 \,, \qquad \textbf{Equation 3.4}$$

this leads to a complete description of the isothermal fluid motion in the capillary.

Due to the given symmetry of the capillary it was chosen to use cylindrical coordinates in this work as indicated in Figure 3.3. Here, z denotes the longitudinal or axial distance coordinate and r denotes the radial distance coordinate of the capillary. Figure 3.3 shows the coordinate system of the considered 2-D cylindrical capillary membrane whose porous walls are separated by a distance d_C, the diameter of the capillary.

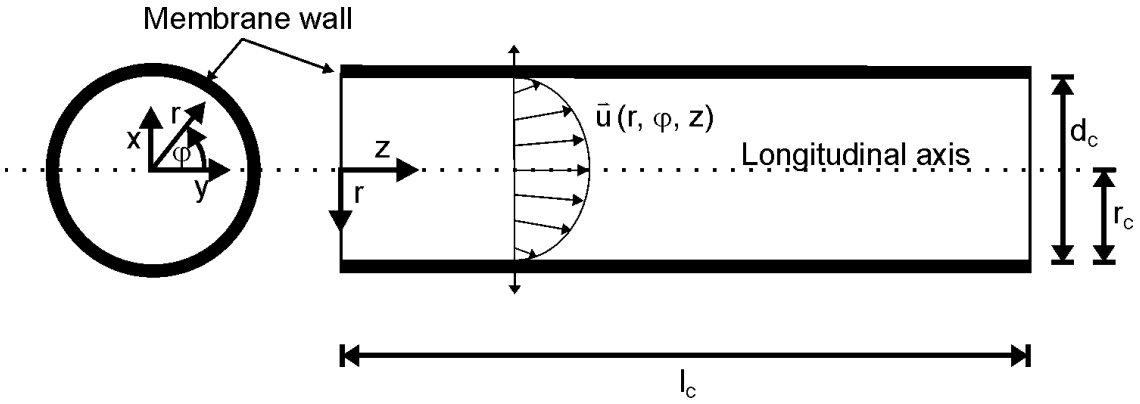

Figure 3.3: Coordinate system of the capillary membrane

Generally, the NS equations describe the flow in viscous fluids through momentum balances for each of the components of the momentum vector in the different spatial dimensions, i. e. the r, φ and *z* direction in cylindrical coordinates. Hence, the velocity vector and the external force vector are defined as $\vec{u} = [u_r, u_\varphi, u_z]^T$ and $\vec{F} = [F_r, F_\varphi, F_z]^T$ respectively. For the chosen coordinate system the NS equations can be generically expressed for each direction as presented by BIRD ET AL. (2002) for instance, given in the appendix, chapter A.3.

3.1.3 The convection and diffusion equation

Mass or concentration distribution arising from the flow of matter in the membrane capillary can be generally described by mass balances, applying the convection and diffusion equation, based on Fick's 1st law and the continuity equation, together i. e. Fick's 2nd law, written in vectorial notation as (BIRD ET AL. (2002)):

$$\frac{\partial c_j}{\partial t} + \nabla \cdot \left(-D_j \cdot \nabla c_j + c_j \cdot \vec{u} \right) = R_j , \qquad \textbf{Equation 3.5}$$

where c_j denotes the concentration of species j, D_j denotes its diffusion coefficient of this species, $\vec{u}$ denotes generally for a velocity vector and R_j denotes the reaction term. In the latter, arbitrary kinetic expressions of reactants and products can be introduced, for example the consumption or production of c_j by chemical reaction. The velocity vector can be generally obtained by coupling the differential diffusion and convection equation with the momentum balance as described in the previous chapter 3.1.2. Considering only one diffusive species without any chemical reaction, i. e. neglecting the reaction term R, Equation 3.5 can be written as:

$$\frac{\partial c}{\partial t} + \nabla \cdot \left(-D \cdot \nabla c + c \cdot \vec{u} \right) = 0 . \qquad \textbf{Equation 3.6}$$

The expression within the brackets represents the mass flux vector $\vec{N}$, where the first term describes the transport by diffusion and the second represents the convective flux with:

$$\vec{N} = -D \cdot \nabla c + c \cdot \vec{u} . \qquad \textbf{Equation 3.7}$$

Using cylindrical coordinates and assuming a constant diffusion coefficient D, Equation 3.6 can be written as (BIRD ET AL. (2002), COMSOL AB (2006B)):

$$\frac{\partial c}{\partial t} + u_r \cdot \frac{\partial c}{\partial r} + \frac{u_\varphi}{r} \cdot \frac{\partial c}{\partial \varphi} + u_z \cdot \frac{\partial c}{\partial z} = -D \cdot \left[\frac{1}{r} \frac{\partial}{\partial r} \left(r \cdot \frac{\partial c}{\partial r} \right) + \frac{1}{r^2} \cdot \frac{\partial^2 c}{\partial \varphi^2} + \frac{\partial^2 c}{\partial z^2} \right] . \qquad \textbf{Equation 3.8}$$

3.2 The flow of porous floc aggregates

While filtering floc suspensions in an inside-out driven capillary membrane, concentration and therefore effective suspension viscosity will change depending on the axial and radial coordinates in the capillary. An increased concentration leads to a change of the fluid velocities in longitudinal and radial direction. Additionally, hydrodynamic forces, such as drag forces, acting on the flocs in the suspension are influenced by the fractal structure and inner porosity of the flocs. This is, because the fluid flow is around and through the porous aggregates. Both points will be briefly discussed in the following subchapters and correction functions will be derived and introduced to be used for the calculation of the acting forces and torques on the flocs in chapter 3.3. However, the flow through the fouling layer formed by deposited flocs is for the flow of the permeating fluid, i. e. water, through porous media only. Hence, the viscosity of water will be used without any correction functions within the formed fouling layers, compare chapter 3.4.6.

3.2.1 Effective floc suspension viscosity

LEIGHTON AND ACRIVOS (1987) presented the ratio of the dynamical or effective suspension viscosity and dynamical fluid viscosity depending on the particle concentration in suspension with:

$$\frac{\eta_S}{\eta} = \left(1 + 1.5 \cdot \frac{\phi}{1 - \frac{\phi}{\phi_{max}}} \right)^2 , \qquad \textbf{Equation 3.9}$$

where ϕ denotes the particle volume concentration in the suspension, η the dynamic fluid viscosity and η_S the dynamic suspension viscosity. ϕ_{max} is called the limit or maximum particle volume concentration in the suspension and was given by LEIGHTON AND ACRIVOS (1987) with 0.58 for rigid, spherical particles after fitting empirically for latex particles of diameter 46 µm and a shear velocity gradient of about G = 24 s^{-1}. A more general relationship was given by LIU AND MASLIYAH (1996), cited in LIU (1999), which is valid for both diluted and concentrated suspension flows of mono-sized spherical particles with:

$$\frac{\eta_S}{\eta} = \left[\left(1 - \frac{\phi}{\phi_{max}} \right)^{-2} + \left(k_E - \frac{2}{\phi_{max}} \right) \cdot \phi + \left(k_H - \frac{6}{\phi_{max}^{\ 2}} \right) \cdot \phi^2 \right]. \qquad \textbf{Equation 3.10}$$

Here, $k_E = 2.5$ denotes the Einstein constant and k_H the Huggins constant, the latter one depending on flow strength. At low velocities k_H is set to $k_H = 6.0$ and at high velocities k_H is set to $k_H = 7.1$. However, LIU (1999) did not give exact ranges for the flow velocities to be used. He showed that the experimental results could be best fitted for values of $\phi_{max} = 0.71$, which is close to the theoretical maximum particle volume concentration of spherical particles with $\phi_{max} = 0.74$, when the suspension flow was strong. The reason for this was found to be that the particles could fill into the gaps which were inaccessible in weaker suspension flows where the particle-particle alignment is more or less at random, leading to $\phi_{max} \approx 0.64$. If the particle concentration was high, i. e. up to values larger than $\phi > 0.54$, it could be shown that Equation 3.10 could be simplified to:

$$\frac{\eta_S}{\eta} = \left(1 - \frac{\phi}{\phi_{max}} \right)^{-2}. \qquad \textbf{Equation 3.11}$$

Considering now the filtration of floc suspensions some assumptions have to be taken to contribute for the porosity of the floc aggregates and its effect on viscosity of the bulk flow. It is assumed that the floc concentration in the bulk may vary from low to high concentrations. The maximum floc volume concentration was chosen to be $\phi_{F,max} = 0.74$, independent of flow strength and the Huggins constant was chosen to be $k_H = 7.1$. However, the maximum floc volume concentration in the concentration polarised layer and the coating layer at the membrane wall will be probably higher for real deformable, compressed and overlapping flocs than for spherical rigid particles (STRENGE (1993), PARK ET AL. (2004)). Further it is assumed that the effective viscosity in the porous floc is equal to the viscosity of the bulk flow as it is often assumed by several authors as stated by VEERAPANENI AND WIESNER (1996).

VAINSHTEIN AND SHAPIRO (2006) calculated the effective viscosity of porous aggregates in dilute suspension η_S and generalised the Einstein equation by introducing a correction factor c_β (β) with:

$$\frac{\eta_S}{\eta} = 1 + k_E \cdot \phi \cdot c_\beta(\beta). \qquad \textbf{Equation 3.12}$$

c_β (β) is a function of the Brinkman parameter β, defined as

$$\beta = \frac{a_F}{\sqrt{k}}, \qquad \textbf{Equation 3.13}$$

where k denotes the permeability coefficient of the porous floc and a_F the floc radius. VAINSHTEIN AND SHAPIRO (2006) presented extended equations for the calculation of the correction factor c_β (β), see appendix chapter A.4. The result is illustrated in the following Figure 3.4.

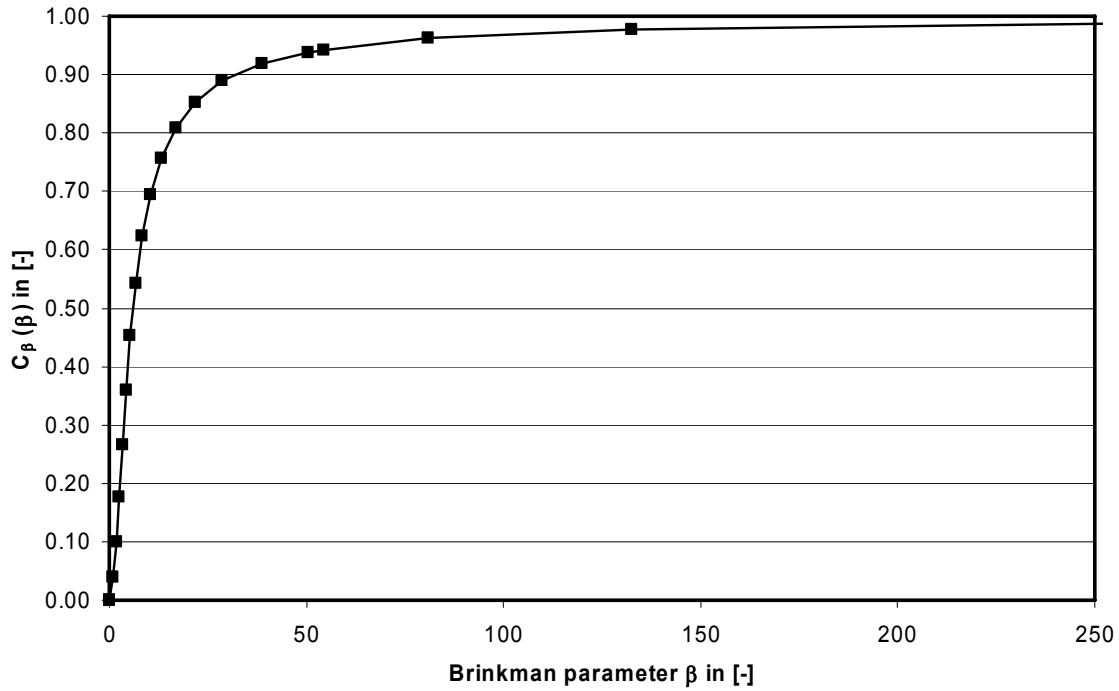

Figure 3.4: Correction factor c_β (β) as function of the Brinkman parameter β (VAINSHTEIN AND SHAPIRO (2006))

If β becomes infinity then c_β (β) becomes unity, which corresponds to the flow around an impermeable particle. This limit will be approached for a decreasing permeability coefficient k of the aggregate. VEERAPANENI AND WIESNER (1996) and PARK ET AL. (2004) presented different models for the description of the permeability of porous aggregates as functions of the aggregates porosity ε_F and the primary particle radius a_P. A selection of the presented permeability models is given in the appendix, chapter A.5 and is illustrated in Figure 3.5. The primary particle radius a_P = 12.25 µm was derived from particle size measurements as described in the experimental part of this thesis, see chapter 4.2. Since Happel's model agrees with the Kozeny-Carman model at low porosities and with the Brinkman and the Howells, Hinch, Kim and Russel model at high porosities, the Happel model was used to evaluate the hydrodynamics of the porous flocs. However, assuming that a porous floc consists of a number of solid spherical primary particles of radius a_P, the maximum packing density in the porous floc can be likewise chosen to be $\phi_{F,max}$ = 0.74. Hence, a minimum porosity of the flocs with $\varepsilon_{F,min}$ = 0.26 can be defined (see Figure 3.5).

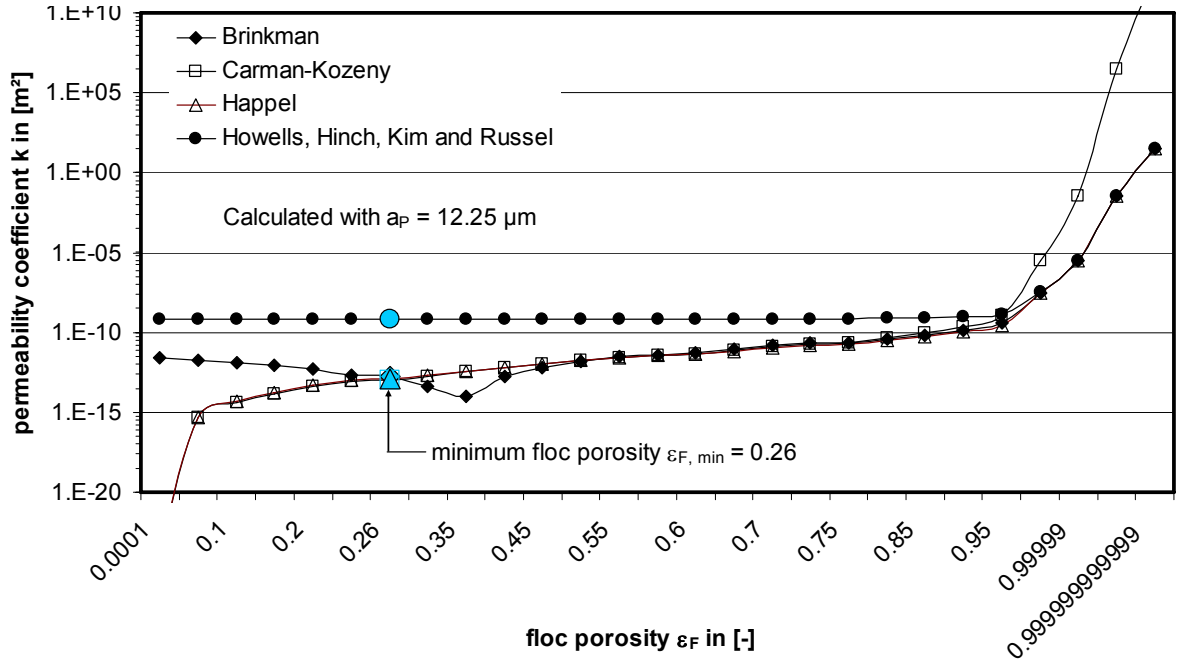

Figure 3.5: Permeability coefficient k of a floc as a function of the aggregates porosity ε_F based on different models presented in VEERAPANENI AND WIESNER (1996) and PARK ET AL. (2004) (not to scale)

Considering now the influence of the porosity on floc volume concentration, the correction factor $c_\beta(\beta)$ can be introduced with:

$$\phi_F = \phi \cdot c_\beta(\beta). \qquad \textbf{Equation 3.14}$$

Hence, Equation 3.10 becomes:

$$\frac{\eta_S}{\eta} = \left[\left(1 - \frac{\phi_F}{\phi_{F,max}}\right)^{-2} + \left(k_E - \frac{2}{\phi_{F,max}}\right) \cdot \phi_F + \left(k_H - \frac{6}{\phi_{F,max}^2}\right) \cdot \phi_F^2\right]. \qquad \textbf{Equation 3.15}$$

Figure 3.6 shows the calculated ratio of suspension and fluid viscosity, i. e. the effective floc suspension viscosity normalised by the fluid viscosity over particle and floc suspension volume concentration to illustrate the different influences of solid particles and porous flocs.

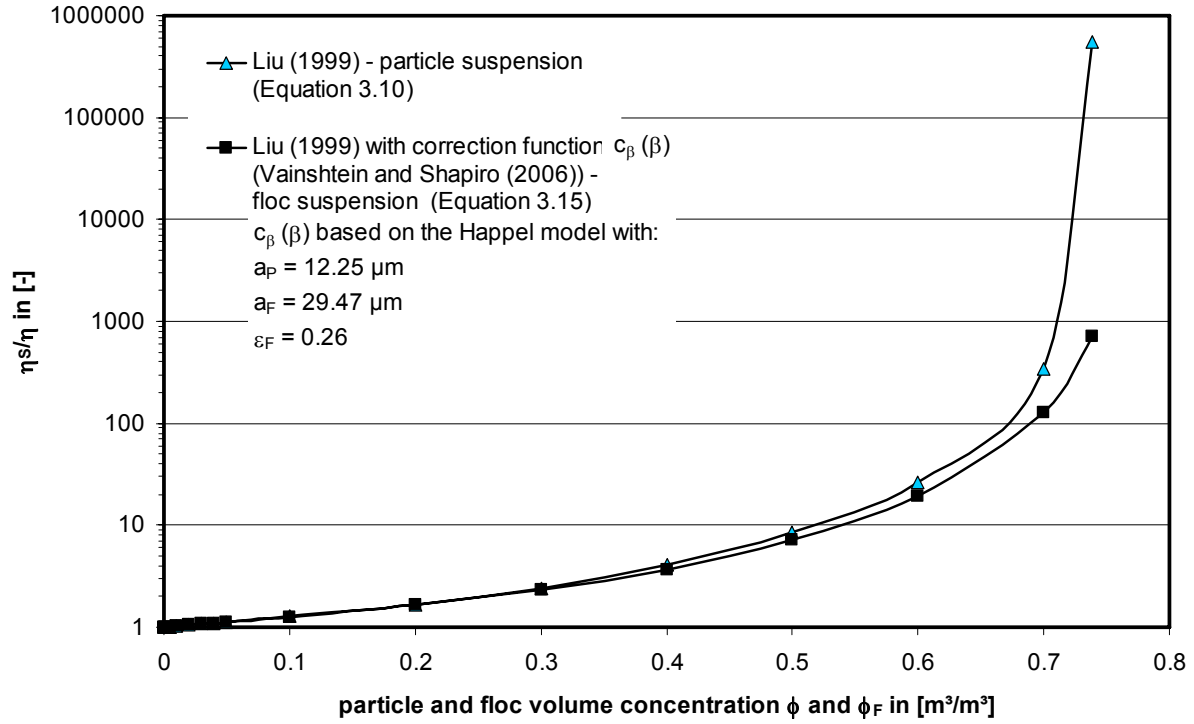

Figure 3.6: Effective particle and floc suspension viscosity normalised by the fluid viscosity over particle and floc volume concentration in [m³/m³], adapted from LIU (1999) and VAINSHTEIN AND SHAPIRO (2006)

With increasing particle and floc volume concentrations the influence of the correction factor $c_\beta(\beta)$ becomes more important and the effective suspension

viscosity resulting from solid particles will be increasingly higher than the effective suspension viscosity of a floc suspension.

For the calculation of the corrected floc volume concentration based on the work of VAINSHTEIN AND SHAPIRO (2006), c_β (β) was calculated using the Happel model. As for the primary particle radius a_P, the floc radius a_F was derived from particle size measurements as described in the experimental part of this thesis, see chapter 4.2. The influence of the floc volume concentration profile has to be considered for the calculations of the forces acting on the flocs by embedding a correction term to account for this concentration gradient in chapter 3.3. This additional influence is due to interparticle hindrance in the concentration profile, e. g. hindered settling or flow of the flocs due to the increasing floc concentration in direction of the membrane wall. LIU (1999) stated that the conventional Richardson-Zaki equation, normally used to characterise the settling velocity for arbitrary systems, can be used to account for this effect with:

$$f(\phi_F) = (1-\phi_F)^{\frac{16}{3}}, \qquad \textbf{Equation 3.16}$$

where $f(\phi_F)$ denotes the hindrance factor and is a function of the floc volume fraction ϕ_F. The correction by Richardson-Zaki can be expressed by using the dimensionless floc volume concentration as:

$$\phi_F^* = \frac{\phi_F}{\phi_{F,max}}, \qquad \textbf{Equation 3.17}$$

with $\phi_{F,max} \cong 0.74$ as the maximum floc volume concentration. Introducing Equation 3.17 into Equation 3.16 yields:

$$f_\phi^t(\phi_F^*) = \left(1-\phi_F^* \cdot \phi_{F,max}\right)^{\frac{16}{3}}. \qquad \textbf{Equation 3.18}$$

This correction function, called the floc hindrance factor, will be used throughout the thesis to account for the floc concentration profile leading to a lowered floc velocity at higher floc concentrations. Figure 3.7 illustrates the hindrance factor and the dimensionless floc volume concentration versus floc volume concentration.

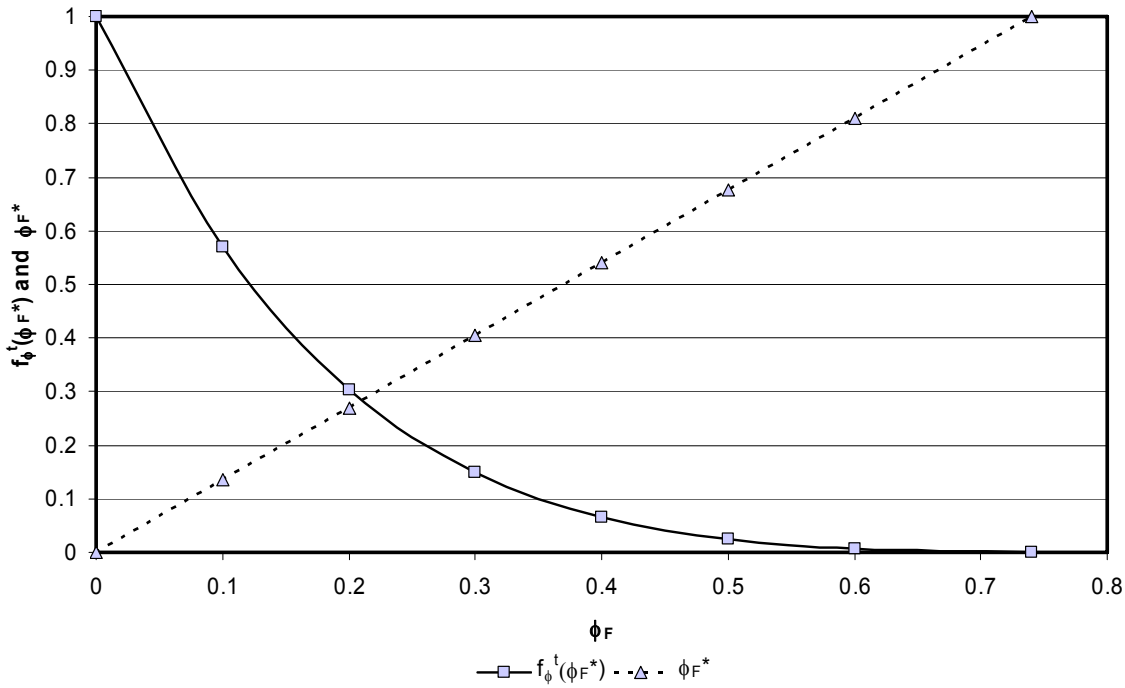

Figure 3.7: Hindrance factor and dimensionless floc volume fraction vs. floc volume fraction with a maximum floc volume fraction of $\phi_{F,max} = 0.74$, adapted from LIU (1999)

3.2.2 Drag coefficient of permeable flocs

Generally, the structural character of flocculated aggregates can be related to the mass fractal dimension, d_F, of the floc aggregate by setting its mass linear proportional to the size to the power of the mass fractal dimension, where $d_F = 3$ defines a sphere and $d_F = 2$ a sheet as in Euclidean dimensions. Typically, flocs have d_F values in the range 1.7 to 2.5, LEE ET AL. (2003). This means, for higher fractal dimensions the shape and structure of a floc aggregate will be more similar to a solid sphere, whereas for smaller fractal dimensions, the structure of the floc aggregates becomes more open and voluminous, more plane and cliffy, LERCH ET AL. (2004).

The floc aggregates porosity ε_F can be related to the primary particle radius a_P, the floc radius a_F and the mass fractal dimension d_F with:

$$\varepsilon_F = 1 - \left(\frac{a_F}{a_P}\right)^{d_F - 3} \qquad \textbf{Equation 3.19}$$

However, because the mass fractal dimension d_F could not be measured throughout the experimental work of this thesis, the hydrodynamic properties of fractal aggregates are evaluated by modelling them as porous aggregates governed by the Happel model as described above. Resistance to the fluid flow through the aggregate is predicted to increase with increasing fractal dimension, i. e. lower inner porosity. VEERAPANENI AND WIESNER (1996) showed that a reasonable estimate of the fluid drag force on a fractal aggregate may be obtained by assigning a constant volume-averaged porosity to the aggregate and using any of the expressions available in the literature for aggregates with uniform permeability. Therefore, VEERAPANENI AND WIESNER (1996) introduced an additional hydrodynamic parameter, the homogeneous drag coefficient Ω. The drag coefficient is defined as the force exerted by the fluid on a permeable aggregate of radius a, normalised by the force exerted by the fluid on an impermeable sphere of radius a. However, even water entering the inner parts of the floc may be immobilised and trapped within while the rest is flowing through the interior of the floc (STRENGE (1993)).

Assuming only flocs with homogeneous permeability, Ω can be calculated with:

$$\Omega_h = \frac{2 \cdot B}{3 \cdot \beta}$$ **Equation 3.20**

where B is a factor used for the calculation of Ω_h, as presented by MASLIYAH ET AL. (1987), cited in VEERAPANENI AND WIESNER (1996) and given in the appendix, chapter A.6. Figure 3.8 shows the homogeneous drag coefficient Ω_h illustrated versus floc porosity.

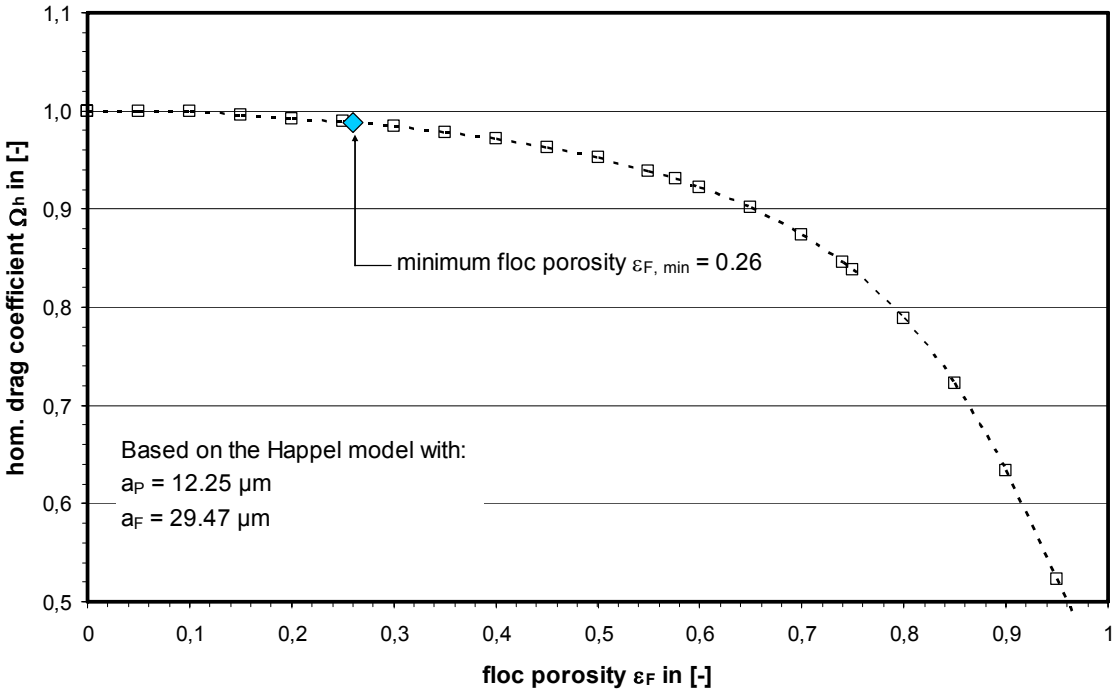

Figure 3.8: Homogeneous drag coefficient Ω_h versus floc porosity ε_F, adapted from VEERAPANENI AND WIESNER (1996) and MASLIYAH ET AL. (1987)

To account for the inner porosity of the flocs in suspension while calculating the acting forces and torques on the permeable flocs in the following chapter 3.3, an equivalent hydrodynamic floc radius a_{hF} can be introduced as proposed by VEERAPANENI AND WIESNER (1996) with:

$$a_{hF} = \Omega_h \cdot a_F . \qquad \textbf{Equation 3.21}$$

Including Ω_h, the hydrodynamic radius of the floc becomes smaller than the physical radius a_F of the floc but accounts for the inner porosity of the flocs and will be used for further calculations as far as hydrodynamic aspects are concerned. Calculations of distances, for example dimensionless parameters, and physical or electrochemical aspects are not effected by this adaptation of floc size. Please note further that flocs larger than a_F = 12.25 µm are generally considered to be formed from primary particles with radius a_P = 12.25 µm and therefore posses a smaller hydrodynamic radius $a_{hF} < a_F$. Flocs smaller than a_F = 12.25 µm are always modelled with $a_F = a_{hF}$.

3.3 Forces and torques acting on flocs

3.3.1 General remarks

At first, some thoughts have to be stated about the chosen notation used in the following for single particles and flocs and their suspensions in water. The referred authors usually applied rigid, solid and spherical particles in their experimental setup and in their theoretical considerations and derived equations. Consequently, the notations are often ‘particle’ or ‘sphere’ and will be introduced as such. Because this thesis is about fouling layer formation due to floc transport and deposition, the behaviour of floc aggregates is discussed in this work. Flocs are always thought of being aggregates consisting of iron or aluminium hydroxide with embedded particles and colloids. Particles and colloids are always considered as single primary particles and colloids, not being embedded in agglomerates. However, flocs are considered to be rigid and ideally spherical and of constant shape, but reveal basic floc properties such as porosity, low density and low zeta potential. This approach is reasonable as a first approximation because of the more macroscopic model investigated in this work. Hence, the presented equations are used for flocs without further adaptations if not stated otherwise.

Nevertheless, the coating layer build-up by floc deposition can be described by trajectory calculations. The floc trajectories can be derived from balances of the acting forces and torques according to the calculated and CFD modelled hydrodynamic conditions inside the capillary lumen and to physical properties of the flocs, usually dominant in the far-field region, and due to electrochemical properties of the flocs and the membrane, usually dominant in the near-field region. The acting forces and torques are introduced and discussed in the following. Various forces and torques act on flocs, which are supposed to be in continuous motion under the influence of these various forces and torques until they get deposited, or in case of cross-flow filtration mode until they get out of the system, i. e. the capillary. Figure 3.9 illustrates the acting forces and torques. Please note that the shown modelled floc and capillary are not illustrated to scale.

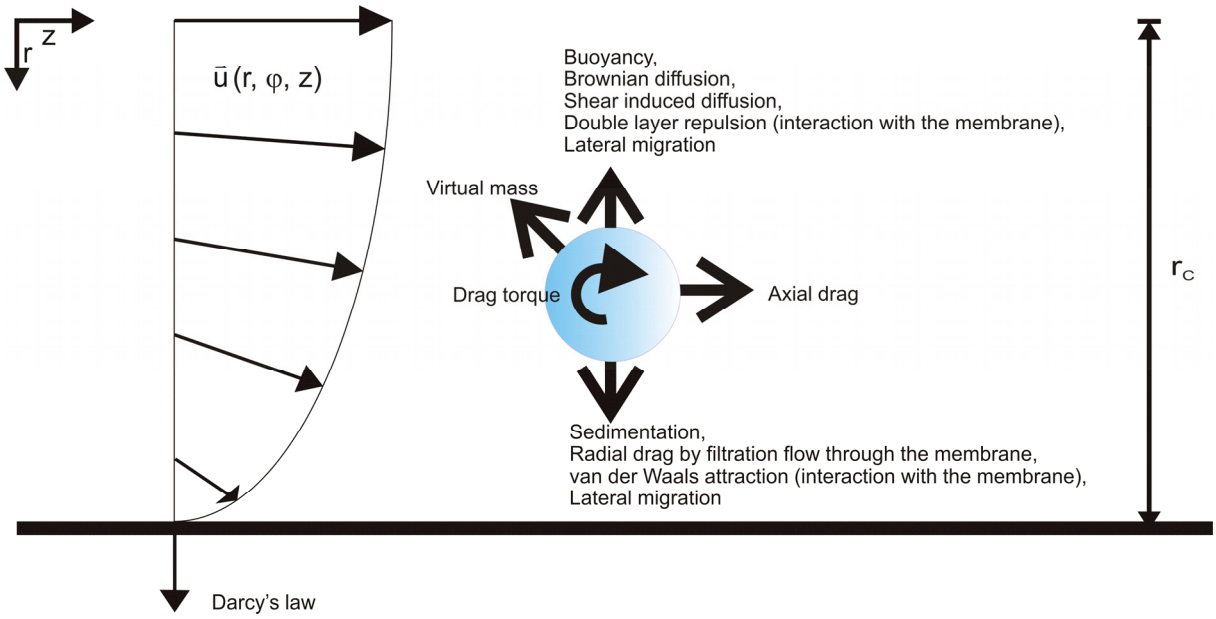

Figure 3.9: Forces and torques acting on a floc in the laminar fluid flow (schematic)

3.3.2 Drag

For a solid object moving through a fluid, drag is the sum of all hydrodynamic forces in the direction of the external fluid flow. For a sphere, here a floc with radius a_F, moving through a viscous incompressible and Newtonian fluid with velocity u_F, the drag force is dependent on the fluid properties, i. e. kinematic fluid viscosity ν or respectively the dynamic fluid viscosity η and fluid density ρ.

The relative velocity $\vec{u}_{Slip}$ between the fluid velocity $\vec{u}$ and the floc velocity $\vec{u}_F$ is termed the slip velocity and calculated as:

$$\left|\vec{u}_{Slip}\right| = \left|\vec{u} - \vec{u}_F\right|. \qquad \textbf{Equation 3.22}$$

The floc Reynolds number Re_F can be defined as:

$$Re_F = \frac{v_{Slip} \cdot 2\, a_{hF}}{\nu}, \qquad \textbf{Equation 3.23}$$

where v_{Slip} denotes the slip velocity component of $\vec{u}_{Slip}$ in longitudinal direction. The frictional drag force $\vec{F}_D$ acting in both, longitudinal and in radial flow direction on a floc

of hydrodynamic radius a_{hF}, is, at low Reynold numbers, linearly proportional to the floc velocity relative to the surrounding fluid, $\vec{u}_{Slip}$ with:

$$\vec{F}_D = -\xi \cdot \vec{u}_{Slip}, \qquad \textbf{Equation 3.24}$$

where ξ is the friction coefficient given by:

$$\xi = 6 \cdot \pi \cdot \eta \cdot a_{hF}. \qquad \textbf{Equation 3.25}$$

Since the theoretical treatment of this subject has grown out of the early work of Stokes, the above equation is often referred to as Stokes' law (ELIMELECH ET AL. (1995)). Stokes showed that the relation provided good agreement with his experimental results obtained at low Reynolds numbers, i. e. $Re_F < 1$ representing creeping flow (see Equation 3.23). This expression can be derived from the so called Stokes equation. The Stokes equation is a special, steady state case of the NS equation, given in Equation 3.3, where the inertia of the fluid, i. e. the left-hand side terms are neglected, assuming further that external forces are absent or negligible. Hence, the Stokes equation for creeping flow can be written as:

$$\frac{1}{\rho}\nabla p = \nu \, \Delta \vec{u}. \qquad \textbf{Equation 3.26}$$

An extension to account for inertia effects at large distances from the obstacle, here the floc, has been made by OSEEN (1910) (cited in ELIMELECH ET AL. (1995)) which has been shown to be valid for $Re_F \leq 5$ (SCHLICHTING (1955) cited in ELIMELECH ET AL. (1995)). However, both expressions given above apply only to flocs moving in an undisturbed, i. e. unbounded flow field of the fluid. Because this case is not given in capillary membrane filtration the presence of the boundary, i. e. the permeable membrane wall at finite distances, necessitates a modification to Stokes' law. Usually such modifications are given in the form of a dimensionless correction factor λ so that the drag force becomes:

$$\vec{F}_D = 6 \cdot \pi \cdot \eta \cdot a_{hF} \cdot \lambda \cdot \vec{u}_{slip}. \qquad \textbf{Equation 3.27}$$

However, a more detailed description of the various hydrodynamic forces arising from a moving particle or floc in a fluid flow field in the vicinity of a (porous) wall can be derived by superposition of three thresholds of the arising interactions between the sphere and the flow (GOLDMAN ET AL. (1967B), GOLDMAN ET AL. (1967A) and GOREN AND O'NEILL (1971), cited in MULDER (1990) and NAHRSTEDT (1999)). The effect of the so called hydrodynamic retardation, i. e. the parasitic drag due to the asymmetric flow field in the vicinity of a (porous) wall, will be corrected by correction functions $f(\delta_{FM}^*)$ for the acting forces and $g(\delta_{FM}^*)$ for the acting torques as discussed in the following. The finite distance δ_{FM} between the moving floc surface and the membrane wall is given by:

$$\delta_{FM} = r_C - r - a_F, \qquad \textbf{Equation 3.28}$$

where a_F denotes the radius of the floc as illustrated in Figure 3.10.

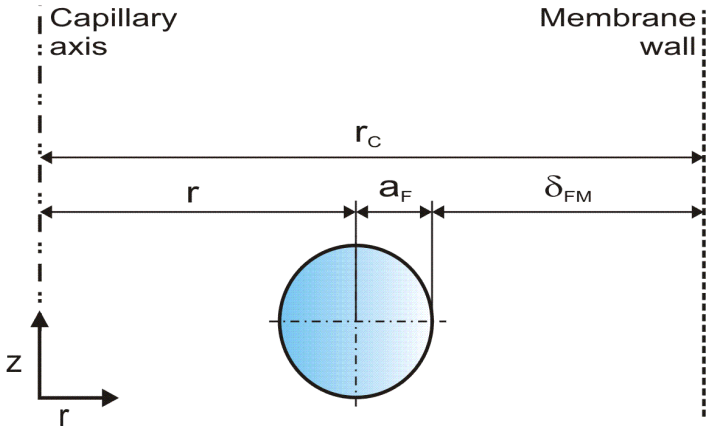

Figure 3.10: Determination of the finite distance δ_{FM} between the moving floc surface and the membrane wall, (not to scale)

The dimensionless distance between the moving floc and the membrane wall δ_{FM}^* is defined as:

$$\delta_{FM}^* = \frac{\delta_{FM}}{a_F}. \qquad \textbf{Equation 3.29}$$

The dimensionless correction functions $f_r^t(\delta_{FM}^*)$, $f_\varphi^t(\delta_{FM}^*)$, $f_z^t(\delta_{FM}^*)$, $g_\Phi^t(\delta_{FM}^*)$, $f_Z^r(\delta_{FM}^*)$, $g_\Phi^r(\delta_{FM}^*)$, $f_r^m(\delta_{FM}^*)$, $f_z^m(\delta_{FM}^*)$ and $g_\Phi^m(\delta_{FM}^*)$ account for the hydrodynamic retardation

excited by the membrane wall. PANGLISCH (2001) mentioned that $f_r^t(\delta_{FM}^*)$ and $f_\varphi^t(\delta_{FM}^*)$ describe the same wall effect in a capillary, because the velocities in direction of the coordinates r and φ are perpendicular and both are orientated to the membrane wall. Hence $f_r^t(\delta_{FM}^*)$ equals $f_\varphi^t(\delta_{FM}^*)$ and just $f_r^t(\delta_{FM}^*)$ will be used in the following. It has to be pointed out that the used approximations and interpolations derived by MULDER (1990) are valid only for the motion of particles in the direct vicinity of just one plane and not for a two dimensional Poiseuille flow in a capillary. However, PANGLISCH (2001) showed for the translatory velocities that the dimensionless functions given by MULDER (1990) could be validated also with correction functions for a two dimensional Poiseuille flow presented in literature, e. g. HO AND LEAL (1974). Furthermore, PANGLISCH (2001) stated that these correction functions are valid over the whole cross section of a capillary, except for $f_r^t(\delta_{FM}^*)$. GOREN (1979) showed for particles approaching a permeable wall, that the dimensionless function $f_r^t(\delta_{FM}^*)$ did not become infinite at the permeable wall as it should for impermeable walls but aims a finite value depending on size and resistance given by the permeable wall, i. e. the membrane resistance R_M. Hence, $f_r^t(\delta_{FM}^*)$ at the membrane wall becomes:

$$f_r^t(0) = f_{r,max}^t = \sqrt{\frac{2}{3} \cdot R_M \cdot a_F} \; . \qquad \textbf{Equation 3.30}$$

The drag force increases as the gap between the approaching floc and the wall is reduced but the increase becomes significantly less pronounced as the permeability of the wall increases. For finite wall permeability, a finite hydrodynamic force on the floc is expected even for the floc coming into contact with the permeable wall. This is in contrast to the infinitely large drag force predicted for impermeable walls as can be seen in Figure 3.11. PANGLISCH (2001) introduced an approximation to calculate the correction function $f_r^t(\delta_{FM}^*)$. On the one hand, his approximation accounts for the influence of the permeable wall at short dimensionless distances δ_{FM}^* but on the other hand for the negligible influence of the permeable wall for larger dimensionless distances δ_{FM}^*. Hence, his approximation will be used to calculate the correction function $f_r^t(\delta_{FM}^*)$ at permeable walls. If impermeable walls have to be considered,

e. g. when modelling pottings as done in the experimental part, see chapter 4, the dimensionless function given by MULDER (1990) was applied. All used equations for the calculation of the correction functions discussed above are listed in the appendix, chapter A.6, and illustrated for flocs of radius a_F = 29.47 µm and permeable walls with membrane resistance $R_M = 5.24 \cdot 10^{11}$ 1/m.

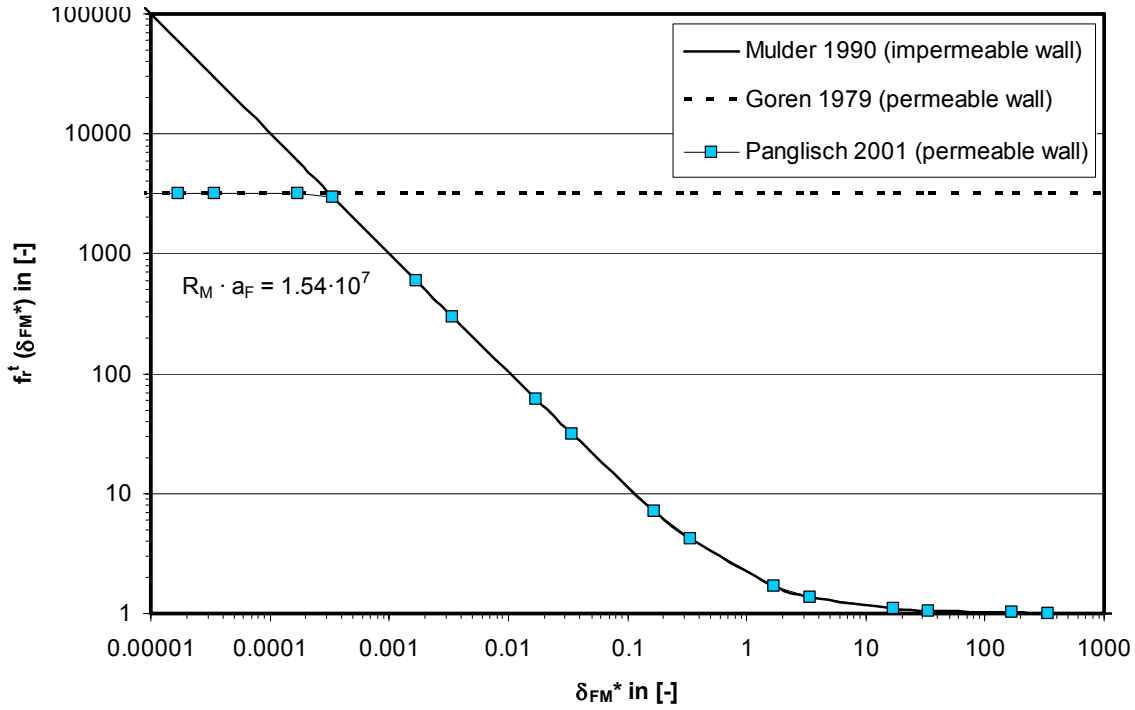

Figure 3.11: Hydrodynamic wall effect of an impermeable wall (MULDER (1990)), a permeable wall (GOREN (1979)) and the approximation given by PANGLISCH (2001)

Because the correction functions introduced above are valid for diluted suspensions only, the concentration profile in direction of the membrane wall has to be considered by superposition of the wall effects and floc concentration effects for the translatory forces and torques. Hence, these forces and torques acting on a spherical floc, moving with the velocities u_F in radial direction, w_F in direction of the angular coordinate φ and v_F in longitudinal direction in stationary fluid, are given with:

$$F_{D,r}^{t} = -6 \cdot \pi \cdot \eta \cdot a_{hF} \cdot u_F \cdot f_r^t(\delta_{FM}^*) \cdot f_\phi^t(\phi_F^*), \qquad \textbf{Equation 3.31}$$

$$F_{D,z}^{t} = -6 \cdot \pi \cdot \eta \cdot a_{hF} \cdot v_F \cdot f_z^t(\delta_{FM}^*) \cdot f_\phi^t(\phi_F^*), \qquad \textbf{Equation 3.32}$$

$$F^{t}_{D,\varphi} = -6 \cdot \pi \cdot \eta \cdot a_{hF} \cdot w_F \cdot f^{t}_{r}(\delta^{*}_{FM}) \cdot f^{t}_{\phi}(\phi^{*}_{F}) \text{ and} \qquad \textbf{Equation 3.33}$$

$$T^{t}_{D,\Phi} = 8 \cdot \pi \cdot \eta \cdot a^{2}_{hF} \cdot v_F \cdot g^{t}_{\Phi}(\delta^{*}_{FM}) \cdot f^{t}_{\phi}(\phi^{*}_{F}), \qquad \textbf{Equation 3.34}$$

where the subscript Φ denotes the rotation axis of the spherical floc.

The rotation of a spherical floc with angular velocity ω in stationary fluid creates a tangential force and torque component in the vicinity of a wall as:

$$F^{r}_{D,z} = 6 \cdot \pi \cdot \eta \cdot a^{2}_{hF} \cdot \omega \cdot f^{r}_{Z}(\delta^{*}_{FM}) \text{ and} \qquad \textbf{Equation 3.35}$$

$$T^{r}_{D,\Phi} = -8 \cdot \pi \cdot \eta \cdot a^{3}_{hF} \cdot \omega \cdot g^{r}_{\Phi}(\delta^{*}_{FM}). \qquad \textbf{Equation 3.36}$$

Considering a stationary spherical floc in a fluid flow, following forces and torques are acting on it as:

$$F^{m}_{D,r} = 6 \cdot \pi \cdot \eta \cdot a_{hF} \cdot u \cdot f^{m}_{r}(\delta^{*}_{FM}), \qquad \textbf{Equation 3.37}$$

$$F^{m}_{D,z} = 6 \cdot \pi \cdot \eta \cdot a_{hF} \cdot v \cdot f^{m}_{z}(\delta^{*}_{FM}) \text{ and} \qquad \textbf{Equation 3.38}$$

$$T^{m}_{D,\Phi} = 8 \cdot \pi \cdot \eta \cdot a^{2}_{hF} \cdot v \cdot g^{m}_{\Phi}(\delta^{*}_{FM}), \qquad \textbf{Equation 3.39}$$

depending of the fluid flow velocities u in radial and v in longitudinal direction.

Balancing the torques arising from the drag acting on the flocs delivers:

$$T^{t}_{D,\Phi} + T^{r}_{D,\Phi} + T^{m}_{D,\Phi} = 0. \qquad \textbf{Equation 3.40}$$

This balance can be used to calculate the angular velocity ω as:

$$\omega = \frac{v_F \cdot g^{t}_{\Phi}(\delta^{*}_{FM}) \cdot f^{t}_{\phi}(\phi^{*}_{F}) + v \cdot g^{m}_{\Phi}(\delta^{*}_{FM})}{a_{hF} \cdot g^{r}_{\Phi}(\delta^{*}_{FM})}, \qquad \textbf{Equation 3.41}$$

to be introduced into Equation 3.35. Balancing the drag forces delivers the following set of equations:

$$F_{D,r} = F_{D,r}^{m} + F_{D,r}^{t} = 6 \cdot \pi \cdot \eta \cdot a_{hF} \cdot \left(u \cdot f_r^m(\delta_{FM}^*) - u_F \cdot f_r^t(\delta_{FM}^*) \cdot f_\phi^t(\phi_F^*) \right), \qquad \textbf{Equation 3.42}$$

$$F_{D,\varphi} = -6 \cdot \pi \cdot \eta \cdot a_{hF} \cdot w_F \cdot f_r^t(\delta_{FM}^*) \cdot f_\phi^t(\phi_F^*). \qquad \textbf{Equation 3.43}$$

$$\begin{aligned} F_{D,z} &= F_{D,z}^{m} + F_{D,z}^{t} + F_{D,z}^{r} \\ &= 6 \cdot \pi \cdot \eta \cdot a_{hF} \cdot \left(v \cdot f_z^m(\delta_{FM}^*) - v_F \cdot f_z^t(\delta_{FM}^*) \cdot f_\phi^t(\phi_F^*) + a_{hF} \cdot \omega \cdot f_Z^r(\delta_{FM}^*) \right) \end{aligned} \qquad \textbf{Equation 3.44}$$

3.3.3 Virtual mass

The expressions for the viscous drag are valid only for constant slip velocities. If an unbalanced force exists, the particle or floc mass accelerates and a finite mass of the fluid immediately surrounding or being within the floc will be accelerated too. Hence, an extra drag or virtual mass force has to be considered. CHELLAM AND WIESNER (1992) stated that the extra fluid mass is proportional to the floc volume and the fluid density. To account for this added mass force, which opposes the motion, the following force acting on a floc has to be considered in the force balances:

$$\vec{F}_{VM} = -k_{vm} \cdot \frac{4}{3} \cdot \pi \cdot a_{hF}^3 \cdot \rho \frac{d\vec{u}_F}{dt}. \qquad \textbf{Equation 3.45}$$

Here, k_{vm} is a proportionality constant presented by CHELLAM AND WIESNER (1992) as a function of the dimensionless distance of the floc to the membrane wall δ_{FM}^* with:

$$k_{vm} = \frac{1}{2} + \frac{3}{16} \cdot \left(\frac{k^*}{\delta_{FM}^*} \right)^3 + \frac{3}{256} \cdot \left(\frac{k^*}{\delta_{FM}^*} \right)^6 + \ldots. \qquad \textbf{Equation 3.46}$$

The factor k^* is called the dimensionless floc radius, i. e. the floc radius a_F normalised with the channel width or capillary diameter d_C respectively as:

$$k^* = \frac{a_F}{d_C} = \frac{a_F}{2 \cdot r_C}. \qquad \textbf{Equation 3.47}$$

Hence, in an unbounded fluid flow k_{vm} becomes 0.5 and for a flow bounded by the membrane wall k_{vm} increases to infinity when the floc approaches the membrane wall as illustrated in Figure 3.12.

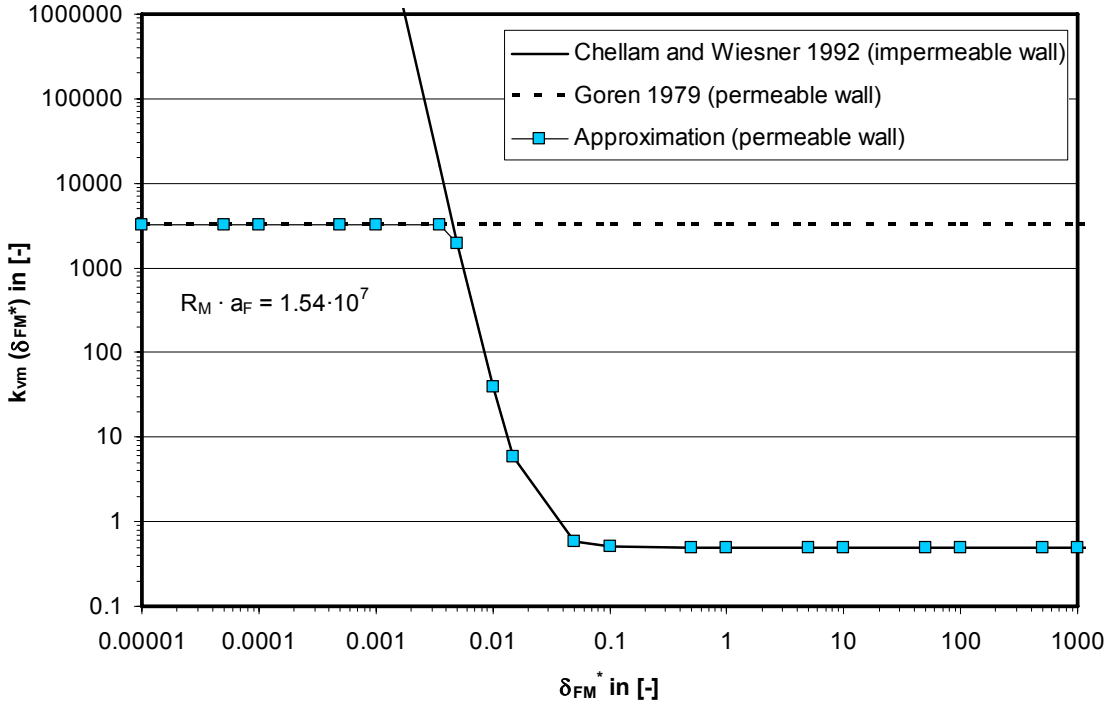

Figure 3.12: Proportionality constant k_{vm} as function of the dimensionless distance δ_{FM}^{*} of the floc to the membrane wall (adapted from CHELLAM AND WIESNER (1992))

However, the proportionality constant is valid for impermeable walls only and has to be adapted to account for permeable walls. This will be done by an approximation to account for the influence of the permeable wall at short dimensionless distances δ_{FM}^{*} as previously shown for the correction function $f_r^t(\delta_{FM}^{*})$, see Figure 3.11. Considering this approximation, the membrane wall and floc concentration, the added mass forces in longitudinal, angular and radial components can be calculated as:

$$F_{VM,z} = -k_{vm} \cdot \frac{4}{3} \cdot \pi \cdot a_{hF}^3 \cdot \rho \cdot \frac{\partial v_F}{\partial t} \cdot \frac{1}{f_z^t(\delta_{FM}^{*}) \cdot f_\phi^t(\phi_F^{*})}, \qquad \textbf{Equation 3.48}$$

$$F_{VM,\varphi} = -k_{vm} \cdot \frac{4}{3} \cdot \pi \cdot a_{hF}^3 \cdot \rho \cdot \frac{\partial w_F}{\partial t} \cdot \frac{1}{f_r^t(\delta_{FM}^{*}) \cdot f_\phi^t(\phi_F^{*})}, \qquad \textbf{Equation 3.49}$$

$$F_{VM,r} = -k_{vm} \cdot \frac{4}{3} \cdot \pi \cdot a_{hF}^3 \cdot \rho \cdot \frac{\partial u_F}{\partial t} \cdot \frac{1}{f_r^t(\delta_{FM}^{*}) \cdot f_\phi^t(\phi_F^{*})}, \qquad \textbf{Equation 3.50}$$

Whereas estimations were given by CHELLAM AND WIESNER (1992) in case the floc velocities are not known with:

$$F_{VM,z} = -k_{vm} \cdot \frac{4}{3} \cdot \pi \cdot a_{hF}^3 \cdot \rho \cdot \frac{v_{max}^2}{l_C} \cdot \frac{1}{f_z^t(\delta_{FM}^*) \cdot f_\phi^t(\phi_F^*)}, \quad \textbf{Equation 3.51}$$

$$F_{VM,r} = -k_{vm} \cdot \frac{4}{3} \cdot \pi \cdot a_{hF}^3 \cdot \rho \cdot \frac{u^2}{2 \cdot r_C} \cdot \frac{1}{f_r^t(\delta_{FM}^*) \cdot f_\phi^t(\phi_F^*)}. \quad \textbf{Equation 3.52}$$

Here, v_{max} denotes the characteristic fluid flow velocity at the flow centre line.

3.3.4 Buoyancy and sedimentation

Balancing buoyancy and gravity as acting forces on a spherical floc, the resulting force will be the so called sedimentation force. Considering just spherical flocs arising torques can be neglected. The sedimentation force can be subdivided into acting components in radial and longitudinal direction r and z respectively, depending on the direction of the acting gravity force. This force can be calculated as the difference of buoyancy and gravity as:

$$F_{BS,z} = (\rho_F - \rho) \cdot \frac{4}{3} \cdot \pi \cdot a_{hF}^3 \cdot g_z, \text{ and} \quad \textbf{Equation 3.53}$$

$$F_{BS,r} = (\rho_F - \rho) \cdot \frac{4}{3} \cdot \pi \cdot a_{hF}^3 \cdot g_r. \quad \textbf{Equation 3.54}$$

Here, g denotes the gravitational acceleration constant, ρ denotes the fluid and ρ_F the floc density respectively. Depending on the direction of the acting gravity, fluid flow in horizontal and vertically orientated capillaries can be described.

3.3.5 Brownian diffusion

In all cases of diffusion, the net flux J of the transported quantity (atoms, energy, or electrons) is equal to a physical property (diffusivity, thermal conductivity, electrical conductivity) multiplied by a gradient (a concentration, a thermal or electric field gradient). According to the general phenomenological Equation 2.1, the 1st Fickian law describes the steady state diffusion flux of matter. The diffusive flux J_{BD} is proportional to the diffusion coefficient D_{BD} and driven by a concentration gradient $\frac{\partial c}{\partial r}$ in the system. It is given by:

$$J_{BD} = - D_{BD} \cdot \frac{\partial c}{\partial r}. \qquad \textbf{Equation 3.55}$$

Diffusion of matter, i. e. submicron or Brownian particles or micro flocs, suspended in water originates from an incessant, sometimes chaotic movement, whereby it comes to a constant but coincidental change of position. If no concentration gradient exists, then the changes of position will be compensated in the statistic mean and no directed transport occurs. For instance, in thermal diffusion, if the temperature is constant, thermal energy will move as quickly in one direction as in the other, producing no heat transport and change in temperature. With presence of a concentration gradient, the coincidental change of position turns into a directed movement in opposite direction of the gradient. Hence, a directed diffusion flux will be developed. A measure for the flexibility of submicron matter was given by the Stokes-Einstein relationship (EINSTEIN (1905)) for the diffusion coefficient with:

$$D_{BD} = \frac{k_B \cdot T}{6 \cdot \pi \cdot \eta \cdot a_F}, \qquad \textbf{Equation 3.56}$$

where k_B denotes the Boltzmann constant.

The effective lateral velocity due to the action of Brownian diffusion in the presence of a concentration gradient of suspended flocs can be expressed by (HO AND LEAL (1974)):

$$u_{BD} = - \frac{D_{BD}}{\phi_F} \cdot \frac{d\phi_F}{dr}. \qquad \textbf{Equation 3.57}$$

For the calculation of u_{BD} neither floc-floc nor floc-wall interactions are considered (PANGLISCH (2001)). Hence, the acting force in radial direction $F_{BD,r}$ can be calculated using the Stokes-equation without using correction terms as:

$$F_{BD,r} = - \frac{D_{BD}}{\phi_F} \cdot \frac{d\phi_F}{dr} \cdot 6 \cdot \pi \cdot \eta \cdot a_{hF}. \qquad \textbf{Equation 3.58}$$

3.3.6 Shear induced diffusion

Larger flocs or particles are able to develop a strong, directed motion if they are present in a sufficiently high concentration and if shearing forces exist (LEIGHTON AND ACRIVOS (1987)). Hence, a fluid moving across a membrane initiates floc migration and at a critical point overcomes the advective force of fluid moving through the membrane. ZYDNEY AND COLTON (1986) proposed that particles in a shear flow are displaced as the result of complex particle-particle interactions arising from the rotation of the particles, the resultant drag force exerted on neighbouring particles and the interception of particles moving along different streamlines. Each displacement is a product of a random configuration of particles and so the motion of an individual particle should behave as a random walk and is characterised by an effective diffusion coefficient D_{SiD}. The frequency or probability of particle-particle interaction will be greater for higher concentrations of particles. ECKSTEIN ET AL. (1977) found that the effective diffusivity of particles in shear flow increased with square of particle diameter and linearly with shear rate. Based on these observations, DAVIS AND LEIGHTON (1987) and LEIGHTON AND ACRIVOS (1986) proposed an expression for the approximation of the effective, or 'shear induced' diffusivity of particles, here written to denote for flocs as:

$$D_{SiD} = \frac{1}{3}\dot{\gamma}\, a_F{}^2\, \phi_F^2 \left[1+\frac{1}{2}e^{8.8\cdot\phi_F}\right], \qquad \textbf{Equation 3.59}$$

where $\dot{\gamma}$ denotes the local shear rate of the Newtonian fluid, considering the limiting influence of the floc suspension with:

$$\dot{\gamma} = \frac{dv}{dr}\cdot\frac{\eta}{\eta_S}. \qquad \textbf{Equation 3.60}$$

In contrast to Brownian diffusion, the shear induced diffusion coefficient increases with increasing floc size. Further, the shear induced diffusion coefficient will increase with increasing floc concentration until it suddenly decreases strongly for values larger than ϕ_F = 0.58 and smaller than the maximum concentration of $\phi_{F,\,max}$ = 0.74, see also PANGLISCH (2001). However, for the acting force in radial direction $F_{SiD,r}$ due to shear induced diffusion, the concentration profile in the capillary has to be

recognised and hence, the correction function $f_{\phi}^{t}(\phi_F^*)$ will be encountered into the formula as:

$$F_{SiD,r} = -\frac{D_{SiD}}{\phi_F} \cdot \frac{d\phi_F}{dr} \cdot 6 \cdot \pi \cdot \eta \cdot a_{hF} \cdot f_{\phi}^{t}(\phi_F^*) . \qquad \textbf{Equation 3.61}$$

3.3.7 Lateral migration

Lateral migration, i. e. migration or lift of a free floc perpendicular to the streamlines in the flow field, is driven by the fluid motion or its shear flow respectively. If there is no shear, there is no lift. As shown in chapter 3.1, the flow inside the capillaries is Poiseuille pipe flow. Here, there is not only a shear, but a shear gradient (curvature) which produces lateral forces acting on the flocs. SEGRÉ AND SILBERBERG (1962A), SEGRÉ AND SILBERBERG (1962B) were the first who experimentally studied the behaviour of neutrally buoyant rigid spheres in Poiseuille pipe flow. They observed that the spherical particles in the flow through a pipe of radius R migrated to an equilibrium radial position located at r* = 0.63 R. Due to the tube-like shape of the annular region to which the spheres migrate, this effect was called the 'tubular pinch effect'. These results were confirmed by several studies, often in the case of neutrally buoyant spherical particles in vertical Poiseuille pipe flow, e. g. COX AND BRENNER (1968), KARNIS ET AL. (1966) and VASSEUR AND COX (1976). However, the authors investigated beside the effect on neutrally buoyant rigid spherical and discoidal particles further the effect of density differences between the particles and the fluid on lateral migration, i. e. nonneutrally buoyant spherical particles. They found that the equilibrium position for those particles may be moved either towards the axis if the particle lags the flow or towards the wall if the particle leads the flow, depending upon their relative densities. In case of neutrally buoyant deformable particles such as elastomer fibres or blood cells, KARNIS ET AL. (1966) and ZHAO AND SHARP (1999) found in experimental studies that those particles migrated always to the axis. As stated in MATAS ET AL. (2004), HO AND LEAL (1974) and later VASSEUR AND COX (1976) eventually predicted most of the experimental observations for neutrally and nonneutrally buoyant particles in linear and quadratic flow fields. Both studies show that there will be in general a competition between an inwards and an outwards directed force, leading to an equilibrium position of about 60 % from the centre to the

walls at small Re numbers. VASSEUR AND COX (1976) presented different lateral migration velocities of spherical particles in Poiseuille flow between two walls, depending on whether the particle is neutrally buoyant or not, whether it is free to rotate or not or if it is sedimenting in a quiescent or a very slowly moving fluid. They presented further cases intermediates among them by superposition. Their considerations assume that the boundary conditions $Re_F << 1$ and $k^* << 1$ are satisfied. Further it is also required that the sphere should not be too close to the wall, i. e $a_F / \delta_{FM}^C << 1$, with δ_{FM}^C as the finite distance between the floc centre and the membrane wall.

Considering at first separately, i. e. without transition within both cases, neutrally and nonneutrally buoyant spherical particles, rotating in the fluid flow, the following equations for the lateral migration velocity were presented by VASSEUR AND COX (1976). The lateral migration velocity $u_{LM,b}$ of a nonneutrally buoyant spherical particle can be expressed as:

$$u_{LM,b} = -\left(\frac{a_{hF} \cdot v_S}{\nu} \right) \cdot v_{max} \cdot f_2(\delta_{FM}^{C*}) \qquad \textbf{Equation 3.62}$$

and the lateral migration velocity of a neutrally buoyant spherical floc as:

$$u_{LM,c} = \left(\frac{a_{hF} \cdot v_{max}^2}{\nu} \right) \cdot k^{*2} \cdot f_3(\delta_{FM}^{C*}). \qquad \textbf{Equation 3.63}$$

Here, v_{max} denotes the characteristic fluid flow velocity at the flow centre line, v_S denotes the (Stokes) sedimentation velocity of the moving floc in quiescent fluid, derived from Equation 3.53 or Equation 3.54 respectively and k* is the dimensionless floc radius as introduced with Equation 3.47. The functions $f_2(\delta_{FM}^{C*})$ and $f_3(\delta_{FM}^{C*})$ are functions of the dimensionless distance of the floc centre from the wall, given by:

$$\delta_{FM}^{C*} = \frac{\delta_{FM}^C}{r_C}. \qquad \textbf{Equation 3.64}$$

They can be considered as dimensionless inertia induced velocities. The equations for the calculation of $f_2(\delta_{FM}^{C^*})$ and $f_3(\delta_{FM}^{C^*})$ are given in the appendix, chapter A.8.

ALTENA AND BELFORT (1984) showed that the considerations of VASSEUR AND COX (1976) may be adapted for particle behaviour in the flow through a slit with one porous wall as well. They extended the work of VASSEUR AND COX (1976) to include the effect of porous boundaries on inertia induced transport for rigid, spherical and neutrally buoyant particles. When superposing permeation drag forces and lateral migration forces they found for a very small relative permeation drag force, that the particle trajectories converge at an equilibrium position reminiscent of flow in a nonporous pipe as described above. As the relative permeation drag force is increased, the equilibrium position moves closer to the porous wall and finally resulting in particle capture. PANGLISCH (2001) mentioned that the dimensionless inertia induced velocity only has one radial component, being constant for all φ in a capillary or pipe flow respectively and substituted the dimensionless particle distance with the dimensionless radial particle distance r*. The derived equations and illustrations of the substituted functions are given in chapter A.8 too.

However, in real world problems, one is unlikely to encounter flocs which are precisely neutrally buoyant, nor flocs which are much lighter or heavier than the fluid. For this reason both cases were superposed which delivers a lateral migration velocity of:

$$u_{LM} = \left(\frac{a_{hF}}{\nu}\right) \cdot v_{max} \cdot \left(k^{*2} \cdot v_{max} \cdot f_3(r^* \cdot \cos\varphi) - v_S \cdot f_2(r^* \cdot \cos\varphi)\right). \qquad \textbf{Equation 3.65}$$

In case of small density differences, irrespective of whether the floc is lighter or heavier than the fluid, the theory presented by VASSEUR AND COX (1976) is in good accordance to those found by FENG ET AL. (1994). FENG ET AL. (1994) and later HUANG ET AL. (1997) found in case of lighter particles that when the density difference is large enough (5 % to 15 %), the equilibrium position shifts back again toward the centreline, i. e. particles being repelled near the wall at an equilibrium stand-away distance. Especially interestingly, FENG ET AL. (1994) and HUANG ET AL. (1997) found that the restrictions, which apply to perturbation theories as used by HO AND LEAL

(1974) and VASSEUR AND COX (1976) do not apply to direct numerical simulation, which was used in their studies. Hence, the effects of the wall on hydrodynamic induced rotations, the lift force, the lateral velocities and equilibrium positions for the particles, here for the flocs could be obtained from direct numerical simulations without compromising assumptions. Summarising the above, inertia induced lateral migration of flocs is caused by the acting inertia force $F_{LM,r}$. Accounting for the presence of the membrane walls the correction function $f_r^t(\delta_{FM}^*)$ and for the floc concentration profile the correction function $f_\phi^t(\phi_F^*)$ have to be included for the calculation of $F_{LM,r}$, acting in radial direction, with:

$$F_{LM,r} = 6 \cdot \pi \cdot \eta \cdot a_{hF} \cdot u_{LM} \cdot f_r^t(\delta_{FM}^*) \cdot f_\phi^t(\phi_F^*). \qquad \textbf{Equation 3.66}$$

3.3.8 DLVO interactions

Within the framework of the DLVO theory, named after the work of DERJAGUIN, LANDAU, VERWEY and OVERBEEK, the total colloidal interaction forces acting on the particles or flocs can be calculated as the sum of the van der Waals and the electrical double layer interactions operating between charged spherical surfaces, i. e. flocs and plane surfaces, i. e. membrane wall, at short distances. Both interactions will be described in the following. Chapter A.9 in the appendix will give a brief overview of how surface charges are developed in aqueous media and about the resulting electrical double layer, based on STUMM AND MORGAN (1996) and NAHRSTEDT (1999). Graphical illustrations of calculated DLVO forces for the investigated systems iron hydroxide floc/membrane wall and latex particle/membrane wall can be found in the appendix, chapter A.10.

3.3.8.1 van der Waals attraction

Due to the motion of electrons around their atomic nuclei, temporary asymmetries of the charge distribution will arise, delivering a fluctuating electromagnetic field around the atoms. For two closely separated atoms or surfaces, their electromagnetic fields will interact, leading to a spontaneous electrical and magnetic polarisation resulting in a synchronised electromagnetic field. The arising force is generally called the van der Waals force and is typically attractive. Van der Waals forces have only small ranges

but are significant when surfaces are very close to each other, i. e. in the nanometer range. GREGORY (1981), cited in NAHRSTEDT (1999), expanded the work of Hamaker and derived the radial acting van der Waals force under consideration of retardation as:

$$F_{vdW,r} = \frac{H}{6} \cdot \frac{a_{eff}}{\delta^2} \cdot \left[1 - \left(1 + \frac{\lambda_c}{5.32 \cdot \delta} \right)^{-1} \right], \qquad \textbf{Equation 3.67}$$

where H is the Hamaker constant, δ is the dimensional distance between a floc and a collector, either floc or membrane wall, and λ_c is the characteristic wavelength of interaction and is close to 100 nm for most particles (GREGORY (1989) cited in CHELLAM AND WIESNER (1992)) and was used to account for flocs too. The effective radius a_{eff} can be expressed as:

$$a_{eff} = a_F, \qquad \textbf{Equation 3.68}$$

for the system floc / membrane or as:

$$a_{eff} = \frac{a_{F1} \cdot a_{F2}}{a_{F1} + a_{F2}}, \qquad \textbf{Equation 3.69}$$

for the system floc / floc or particle / particle as presented by NAHRSTEDT (1999).

The range of Hamaker constants of suspended solids of material 1 (index 1) in water (index 3) is in between $H_{131} = (0.1 \ldots 10)*10^{-20}$ J (GREGORY (1975), cited in NAHRSTEDT (1999)). The lower range represents polymers, the middle range crystalline solids and the upper one metallic solids and graphite. Elaborate libraries can be found in VISSER (1972), LYKLEMA (1991) and BERGSTRÖM (1997). However, depending on the accuracy of the measurements and the used experimental equipment, the values may vary significantly. PANGLISCH (2001) presented two Hamaker constants for typical membrane materials with $1.0 \cdot 10^{-19}$ J (polysulfone) and $1.8 \cdot 10^{-19}$ J (cellulose acetate). BEHRENS AND BORKOVEC (1999) used a Hamaker constant of $H_{131} = 6 \cdot 10^{-20}$ J and VISSER (1972) of about $H_{131} = 2 \cdot 10^{-19}$ J for iron hydroxides across water and $H_{131} = 1.26 \cdot 10^{-19}$ J for aluminium hydroxides across water. To account for two different materials (index 1 for material 1 and index

2 for material 2) in the system of interest, fitted Hamaker constants, based on the specific Hamaker constant of each involved material can be calculated using different correlations as presented by VISSER (1972). For instance, PANGLISCH (2001) calculated a Hamaker constant of $H_{132} = 1.54 \cdot 10^{-20}$ J for the combination polystyrol / water / polyethersulfone, representing the system of suspended latex particles in the vicinity of the membrane. Based on the values mentioned above, fitted Hamaker constants were calculated for the system iron hydroxide floc and membrane across water with $H_{132} = 2.63 \cdot 10^{-19}$ J and with $H_{132} = 6.51 \cdot 10^{-20}$ J for aluminium hydroxide flocs and membrane across water respectively. These values were used throughout the thesis if not indicated otherwise.

3.3.8.2 Double layer repulsion

Solids like particles, flocs or membranes located in aqueous media may develop an electric charge at their surface. This electric charge is depending on the pH value of the aqueous media and is typically negative for the interesting particles or flocs at the pH range of natural waters. The values obtained in the experimental part of this work are described in chapter 4.1 and 4.2.

As elucidated by NAHRSTEDT (1999), the theoretical description of the potential distribution in the diffusive double layer, introduced by GOUY and CHAPMAN, is based on a combination of the Poiseuille equation for charge densities and the Boltzmann expression, giving the charge density depending on the local concentration of anions and cations and these depending on the local potential. A more detailed description can be found in ELIMELECH ET AL. (1995) for instance. The force arising by superposition of single potential distributions of two solids may be calculated by using the so called linear superposition approximation (LSA) method. For two approaching solids, the LSA method represents a good compromise for the limiting cases of a constant surface charge on the one hand and the constant potential of the outer Stern plane on the other hand, compare Figure A.13 in the appendix. Using the LSA method, following force distribution for small distances between a collector and a floc or particle in a symmetrical electrolyte is given by GREGORY (1975), cited in NAHRSTEDT (1999), with:

$$F_{DL,r} = -\frac{128 \cdot \pi \cdot n \cdot k_B \cdot T}{\kappa} \cdot a_{eff} \cdot \Gamma_1 \cdot \Gamma_2 \cdot \exp\left(-\kappa(\delta - \delta_0)\right). \quad \textbf{Equation 3.70}$$

Here, the number concentration of ions per unit volume n is considered either for anions or cations. Γ_1 and Γ_2 can be written as:

$$\Gamma_1 = \tanh\left(\frac{z \cdot e \cdot \Psi_{S,1}}{4 \cdot k_B \cdot T}\right), \text{ and} \quad \textbf{Equation 3.71}$$

$$\Gamma_2 = \tanh\left(\frac{z \cdot e \cdot \Psi_{S,2}}{4 \cdot k_B \cdot T}\right). \quad \textbf{Equation 3.72}$$

In Equation 3.70 to Equation 3.72 k_B denotes the Boltzmann constant, T denotes the absolute temperature, κ denotes the Debye-Hückel parameter, δ denotes the distance between the surfaces, δ_0 denotes the minimum possible adhesion distance between two surfaces, $\Psi_{S,i}$ denotes the stern potential of the interacting surfaces i, i. e. 1 and 2 respectively, z denotes the valency of the counterions and n denotes the number concentration of all counterions (approximately also valid for asymmetrical electrolytes (GIMBEL (1984), cited in NAHRSTEDT (1999)). The effective radius a_{eff} can be derived analogous as introduced in chapter 3.3.8.1 with Equation 3.68 and Equation 3.69. The Debye-Hückel parameter is given with:

$$\kappa = \sqrt{\frac{e^2}{\varepsilon_r \, \varepsilon_0 \, k_B \, T} \sum_i (n_i \, z_i^2)}, \quad \textbf{Equation 3.73}$$

where e denotes the electron charge, ε_0 denotes the electrical permittivity, ε_r denotes the relative dielectric constant, i. e. 78 for water, n_i denotes the number concentration of counterions of species i and z_i denotes the valency of the ions of species i.

3.3.9 Force balances

The balances of the forces acting on the moving floc in the capillary membrane during filtration deliver the following set of equations in r-, φ- and z-direction with:

$$F_{D,r} + F_{VM,r} + F_{BS,r} + F_{LM,r} + F_{vdW,r} + F_{DL,r} + F_{SiD,r} + F_{BD,r} = 0, \quad \textbf{Equation 3.74}$$

$F_{D,\varphi} + F_{VM,\varphi} = 0$, and **Equation 3.75**

$F_{D,z} + F_{VM,z} + F_{BS,z} = 0$. **Equation 3.76**

Arranging the equations given above to solve for the resulting floc velocities in r-, φ- and z-direction following expressions were found:

$$u_F = u \cdot \frac{f_r^m(\delta_{FM}^*)}{f_r^t(\delta_{FM}^*) \cdot f_\phi^t(\phi_F^*)} + \frac{\sum F_r}{6 \cdot \pi \cdot \eta \cdot a_{hF} \cdot f_r^t(\delta_{FM}^*) \cdot f_\phi^t(\phi_F^*)}, \quad \textbf{Equation 3.77}$$

with $\sum F_r = F_{VM,r} + F_{BS,r} + F_{LM,r} + F_{vdW,r} + F_{DL,r} + F_{SiD,r} + F_{BD,r}$

$$w_F = \frac{F_{VM,\varphi} + F_{BS,\varphi}}{6 \cdot \pi \cdot \eta \cdot a_{hF} \cdot f_r^t(\delta_{FM}^*) \cdot f_\phi^t(\phi_F^*)}. \quad \textbf{Equation 3.78}$$

$$v_F = \left[v \cdot \left(f_z^m(\delta_{FM}^*) + \frac{f_Z^r(\delta_{FM}^*) \cdot g_\Phi^m(\delta_{FM}^*)}{g_\Phi^r(\delta_{FM}^*)} \right) + \frac{F_{VM,z} + F_{BS,z}}{6 \cdot \pi \cdot \eta \cdot a_{hF}} \right] \cdot \frac{1}{f_z^t(\delta_{FM}^*) \cdot f_\phi^t(\phi_F^*) - \frac{f_z^r(\delta_{FM}^*) \cdot f_\phi^t(\phi_F^*) \cdot g_\Phi^t(\delta_{FM}^*)}{\cdot g_\Phi^r(\delta_{FM}^*)}} \quad \textbf{Equation 3.79}$$

The forces and velocities will be used to derive the floc concentration distribution within the capillary and the trajectories of flocs of certain diameter in capillaries of arbitrary size. The transformation into the model will be shown and discussed in the following chapters.

3.4 CFD/FEM Modelling

3.4.1 Brief introduction into COMSOL

The physical aspects of any flow are generally governed by the following three fundamental principles: 1. mass conservation, 2. Newton's second law $F = m \cdot a$ and 3. energy conservation. These fundamental principles can be expressed in terms of mathematical equations, which in their most general form are usually partial differential equations (PDE). CFD is, in part, the art of replacing the governing partial differential equations with numbers, and advancing these numbers in space and/or time to obtain a final numerical description of the complete flow field of interest

(ANDERSON ET AL. (1992)). The numerical procedures can be used to approximately solve different equations of a certain flow problem under the compliance of defined boundary and start conditions without encountering too serious simplifications and assumptions. Hence, these methods can be normally used for the calculation of technical flows for complex and arbitrary geometries, e. g. describing the fluid flow in entire membrane modules or single capillaries. COMSOL Multiphysics is an advanced software environment for modelling and simulation of physical processes in scientific and engineering problems based on partial differential equations, developed and distributed by the company COMSOL AB (Sweden). The software can be used for linear and nonlinear stationary, transient, i. e. time dependent and eigenvalue analyses of arbitrary models. The analyses are initially performed for dimensional systems but can be manually rearranged for dimensionless analyses too. The software package can handle systems of first and second order partial differential equations in one, two and three space dimensions, i. e. 1D, 2D and 3D. They are discretised by FEM using unstructured elements on triangles (in 2D) and tetrahedrons (in 3D), or structured elements on quadrilateral (in 2D) and hexahedral (in 3D) elements, respectively. Mapped quadrilateral mesh elements can be used for geometries fairly regular in shape. A graphical user interface allows for an efficient graphical design of rather complex geometries in one, two and three dimensions. COMSOL 3.3a was used to model the fluid flow field, the floc concentration distribution, the floc trajectories within the capillary, the fouling layer build-up and resulting pressure drop increase. The flow and the floc concentration distribution inside the capillary were modelled by using the application modes ‘incompressible Navier-Stokes’ and ‘convection and diffusion’ of the ‘Chemical Engineering Module’ provided by the COMSOL software. The fouling layer build-up was modelled by a so called PDE general form, a framework offered by the software to implement and calculate user defined nonlinear PDE. Here, extrusion coupling variables were additionally used, which maps values from the source domain, subdomain or boundary to the destination domain, subdomain or boundary. For additional information refer to COMSOL AB (2006B).

3.4.2 Geometry of the model, constants, parameters and mesh

The membrane capillary was modelled in 2D, but the independent variables were chosen to be r, φ and z for the radial, angular and longitudinal cylindrical coordinates in a 3D flow field respectively. An axial symmetry is naturally given at the capillary centre axis, i. e. at r = 0, which was used to save computational memory consumption during modelling. However, the obtained 2D geometry, mesh and results can be transformed into 3D using a general transformation technique of the software for coupling variables as illustrated later in chapter A.13 in the appendix and chapter 3.5.1.

The geometry of the model was adapted to the capillaries geometry as used in the experimental part, see chapter 4, and could be determined in dimensional or dimensionless form. In order to analyse the model in dimensional form, the capillary radius was set to $r_C = 0.4 \cdot 10^{-4}$ m and the length of the modelled capillary was set to $l_C = 1$ m if not stated otherwise. In order to analyse the model in dimensionless form, the geometry was normalised by some scaling factors SR and SZ. The scaling factor SR was chosen to be r_C, denoting the parameters in radial direction and the scaling factor SZ was chosen to be l_C, denoting the parameters in longitudinal direction, respectively. However, the dimensionless approach was primarily used within this work. The dimensionless geometry and definition of the model subdomains and boundaries are illustrated in Figure 3.13. The boundaries of the 2D model were chosen to be: boundary 1 as the capillary centre axis, representing the axial symmetry; boundary 2 and 5 as the capillary inlet; boundary 3 and 6 as the capillary dead-end or outlet in cross-flow mode respectively and boundary 7 as the membrane wall. An interior boundary 4 was introduced to account for the fouling layer formation, see red dashed line in Figure 3.13, dividing the domain into two subdomains. The distance of boundary 4 to the membrane wall was always set to the physical radius of the flocs to be modelled, hence representing the distance when contact occurs, while compaction of the flocs was neglected.

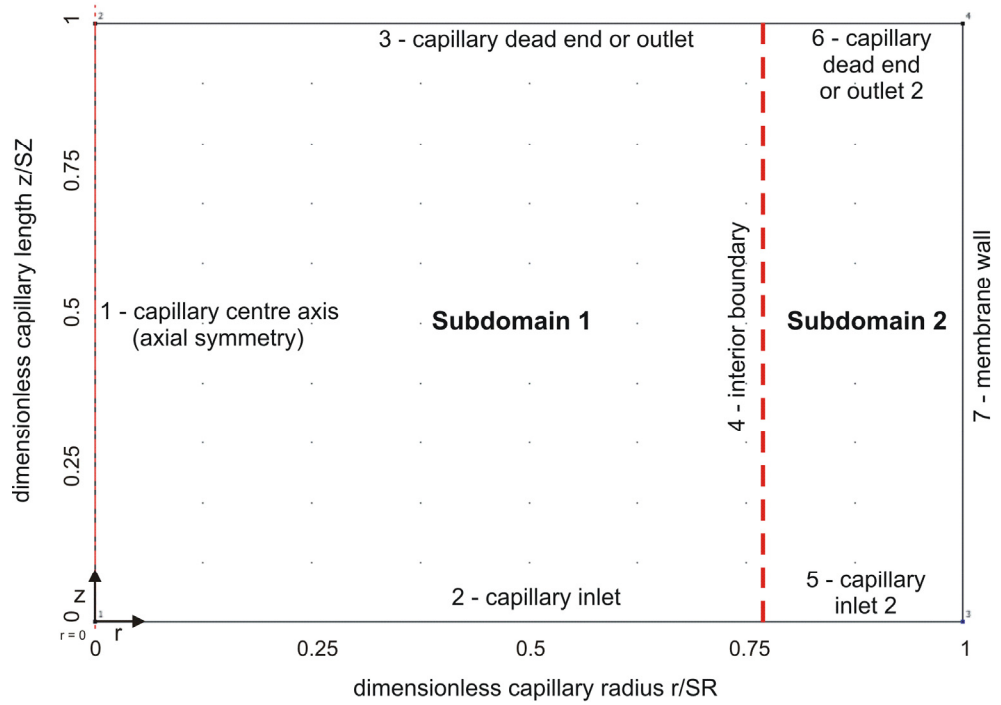

Figure 3.13: Geometry and definition of the modelled subdomains and boundaries

Constants, for instance membrane resistance R_M, capillary diameter r_C and length l_C, were used for modelling the flow field and the concentration distribution in the membrane capillary as given in Table A.3 in the appendix. Additionally, some initial parameters at time $t_0 = 0$ were defined for the numerical analysis of the Navier-Stokes equations. As presented by PANGLISCH (2001), the initial inlet pressure p_0 and velocity v_0 of the fluid at the capillary entry can be calculated with:

$$v_0 = \frac{\dot{V}_0}{\pi \cdot r_C^2} \text{ and} \qquad \textbf{Equation 3.80}$$

$$p_0 = \frac{8 \cdot \dot{V}_0 \cdot \eta}{\tanh(a \cdot l_C) \cdot a \cdot \pi \cdot r_C^4} + p_p \,. \qquad \textbf{Equation 3.81}$$

The parameter a was introduced by PANGLISCH (2001) as a parameter depending on membrane resistance R_M and capillary radius r_C with:

$$a = \sqrt{\frac{16}{r_C^3 \cdot R_M}} \,. \qquad \textbf{Equation 3.82}$$

Further, the membrane surface area A_M and the inlet volume flow $\dot{V}_0$ were calculated with:

$$A_M = 2 \cdot \pi \cdot r_C \cdot l_C, \text{ and} \qquad \textbf{Equation 3.83}$$

$$\dot{V}_0 = A_M \cdot J. \qquad \textbf{Equation 3.84}$$

The dynamic fluid viscosity η_0 at the capillary inlet could be calculated using a polynomial approximation as function of temperature, compare Equation 2.10. The initial fluid density ρ_0 can be approximated with following polynomial equation as:

$$\rho_0 = (17.9098 - 0.6003 \cdot T + 0.01299 \cdot T^2 - 0.000134 \cdot T^3) \cdot 0.0001, \qquad \textbf{Equation 3.85}$$

derived by regression of listed values in VEREIN DEUTSCHER INGENIEURE (1988) and PERRY ET AL. (1984). The determined values for different initial parameters, for instance fluid inlet velocity in radial and longitudinal direction, u_0 and v_0, and fluid inlet pressure p_0 at time $t_0 = 0$ are listed in Table A.4. Please note that the gravitational forces F_r and F_z were defined to account for gravitation in a horizontally orientated capillary.

As mentioned above, the software is able to work with triangular, quadrilateral, tetrahedral, brick, and prism meshes using fully automatic and adaptive mesh generation. However, some general remarks and limitations of quadrilateral elements are given in chapter A.13 while all conditions were met in the existing case of the capillary. Especially for numerical calculation of the fluid flow quadrilateral elements were usually used, because less element numbers were needed to meet the high convergence criteria, chosen to be $1 \cdot 10^{-6}$. The mesh was always set up to account for a sufficient high resolution especially at boundary 4 where interacting forces between fluid flow, moving flocs and membrane wall will be likely highest and where the fouling layer formation occurs. Nevertheless, the mesh has to be adapted for each model. For example, one chosen mesh used for modelling the velocity profile within a capillary consists of 78.750 elements over the whole modelled capillary, with 1.380 elements directly at the boundaries, delivering 1.644.941 degrees of freedom

(DOF), i. e. a finite number of coefficients used to describe the variables with a function for numerical calculations.

Figure 3.14 shows the resulting mesh, becoming increasingly finer at closer distances to the membrane wall, with extremely fine meshed areas directly at the membrane wall and the capillary inlet and coarser meshed areas at the capillary centre and the capillary lumen at some distance from the membrane wall. Each 2D mesh can be transformed into 3D by using extrusion coupling variables, which maps values from the source domain, here in 2D, to the destination domain in 3D. This mapping is explained more detailed in chapter A.13 in the appendix.

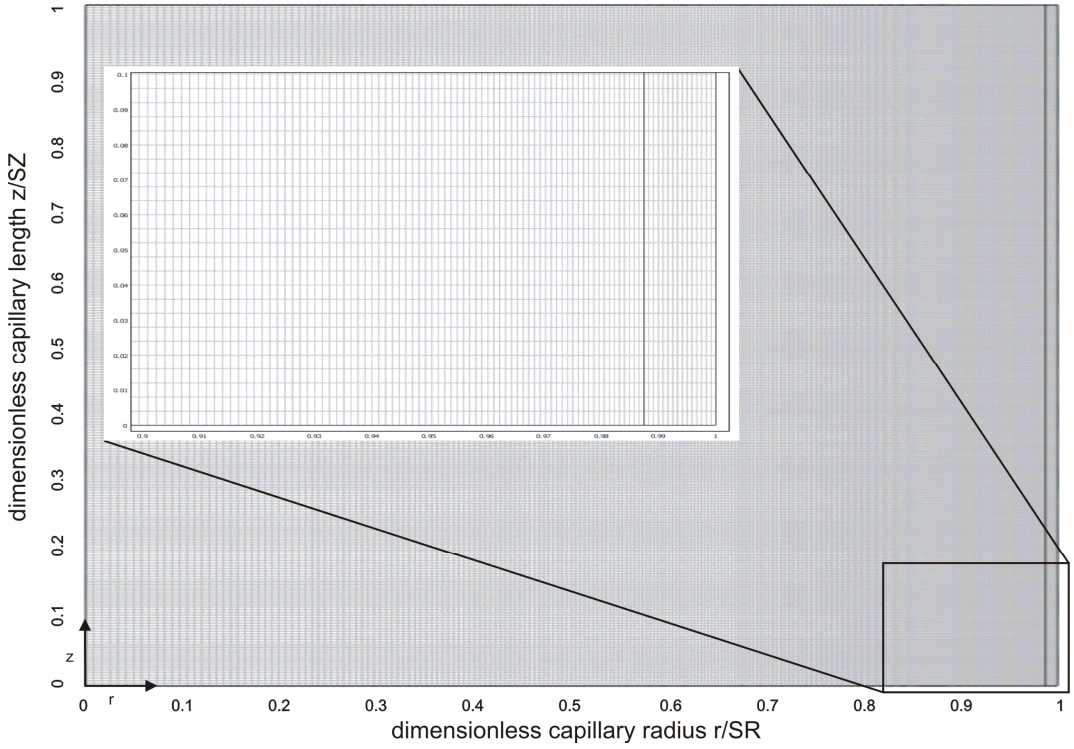

Figure 3.14: Structured (mapped) mesh of a dimensionless model in 2D

Once a mesh is established, one can introduce approximations to the dependent variables of interest. The idea is to approximate the variables with a function that one can describe with a finite number of coefficients, the DOF, whereas the approximation generates a system of equations for each DOF. Hence, the mesh determines the number of DOF to be solved. Generally, the number of DOF able to be used for the simulation is limited by the used hardware configuration with its available memory. This implies that a given mesh cannot always properly resolve

small-scale effects. The used computer was equipped with a Windows XP64 and a SUSE Linux 10.1 system, two Intel Xeon Dual Core CPUs 5160 with a frequency of 3 GHz and 16 GB RAM plus 30GB virtual memory. The number of DOF usually solved for was approximately 400,000.

3.4.3 Determination of the flow field

As introduced in chapter 3.1.2 the Navier-Stokes equations are used for the description of the fluid flow in the capillary lumen. The software uses a generalised version of the Navier-Stokes equations to allow calculations of variable viscosity too, i. e. non-Newtonian fluids (COMSOL AB (2006B)). The generalised equations as used in the incompressible Navier-Stokes application mode, denoted as the total stress tensor formulation are defined by Equation 3.86 and Equation 3.87 as given below:

$$\rho\frac{\partial\vec{u}}{\partial t}-\nabla\cdot\left[-p\cdot I+\eta\left(\nabla\vec{u}+(\nabla\vec{u})^{T}\right)\right]+\rho\left(\vec{u}\cdot\nabla\right)\vec{u}=\vec{F}\ \text{and} \qquad \textbf{Equation 3.86}$$

$$\nabla\cdot\vec{u}=0\,. \qquad \textbf{Equation 3.87}$$

where I is the identity matrix or unit diagonal matrix. The incompressible Navier-Stokes equations were solved for the pressure p and the velocity vector components of $\vec{u}$ in stationary and transient analysis. The solver applied was the so called 'Direct (UMFPACK)' solver for nonlinear, stationary or transient flow problems and the convergence criteria was chosen to be $1\cdot10^{-6}$. For more detailed information about the numerical analysis refer to COMSOL AB (2006B) and COMSOL AB (2006A). However, some additional terms and parameters related to the Navier-Stokes equations used in the software will be introduced in the following. The viscous stress tensor τ is defined as:

$$\tau=\eta\left(\nabla\vec{u}+(\nabla\vec{u})^{T}\right). \qquad \textbf{Equation 3.88}$$

Due to the fluid pressure p, internal stresses can arise in addition to the stress due to viscous forces. Hence, the total stress tensor σ is introduced and defined as:

$$\sigma = -p\,I + \tau = -p\,I + \eta\left(\nabla\vec{u} + (\nabla\vec{u})^T\right). \qquad \textbf{Equation 3.89}$$

From these stress tensors, one can further define the viscous boundary force $\vec{K}$, which is per unit area as:

$$\vec{K} = \tau\vec{n}, \qquad \textbf{Equation 3.90}$$

and the total boundary force $\vec{T}_B$, also per unit area as:

$$\vec{T}_B = \sigma\vec{n}, \qquad \textbf{Equation 3.91}$$

where $\vec{n}$ is the outward normal vector on the boundary.

The equation system form was chosen to be set to ‘General’ in case of dimensional models, using generally the equations as presented above, and to ‘Weak’ for analysing dimensionless models. In the latter one, the provided equations of the software were adapted by normalising the r and z derivates of the fluid velocity vector $\vec{u}$ by the scaling factors SR and SZ respectively as introduced in chapter 3.4.2. Additionally, the radial variable r was adapted by multiplication with the scaling factor SR too. If internal variables of the software were needed for modelling the fluid flow and the floc movement, they were treated in the same way as described. All following model information are valid for both, the dimensional as well as the dimensionless case. Further, all variables and parameters are always introduced as dimensional values if not stated otherwise.

3.4.3.1 Model boundaries

The software package offers several predefined boundary conditions, but only those are discussed here which were applied in the flow field model. For additional information about the boundary conditions refer to the software users guides, i. e. COMSOL AB (2006A) and COMSOL AB (2006B), for instance. The governing equations of the chosen boundary conditions and the chosen calculation of the expressions are discussed in the following. Boundary 1 represents the axial symmetry of the capillary. Hence, the radial coordinate was set to:

$r = 0$. **Equation 3.92**

For the imposed fluid velocity at boundary 2 and 5, together representing the capillary inlet, the velocity vector normal to the boundary can be specified by:

$\vec{u} \cdot \vec{n} = u_0$. **Equation 3.93**

This boundary condition is called the inflow/outflow boundary condition. For modelling the fluid flow at the capillary inlet just the longitudinal velocity component has to be considered. Hence, the radial component u was set to u = 0 m/s and the longitudinal velocity v was set to $v = v_0$ as introduced in Table A.4.

Boundary 3 and 6 represent the dead-end of a capillary driven in dead-end mode and the slip or symmetry condition was used. A slip condition means that the normal component of the velocity equals zero with:

$\vec{u} \cdot \vec{n} = 0$ **Equation 3.94**

and that the tangential component of the viscous force vanishes with:

$\vec{t} \cdot \vec{K} = 0$. **Equation 3.95**

Hence, the chosen condition states that there are no velocity components perpendiculars to that boundary. However, for a capillary driven in cross-flow mode operation boundary 3 and 6 have to be set as the so called outflow/pressure condition to:

$\vec{T}_B = -p_0 \vec{n}$. **Equation 3.96**

This boundary condition states that the total force on the boundary is a pressure force defined by p_0, where the pressure can be set to the outlet pressure p_{out} of the capillary, compare Equation 2.6. If the outlet pressure is not known, boundary 3 and 6 can be set to a fixed outflow velocity as given by Equation 3.93. This flow velocity can be represented by a laminar flow profile too.

The interior boundary 4 is set to neutral. The software treats a neutral boundary as if there were no boundary, which means that the total or viscous force vanishes, i. e.

$\vec{K} = 0$, and **Equation 3.97**

$\vec{T}_B = 0$. **Equation 3.98**

Boundary 7 represents the membrane wall where the filtrate leaves the modelled geometry. The so called normal flow/pressure or straight-out boundary condition is applied to set the velocity components in the tangential direction to zero with:

$\vec{t} \cdot \vec{u} = 0$, **Equation 3.99**

and further, to set the pressure to a specific value with:

$\vec{n} \cdot \vec{T}_B = -p_0$. **Equation 3.100**

This boundary condition is usually provided to simulate channels that are long in length where flow is assumed to have stabilised so that all velocity occurring in the tangential direction is negligible. The equation used for boundary 7 is given with:

$p = u \cdot \eta \cdot R_M + p_{Filtrate}$. **Equation 3.101**

Please note that η is denoted to the local dynamic fluid viscosity. Equation 3.101 could be derived from Darcy's law as introduced with Equation 2.2 when considering radial outflow of the filtrate only, i. e. perpendicular to the boundary. Here, the pressure drop in radial direction through the membrane has to be considered. The radial pressure drop depends on the active membrane thickness δ_M, but can be mathematically cancelled after introducing the permeability coefficient k_M with:

$k_M = \frac{\delta_M}{R_M}$. **Equation 3.102**

Solving Equation 3.101 within the model will deliver the initial fluid flow field. Please note, if different membrane resistances were used within one capillary, as it was done in the experimental part of this work, the actual local membrane resistance was

used. As it will be described later in chapter 3.4.6, the boundary condition will be changed to account for the additional resistance of the formed fouling layer when solving the transient suspension flow problem, i. e. over time, to

$$p = u \cdot \eta \cdot R_{Tot} + p_{Filtrate} \,. \qquad \textbf{Equation 3.103}$$

Another boundary condition has to be introduced as the no-slip condition, which is normally used at walls. For no-slip conditions, all components of the velocity vector are eliminated by:

$$\vec{u} = 0 \,. \qquad \textbf{Equation 3.104}$$

This boundary condition will be used in the experimental part of this thesis as described in chapter 4 when modelling pottings for example.

3.4.4 Determination of the floc trajectories

Generally, the software generates trajectories by solving the fundamental equation of motion:

$$m_F \cdot \frac{\partial^2 \vec{x}}{\partial t^2} = \vec{F}\left[t, \vec{x}, \frac{\partial \vec{x}}{\partial t}\right], \qquad \textbf{Equation 3.105}$$

for $\vec{x}$ (t) being the trajectory. Here, m_F is the flocs mass, F equals the force component acting on the floc as introduced in chapter 3.3, and t is time. This delivers a system of ordinary differential equations (ODE) for $\vec{x}$, which COMSOL Multiphysics solves using a pair of Runge-Kutta methods of orders four and five, compare FINLAYSON (2006), which are iterative numerical methods for the approximation of solutions of ODE systems. The solver advances the algorithm with the solution of order five and uses the difference between the order-five and order-four solutions to obtain the local error estimate. For the used 2D axis-symmetric model all three force components were used. Hence, the algorithm solves for a trajectory in 3D in cylindrical coordinates, but only the projection on the axis-symmetry plane is plotted in 2D. For neutrally buoyant particles, the equation of motion is given by:

$$\frac{\partial \vec{x}}{\partial t} = \vec{u}_F\ [t, \vec{u}]. \qquad \textbf{Equation 3.106}$$

3.4.5 Determination of the concentration distribution

For modelling mass balances in the convection and diffusion application mode of the Chemical Engineering Module two mass balance formulations are available: a so called conservative and non-conservative formulation. The conservative formulation was given by Equation 3.5 in chapter 3.1.3. The non-conservative formulation removes the convective term from the divergence operator in Equation 3.5, which gives more stability to systems coupled to momentum balances. It should only be applied to systems that contain incompressible or slightly compressible fluids, because the continuity equation, as introduced with Equation 3.4, is already satisfied for such coupled systems. However, this validity of the continuity equation is only given for fluid elements when coupled to the momentum balance and therefore for dissolved species in the fluid. Considering now the flow of flocs, $\vec{u}$ has to be chosen to denote the actual floc velocity vector $\vec{u}_F$, as introduced in chapter 3.3.9. Accordingly, the continuity equation has to be solved again for the velocity components of flocs to achieve mass conservation. Hence, the conservative form was used as presented with Equation 3.5. For additional information refer to COMSOL AB (2006A) and COMSOL AB (2006B), for instance.

Accounting for the floc volume concentration ϕ_F, the floc velocity vector $\vec{u}_F$ as introduced in chapter 3.3.9 and neglecting any reaction Equation 3.5 becomes:

$$\frac{\partial \phi_F}{\partial t} + \nabla \cdot \left(- D \cdot \nabla \phi_F + \phi_F \cdot \vec{u}_F \right) = 0\,. \qquad \textbf{Equation 3.107}$$

For stationary analysis the term with the time derivative gets dropped. As introduced in chapter 3.4.3, the equation system form was set to ‘General’ in case of dimensional models, using generally the equation as presented above, and to ‘Weak’ for analysing dimensionless models. In the latter case, adoption was performed as described in chapter 3.4.3. The used diffusion coefficient was derived by superposition of the Brownian diffusion coefficient as introduced in chapter 3.3.5 and

the shear induced diffusion coefficient as introduced in chapter 3.3.6 to account for the diffusion of flocs. This superposition delivers:

$$D_{BD} + D_{SiD} = \frac{k_B \cdot T}{6 \cdot \pi \cdot \eta \cdot a_F} + \frac{1}{3} \dot{\gamma}\ {a_F}^2\ \phi_F^2 \left[1 + \frac{1}{2} e^{8.8 \cdot \phi_F} \right]. \qquad \textbf{Equation 3.108}$$

3.4.5.1 Model boundaries

The software package offers several boundary conditions, but only those are discussed here which were applied in the model. For additional information about the boundary conditions refer to the software users guides, i. e. COMSOL AB (2006A) and COMSOL AB (2006B), for instance. Boundary 1 still represents the axial symmetry of the capillary and the condition was set to:

$$r = 0\,. \qquad \textbf{Equation 3.109}$$

At the inlet, boundary 2, the boundary condition was chosen to account for an imposed mass flux condition with:

$$\vec{N}_i \cdot \vec{n} = N_0\,, \qquad \textbf{Equation 3.110}$$

where N_0 denotes the boundary source term. The condition at boundaries 3, 5 and 6 were set to the so called insulation/symmetry condition, given with:

$$\vec{N}_i \cdot \vec{n} = 0\,. \qquad \textbf{Equation 3.111}$$

Here, no particulate and colloidal matter will be transported perpendicular to the boundary to the inside nor the outside but is allowed to move along the boundary. This condition was chosen for the dead-end and for boundary 5. The latter one defines that no floc will enter the capillary at radial coordinates smaller than the dimensionless distance δ_{FM}^* between the flocs centre of mass and the membrane wall. If the capillary will be driven in cross-flow mode, boundary 3 and 6 will be set to convective flux with:

$$\left(-D \nabla \phi_F\right) \cdot \vec{n} = 0\,. \qquad \textbf{Equation 3.112}$$

The condition at boundary 4 was set to continuity, i. e. there is no change in transport of matter along boundary 4 from subdomain 1 into subdomain 2, compare Figure 3.13. This condition can be expressed as:

$$\vec{n} \cdot \left(\vec{N}_{i,1} - \vec{N}_{i,2} \right) = 0 , \qquad \textbf{Equation 3.113}$$

whereas $\vec{N}_{i,1}$ and $\vec{N}_{i,2}$ represent the mass flux vectors of species i in subdomain 1 and subdomain 2 respectively. The condition at boundary 7 was set to convective flux with:

$$\left(-D \nabla \phi_F \right) \cdot \vec{n} = 0 . \qquad \textbf{Equation 3.114}$$

This condition was chosen to account for the high Péclet numbers in the modelled domains. The Péclet number is a dimensionless number, defined as the product of the Reynold and Schmidt numbers as:

$$Pe = Re \cdot Sc = \frac{v_F \cdot d_C}{D} , \qquad \textbf{Equation 3.115}$$

and describes the ratio of convective to diffusive transport. Due to the high velocities and the low diffusion coefficients used in the model, convective transport of the flocs is far more dominant than diffusive transport. Calculated Pe numbers are in the range of 30,000 to 30,000,000. Initially it was intended to choose the boundary condition at boundary 7 to be insulating as well to account for a 100 % retention efficiency of the membrane wall for flocs. However, this could not be realised due to major problems in using FEM to solve the problem numerically. Here, discretisation of convection-dominated transport problems can introduce instabilities in the solution. Instabilities might be detected as oscillations in the studied fields, primarily where steep gradients are present. These oscillations can even be large enough to prevent the solution from converging. All of these problems result from the poor (mesh) discretisation of the continuous equations and are not general properties of the equations themselves. As long as any diffusion is present in the problem, there is - at least in theory - a mesh resolution beyond which the discretisation is stable. However, in most cases the mesh size is determined by available memory in the computer used

for the simulation, which implies that a given mesh cannot always properly resolve small-scale effects. As a rule of thumb for sizing the initial mesh in dimensionless grid scale one should use 1/Pe (email correspondence with Prof. Will Zimmerman). Inserting the Pe numbers mentioned above, this would result in extremely fine meshes, not able to be dealt with by the used computer hardware. To address this problem, COMSOL Multiphysics offers several stabilisation techniques, available to handle local numerical instabilities without the need for mesh refinement. These techniques can all be grouped under the name artificial diffusion (artificial viscosity or numerical diffusion/viscosity are also commonly used terms). However, in this work stabilisation was usually done where needed by using the build-in function of the so called compensated Petrov-Galerkin method, which introduces artificial diffusion along the streamlines. It operates on the test functions of the variables solved for, and, theoretically, does not change the original problem. This is all true in theory, but in practice the solutions might be somewhat smeared out along the streamlines. For more information about stabilisation techniques please refer to the software users guides, i. e. COMSOL AB (2006A) and COMSOL AB (2006B), for instance. However, the condition of convective flux was chosen to minimise numerical instability during the calculations and to find convergence during modelling. Physically, particulate and colloidal matter will not be modelled to accumulate after being deposited, but to leave the capillary at the membrane wall. Because the interest is set in describing accumulation of flocs at the membrane wall, the resulting mass flux will be integrated along boundary 4 to calculate the accumulated mass of particulate matter through this boundary. The accumulation can then be used to calculate the height of the fouling layer, see chapter 3.5.3.

3.4.6 Determination of fouling layer formation

While filtering the feed suspension, foulants are retained and accumulated at the membrane wall. This causes the formation of a concentration polarisation layer and of a coating layer as illustrated in Figure 3.15.

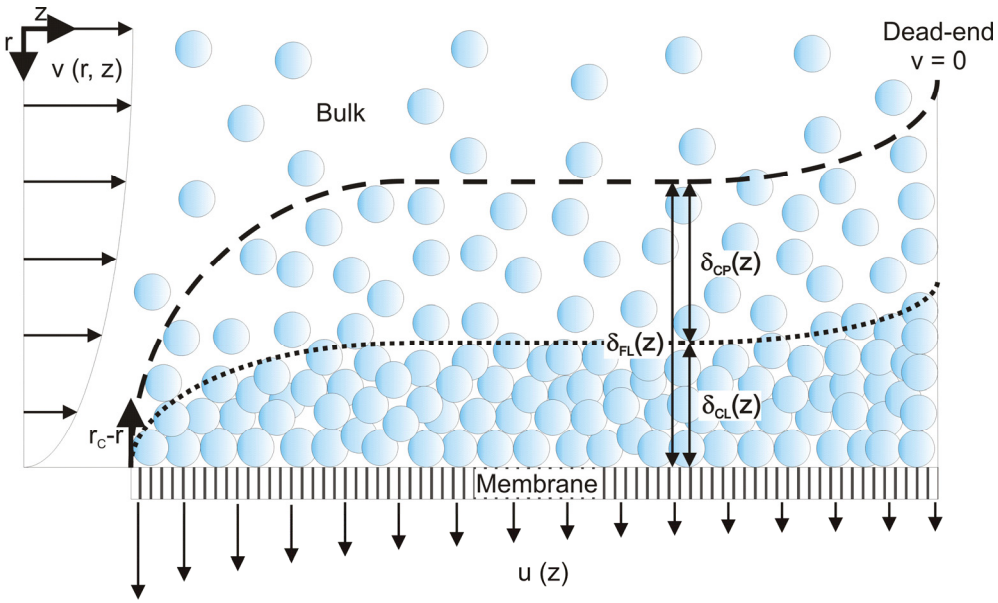

Figure 3.15: Schematic diagram of the concentration polarisation and fouling layer inside the capillary lumen (capillary driven in dead-end mode)

Here, δ_{CP} and δ_{CL} represent the thickness of the concentration polarisation and the coating layer, respectively. Particles or flocs with a bulk volume concentration ϕ_0 are carried from the bulk to the membrane surface, initially establishing a concentration polarisation layer. The coating layer is characterised by a vanishing gradient of the volume concentration (or porosity) with respect to r_C-r and forms between the membrane surface and the concentration polarisation layer. Generally, both layers will act as resistance, i. e. R_{CP} and R_{CL}, in opposition to the driving force, inhibiting the transport of water across the membrane. The combined resistance can be described together with the intrinsic membrane resistance R_M by the resistance in series model as the total resistance R_{Tot} as introduced in chapter 2.1.5. However, it is difficult to determine the coating layer resistance independently of the concentration polarisation resistance, making it easier to lump these into one, i. e. fouling layer resistance R_{FL} in the following. Further, in the presence of a coating layer, the concentration polarisation layer resistance is assumed to become negligible and transient flux decline mainly results from the increasing thickness of the cake layer. Hence, considering long term operation Equation 2.7 satisfies to characterise the resulting total resistance, even if R_{CP} vanishes. The thickness of the fouling layer δ_{FL} can be expressed as the integral of the mass flux, which is the deposition rate of the flocs due to their convective transport onto the membrane wall with:

$$\delta_{FL} = \int_0^t u_F(z) \cdot \phi_F(z)\, dt . \qquad \textbf{Equation 3.116}$$

Integration of Equation 3.116 over filtration time delivers the fouling layer thickness. As mentioned in chapter 3.4.5, this will be realised by integrating the convective floc flux through boundary 4 over time. A user specified PDE was introduced in the model to account for this additional step by solving numerically Equation 3.116 as

$$\frac{\partial \delta_{FL}}{\partial t} = u_F \cdot \phi_F . \qquad \textbf{Equation 3.117}$$

The PDE is calculated over the entire domain and linked to boundary 4 by introducing a so called boundary extrusion coupling variable, see chapter 3.4.1. The deposited fouling layer will increase with time and therefore, flux will decrease as the thickness of the layer increases. The resulting resistance R_{FL} of this layer can be calculated as the ratio of its thickness and permeability coefficient k_{FL} with:

$$R_{FL} = \frac{\delta_{FL}(t)}{k_{FL}} . \qquad \textbf{Equation 3.118}$$

Assuming a homogeneous fouling layer structure, the fouling layer permeability coefficient k_{FL} can be calculated based on the Happel model as introduced and discussed in chapter 3.2.1, using the hydrodynamic floc a_{hF} size as primary particle size. Other authors, e. g. ALTMANN AND RIPPERGER (1997), SONG (1998), KIM AND HOEK (2002), HOEK AND ELIMELECH (2003) and LEE ET AL. (2003) often apply the Carman-Kozeny model to describe the permeability coefficient of the formed fouling layer. Figure 3.16 shows the difference between both models over the investigated fouling layer porosity range from 0.26 to 0.74. The results delivered by the Happel model will be larger than the results delivered from the Carman-Kozeny model up to a fouling layer porosity of $\varepsilon = 0.58$ and smaller for larger porosities. At the minimum porosity of $\varepsilon = 0.26$ the difference was calculated to be approximately 11.5 % and at the maximum porosity of $\varepsilon = 0.74$ approximately 24.6 %.

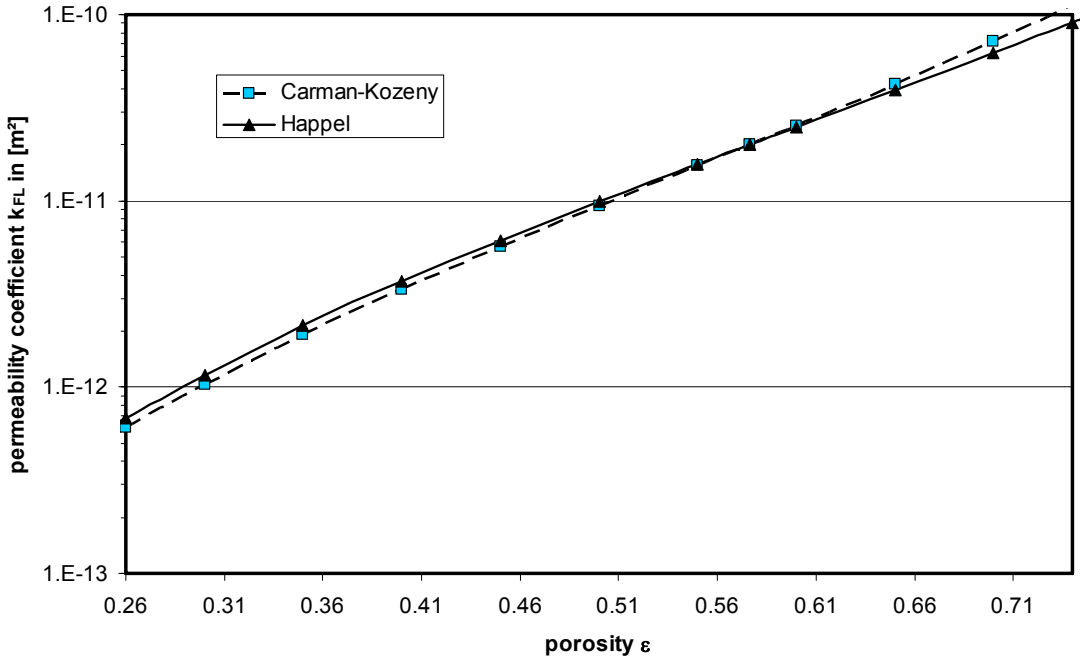

Figure 3.16: Permeability coefficient k_{FL} based on the Happel and the Carman-Kozeny model respectively vs. porosity of a layer of flocs of radius a_F = 29.47 µm

However, the total resistance R_{Tot} can be expressed as:

$$R_{Tot} = \frac{A_M \cdot \Delta p}{\eta \cdot \dot{V}} + \frac{\delta_{FL}(t)}{k_{FL}}. \qquad \textbf{Equation 3.119}$$

If the system is driven at constant flux operation, then the applied pressure needs to be increased as the thickness of the fouling layer increases to maintain constant flux. To account for this, the flow field can be recalculated, delivering a new fluid flow field influenced by the actual fouling layer thickness. Hence, the fluid flow field will be calculated in parallel to layer formation, delivering transient solutions for the influenced fluid flow field, resulting in different floc trajectories, accompanied with changes in formation of the fouling layer as will be shown and discussed in chapter 3.5.3. Please note that the model does not account for compressibility of the formed fouling layer nor single floc aggregates, even this was observed within this work and others, LEE ET AL. (2003) or GITIS ET AL. (2005) for instance. This will be briefly discussed in chapter 3.5.3 too.

3.5 Results of the theoretical considerations and modelling

The delivered results of the numerical calculation for the determination of the initial steady state fluid flow field, the floc transport and fouling layer formation and resulting transient flow field are shown and discussed in the following. Furthermore, different flow fields and different capillary alignments, i. e. horizontal or vertical, etc. are compared to visualise the influence of some parameters, like different fluxes, floc porosities and sedimentation effects for instance. In the following, the type of illustration used for presenting the floc trajectories was chosen to be in 2D at a certain section plane within the capillaries geometry. The section plane considered here is spanned by the complete capillary length and radius at $\varphi = 270°$, i. e. below the symmetry axis at r = 0 as indicated in Figure 3.17.

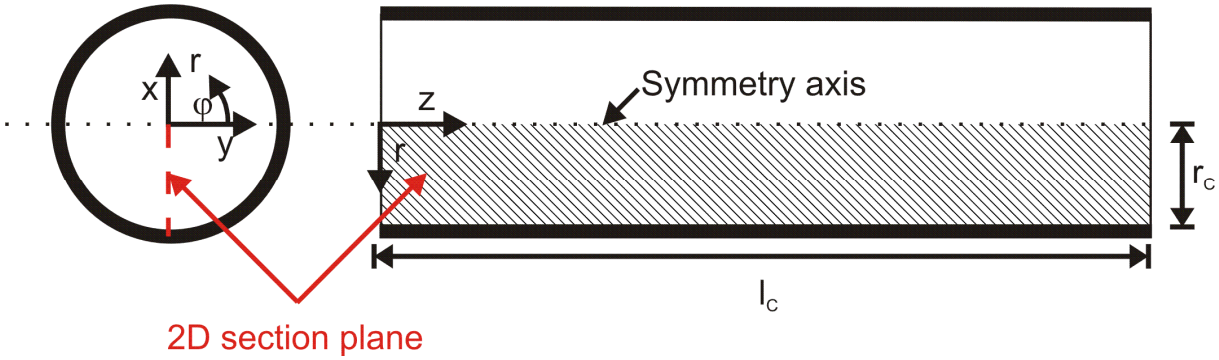

Figure 3.17: 2D section plane for illustration of trajectories

Generally, horizontal aligned capillaries are considered. If other alignments of the capillaries are discussed, it will be additionally mentioned. For purposes of clarity, the direction of the acting gravity was introduced in the figures too. However, the considered section plane in these cases is similar to the one shown above. In the figures, the dimensionless capillary radius is usually considered as abscissa. Hence, the floc trajectories usually start at the bottom line and will end at the right hand side, i. e. the membrane wall, in the following 2D plots.

3.5.1 Initial fluid flow field

The initial fluid flow fields discussed in the following are generally from dead-end operated single capillaries, driven with a flux of 80 L/m²/h if not stated otherwise. The flow fields base further on constants and parameters as introduced in chapter A.11 in

the appendix. Figure 3.18 presents the initial 2D axial symmetric flow field and fluid streamlines in a single membrane capillary driven in dead-end mode. The colour-bar at the right hand side represents the fluid flow field velocity from blue to red with increasing values.

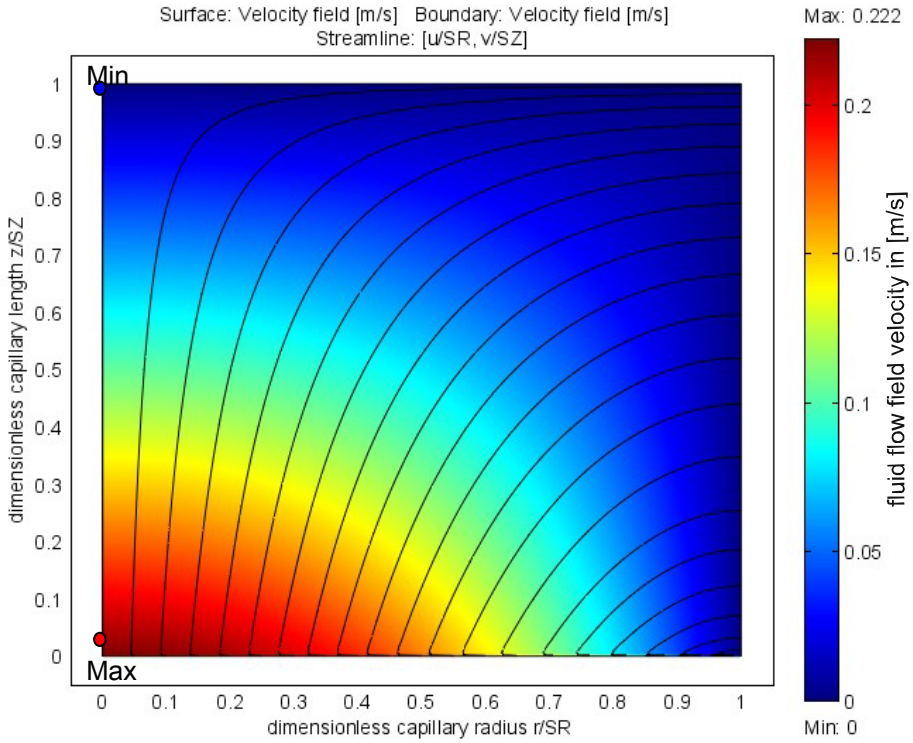

Figure 3.18: Axial symmetric velocity field and fluid flow streamlines

For example, the minimum velocity of 0 m/s, indicated with ‘Min’, will be found at the end of the capillary axis at the dead-end, i. e. z/SZ = 1 and r/SR = 0. The maximum velocity of 0.222 m/s, indicated with ‘Max’, will be found at the capillary axis at about z/SZ = 0.0049 and r/SR = 0. Figure 3.18 indicates further some constriction of the fluid flow streamlines directly after entering the capillary. In this example, the fluid enters the capillary with constant fluid velocity over the complete capillary radius and a laminar flow profile will be developed as introduced in chapter 3.1. The start up length for the development was found to be smaller than 0.5 % of the total capillary length as shown in Figure A.16, approximately 6 times smaller than predicted by Equation 3.2. For this reason it was decided to model the flow into the capillary with a laminar flow profile in the following, giving the numerical model more robustness.

The calculated flow field velocity can be further used to validate the accuracy of the numerical model by integration of the velocity on boundary 2 and 5, i. e. the capillary inlet and boundary 7, i. e. the capillary membrane wall. The integration of the surface integrals deliver the volume flow through the boundaries and can be used to control if no volume of the fluid is 'lost'. Integration of the surface integral on boundary 2 and 5 delivers $5.585054 \cdot 10^{-8}$ m³/s and $5.585529 \cdot 10^{-8}$ m³/s on boundary 7. Because the difference of the result is smaller than 0.009 % mass conservation can be assumed. If coarser meshes are used the difference may increase but is usually much smaller than 0.1 %.

Figure 3.19 and Figure 3.20 show the radial and axial fluid velocity, u and v respectively, within the capillary, represented as contour plots of the dimensionless model. The colour-bar at the right hand side of the figures indicates the velocity isolines, i. e. lines of equal velocity, which are also indicated at the isolines themselves. As illustrated in Figure 3.19, the radial velocity u increases with closer distances to the wall. The radial velocity u at the capillary centre was found to be zero. Further, a line of local maxima develops as function of the axial coordinate z at about r/SR = 0.8. The values of these maxima are higher at the capillary inlet rather than at its end. This was found for different fluxes at the same radial position r/SR too, whereas the values of the maxima increased with increased fluxes and decreased with decreased fluxes. Figure 3.20 indicates the developed laminar flow profile inside the capillary lumen. The axial velocity is highest at the capillary centre and decreases with capillary length until it becomes zero at the dead-end of the capillary. The velocities are always twice as high at the capillary axis as the average longitudinal velocity as is typical for laminar pipe flow.

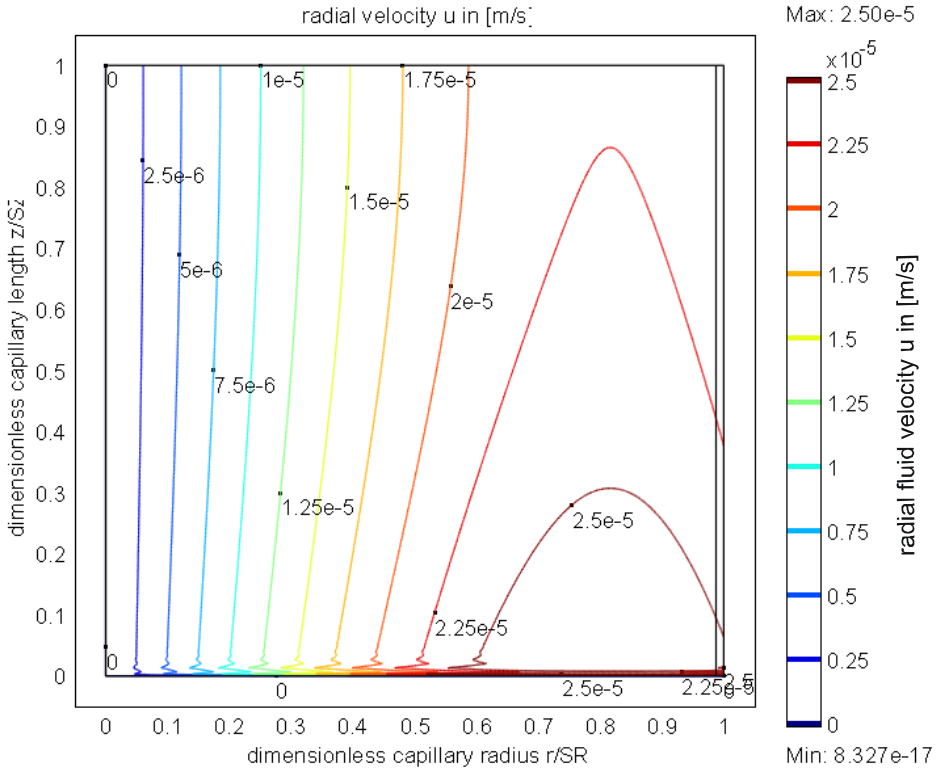

Figure 3.19: Radial velocity contour plot

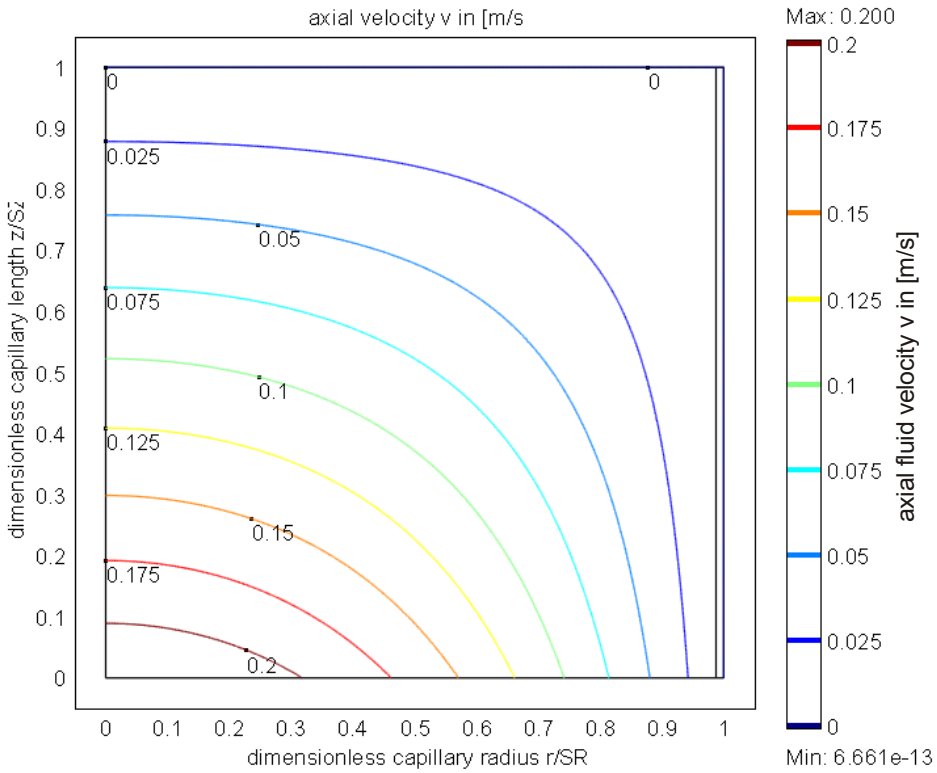

Figure 3.20: Axial velocity contour plot

The laminar flow profiles and velocities at a flux of 80 L/m²/h are illustrated in Figure 3.21 on the left hand side too, presenting the axial velocity vs. dimensionless capillary radius at different axial length coordinates. The right hand side of Figure 3.21 shows the axial velocity v at the capillary symmetry axis for different modelled fluxes vs. the dimensionless capillary length z/SZ. The fluxes were chosen to vary from 60 to 120 L/m²/h in steps of 20 L/m²/h. Of course, the axial velocity at capillary inlet increased with increasing flux. A flux increase of 20 L/m²/h will lead to an increase of 5.56 cm/s for the axial velocity at capillary inlet.

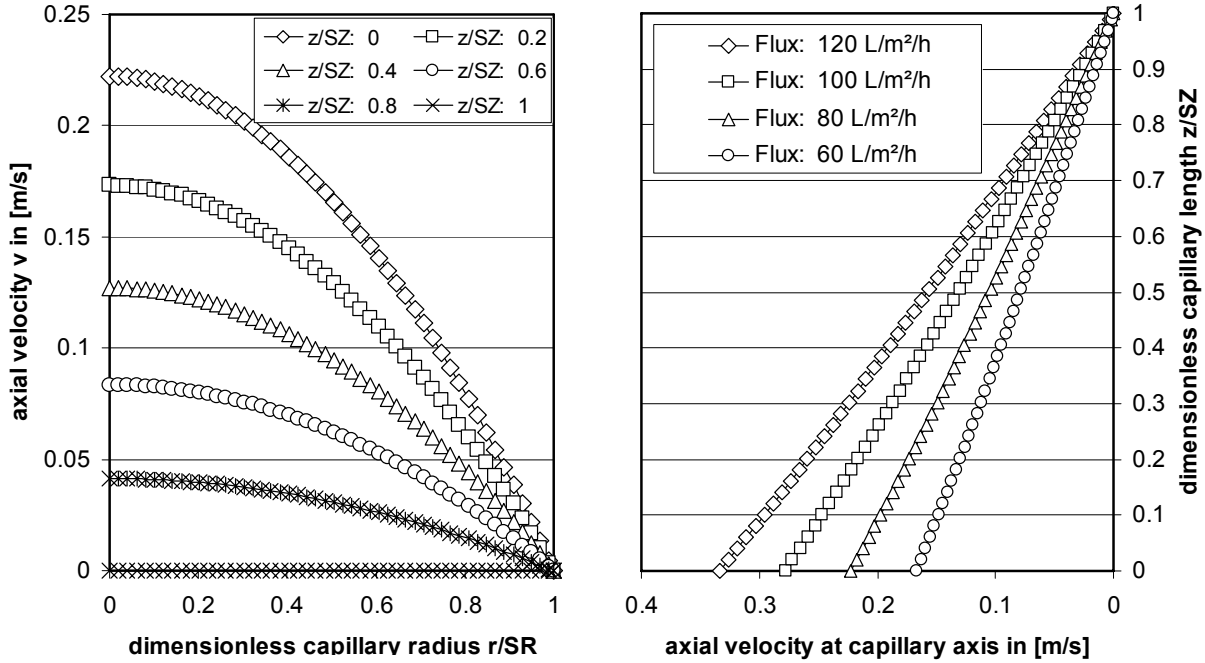

Figure 3.21: Axial velocity v in [m/s] at flux of 80 L/m²/h vs. dimensionless capillary radius r/SR at different axial coordinates (left) and at the capillary axis along the capillary length z/SZ for different modelled fluxes (right)

Figure 3.22 shows the radial velocity u and pressure p of the fluid flow at the membrane wall vs. length of the capillary for different fluxes. Both are in good correlation and there is a 2nd order decrease of them along capillary length, as could be derived from regressions of the calculated values. Additionally, there is a very small linear change in pressure over the radius, corresponding to static pressure due to the dimension of the capillary. The pressure was about 4 Pa, i. e. about 0.04 cm water column, higher at the membrane wall than at the capillary axis over the whole capillary length. It is further shown, that the generally used TMP approximation, given with Equation 2.6, is just quite rough, where it is assumed that the outlet pressure p_{out}

at the dead-end of the capillary equals the inlet pressure p_{in}, which is in fact not true, even for clean membranes.

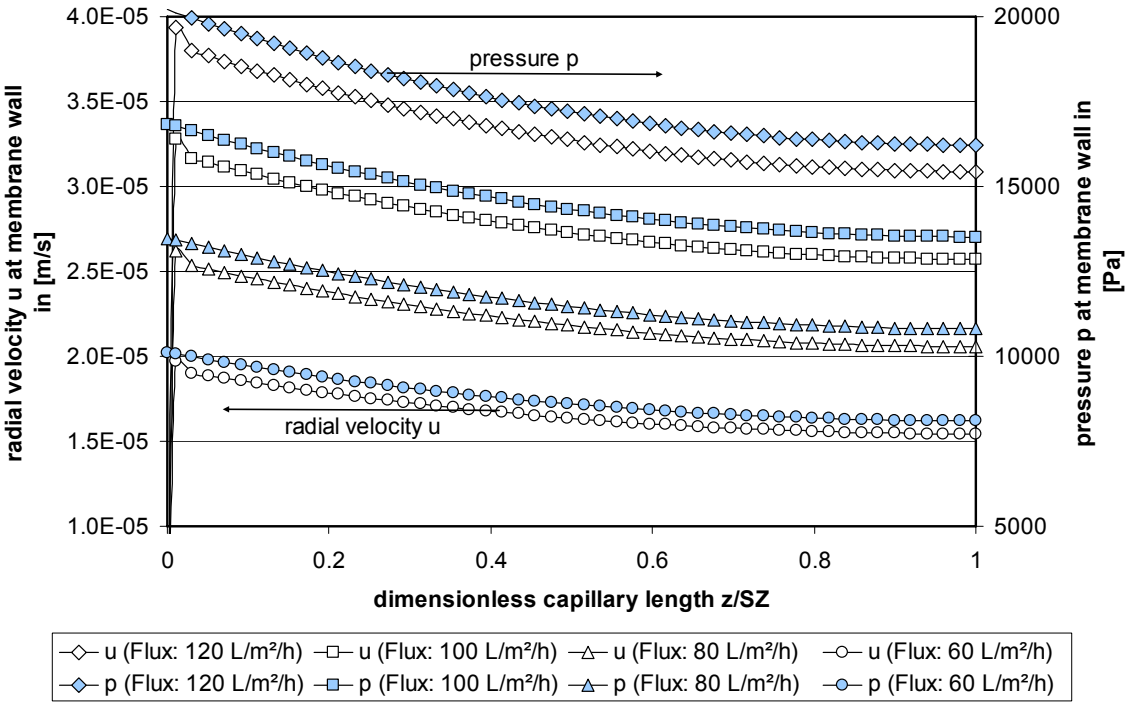

Figure 3.22: Radial velocity u in [m/s] and pressure p in [bar] of the fluid flow at the membrane wall vs. dimensionless capillary length z/SZ

After transformation of the geometry and velocity components, see chapter A.14, additional 3D figures can be plotted, e. g. as given with Figure 3.23 and Figure 3.24 for the visualisation of the fluid flow inside the capillary. Figure 3.23 shows the 3D fluid flow field, comparable to Figure 3.18, combined with an arrow plot in two quadrants, representing velocity and direction of the flow magnitude. The flow is from the left to the right as indicated by the colour of the axial velocity, which increases from blue to red, showing again the typical flow pattern for laminar pipe flow. Figure 3.24 shows a streamline plot inside the capillary to visualise the trajectories of certain fluid flow elements. The flow is from the rear left to the front right, length and radius of the capillary are dimensionless. It is shown that fluid elements entering the capillary at the neighbourhood of the capillary axis will be transported towards the dead-end and leaves the system close to it. Further, no gravity effects are visible, hence assuming only negligible influence of gravity on the flow of the fluid elements.

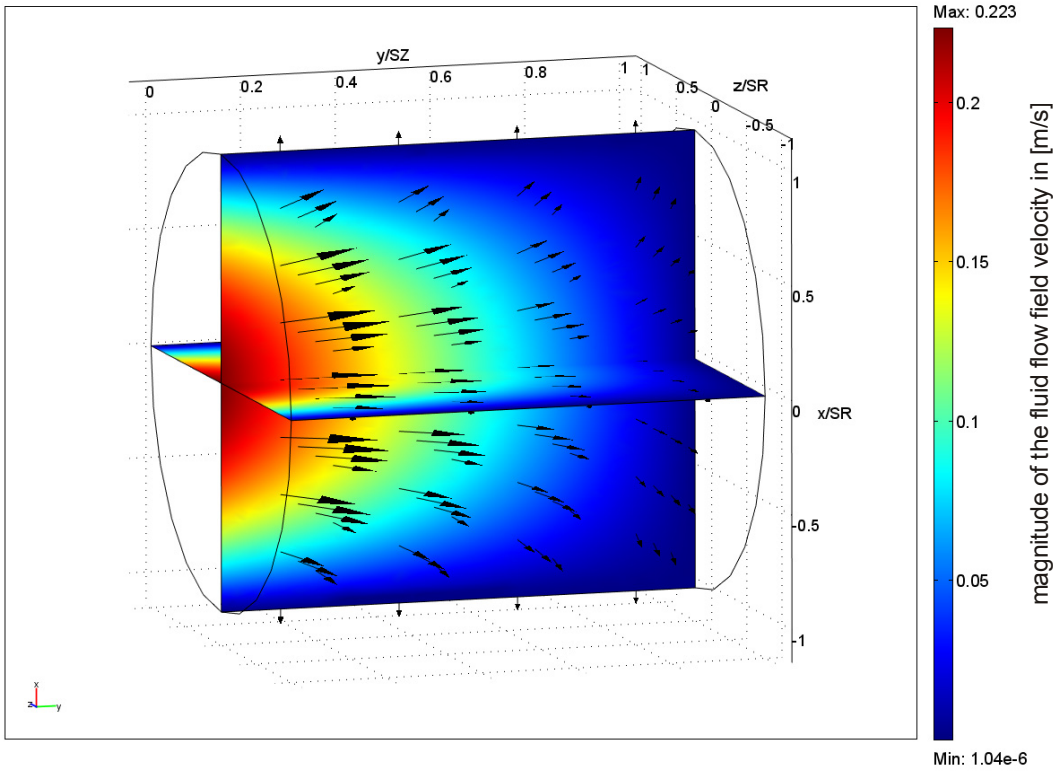

Figure 3.23: Velocity flow field and arrow-plot of the velocity inside the capillary

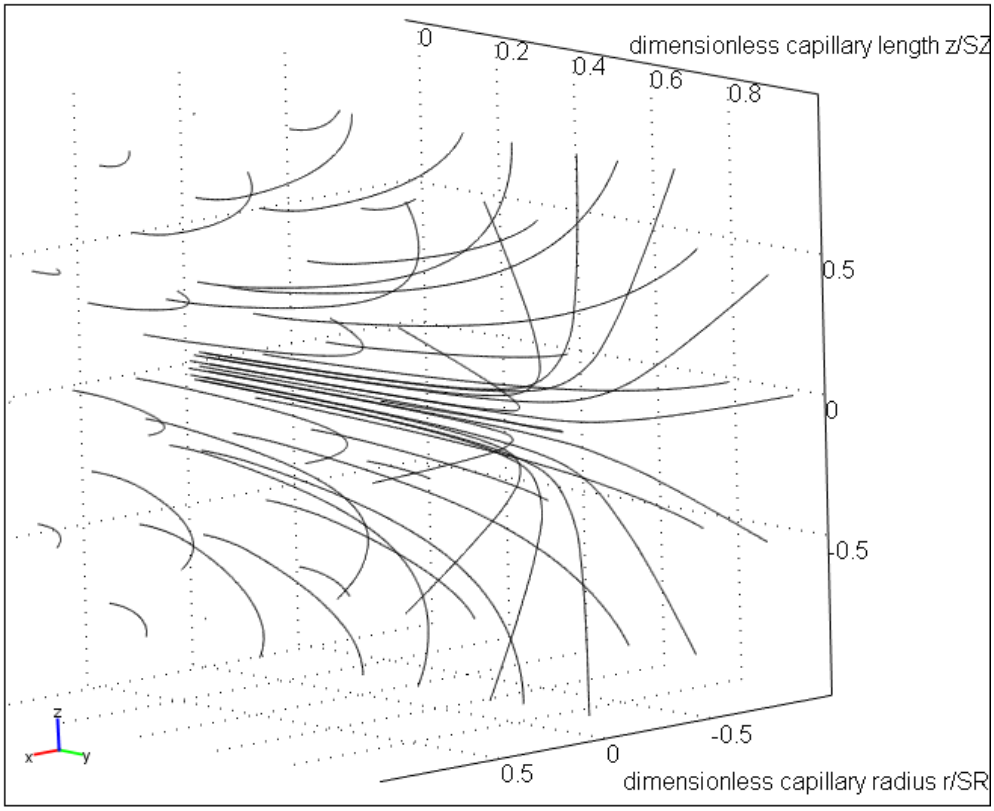

Figure 3.24: Fluid flow streamlines inside the capillary

3.5.2 Floc transport

The forces and velocities derived and presented in chapter 3.3 can be used to determine the floc trajectories. The used constants and initial parameters are summarised in Table A.2, Table A.3 and Table A.4 in the appendix if not stated otherwise in this work. Furthermore, the alignment of the capillaries is always horizontal if not stated otherwise. The trajectories can be calculated starting from any position within the capillary, even backward integration is possible. Floc agglomeration along the trajectories is not considered but will be discussed in chapter 3.5.2.4. Further, there is initially no affection on the modelled flow field by motion of the flocs. Therefore, the results shown here are neither influenced by floc concentration at the membrane wall nor inside the lumen, hence representing initial conditions at start of operation. The influence of increasing floc concentration within the capillary and floc deposition, resulting in change of the acting resistance against fluid flow, on the trajectories of following flocs will be considered and discussed later. However, the discussed points are valid for both, initial and dynamic transport behaviour. Generally, the findings obtained by the developed model are in strong agreement with findings shown by CHELLAM AND WIESNER (1992), SONG AND ELIMELECH (1995) and PANGLISCH (2001) for instance.

The convective transport of dissolved and colloidal matter up to particulate micro sized flocs can be generally described according to the transport of fluid elements and will therefore follow the fluid streamlines as shown in chapter 3.5.1. Figure 3.25 illustrates the trajectories of micro flocs with radius a_F = 0.5 µm inside the capillary, driven in dead-end mode. Due to this flow behaviour, the complete inner surface of the capillary will be fouled by micro flocs, if the membrane is able to retain them. However, the resulting fouling layer may vary in height over the capillary length and estimation will be discussed in the following. The imposed mass flux of micro sized flocs into the capillary depends on the fluid flow rate and the floc volume concentration. The latter one was assumed to be constant over the capillary cross section area, whereas the flow rate depends on the radial position due to the laminar flow profile and hence on velocity and considered cross section area. The flow rates can be obtained by boundary integration as introduced in chapter 3.5.1.

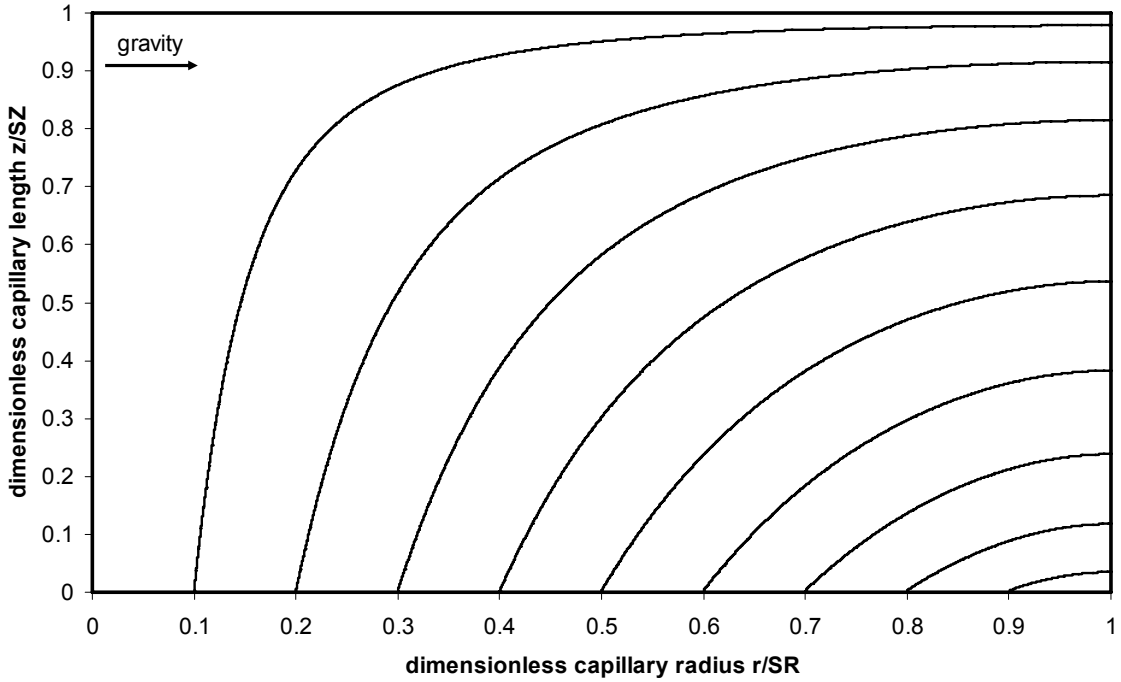

Figure 3.25: Floc trajectories of micro flocs of size a_F = 0.5 µm inside the capillary driven in dead-end mode

Considering exemplarily the inlet sections spanned by trajectory pairs starting at the radial position of r/SR = 0 and r/SR = 0.1 as well as r/SR = 0.5 and r/SR = 0.6, the boundary integration delivered volume flow rates of $1.1 \cdot 10^{-9}$ m³/s and $8.5 \cdot 10^{-9}$ m³/s, respectively. It has to be mentioned that the distances in between the radial starting positions of the trajectory pairs were equal but not their spanned area of the front section as illustrated in Figure 3.26, which were found to be 1 % and 11 % of the complete available front section of the capillary. Further, the different fluid velocities due to the laminar flow profile were considered, being approximately 30 % higher at the front section area 0 - 0.1 than at the front section area 0.5 - 0.6. Nevertheless, for an estimation of the formed fouling layer height the mass flux towards the membrane wall has to be approximately determined. Therefore, it is necessary to know the floc volume concentration and the floc velocity at the membrane wall. Again, the fluid volume flow could be determined by boundary integration over certain areas. The area chosen was the projected surface ring area, indicated in red in Figure 3.26, spanned by the pairs of floc trajectories. It can be seen that the surface ring section area 0 - 0.1 is much smaller than the surface ring section area 0.5 - 0.6. However, boundary integration delivered values for the fluid volume flow through the section ring areas of about $1.14 \cdot 10^{-9}$ m³/s through area 0 - 0.1 and $8.43 \cdot 10^{-9}$ m³/s through

area 0.5 - 0.6, respectively. Hence, the radial fluid velocities were calculated with $2.06 \cdot 10^{-5}$ m/s at area 0 - 0.1 and $2.19 \cdot 10^{-5}$ m/s at area 0.5 - 0.6, respectively. The floc volume concentrations were estimated by a simple mass balance of the mass flux within the outlined areas. They were found to be approximately 10 m³/m³ at area 0 - 0.1 and 6.7 m³/m³ at area 0.5 - 0.6, respectively. Please note that no restrictions with respect to packing density etc. were used within this estimation. Considering the above, it can be estimated that the formed fouling layer height will be approximately 30 % higher at the surface ring section area 0 – 0.1 than at area 0.5 – 0.6. Generally, assuming a (developing) laminar flow profile at the capillary inlet, the formed fouling layer will be higher for longer distances to the inlet. This effect is due to the curvature of the velocity profile with its highest velocity at the centre line. Hence, the mass flux brought into the system will be also highest at the centre line, assuming constant floc volume concentrations. However, influences caused by floc transport over time, e. g. increase of TMP and resulting fluid flow, were not included in this estimation. These effects may essentially influence floc transport and deposition and possibly causing a more homogenously formed layer height, compare chapter 3.5.3.

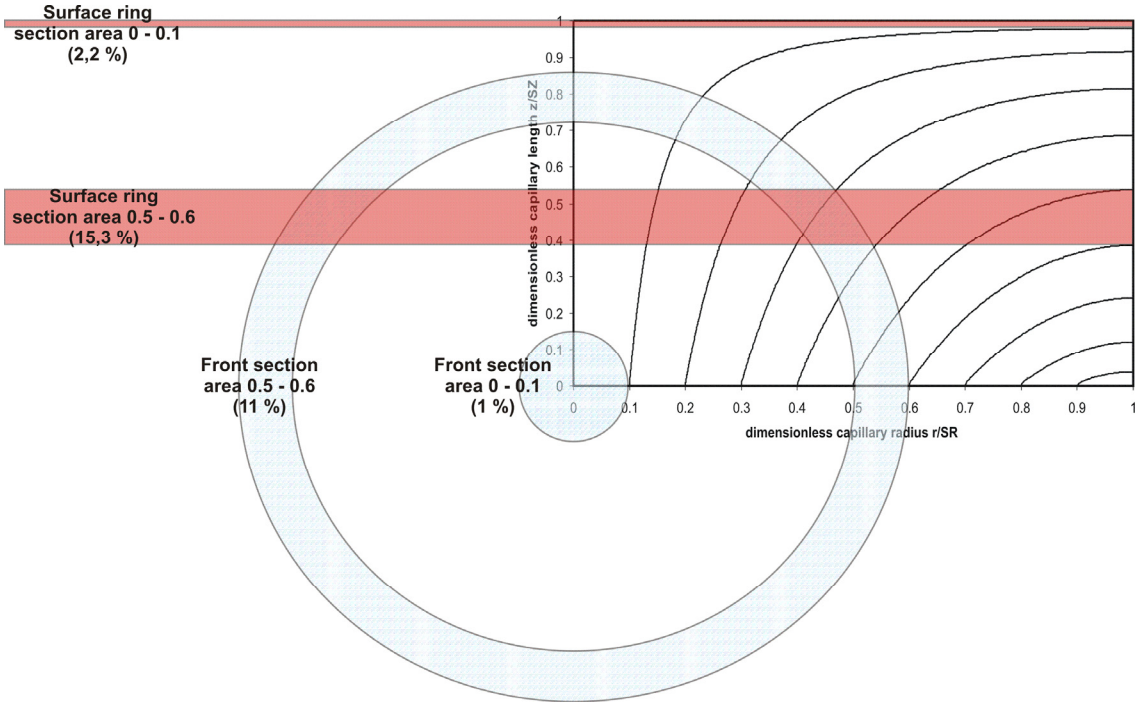

Figure 3.26: Resulting surface ring areas, indicated in red, and front section areas, indicated in shaded blue, spanned by pairs of floc trajectories at a radial starting position of r/SR = 0 and r/SR = 0.1 as well as r/SR = 0.5 and r/SR = 0.6

If the floc size is increased to radii larger than a certain ‘limiting radius’, the transport behaviour will change even under the same flow conditions and physical properties and an equilibrium trajectory will be developed where individual trajectories merge into one, compare Figure 3.27. At the equilibrium trajectory, the acting forces directed towards the membrane are equalised by forces directed away from the membrane wall towards the capillary axis. The corresponding limiting floc radius can be determined by balancing the radial velocity component of the floc. For being deposited all-over the capillaries membrane wall, the radial velocity has to be always larger zero along the complete capillary length. The first radius which does not fulfil this inequality is called the limiting radius and was calculated to be a_F = 3.27 µm for the given flow conditions and physical properties. This effect is due to the acting repulsive forces, which usually increase with increasing floc sizes, closer distances to the membrane wall and increasing longitudinal flow velocities. The developed theoretical model shows that this is mainly caused by lateral migration.

Figure 3.27 illustrates calculated floc trajectories of small flocs with radius a_F = 5 µm, just a bit larger than the limiting radius, whereas the right hand side of Figure 3.27 shows a display detail at the membrane wall of the same trajectories. It has to be pointed out that the shown trajectories represent the moving centre of mass of the flocs. The dashed red line at the right hand side indicates the distance of the centre of mass to the membrane at contact as explained in chapter 3.4.2. For smaller floc sizes this equilibrium trajectory can be usually found at closer distances to the membrane wall, approaching the wall only slightly until deposition occurs. This is due to the arising floc wall interactions such as repulsive double layer forces and lateral migration as described in chapter 3.3. In case of dead-end mode this equilibrium trajectory is usually much closer to the wall than in cross-flow mode operation, as shown by CHELLAM AND WIESNER (1992), likely due to the higher local maximum longitudinal fluid flow velocities. In contrast, fluid elements are not exposed to those interactions and additional forces, and hence their streamlines are approaching the membrane wall directly as indicated by the blue dotted lines in the figures. Due to the equilibrium trajectory, flocs of radius 5 µm will be deposited at the membrane only after passing approximately the first 61 % of its length; i. e. only 30 % of the membrane area is used for deposition of flocs of this size.

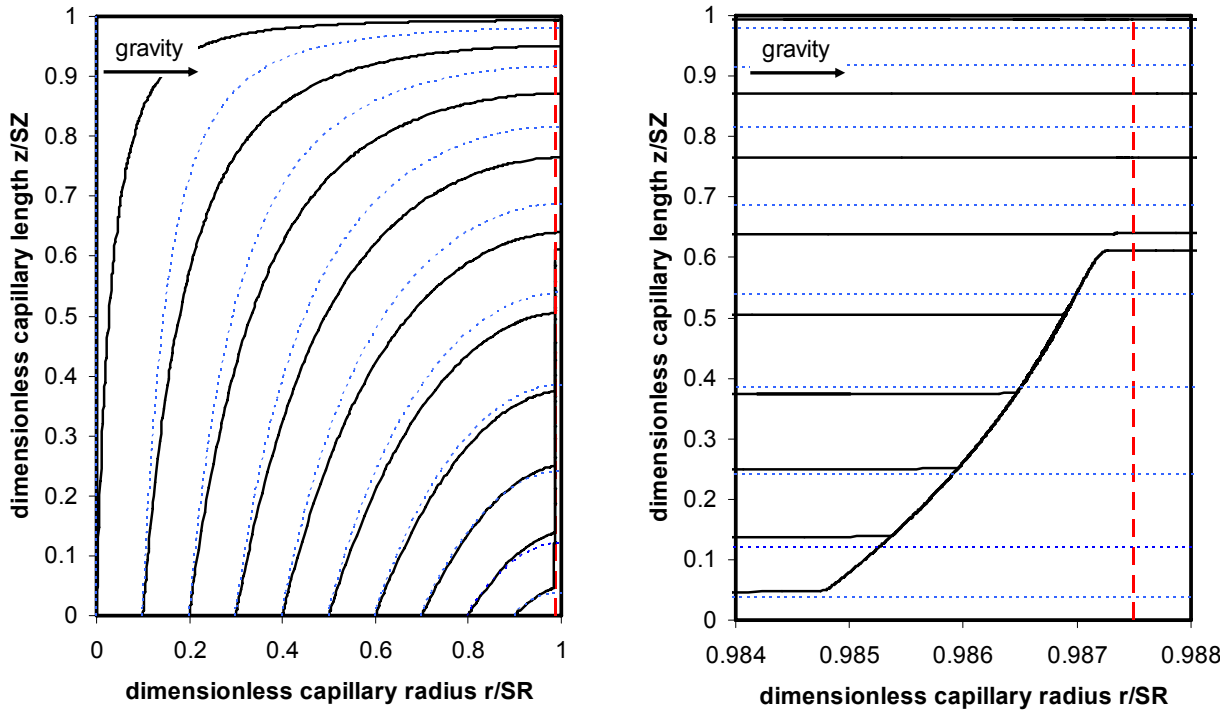

Figure 3.27: Floc trajectories of small flocs (a_F = 5 µm, black lines) and fluid streamlines (blue dotted lines) inside the capillary driven in dead-end mode (left) and display detail (right)

The effect of an increased floc radius can be seen in Figure 3.28, where the modelled floc radius was increased to a_F = 10 µm (left) and 29.47 µm (right) respectively. The front contact point, i. e. the longitudinal coordinate where contact between the equilibrium trajectory and the membrane occurs is shifted more inwards. Further, due to the increased floc size the equilibrium trajectory is moved away from the membrane wall towards a position closer to the capillary axis, eventually towards a position at approximately two thirds of the capillary radius for flocs of 30 µm in radius. For further increased floc sizes, this position will be located eventually at r/SR = 0.622, which is in very good agreement to the findings of SEGRÉ AND SILBERBERG (1962A), see chapter 3.3.7. Figure 3.28 right hand side shows that all flocs entering the capillary, independent of their starting radial position at the inlet, will merge a final equilibrium trajectory and travel along it until deposition occurs at the rear lumen end. Hence, most of the membrane area is initially not affected by floc deposition of larger flocs.

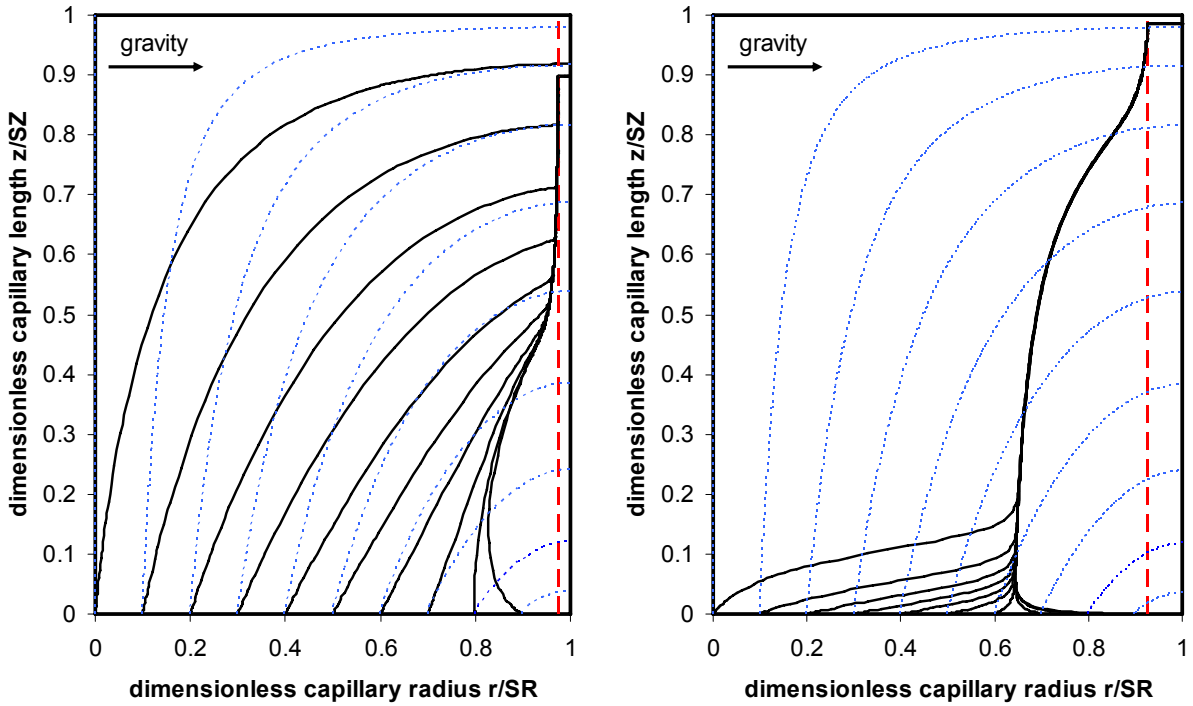

Figure 3.28: Floc trajectories of flocs with radius a_F = 10 µm (black lines), (left) and with radius a_F = 29.47 µm (black lines), (right) and fluid streamlines (blue dotted lines) inside the capillary

An additional effect occurs at the dead-end of the capillary. Flocs entering the capillary at its axis will not reach the rear end of the capillary but will contact the membrane wall at closer distances to the inlet, called rear contact point in the following. The developed theoretical model shows that this behaviour is mainly caused by lateral migration, because larger flocs will be exposed to lateral forces towards the membrane wall in the neighbourhood of the capillary axis, compare chapter 3.3.7. Additionally, sedimentation forces acting towards the membrane wall play a decisive role with increasing floc size too, see chapter 3.5.2.2. However, the distance between dead-end and rear contact point increases with increasing floc radius, see Figure 3.28 (left), until all incoming flocs will be forced to merge the equilibrium trajectory as can be seen in Figure 3.28 (right). This is also illustrated in Figure 3.29, which shows the axial distances from the capillary inlet of modelled front and rear contact points vs. increasing floc radii. Hence, Figure 3.29 illustrates a summary of calculated expectations for the front and rear contact points of the floc at the membrane wall. The difference between rear and front contact point gives the length of capillary area theoretically available for initial deposition for flocs of certain

size. But, the loss in membrane area available for deposition is mainly governed by the front contact points. Immediately after exceeding the limiting floc radius of a_F = 3.27 µm the available length for deposition will decrease and the front contact points will be shifted towards the capillary end.

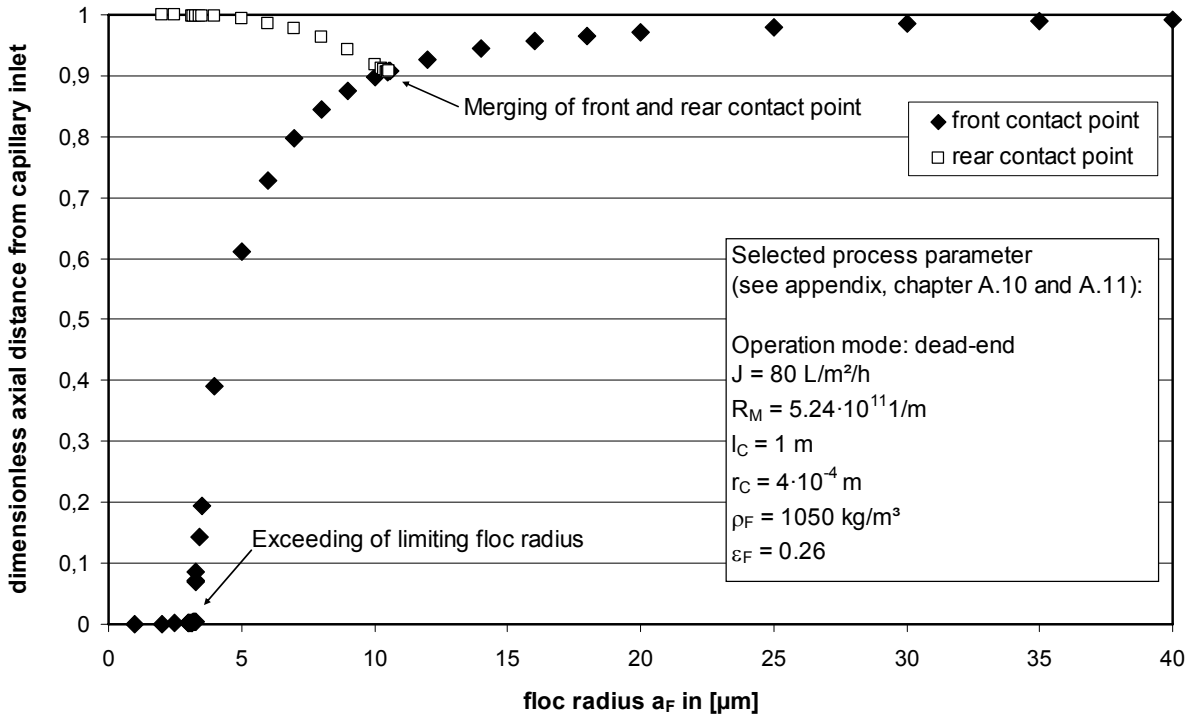

Figure 3.29: Front and rear contact points at dimensionless axial distance to capillary inlet vs. floc radius a_F in [µm]

If the flocs are larger than 10.55 µm in radius, all flocs will be merged together and only one equilibrium trajectory will come into contact with the membrane wall, of course under the given flow conditions and properties. This means that all flocs entering the capillary, independent of their radial starting position at capillary inlet, will be deposited theoretically at one single point at the membrane wall. This expected point will be shifted towards the dead-end with increasing floc size.

Considering not only a section plane in 2D but the 3D geometry of the capillary, the calculated expectations will form a ring at this certain point or area. If gravity acts perpendicular to the length coordinate, i. e. a horizontal aligned capillary, sedimentation effects will deform this ring to a ring section as discussed later in chapter 3.5.2.2

3.5.2.1 Influence of DLVO forces

Beside floc radius and dimensionless distance to the membrane wall, the values of the acting DLVO forces are mainly influenced by the surface potential of the membrane materials and flocs, the ion concentration present in the water and the Hamaker constants between the flocs and/or the flocs and the membrane as shown in chapter 3.3.8. The influences by the mentioned parameters are very complex and values are not always exactly known, making it nearly impossible to derive accurate quantitative predictions. Furthermore, crucial information like surface roughness of the membrane and shape of the floc are usually not available and are substituted by simplified considerations and assumptions. For example, a spherical, rigid particle or floc interacting with a flat plate has a well defined area of interaction and minimum separation distance, see chapter 3.3.8. However, a floc, which is usually not ideally spherical, approaching a rough surface, such as a porous membrane, may interact with a roughness peak, a flat planar area or a roughness valley. This leads unavoidably to local variations of the interaction energy, which might be locally smaller or higher than the expected sphere-plate interaction profile, whereas the magnitude of the average interaction energy profile is reduced (HOEK AND AGARWAL (2006)). Nevertheless, influences caused by variations of the above mentioned parameters, by coagulation for instance, can be considered and discussed qualitatively, which will be done briefly in the following.

Considering DLVO forces between an interacting floc and membrane wall it will not come to deposition as long as repulsive forces are dominant and higher than the local flow forces including lateral migration forces acting on the floc towards the membrane wall, resulting in formation of an equilibrium trajectory close to the membrane. Theoretically, this would lead to a transport of the floc to the rear end of the capillary, see Figure 3.30 (right) and Figure 3.31, nearly independent of its size (PANGLISCH (2001)) under favourable conditions. The equilibrium trajectory runs through the centre of mass of the considered flocs and will be therefore closer to the membrane wall for smaller flocs than for larger flocs, even if the distance between the flocs outer surface to the membrane wall is identically for all floc sizes. Hence, in case of attractive DLVO forces, the limiting radius will not be significantly heightened because DLVO forces are genuine short distance forces and larger flocs will not

come into any interaction with DLVO forces until they are just to be deposited at the membrane wall. In comparison to hydrodynamic flow forces, values of the DLVO forces are independent of the distance to the capillary inlet, depending on the radial distance of the surfaces only. Deposition will only occur if the flow forces are high enough to overcome repulsive Double-Layer forces, transporting the floc into ranges where attractive van der Waals forces are dominant. Hence, low surface potentials and high Hamaker constants are favourable for deposition of flocs on the membrane surface, as can be seen in Figure 3.30. Here, the effect of different floc surface potentials is illustrated, whereas the surface potential of the membrane and the Hamaker constant was kept constant with – 15 mV and $H_{132} = 2.63 \cdot 10^{-19}$ J respectively, representing the interaction of iron hydroxide and PES across water.

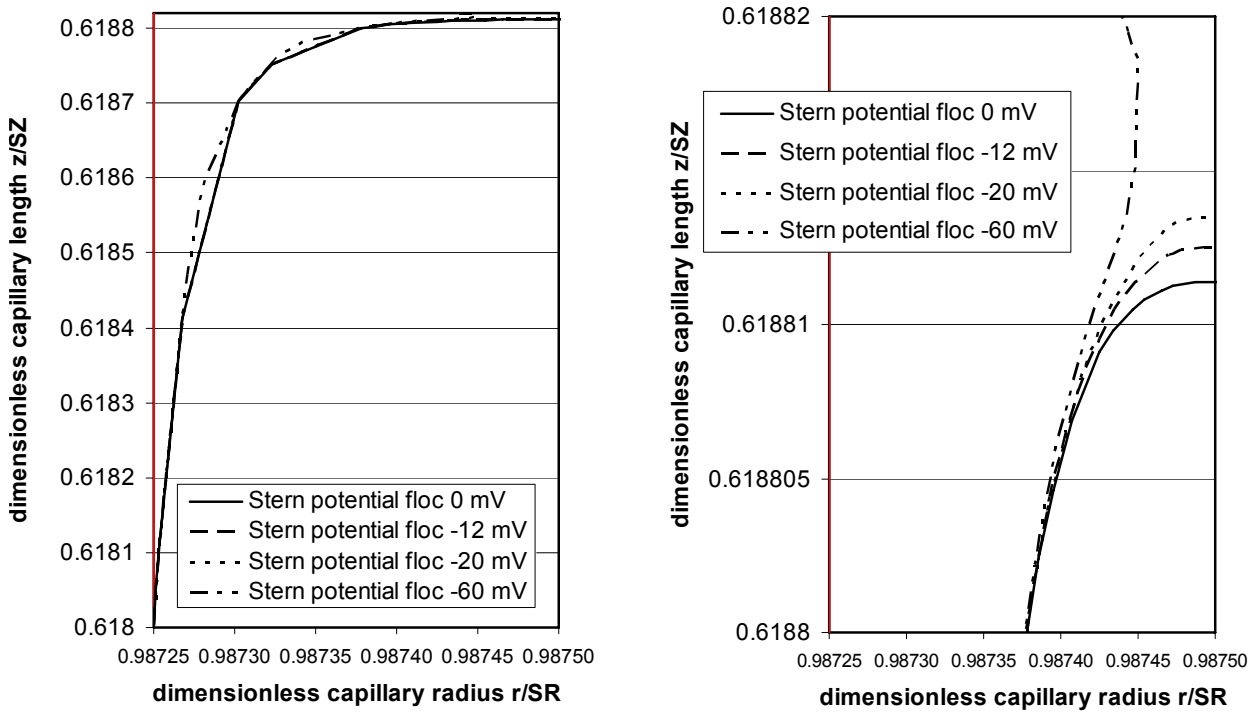

Figure 3.30: Floc trajectories of flocs with radius a_F = 5 µm for different floc surface potentials (left) and display detail (right)

Considering the surface potentials and Hamaker constants as system immanent, deposition will be facilitated by higher ion concentrations present in the water due to compaction of the double layer as illustrated in Figure 3.31. The amount of ion concentration is represented as hardness of the water, whereas the chosen values range from very soft to very hard waters, theoretically from 1.121 °dH (20 ppm

$CaCO_3$) to 112 °dH (2000 ppm $CaCO_3$). In practice, the hardness of potable water should be in the range between 0.89 mmol/L (5 °dH) and 4.46 mmol/L (25 °dH). For the lowest ion concentration shown, an equilibrium trajectory will be developed and the floc will not be transported towards the membrane because the repulsive double layer forces could not be exceeded by the acting flow forces. With increasing ion concentration the double layer will be compressed, hence its effective range of interaction is reduced and the flow forces will be able to bring flocs into positions where attractive van der Waals forces become dominant, finally resulting in deposition.

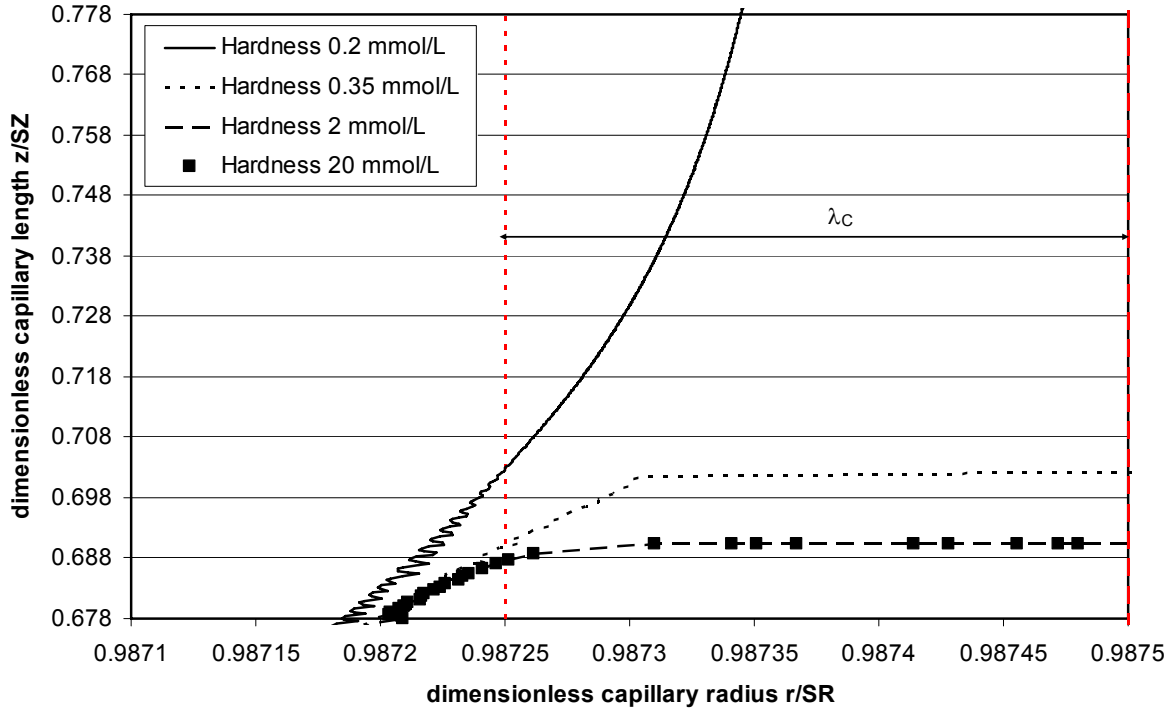

Figure 3.31: Floc trajectories (display detail) of flocs with radius a_F = 5 µm for different ion concentrations, indicated as hardness and indication of range of the characteristic wavelength of interaction floc/membrane wall

The qualitative influences discussed above are of course also applicable considering coagulation. Due to coagulation, primary particles were embedded into (iron) hydroxide flocs, accompanied by a change of their surface potential and Hamaker constant to values describing the chemical-physical properties of the formed floc agglomerate, see chapters 4.1 and 4.2 and Table A.2. The primary particles used in the experimental part of this work showed always repulsive DLVO forces as illustrated in Figure 3.32. The calculated double layer and van der Waals forces are

given in Figure A.14 in the appendix. After coagulation, the formed hydroxide flocs showed always attractive DLVO forces, making floc deposition more favourable by their lower surface charge and higher Hamaker constants if compared to the values of the primary particles. This is additionally enhanced due to the accompanied increase of the ion concentration present in the water and therefore double layer compaction. Furthermore, the average radius of the formed flocs will be 2.4 times larger than the radius of their primary particles, see chapter 4, increasing the affective radius and therefore DLVO forces, making deposition even more favourable as illustrated in Figure 3.32.

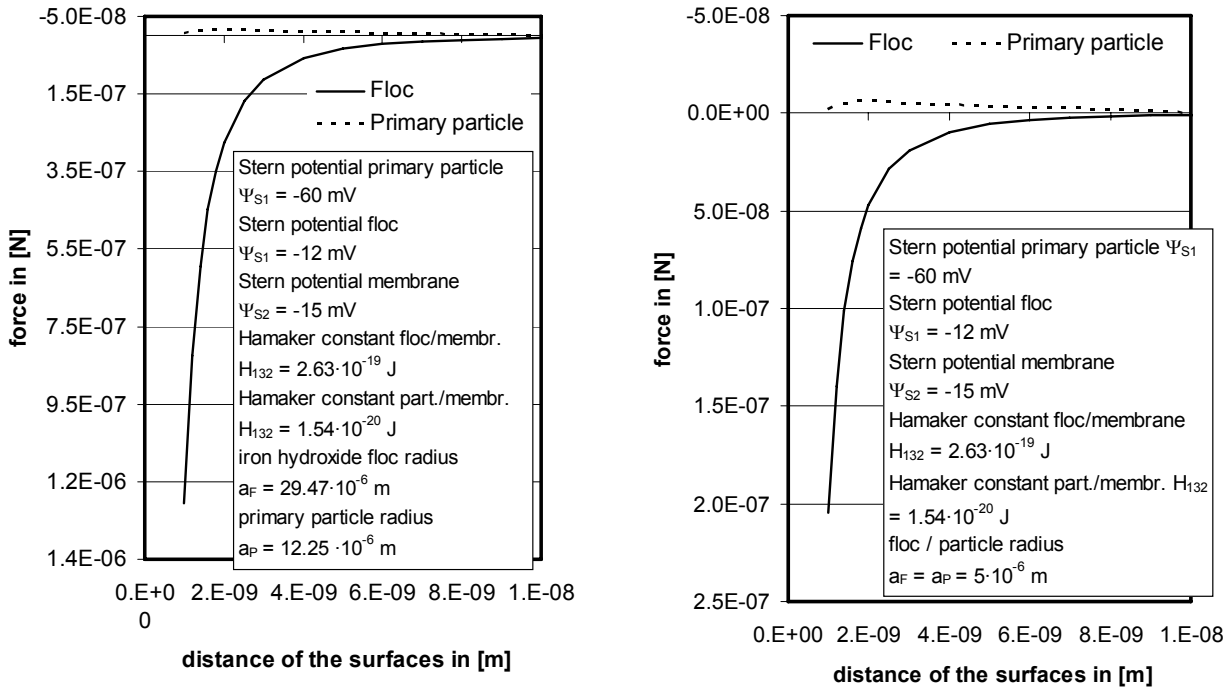

Figure 3.32: DLVO force between floc and membrane wall and between primary particle and membrane wall vs. distance of the surfaces for different and equal sized floc and primary particle radii (Left: a_F = 29.47 µm, a_P = 12.25 µm; Right: $a_F = a_P$ = 5 µm)

3.5.2.2 Influence of sedimentation

Floc agglomerates in this work are usually considered to be slightly denser than the fluid with a relative density of 1.05, comparable to activated sludge flocs (SEARS ET AL. (2006). In case of flocs, gravity effects are existent and relatively small but will become more significant for increasing floc sizes, see Figure 3.33, Figure 3.34 and Figure 3.35 (left). As a result, the trajectory field is not rotation-symmetric along the

capillary axis anymore within the horizontal aligned capillary, especially not in longer ones. This asymmetry will be faster developed and more pronounced if the flocs or particles to be modelled become much denser than the fluid, for example quartz particles. For comparison see Figure 3.35 (right), here modelled with a relative density of 2.65. Depending on the radial position of the flocs, gravity effects will amplify or dampen the effects caused by lateral migration. Smaller flocs, here of radius 5 µm, will still be deposited at the upper part (r/SR from 0 to -1), i. e. above the symmetry axis of the horizontal aligned capillary, compare Figure 3.17, because the density difference is small and because the flow field is strong enough. This can be seen in Figure 3.35, left hand side, where gravity acts from the left to the right and the rotation-symmetry axis is indicated as red dotted line at r/SR = 0. Further calculation showed that this behaviour declines with increasing floc size. For an increasing floc size more and more flocs will not be able to stay in the upper part, being transported into the lower part (r/SR from 0 to 1), i. e. below the symmetry axis of the horizontal aligned capillary, and will be deposited there. It was found that nearly no flocs will be retained by the upper part of the membrane capillary for flocs with a radius larger than approximately 14.75 µm under the given flow conditions, compare Figure 3.33. Here, the flow is from the rear to the front and gravity acts from top to bottom. The diameter of the tubes was scaled to the modelled floc radius a_F/SR and the colour bar at the right hand side of each plot indicates the floc velocity. Due to repulsive DLVO forces and sedimentation, the flocs will slide close to the membrane wall along its surface to the bottom. If the floc radius is increased further even areas of the lower capillary part will not be available for floc deposition and the flocs will finally merge for deposition at the rear end into one trajectory at the bottom of the capillary.

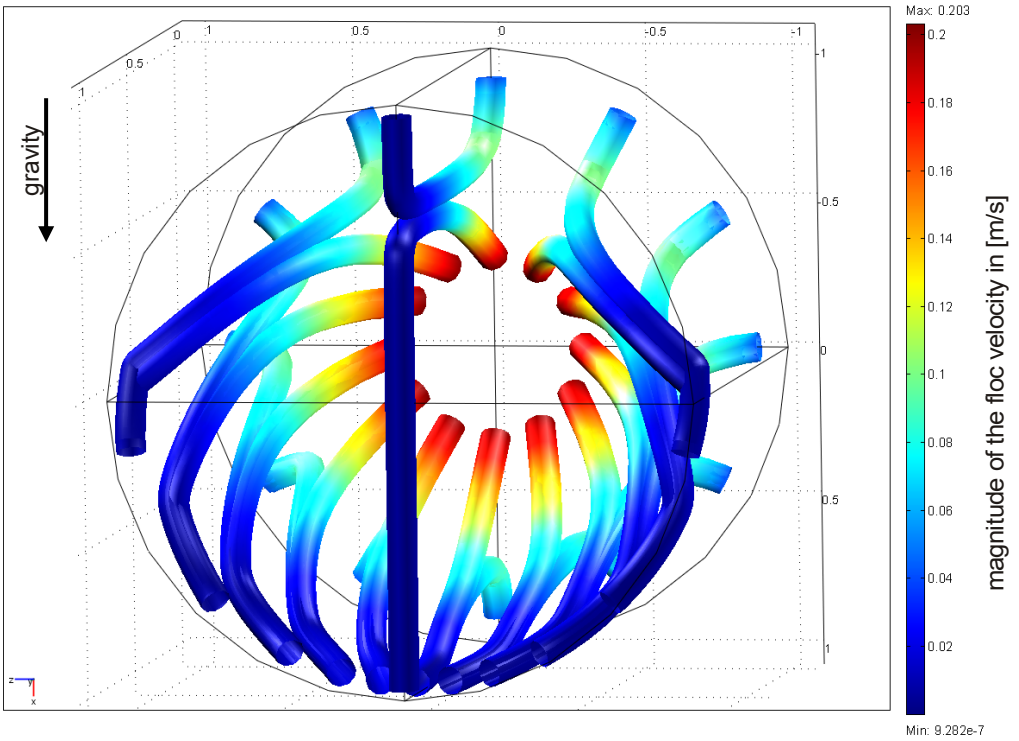

Figure 3.33: Floc trajectories of flocs with radius a_F = 14.75 µm (scaled to floc radius a_F/SR)

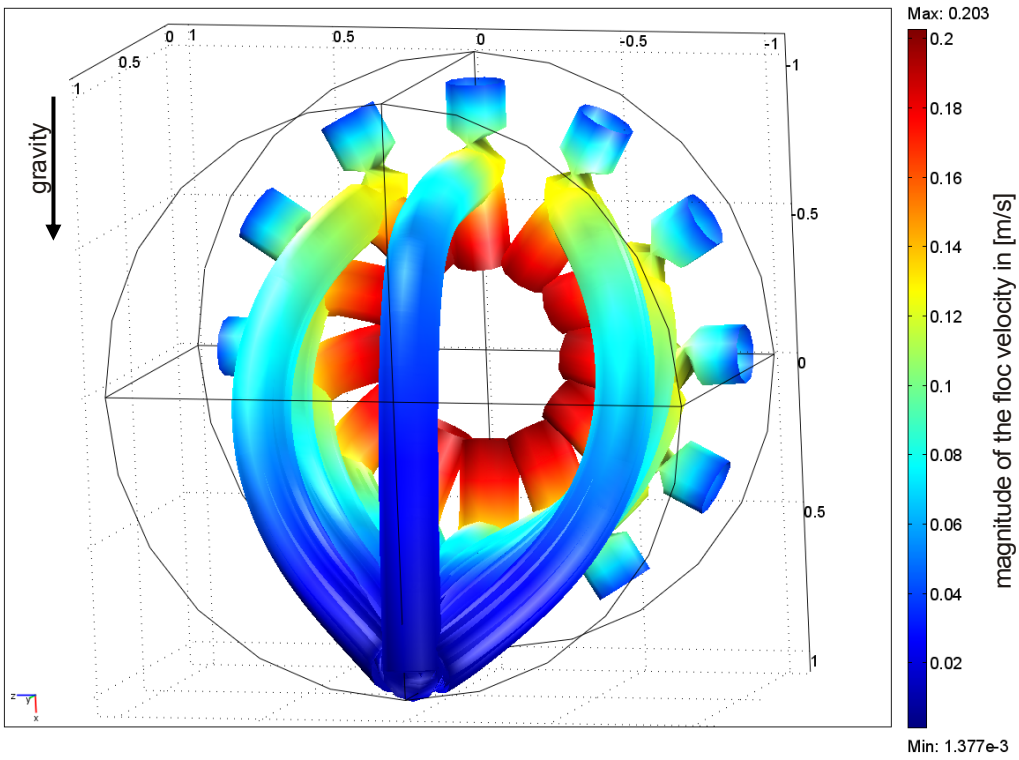

Figure 3.34: Floc trajectories of flocs with radius a_F = 29.47 µm (scaled to floc radius a_F/SR)

The influence of increasing density is illustrated in Figure 3.35, right hand side, where trajectories of spherical quartz particles of radius a_{QP} = 5 µm are modelled. Here, the trajectories indicate that nearly no particle will be collected at the upper part of the capillary. The particles will be transported into in the lower part (r/SR from 0 to 1) of the capillary, being deposited along the membrane wall. Nevertheless, equilibrium trajectories close to the membrane wall will be developed in both cases, whereas an equilibrium trajectory will be found only at the lower capillary part for high densities.

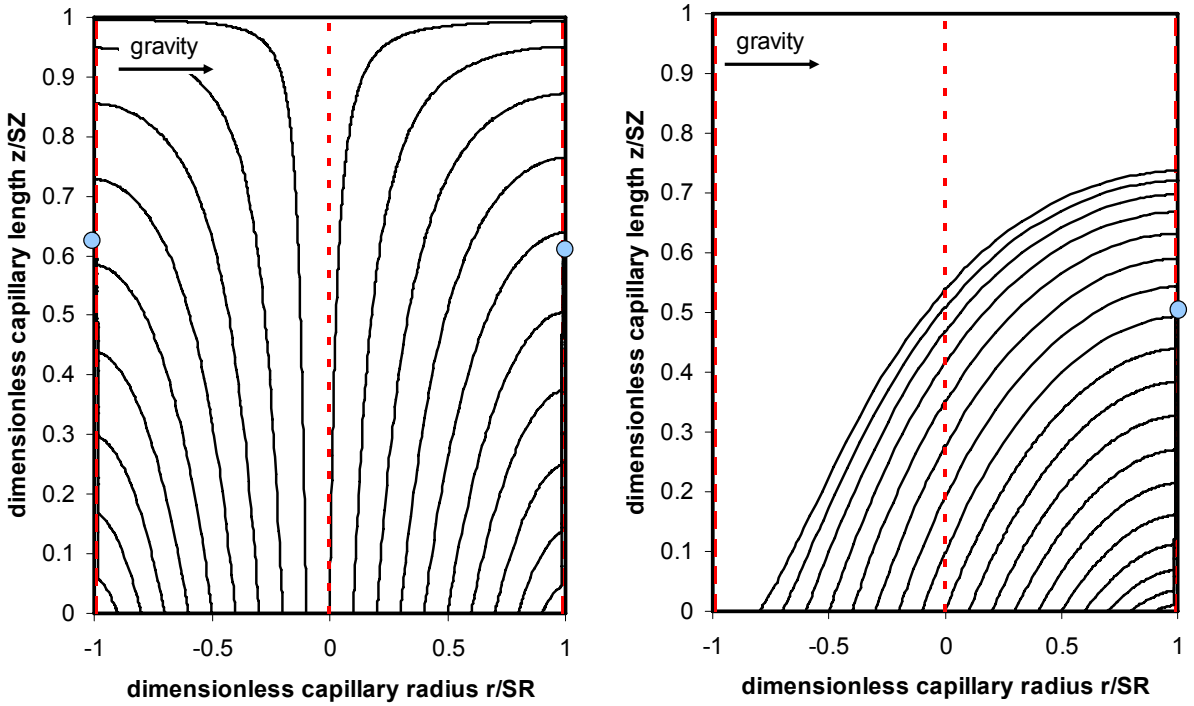

Figure 3.35: Floc trajectories of flocs with radius a_F = 5 µm, rel. density of the flocs set to 1.05 (left) and trajectories of quartz particles with radius a_{QP} = 5 µm, rel. density of the quartz particles set to 2.65 (right)

Hence, even particles with high densities will be transported deeper into the capillary, here approximately to a position of the front contact point of z/SZ = 0.51, as indicated by the blue dot in Figure 3.35, but due to the higher density and resulting sedimentation force not as far as flocs. The front contact points for flocs are indicated at the left hand side, whereas the front contact point at the lower part of the capillary was calculated to be z/SZ = 0.61 and at the upper part z/SZ = 0.62. The effect shown in Figure 3.35 is due to the increased sedimentation force, supported by an increased lateral migration, whereas the influence of the acting DLVO forces was kept constant to account for floc properties for comparison reasons. For denser

particles there will be a larger shift of the rear contact point towards the capillary inlet too, which was found in this calculation to be about z/SZ = 0.74, whereas the shift of the rear contact point for flocs was not significant to a position of z/SZ = 0.993.

Considering a vertical aligned capillary, all forces, including sedimentation will be axially symmetric along the axis of rotation, here the z axis, so the trajectory field will be axially symmetric as well. The influence of sedimentation is shown in following Figure 3.36 and Figure 3.37. Here, floc trajectories are illustrated for flocs with a relative density of 1.05 and spherical quartz particles with a relative density of 2.65 of the same sizes $a_F = a_{QP} = 5$ µm (left) and $a_F = a_{QP} = 29.47$ µm (right). The symmetry axis is on the left hand side of each plot of Figure 3.36 and Figure 3.37 at r/SR = 0. Furthermore, the contact points are indicated by blue and red dots, representing flocs and quartz particles respectively. Figure 3.36 shows 'bottom-up' operation, i. e. gravity acts from top to bottom and the fluid enters the capillary at the bottom.

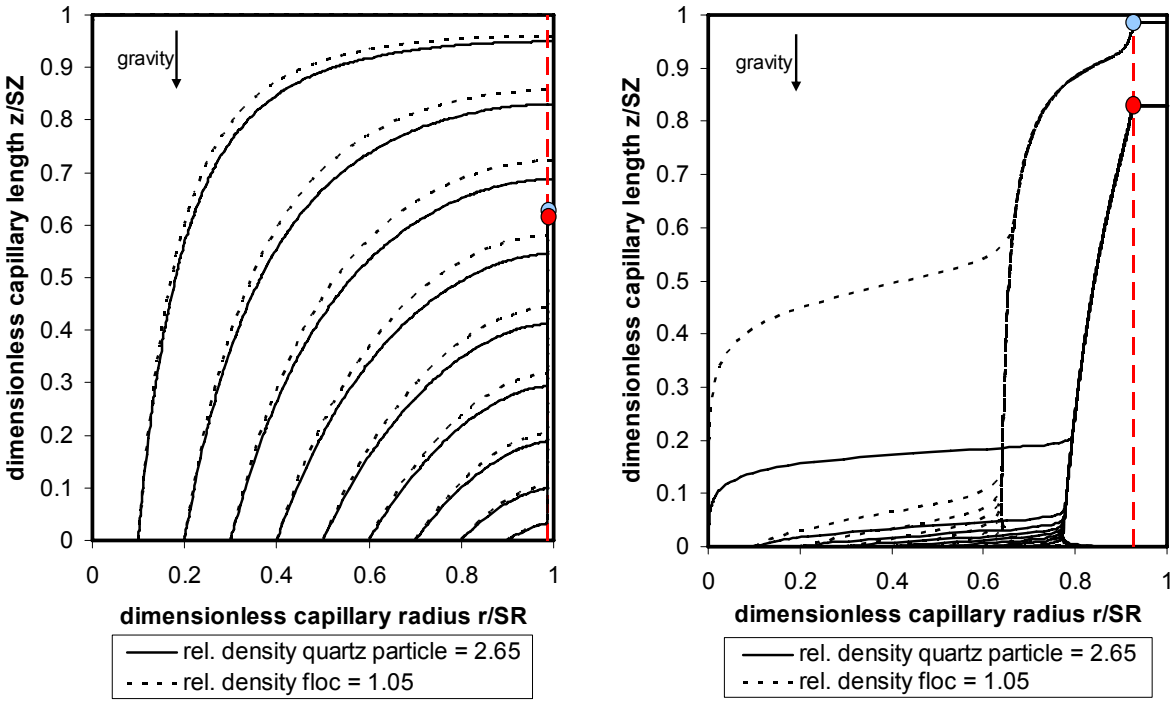

Figure 3.36: Trajectories of flocs (rel. density of 1.05) and quartz particles (rel. density of 2.65) with radius $a_F = a_{QP} = 5$ µm (left) and $a_F = a_{QP} = 29.47$ µm (right) in a vertical aligned capillary, bottom-up operation

All radially acting forces still play a dominant role, especially lateral migration and DLVO forces will cause the development of an equilibrium trajectory, but the effects are superposed by sedimentation, acting perpendicular to the radial forces. Denser

particles will be transported closer and deposited earlier at the membrane wall, but the difference is small for smaller sized flocs/particles and will increase with increasing floc/particle size as illustrated in Figure 3.36. The resulting equilibrium trajectories of flocs are comparable as in horizontal aligned capillaries, whereas for denser particles the area available for deposition would be increased by the use of vertical aligned capillaries, because the whole inner circumference of the lumen can be used for deposition.

Figure 3.37 shows 'top-down' operation and the plots here are shown as in real alignment, i. e. gravity also acts from top to bottom and the fluid enters the capillary at the top. In contrast to bottom-up operation, less dense particles will now be transported closer and deposited earlier at the membrane wall. The difference is quite small for smaller sized flocs/particles but will increase strongly with increasing floc/particle size as illustrated in Figure 3.37.

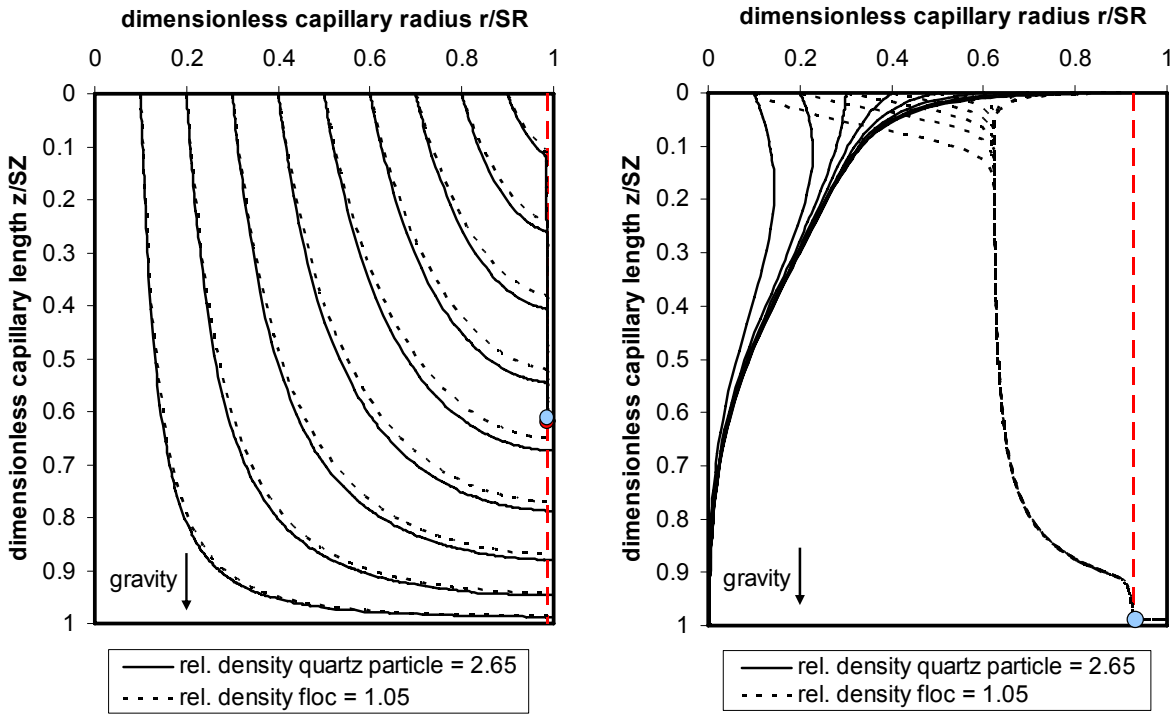

Figure 3.37: Trajectories of flocs (rel. density of 1.05) and quartz particles (rel. density of 2.65) with radius $a_F = a_{QP} = 5$ µm (left) and $a_F = a_{QP} = 29.47$ µm (right) in a vertical aligned capillary, top-down operation

After exceeding a certain size, which was here found for quartz particles to be $a_{QP} = 18.04$ µm, the particles will still be collected on an equilibrium trajectory but

now further transported towards the capillary axis and not towards the membrane wall. Finally, they will be retained at the dead-end of the capillary. This behaviour is caused by lateral migration and sedimentation as described above. Especially lateral migration has a major impact if gravity and flow are acting in the same direction and are superposed, compare chapter 3.3.7. Hence, considering less dense flocs, transport is comparable as in bottom-up operation of vertical aligned capillaries and in horizontal aligned capillaries. However, with increasing density or floc size the differences will consequently increase and the transport behaviour will eventually be similar as for the denser quartz particles. For example, flocs of size a_F = 29.47 µm will merge to an equilibrium trajectory but not being transported towards the membrane wall for relative densities larger than 1.72. The same behaviour was found for flocs larger than a_F = 83.9 µm with a relative density of 1.05.

3.5.2.3 Influence of floc porosity

The influence of floc porosity on transport behaviour is illustrated in Figure 3.38, where just the inner- and outermost floc trajectories and resulting equilibrium trajectories within the capillary are shown for flocs of size a_F = 29.47 µm with different porosities. It can be seen that the resulting equilibrium trajectories are comparable for all investigated floc porosities, at least after longer distances to the capillary inlet, here after approximately 30 %, where the influence of floc porosity will get small. Considering the development of the equilibrium trajectory it can be seen that it is developed more slowly if the floc porosity is increased. Flocs starting at a radial position close to the capillary axis will merge the equilibrium trajectory faster for lower porosities. When the flocs approach the membrane wall, flocs with smaller porosities will travel a bit closer along it and are being deposited earlier. This is due to sedimentation and lateral migration forces combined with the porosity model as introduced in chapter 3.2.2. According to Equation 3.21, the effective hydrodynamic radius of the flocs a_{hF} becomes smaller if the porosity is increased. Therefore, high porosity flocs behave hydrodynamically like smaller spherical particles. In the shown example, the hydrodynamic radii were calculated to be 29.12 µm, 25.76 µm and 18.66 µm for the shown porosities 0.26, 0.7 and 0.9, respectively.

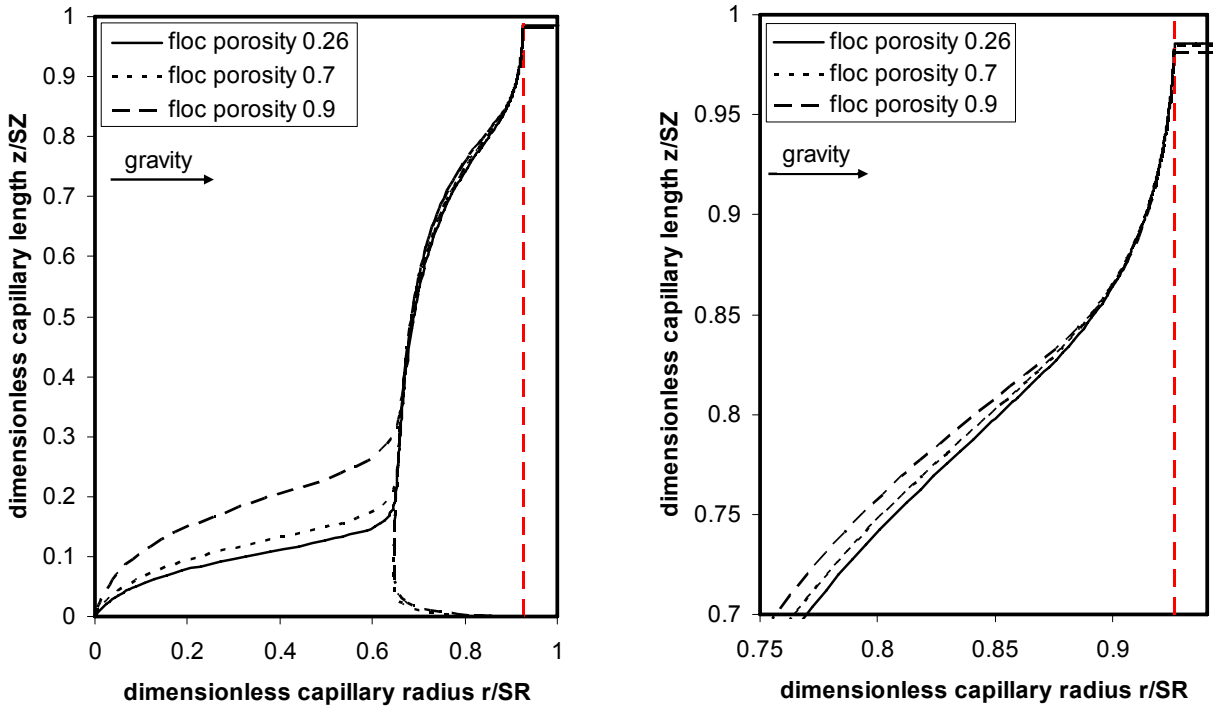

Figure 3.38: Floc trajectories and resulting equilibrium trajectories of flocs (a_F = 29.47 µm, a_P = 12.25 µm) with different porosities (left) and display detail (right)

3.5.2.4 Influence of floc growth

Within the capillary lumen one should consider further floc agglomeration during transport. This effect was neither measured nor modelled but observed during experiments within this work and others, HAGMEYER ET AL. (2003) for instance, and will be discussed qualitatively in the following. Flocs with radii larger than the limiting radius will be forced to travel along merging trajectories and finally in a resulting equilibrium trajectory until being deposited. With increasing floc size this will lead to a point where all incoming flocs, independent of their radial starting position at the capillary inlet, will be forced to merge this trajectory. Furthermore, the larger the size the faster all flocs will be forced to merge, but as shown above in Figure 3.38, this will be postponed for higher porosities. As a result, flocs will be brought into very close and assumably unavoidable contact to each other, being exposed to moderate shear rates concomitantly with an increased concentration of flocs on this trajectory. PANGLISCH (2001) showed that the concentration on the equilibrium trajectory depends on size of the particles. Higher concentrations were found for smaller sized particles, whereas even larger sized particles will be concentrated along the

trajectory up to the maximum packing density with increasing bulk concentration. If contact occurs and larger floc aggregates are formed, they will be immediately exposed to the same hydrodynamic conditions as before when they have been individual and smaller, resulting in stronger forces acting on the new and larger aggregate. This will lead to an additional lateral shift, whereas the direction depends on the new size and local position in the capillary. Eventually, the floc aggregates will be moved towards the final position of the equilibrium trajectory at approximately r/SR = 0.62, resulting in transport downwards towards the dead-end of the capillary and in an increased floc concentration in the equilibrium trajectory at this limiting radial position. Furthermore, considering a polydisperse size distribution of flocs accompanied with their different trajectories during transport, an increase in collisions rate, i. e. the number of collisions of flocs, can be furthermore assumed due to crossing and/or constriction of trajectory bundles as shown in Figure 3.39.

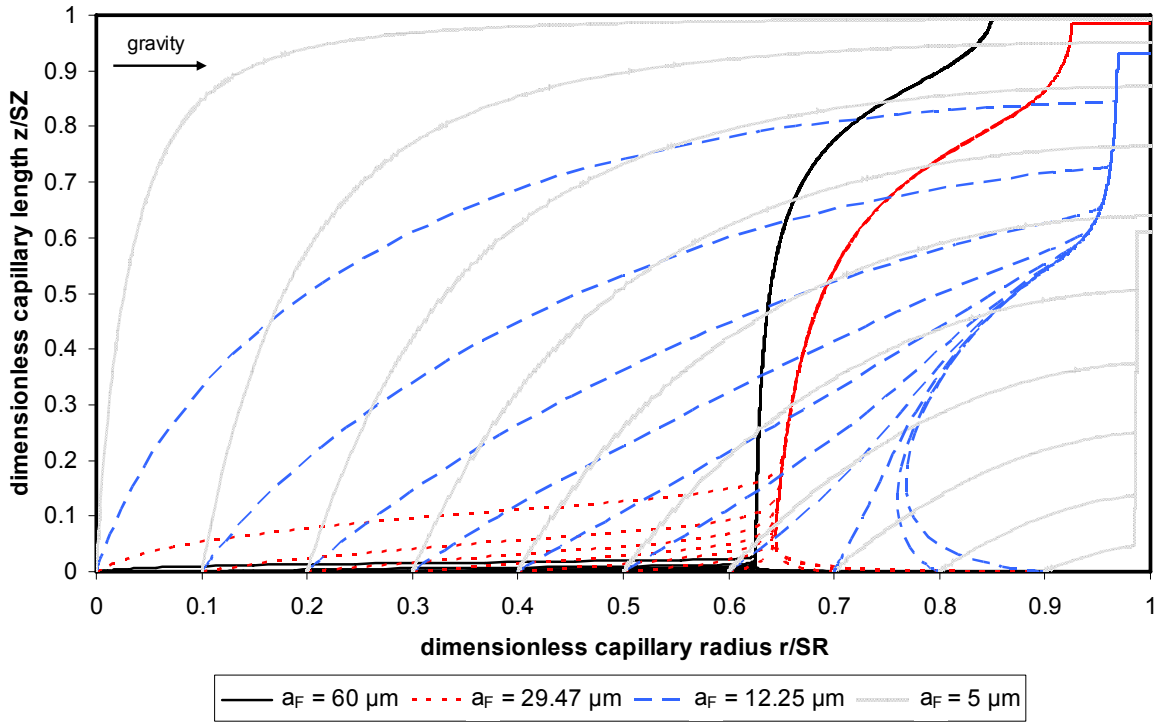

Figure 3.39: Floc trajectories of different sized flocs within the capillary

According to the conventional coagulation theory and considerations above this should lead to floc aggregation by some kind of orthokinetic aggregation (IVES (1978), ELIMELECH ET AL. (1995)). The calculated shear rates are illustrated in Figure 3.40 and were found to be highest with G = 1100 s^{-1} at the capillary inlet, directly at the

membrane wall due to the no slip condition for the inflowing fluid at this boundary. Due to the moderate and axially decreasing shear gradients floc growth will be probably more dominant than floc destruction. For longer travelled distances of the flocs, this will be especially true for larger floc aggregates, which will be transported in areas of lower shear rate, compare Figure 3.39 and Figure 3.40.

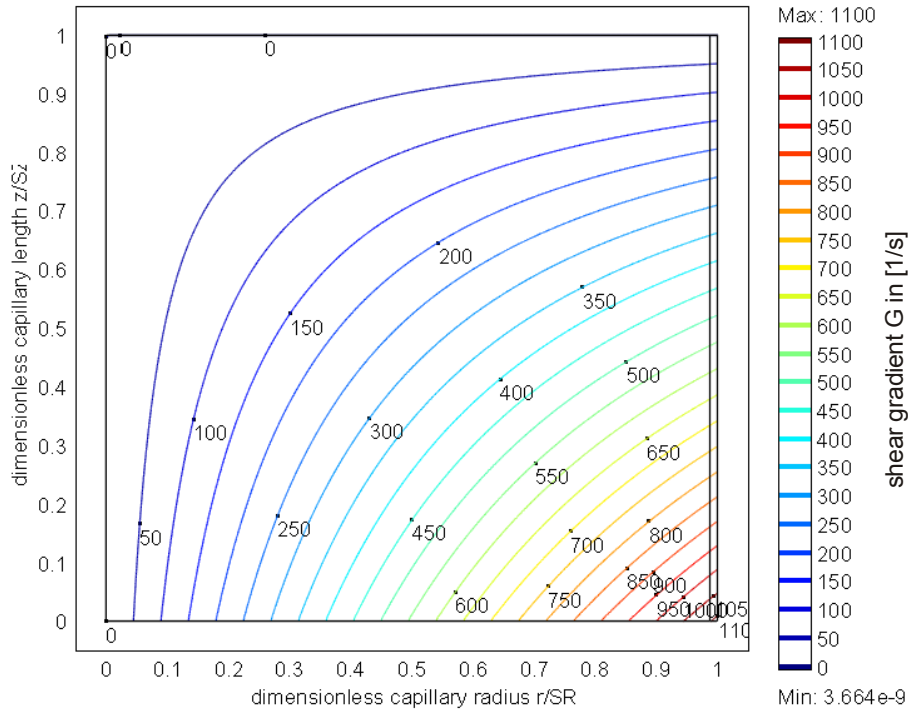

Figure 3.40: Shear gradients G in [1/s] within the capillary, driven in dead-end mode at a flux of 80 L/m²/h

3.5.3 Fouling layer formation and resulting transient flow field

When calculating the fouling layer formation and corresponding layer thickness as function of time it came to major convergence problems as previously discussed, especially if larger flocs were modelled. This is because of locally arising very high floc volume concentrations along the equilibrium trajectory compared to areas in the vicinity. Flocs were actually not distributed within the capillary lumen but accumulated along the developed single equilibrium trajectory. From FEM point of view, resolution of the applied mesh could not be adapted to resolve the sharp gradients to deliver acceptable results. Even when artificial diffusion was used to reasonable extent, no convergence could be achieved when calculating the dynamic model. Additionally, intensified use of artificial diffusion would falsify the results furthermore, compare

chapter 3.4.5.1. Figure 3.41 shows exemplarily the stationary solution of the calculated floc volume concentration of flocs of radius a_F = 29.47 µm at different longitudinal coordinates. The position of the peaks depends on the characteristics of the resulting equilibrium trajectory, compare Figure 3.28. The floc volume concentration increases along the trajectory and gets highest when approaching the membrane wall. The contact distance for this floc size is indicated as red dashed line at the right in Figure 3.41.

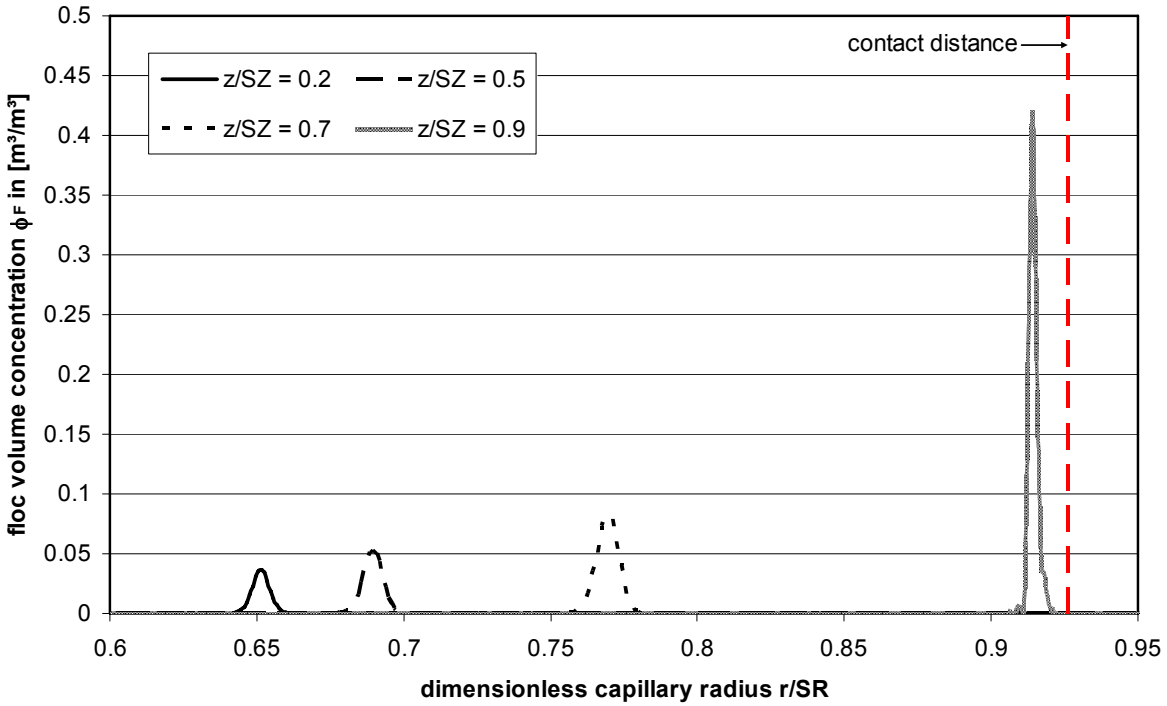

Figure 3.41: Floc volume concentration ϕ_F of flocs of radius a_F = 29.47 µm vs. dimensionless capillary radius r/SR at different dimensionless capillary lengths z/SZ (display detail)

Generally, the floc volume concentration will get highest when the floc velocity decreases to its local minimum. Here, a floc will be closer to its neighbouring floc in front of its trajectory than to its following neighbour. In radial direction, repulsive hydrodynamic forces will increase with decreasing distances to the wall and therefore decelerate the floc velocity. Coming into the range of acting DLVO forces, the radial floc velocity will be further slowed down or accelerated, depending on the relevant algebraic sign. When a floc approaches the membrane wall, the floc volume concentration and the concentration gradient will increase first linearly and at closer distances exponentially (PANGLISCH (2001)). Concentration will be constant and

maximal as soon as the floc is deposited in the fouling layer and the gradient vanishes.

If the floc volume concentration distribution was modelled for smaller flocs, convergence could eventually be achieved. Even here, the quality of the modelled results is not very high because the applied meshes were still quite coarse for this modelling purpose. However, the following will give an overview of results for smaller floc aggregates, chosen to illustrate and discuss transient fouling layer formation and the according flow field.

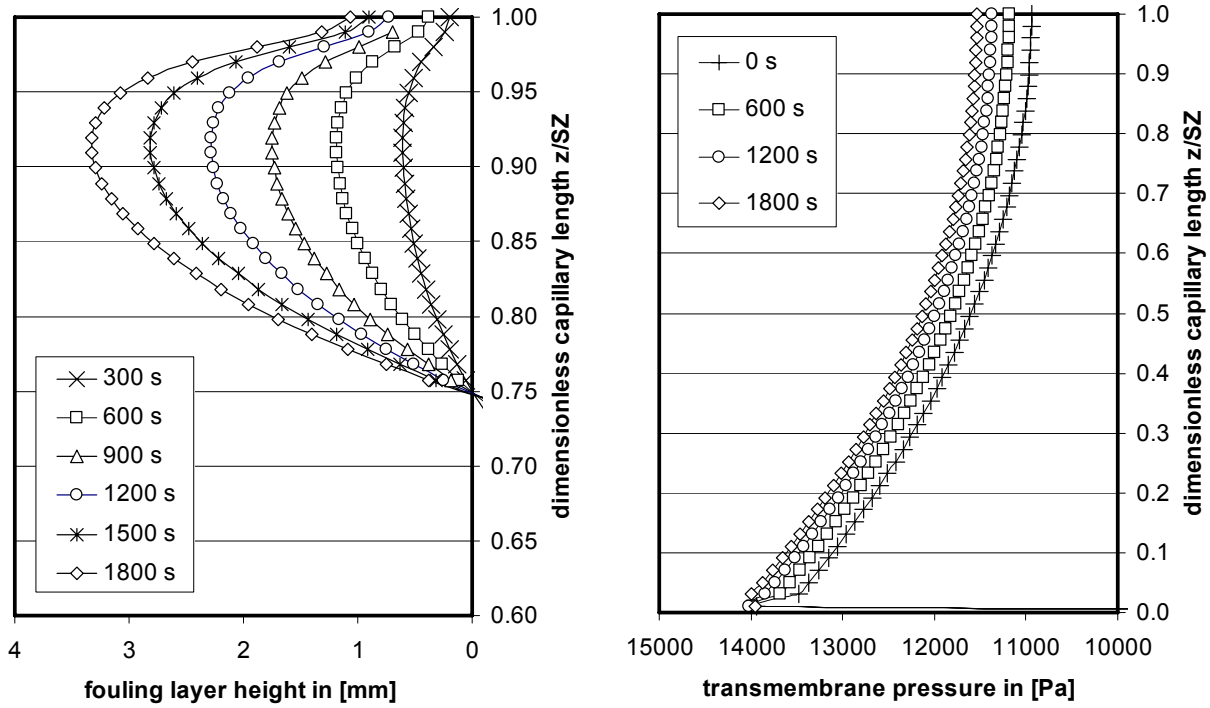

Figure 3.42: Fouling layer height δ_{FL} in [mm] (left) and transmembrane pressure (TMP) in [Pa] (right) vs. dimensionless capillary length after different filtration times of flocs of radius a_F = 5 µm

Figure 3.42, left hand side, shows the calculated fouling layer thickness δ_{FL} at the membrane wall after different filtration times resulting from transport of 5 µm flocs. The fouling layer starts to develop at a dimensionless capillary length z/SZ of about 0.75, later than expected by the trajectory analyses with about 0.61, compare Figure 3.29. This might be due to the mesh quality too, delivering somewhat oscillating results, especially in the vicinity of boundary 4 where the largest concentration gradients will arise. The illustration in Figure 3.42 indicates further that the modelled

maximum height after 30 minutes of filtration was modelled to be δ_{FL} = 3.32 mm, which is 8.3 times higher than the physical radius of the capillary. According to the shown results, the formed fouling layer would have led to a fast formation of a porous plug at a dimensionless capillary length z/SZ of about 0.9 after approximately 300 seconds of operation. With ongoing filtration, additional flocs would be transported towards this plug and finally being captured in it, letting the plug grow and probably compressing it. Over time, the porosity would therefore decrease and the resistance to flow would increase. Finally, this would end after potentially long filtration times in a complete clogging of the membrane at this part of the capillary, making the membrane area further downstream towards the dead-end unavailable for further floc deposition (LERCH ET AL. (2005B)). In reality, this clogging may occur close to the dead-end as expected due to the size of the flocs to be filtered, but may also happen somewhere else further upstream within the capillary. Both were often experienced in laboratory experiments. If the plugs were located at the beginning or middle of the capillary it came to a sudden release of the blocked membrane area in most cases and it was assumed that the formed plug was pushed towards the dead-end due to the increasing pressure (GITIS ET AL. (2005)). However, the model was neither equipped to account for compaction of the flocs nor of the fouling layer and further not bounded by some geometrical values like the capillary radius. The uncompressed height of the layer, as can be seen in Figure 3.42, was utilised as an easy to use first estimation for probably occurring layer compaction, assuming that the uncompressed layer will offer a comparable resistance to flow than a compressed layer with a maximum height equal to the capillary radius.

The right hand side of Figure 3.42 shows the corresponding TMP along the membrane wall, presenting a maximum pressure increase of 0.59 kPa after 30 minutes of operation. Surprisingly, the results obtained for the TMP are indicating an increase over the complete length of the capillary. However, larger differences between the initial TMP and the TMP after some filtration time were found to start at approximately two thirds of the dimensionless capillary length, corresponding to the outcomes of the trajectory analyses. Hence, the results were used for qualitatively interpretations.

Generally, a fluid will flow through those surface areas of the membrane giving the least resistance to its flow. Due to the local pressure increase at surface areas used for deposition of floc aggregates of certain size, the fluid will flow through uncoated or less coated surface areas. Accordingly, different floc trajectories will be developed over time, exemplarily illustrated for certain time steps in Figure 3.43. Here, the resulting transient flow field over 30 minutes of filtration of flocs of radius a_F = 5 µm is presented. The trajectories will be shifted towards the capillary inlet, i. e. towards areas less fouled, whereas this shift is larger at areas with increased fouling layer height and resulting higher pressure drop, compare Figure 3.42. These findings correspond very well with general experiences made in experiments with constant flux operation, where the flow rate through upstream surface areas was increased if the resistance due to fouling layer formation was increased (GITIS ET AL. (2005)).

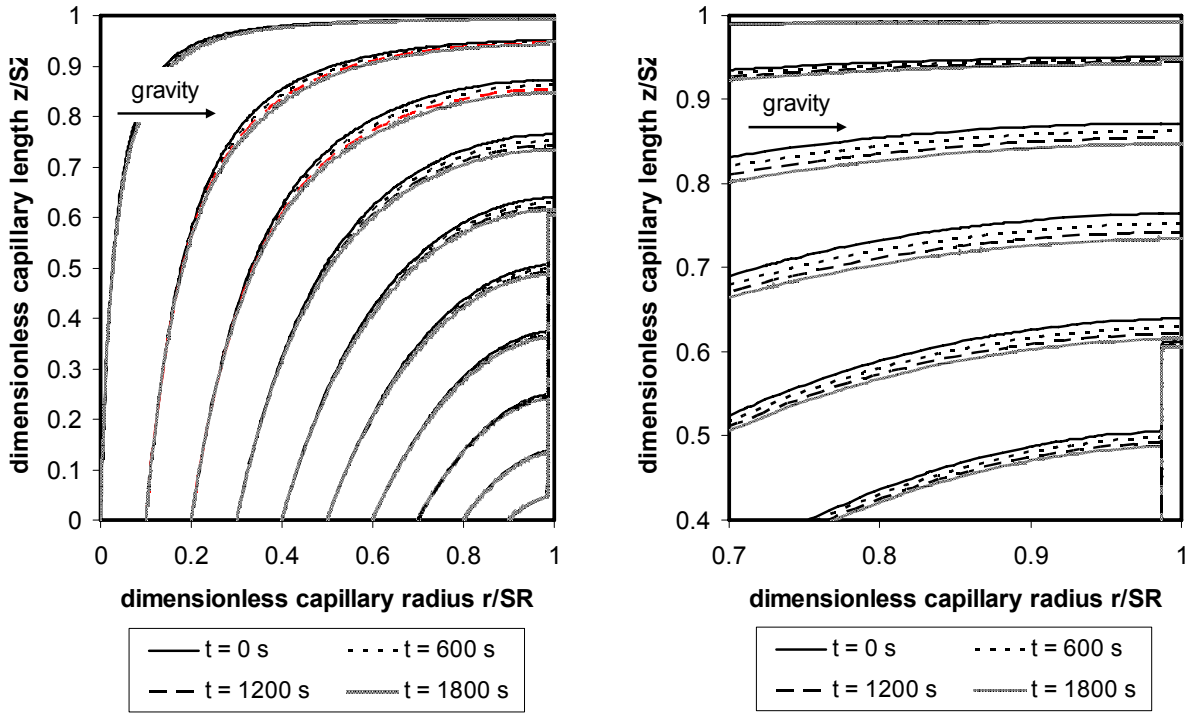

Figure 3.43: Floc trajectories of flocs with radius a_F = 5 µm at different times of filtration (left) and display detail (right)

The influence on the developed equilibrium trajectory was found to be small and the front contact point is shifted only very slightly towards the capillary inlet, see Figure 3.43 (right). Combining the results of the transient model as discussed above with the findings and discussions of the previous chapter, one can conclude that fouling layer formation will theoretically take place from the end towards the inlet and from the

bottom to the top of the capillary in a horizontal aligned capillary. However, this will not lead to immediate clogging of the capillary due to the inner porosity of the formed fouling layers until this inner porosity is lost due to further added flocs or compression.

Considering the formation of the fouling layer and its porosity one has to consider the floc properties such like inner porosity, size and surface charge too, because they will have an decisive influence on the resulting fouling layer, not only on the place of deposition but also on its formation and porosity. As described in chapter 3.4.6, applying the Happel model with Equation A.17 and Equation A.18, the permeability coefficient k_{FL} of the formed fouling layer will be generally higher for larger flocs of identical porosity, resulting in lower specific resistance of the formed fouling layer. This specific resistance will be further reduced for increasing inner floc porosities, leading to more constant fluid flow field and therefore floc transport conditions over filtration time.

However, the porosity of the formed fouling layer will be further influenced by near-field forces between two flocs of equal size approaching each other to form the layer. Among other forces, the resulting final distance in this layer will be determined by their interacting DLVO forces too. This effect is much more significant for very small flocs, such as micro flocs, because all other hydrodynamic forces acting on the flocs will be of the same magnitude due to the comparatively same position. If repulsive forces are dominant, then there exists a limiting distance where no additional approach will be possible, resulting in a porous fouling layer. If the repulsive forces are overcome and maybe become attractive, then the flocs might be brought into closer contact and form a denser fouling layer, whereas the final porosity is mainly influenced by the inner floc porosity. Overcoming repulsive forces is more likely if larger floc aggregates are involved, because the difference in their local position might be significant and therefore the difference in hydrodynamically acting forces might be very large, especially in the neighbourhood of the membrane wall. If the acting hydrodynamically forces are higher than the maximum repulsive forces between the flocs within the layer, i. e. for higher flux operation for example, the distance between the deposited flocs will be minimised and therefore the layers porosity too. If the repulsive forces cannot be overcome by hydrodynamic flow forces,

then the final limiting distance between two flocs will be independent of their size. The resulting free volume, hence porosity, in the layer is then relatively smaller for large flocs than for smaller flocs (PANGLISCH (2001)). For instance, PANGLISCH (2001) stated that the porosity of a fouling layer formed by 0.1 µm sized particles, with a final distance between the particles surfaces of about 10 nm, will be about 0.36, while the porosity of a layer formed by 35 µm sized particles and same distance between them will be about 0.26. However, due to relatively high flow forces repulsive forces are usually overcome, especially due to the lowered double layer forces after coagulation and formation of floc aggregates.

If the flow forces are large, compression of the formed fouling layer will be possible and probable. LEE ET AL. (2003) confirmed with their investigations on dead-end MF that there is an interaction between floc size and structure and that layers formed of smaller flocs are more sensitive to floc structure effects than layers of larger flocs. The compressibility of the formed layer was found to be strongly related to the applied TMP, particularly for smaller floc sizes. The deposition of porous aggregates onto the membrane resulted in the formation and maintenance of porous fouling layers, provided a low TMP (< 10 kPa) was applied. At higher TMP (> 60 kPa) rapid compression of the layer occurred, indicated by the significantly lower porosity. Under high TMP conditions, the layer porosity exhibits strong size dependence with larger floc sizes yielding higher porosities. This result may indicate formation of relatively impermeable layers with flow around the compressed flocs at higher TMP, rather than through them at low TMP.

Further, large floc aggregates are usually looser, more open in structure than smaller flocs, whereas looser flocs are likely to form layers with higher porosities and therefore lower resistances than layers made of compact flocs of similar size (LEE ET AL. (2003)). From a practical perspective with respect to highly porous fouling layers, one can summarise that large, porous flocs, low Hamaker constants, high surface potentials, low ionic concentrations and filtration at low TMP will be favourable.

4 Experiments

4.1 Used materials

4.1.1 UF capillaries

Single UFC M5 ultrafiltration capillaries of the company X-Flow B. V. with an inner diameter of d_i = 0.8 mm and an average length of about 1 m were used throughout the experiments. The capillaries are micro porous and reveal an asymmetric structure, are hydrophilic and composed of a blend of polyvinylpyrrolidone and polyethersulfone. The company nominates a MWCO of 200 kDa determined on dextrans. The established zeta potential of the membrane in water was not measured but estimated to be about - 15 mV in the neutral pH range, which is in good agreement to values found in literature for polyethersulfone membranes, e. g. ZHAO ET AL. (2002), CHO ET AL. (2002) and SOFFER ET AL. (2005). However, the membrane structure and/or material revealed some inhomogeneities as observed in the experiments by recording high deviations of the initial membrane resistance as described in chapter 4.4.

4.1.2 Primary particles

Latex particles, i. e. polymer microspheres, were used as primary particles in this work. The particles had a nearly ideal spherical shape as exemplarily shown in the optical microscope photograph given in Figure 4.1.

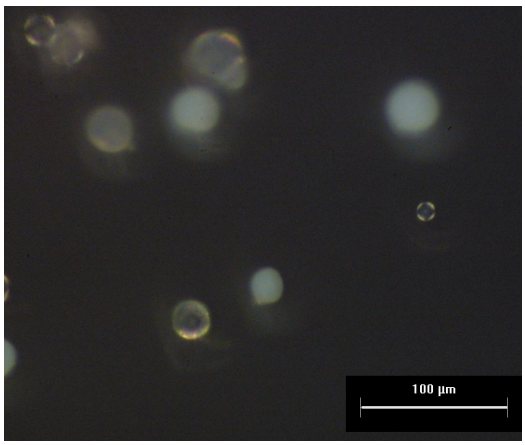

Figure 4.1: Optical microscope photographs of the used ABS latex microspheres

The used microspheres were made of acrylonitrile butadiene styrene (ABS), a thermoplastic which is a copolymer made by polymerising styrene and acrylonitrile in the presence of polybutadiene. The average density was measured with about 1050 kg/m³. The diameters were found to be in the range of 1 - 40 µm as illustrated in the cumulative and distributive size distribution in Figure 4.3. The zeta potential was measured to be about - 60 mV at neutral pH-values and determined by electrophoretic mobility measurements using a Zetasizer 3000 of the company Malvern Instruments GmbH. The measured zeta potential of the ABS latex is illustrated in Figure 4.2 according to the data provided by NAHRSTEDT (1999). It has to be noted that the measurement was performed using Mülheim a. d. Ruhr tap water, see NAHRSTEDT (1999) for details. Due to the high negative potential, particle agglomeration without coagulation can be essentially neglected and the ABS particles were considered as primary particles.

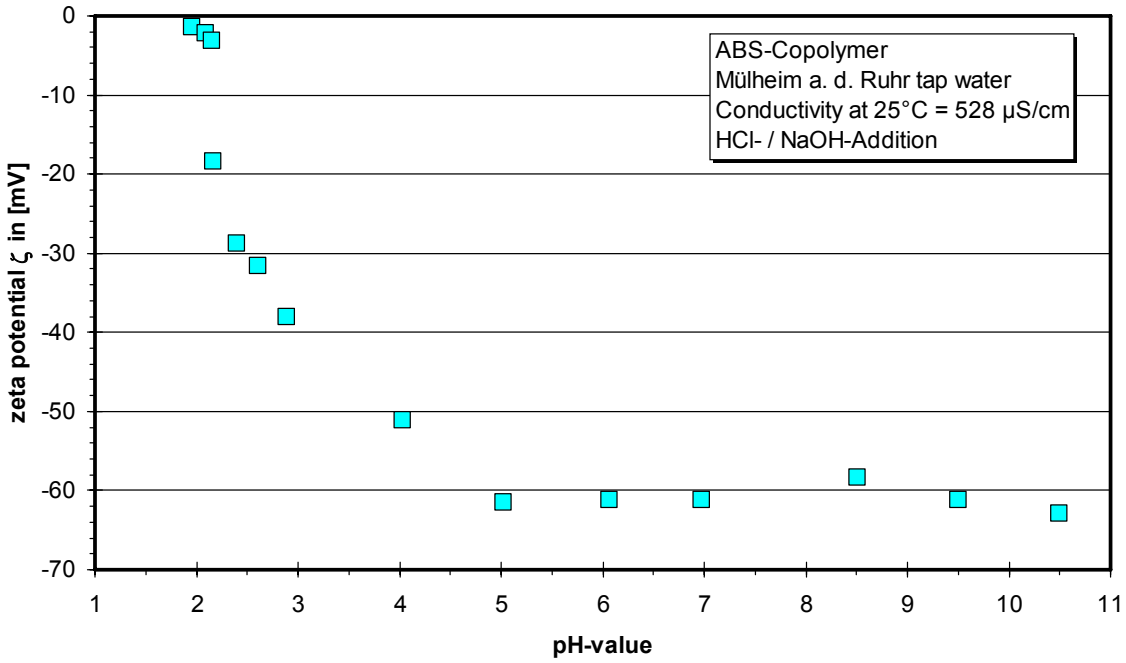

Figure 4.2: Zeta potential ζ of the used ABS latex microspheres at different pH-values (NAHRSTEDT (1999))

4.2 Coagulation and floc formation

Trifloc S, an iron-III-chloride of the company BK Giulini GmbH was used as coagulant for the coagulation of the latex suspension with ABS microspheres. The solution contains 13.8 weight-% of Fe^{3+} and 0.3 mmol Fe^{3+}/L were dosed throughout the

experiments if not stated otherwise. A concentration of 1 g/L of ABS microspheres was used as primary particle concentration and dosed into 1.8 L of Duisburg tap water. Coagulation and floc formation was achieved in a 2 L jar equipped with stators according to DVGW-ARBEITSBLATT W 218 (1997). After dosing the coagulant, rapid mixing and distribution of the small coagulant volume in the jar and fast destabilisation was achieved at G values > 1000 s^{-1} for 30 s using a high performance disperser T 25 ULTRA-TURRAX® and S 25 G as dispersing element of the company IKA®. The coagulation pH value was set to pH 6 and adjusted with 0.1 M HCl. Floc formation was achieved by stirring the coagulated suspension with a two blade stirrer in the jar at temperature corrected G values of 40 s^{-1} for 25 minutes.

Figure 4.3 shows the floc and primary particle size distribution of the suspension at the capillary entrance, directly after passing the inlet adapter and the capillary cross section area (see also Figure 4.5).

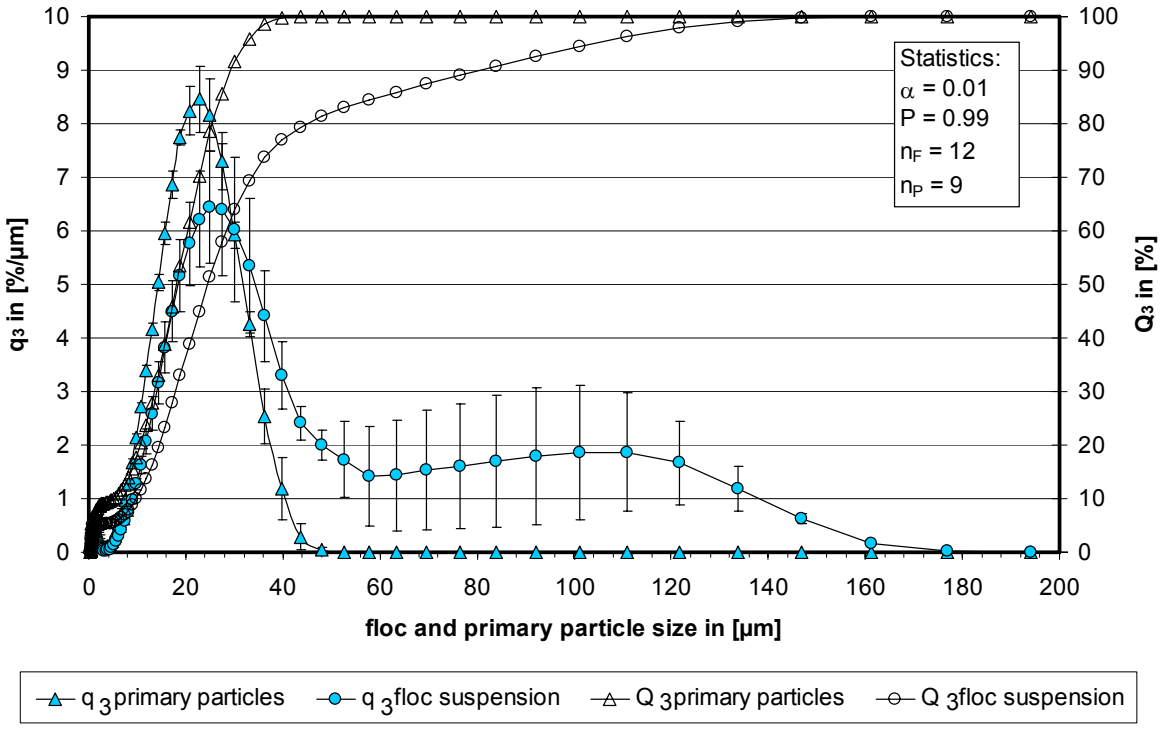

Figure 4.3: Distributive $q_3(x)$ and cumulative $Q_3(x)$ percentage volume distribution of the primary particles (ABS) and the floc suspension at capillary entrance (error bars represent 99 % confidence interval)

The size distribution was measured using a laser diffraction particle size analyzer LS230 (Beckman Coulter GmbH, Germany). The volume percentage distribution of

the used primary particle suspension showed to be typically narrow and the mean volume diameter was calculated according to DIN ISO 9276-1 AND 9276-2 (2004) to be 24.5 µm. However, the distributive $q_3(x)$ distribution of the floc suspension is much wider than for the primary particles and showed a second local maximum at approximately 110 µm. Hence, it was very difficult to determine just one corresponding parameter for the complete description of this distribution. In addition, it is obvious that flocs with diameters in between 40 to 160 µm were formed, but that the majority of the measured flocs still remain in the same size range as the primary particles. This indicates that floc formation took place but further that floc break-up occurred after the flocs were exposed to an increased shear rate when entering the capillary lumen and passing the inlet adapter. This was confirmed by comparing the data with size distributions of flocs in the jar directly after coagulation and floc formation where a mean volume diameter of 95.02 µm was determined. However, the mean volume diameter of the flocs after passing the adapter was calculated according to DIN ISO 9276-1 AND 9276-2 (2004) to be 58.94 µm. The values were evaluated from 4 experiments with different capillaries, whereas 3 samples were taken and analysed, hence delivering n_F = 12 data sets for the statistical analysis of the flocs (compare chapter A.15). For the statistical analysis of the primary particles n_P = 9 different data sets were obtained. The 99 % confidence interval for each measured point is illustrated in Figure 4.3 too, indicating that the floc size was varying quite a lot, especially at higher sizes.

The zeta potential of the coagulated suspension at coagulation pH-value could unfortunately not be measured due to a breakdown of the analytical equipment. Hence, the zeta potential was estimated to be about -12 mV, taken as average value from different experiments (LERCH ET AL. (2005A)), where Twente channel water, a raw water with usually high particle concentrations, was treated by coagulation and ultrafiltration using Trifloc S as coagulant and dosage concentrations in the range of 0.05 to 0.15 mmol/L Fe^{3+} at comparable pH-values.

4.3 Setup of the test unit for single capillaries

The test unit presented in Figure 4.4 was designed and assembled to operate single inside-out driven capillaries at constant flux in cross-flow and dead-end mode to

investigate the influence of the coating layer formation on flux decline in different sections of the capillaries.

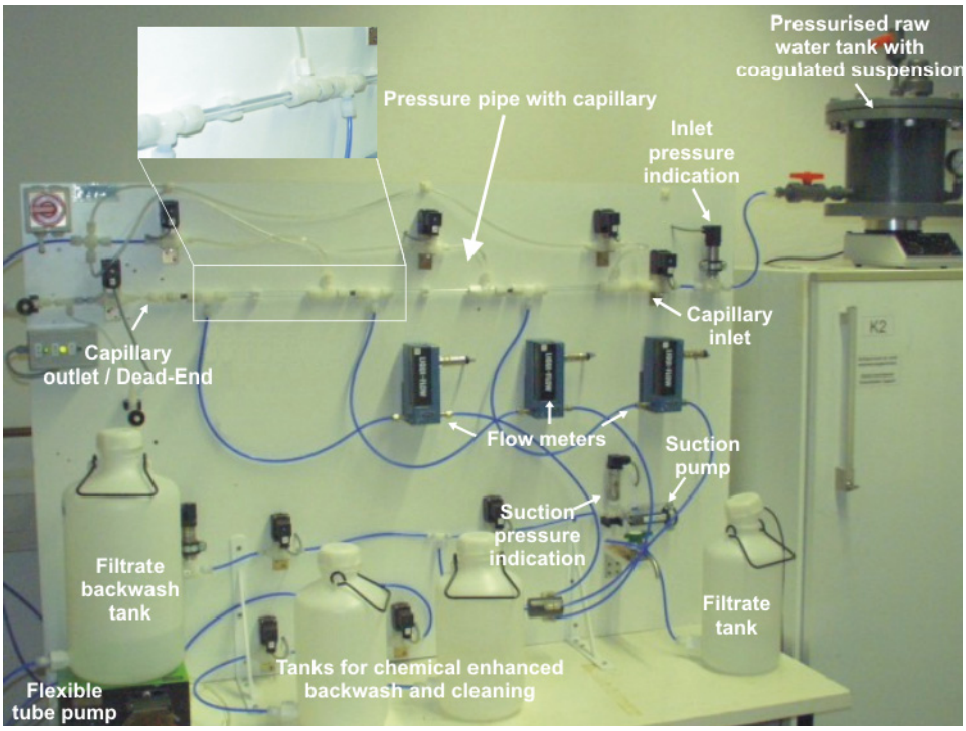

Figure 4.4: Setup of the designed and used test unit for single capillaries

The single capillaries were fitted into a pressure pipe to allow backwashing, enhanced chemical backwashing and chemical cleaning of the capillaries. The capillary and the pressure pipe were divided by hot-melt adhesive and adapters into three different sections, i. e. begin (I), middle (II) and end (III) section, as illustrated in Figure 4.5.

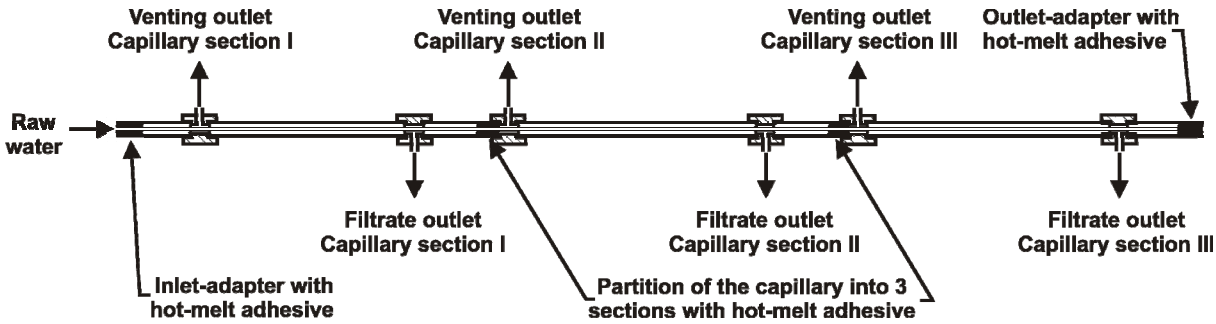

Figure 4.5: Configuration of the pressure pipe used in the test unit

The coagulated raw water suspensions were stored in a pressurised tank, which was set on a magnetic stirrer to avoid sedimentation of the flocs in the tank. Further, no

significant variation in floc size over storage time was observed. The tank was additionally equipped with a heating system and a resistance thermometer PT 100 TR 101 (WIKA Alexander Wiegand GmbH & Co. KG, Germany) to measure, control and adjust the temperature of the used suspension. A micro annular gear pump mzr-4622 (HNP Mikrosysteme GmbH, Germany) was employed as suction pump in the system and forced the floc suspension or filtrate, respectively, to flow through the capillary and the membrane wall into the filtrate tank. The total filtrate flow, hence the overall flux through the capillaries, was kept constant but the flux at the different sections was allowed to decline. That is, if fouling layer formation occurred and let to a flux decline at the end of the capillary, then the flux in the upstream sections increased automatically. The flow rate through each section of the capillary was measured by LIQUI-FLOW flow meters (Bronkhorst Mättig GmbH, Germany). The constant overall flow rate was controlled automatically by a closed control loop between the pump revolution speed as actuating variable and the flow meters signal as the controlled process variable. The pressure was measured at the capillary inlet and at the suction side of the pump with standard pressure transducers S10 (WIKA Alexander Wiegand GmbH & Co. KG, Germany). When the capillaries were driven in cross-flow mode, the pressure was additionally measured at the capillary outlet. Conventional and chemical enhanced backwashing as well as chemical cleaning of the capillaries could be achieved by employing a 4 channel flexible tube pump REGLO 100 (ISMATEC Laboratoriumstechnik GmbH, Germany), connected to filtrate, acid and base tanks. The piping of the test unit was equipped with 2-way electromagnetic valves type A12 - 82 080 (IMI Norgren Buschjost GmbH + Co. KG, Germany). The setup of the test unit allowed fully automatic control and different operating conditions. Measurement data acquisition, storage, monitoring and control were achieved by a data acquisition and control unit TopMessage (Delphin Technology AG, Germany).

4.4 Determination of the initial membrane resistance R_M

The initial membrane resistance R_M of each capillary used was determined at the single capillary test unit as described in chapter 4.3. The capillaries were operated in filtration mode with ultra pure water for about 45 minutes at a flux of 100 L/m²/h to rinse out chemicals used for protection of virgin capillaries, i. e. glycerine for pore

protection and bisulfite for prevention of microbiological growth. Characteristic data of the used ultra pure water are presented in Table 4.1.

Table 4.1: Characteristic data of the ultra pure water used for the rinsing procedure

Parameter	Unit	value
No. of particles > 0.7 µm	1/mL	< 45
Conductivity	µS/cm	< 0.5
DOC	mg/L	< 0.1

The data obtained by this rinsing procedure, i. e. filtrate flow in each membrane section, transmembrane pressure and temperature, were recorded. The resulting sets of data were evaluated to determine the initial membrane resistance R_M of each capillary section as described in the following. Evaluation of data for the first 20 minutes of rinsing was neglected to exclude any additional effects of initially remaining chemicals on resistance. Each data set was subdivided into 10 classes and used to calculate the initial membrane resistance over time of operation. The slope of the resulting function R_M (t) was statistically analysed as described in chapter A.15. The average of the remaining data was then considered to represent the measured initial membrane resistance as illustrated in Figure 4.6.

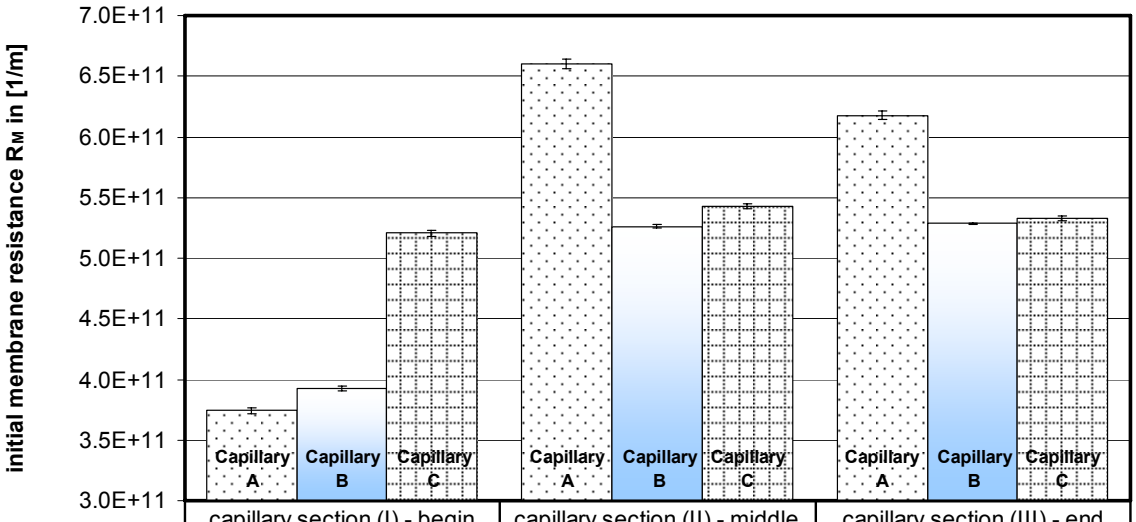

	capillary section (I) - begin	capillary section (II) - middle	capillary section (III) - end
Capillary A	3.742E+11	6.600E+11	6.178E+11
Capillary B	3.929E+11	5.262E+11	5.286E+11
Capillary C	5.206E+11	5.430E+11	5.327E+11

Figure 4.6: Initial membrane resistances R_M at three different capillary sections (begin, middle and end) of the investigated capillaries A, B and C

Figure 4.6 represents the calculated initial membrane resistances and demonstrates that they were neither homogeneously constant in between the different capillaries nor over their length, i. e. the membrane resistance was varying over capillary length. However, a general mean value of the initial resistance R_M could be derived as modelling parameter with $5.24 \cdot 10^{11}$ 1/m and was used for the theoretical investigations described previously in chapter 3.4. For modelling the flow in the capillaries investigated, the initial membrane resistances of each section, as given in Figure 4.6, were used. Further, all potted capillary parts were then considered as impermeable walls.

4.5 Experimental examination of fluid flow and floc deposition and comparison with modelled results

Three single capillaries were operated as described previously for different times with similar flux of about 80 L/m²/h in dead-end. Capillary A was operated 5 minutes, capillary B 20 minutes and capillary C 45 minutes. By using different times of operation it was assumed to follow the coating layer build up over time. The inhomogeneities of the capillaries membrane resistance over length led to varying fluxes at the different capillary sections as can be seen in Figure 4.7 and the listed calculated values in Table 4.2 .

Table 4.2: Percentage deviation of the fluxes at the different capillary sections begin (I), middle (II) and end (III) of the capillaries A, B and C from the total average flux of the capillary

Capillary	Average flux in [L/m²/h]	Deviation in [%] section I (Begin)	Deviation in [%] section II (Middle)	Deviation in [%] section III (End)
A	77.77	29.37	- 32.86	- 20.27
B	83.96	12.32	- 14.7	- 12.14
C	79.69	5.53	3.63	- 2.31

It has to be mentioned that in case of capillary C, data were not recorded for the first 32 minutes of operation due to computer problems. However, flux was stable over the whole time of operation and no flux decline could be observed for this capillary at the end of operation. Furthermore, the deviation of the fluxes at the different capillary sections from the total average flux with about 79.7 L/m²/h was little, ranging from

5.5 % in the first section over -3.6 % in the second to -2.3 % in the last section. The contrast was found for capillaries A and B as can be seen in Figure 4.7 and the listed calculated values in Table 4.2.

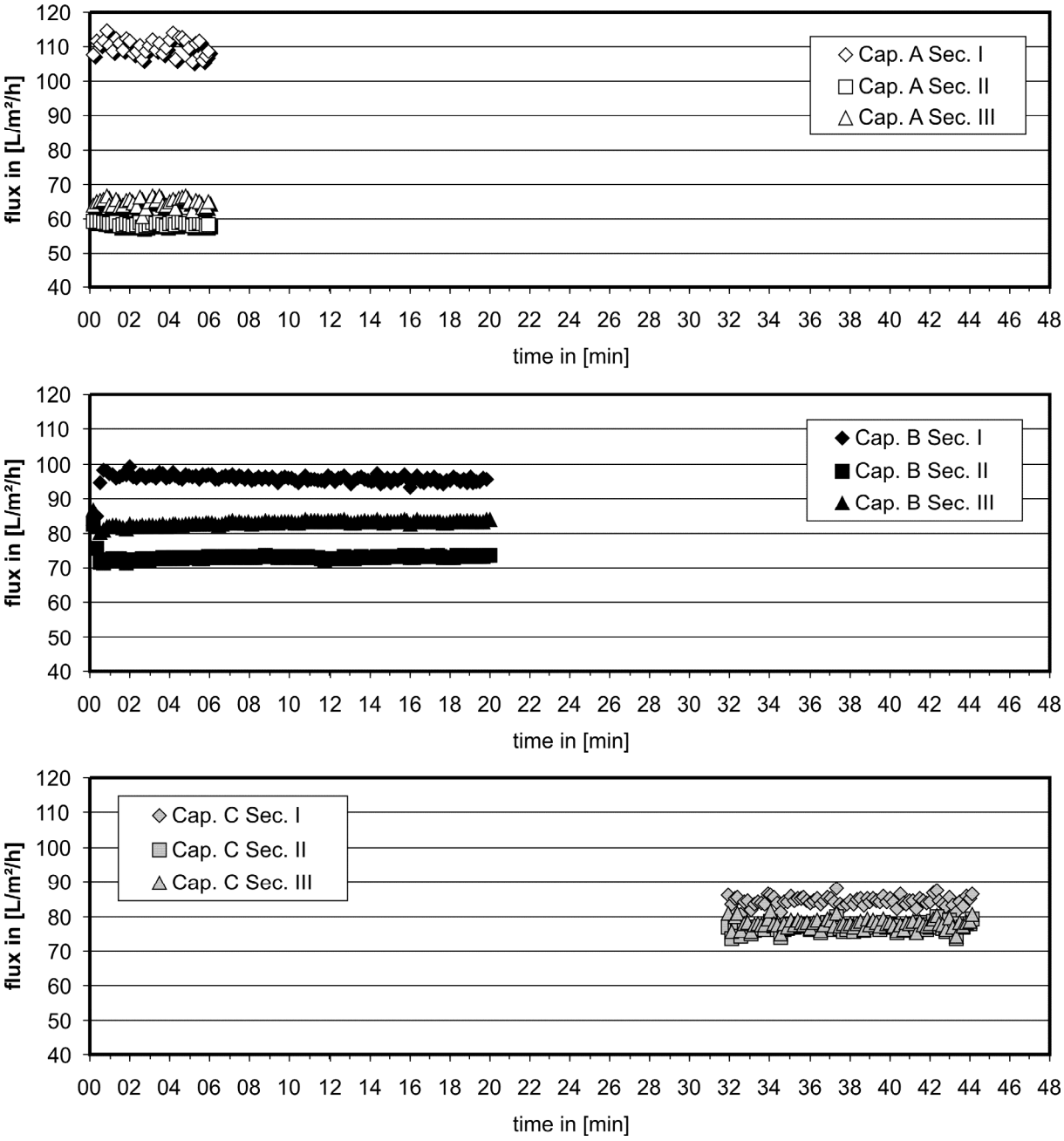

Figure 4.7: Flux in [L/m²/h] vs. time in [min] at the three sections begin (I), middle (II) and end (III) of the capillaries A, B and C, operated in dead-end

All three capillaries showed lower fluxes in the middle and end section and higher fluxes at the inlet section compared to their total average fluxes, as indicated by their sign in Table 4.2. However, capillary B showed a decrease in flux over time in

section I. Because the membranes were operated at constant flux, the flow through section II and III increased at the same time. This behaviour indicates some kind of increased resistance at section I during operation. This was confirmed when considering the average transmembrane pressure increase over time over all three sections. It was found that there was none for the experiments using capillary A and C but that there was a small increase in the experiment with capillary B as indicated in Figure 4.8. The modelled values differ quite a lot from the experimental data, especially for capillary A and C. Here, the initial transmembrane pressure, i. e. at time t = 0, was calculated to be 12.67 kPa and 13.56 kPa respectively. The value for capillary B was calculated to be 12.69 kPa, which is in good accordance to the experiment, compare Figure 4.8 at time t = 0. The pressure drop along the membrane wall was calculated to be approximately 2.5 kPa, compare Figure 3.22.

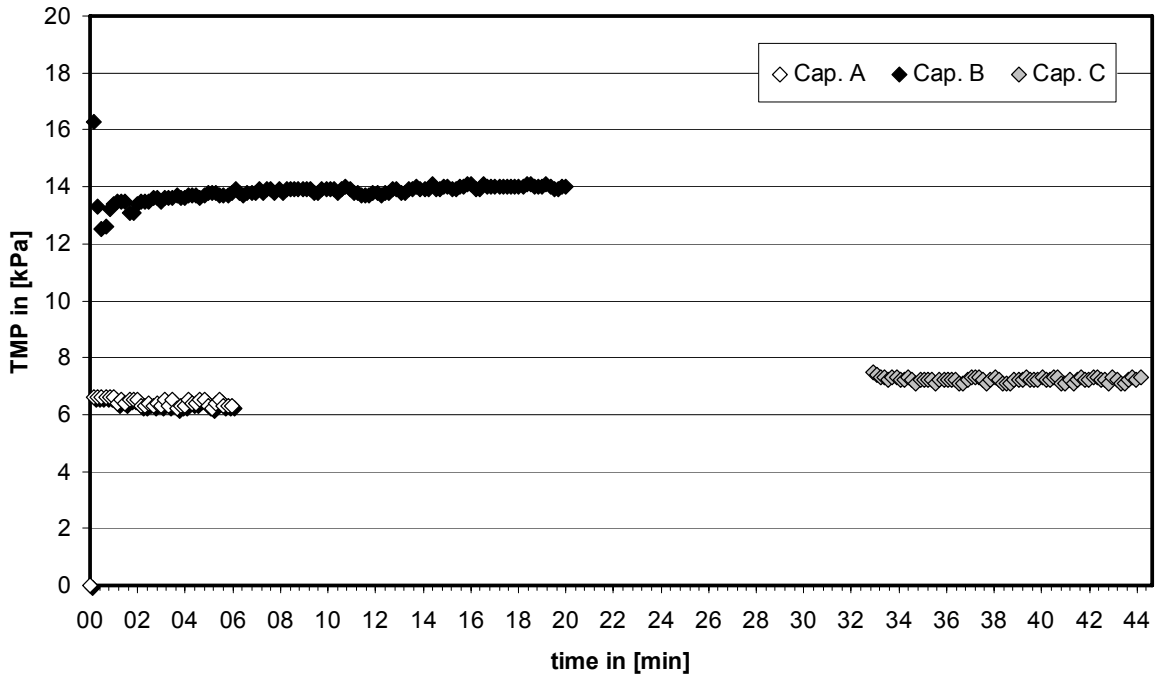

Figure 4.8: Measured transmembrane pressure (TMP) in [kPa] vs. time in [min] during operation of the capillaries A, B and C

The validation of the model with respect to its initial flow regime could be proven by comparing the average filtrate volume flow of each experiment and capillary section with the modelled filtrate volume flow as function of the capillary length z, as illustrated in Figure 4.9. The calculated values of the model were based on the measured initial membrane resistance at each section, the average measured total

flux of the experiments and the capillary as given in the previous paragraphs and on the potting geometry as given in chapter A.16.

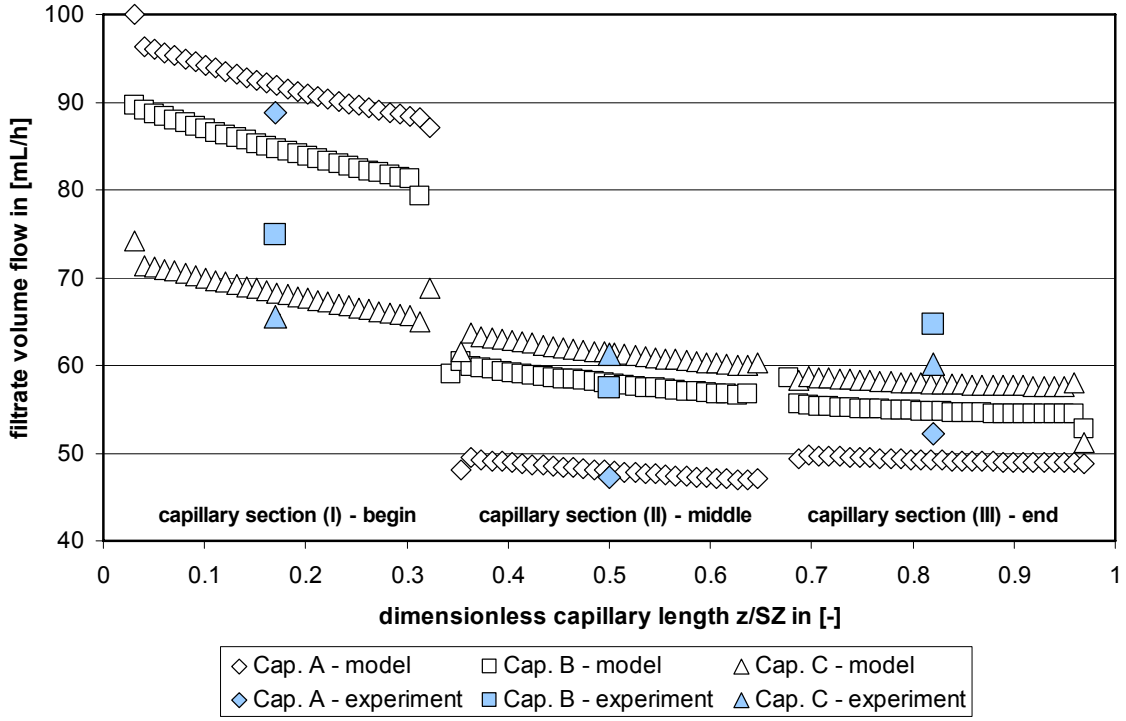

Figure 4.9: Filtrate volume flow in [mL/h] of the models at time t = 0 vs. dimensionless capillary length z and average filtrate volume flow in [mL/h] of the experiments at the different capillary sections begin (I), middle (II) and end (III) of the capillaries A, B and C

It can be seen that the model overestimates the filtrate flow through all three capillaries in the first section, whereas the experiment A and C showed lower deviations of the modelled values over time from the average experimental, compare Table 4.3. The model fits the experimental data very well for flow through section II for all investigated capillaries. At section III the model generally underestimates the average measured values as indicated by the negative sign of the values in Table 4.3, whereas the deviation differs between the capillaries. Deviation was highest for capillary B with -17.8 % and lower but still quite high for the capillaries A and C. The difference over the total capillary length of the modelled average filtrate flow from the average measured values was calculated to be quite small with -0.30 %, -1.59 % and 0.23 % for the capillaries A, B and C. This shows, that the model calculations

predicted the measured filtrate volume flow quite well. Especially if it is considered that the measurements show pronounced scattering.

Table 4.3: Percentage deviation of the modelled filtrate volume flow from the measured average filtrate volume flow at the different capillary sections begin (I), middle (II) and end (III) of the capillaries A, B and C

Capillary	Deviation in [%] section I (Begin)	Deviation in [%] section II (Middle)	Deviation in [%] section III (End)
A	3.46	1.66	- 6.01
B	11.75	1.27	- 17.8
C	4.32	0.38	- 4.02

The following demonstrates the modelled floc transport and deposition of the experimental examinations. Due to the varying initial membrane resistances between the three capillaries and each capillary section the resulting flow fields and initial floc trajectories will be varying as well. For larger floc aggregates the influence on the transport behaviour shows to be little but increased for the smaller floc size as can be seen in Figure 4.10, which illustrates modelled floc trajectories of flocs with radius a_F = 29.47 µm (right) and a_F = 5 µm (left) exemplarily for all three capillaries. It has to be mentioned that for the purpose of clarity only the trajectories initially started at r/SR = 0 and r/SR = 0.9 are illustrated for the larger flocs here, hence delivering the outermost and innermost trajectories. For smaller floc aggregates the effect is comparable to those obtained when modelling the floc trajectories over time, considering fouling layer formation and resulting additional resistance to flow. Even here the fluid will flow along the parts of the membrane where resistance is likely lowest. As long as the smaller floc aggregates are not merged together on the equilibrium trajectory they will be dominated by the fluid flow forces and will follow the fluid to great extent. When the floc trajectories eventually merge together on the equilibrium trajectory close to the membrane wall the influence vanishes. One can conclude that the equilibrium trajectories for all floc sizes investigated are not significantly affected by the varying membrane resistance. It is dominated by lateral forces in the far field region of the membrane wall and in the near field region by lateral and DLVO forces as discussed previously in chapter 3.5.2. In both cases the forces are equalising the drag forces which are varying due to the different fluid flow

velocities resulting from the different resistances of the membrane wall against flow, resulting in a stable position of the trajectory. This can be further seen if the trajectories were passing the pottings between the different sections in the experimental setup at dimensionless capillary lengths of about z/SZ = 0.35 and 0.67. Here, the trajectories are distracted but immediately came back to their stable equilibrium position. Therefore, the floc contact points in all modelled experiments were found to be in the range as shown in chapter 3.5.2.

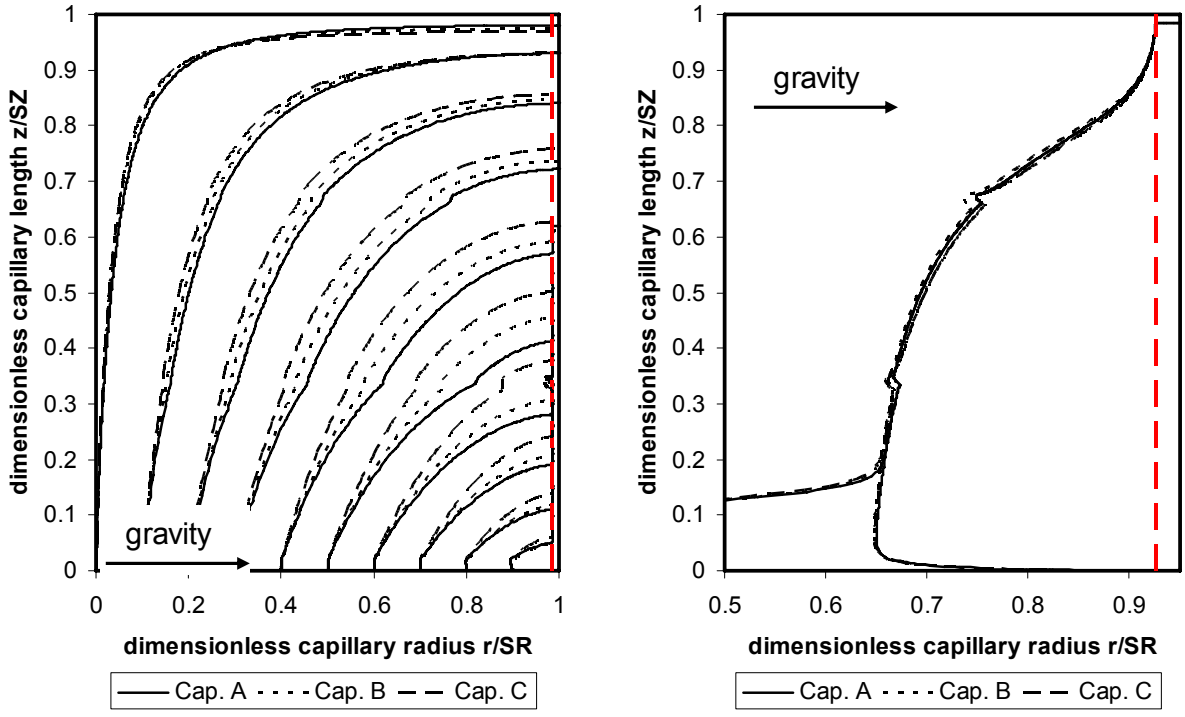

Figure 4.10: Floc trajectories of flocs with radius a_F = 5 µm (left) and a_F = 29.47 µm as display detail (right) of the modelled experimental data

After filtration, the capillaries were analysed for iron and primary particles for validation purposes of the model with respect to the modelled transport and deposition behaviour of floc aggregates. Therefore, the capillaries were divided into different pieces according to the sampling point scheme given in Figure 4.11. The abbreviations used are B, M and E for begin, middle and end of the capillary, respectively. The subscripts M and P are used for metal and particle analysis and the numbers indicate the sample taken in each capillary section, hence 1 is closer to the capillary inlet than 2. The pieces for particle analyses were 10 cm long, whereas the pieces for iron were 2 cm long. Each piece of sample for particle analysis was stored

in a closed jar filled with 200 mL ultra pure water. The water was acidified to pH 3 using hydrochloric acid to resolve the coagulated iron. The jar was then stored over night on magnetic stirrers. The samples were then rinsed out from both sides four times using a micro litre syringe and the rinsing suspension was collected in a jar. The particles in suspension were counted using the particle counter Abakus mobil fluid (Klotz Analytische Messtechnik, Germany).

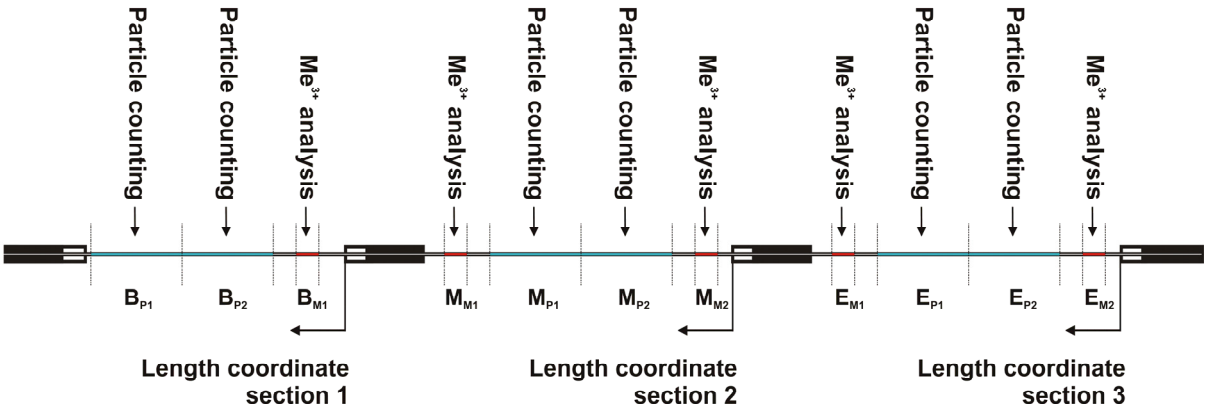

Figure 4.11: Sampling points of the single capillaries used in the experiments

The samples for iron analysis were exposed to digestion with 4 mL nitric acid (HNO_3), afterwards diluted with 30 mL distilled water and measured with ICP/OES (Inductively Coupled Plasma/Optical Emission Spectrometry) for iron. The experimental results expressed as total iron in µg/cm are presented in Figure 4.12. Please note that there was no sample taken at M_{M1} using capillary B. In case of capillary C it is apparent that the amount of total iron close to the dead-end of the capillary was measured to be 2.28 µg/cm, whereas the average of the first four samples was calculated to be 5.5 times smaller with 0.42 µg/cm. This is in very good agreement with the discussed theoretical considerations. Due to the longest time in operation with 45 minutes, sufficient time was given for transport of the flocs and deposition at the rear end of the capillary. However, this increased floc deposition at the rear end of the capillary did not force the TMP to increase to maintain constant flux operation, compare Figure 4.8. Hence it is concluded that a stable and porous fouling layer was formed along the capillary and that no significant compaction, accompanied with decreasing porosity of the flocs, occurred. The second longest run was performed with capillary B. Even here the highest measured value of total iron was found at the sampling point E_{M2}, close to the membrane dead-end. The value was measured to be

0.56 µg/cm, about 2.5 times larger than the average of the samples closer to the capillary inlet but 4 times smaller than measured in capillary C. However, Figure 4.8 shows a small but consistent transmembrane pressure increase during operation of capillary B which cannot be linked to certain measured values.

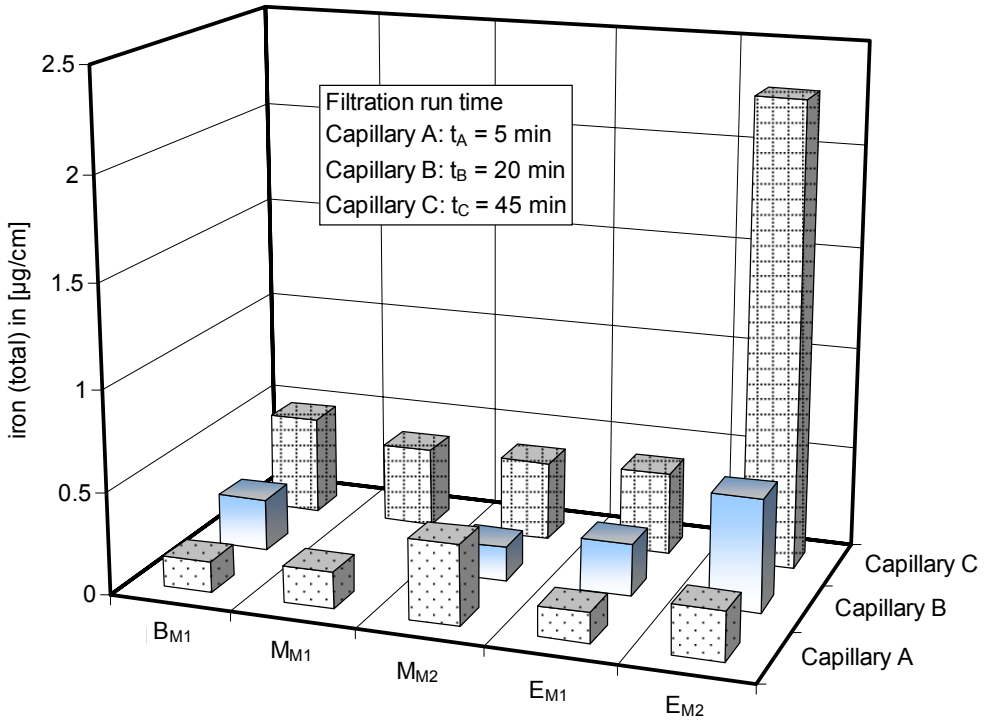

Figure 4.12: Total iron in [µg/cm] at different sampling points at the capillary sections begin (B), middle (M) and end (E) of the capillaries A, B and C

The measured values of the shortest experiment for capillary A vary most, whereas no indications were given by transmembrane pressure. Hence, it has to be assumed that a porous and probably temporary plug was formed in the middle section at sampling point M_{M2} to explain the highest value for total iron with 0.39 µg/cm, which is approximately twice as high as the average of the two other measured values in this capillary. One reason for this might be that the experimental equipment was susceptible for fluctuations in engine speed of the used pump and control of the chosen flux to be adjusted, especially at start of the experiment. However, particularly the results obtained from the experiments B and C are in good accordance with the theoretical considerations discussed in chapter 3.5. Due to the arising numerical convergence problems described above, neither comparison of the

experimental and theoretical data nor validation of the modelled values could be performed in this respect.

Nevertheless, particle counting was applied to proof that the more widely homogeneous distribution and the preferential deposition of smaller and mid sized primary particles decrease in concentration or will nearly vanish due to coagulation prior UF. Unfortunately, due to malfunction of the used particle counter, no adequate particle counts of the experiments discussed above could be evaluated. But, a series of experiments were performed for other purposes earlier and could be ideally used in this framework as well. In these experiments, single capillaries were operated in dead-end and at constant TMP rather than constant flux. The TMP used were 0.4 bar and 0.7 bar. The capillaries, the coagulant and coagulation conditions, the type of primary particles and concentration etc. used in this set of experiments were identical to those presented in the chapters 4.1 and 4.2. In principal, the experimental equipment and setup used was comparable to the one explained in chapter 4.3, just more manually operated. For further details please refer to PANGLISCH (2001). Analysis was performed as described in chapter 4.5 too, whereas the complete capillary was subdivided into ten pieces of equal length of 10 cm.

It has to be mentioned that the results shown here may vary from the theoretical considerations to some extent. This is of course due to the experimental procedures with its challenging analysis and related scattering of the results, rinsing of the capillary sections after resolving the iron hydroxide flocs for instance. Furthermore, the capillaries used are usually not homogenously in terms of membrane resistance as described above. Figure 4.13 shows exemplarily measured results of deposited ABS primary particles after filtration at constant TMP of 0.7 bar as uncoagulated suspension vs. dimensionless capillary length z/SZ and primary particle radius a_P. The Π value indicates the fraction of primary particles of certain size at each capillary section related to the total number of inflowing primary particles of this size into the capillary. The limiting radius in the experiments shown could be just roughly estimated to be smaller than 2 to 3 µm, due to the high fluxes. However, Figure 4.13 indicates that smaller and mid sized primary particles were not transported up to the end of the capillary, being deposited after shorter distances to the capillary inlet, which is in good accordance to the theoretical considerations, see chapter 3.5.2.

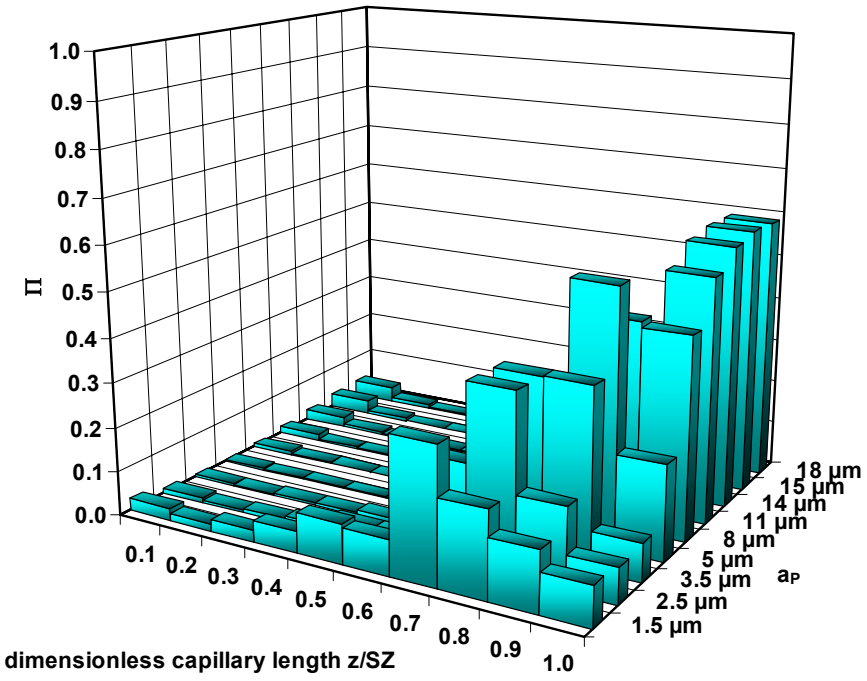

Figure 4.13: Fractions of deposited primary particles after filtration (TMP = 0.7 bar, average flux of approx. 157 L/m²/h) as uncoagulated suspension vs. dimensionless capillary length z/SZ and primary particle radius a_P

Figure 4.14 and Figure 4.15 show the measured results for deposited primary particles after filtration at constant TMP of 0.7 bar as coagulated suspension vs. dimensionless capillary length z/SZ and primary particle radius a_P. The comparison of Figure 4.13, Figure 4.14 and Figure 4.15 delivers that the fractions of small and mid sized primary particles in the range from a_P = 1.5 µm to about a_P = 14 µm was increased in the last two capillary length sections at z/SZ = 0.9 and z/SZ = 1, hence at the end of the capillary for the coagulated suspensions. Accordingly, the fraction of primary particles of the same size range decreased in the middle and the third quarter of the capillary length at z/SZ = 0.5 to z/SZ = 1. This clearly indicates that smaller and mid size particles were transported as floc agglomerate more deeply into the capillary as they would have actually done due to their own size. The considerably reduction of deposited small and mid sized primary particles along the capillary in relation to the pure solid primary particle suspensions was also found in other particle count experiments at constant TMP of 0.4 bar. Their results are given in chapter A.17, whereas both, fractions of deposited primary particles after filtration as uncoagulated and as coagulated suspension vs. dimensionless capillary length z/SZ and primary particle radius a_P are shown for comparison.

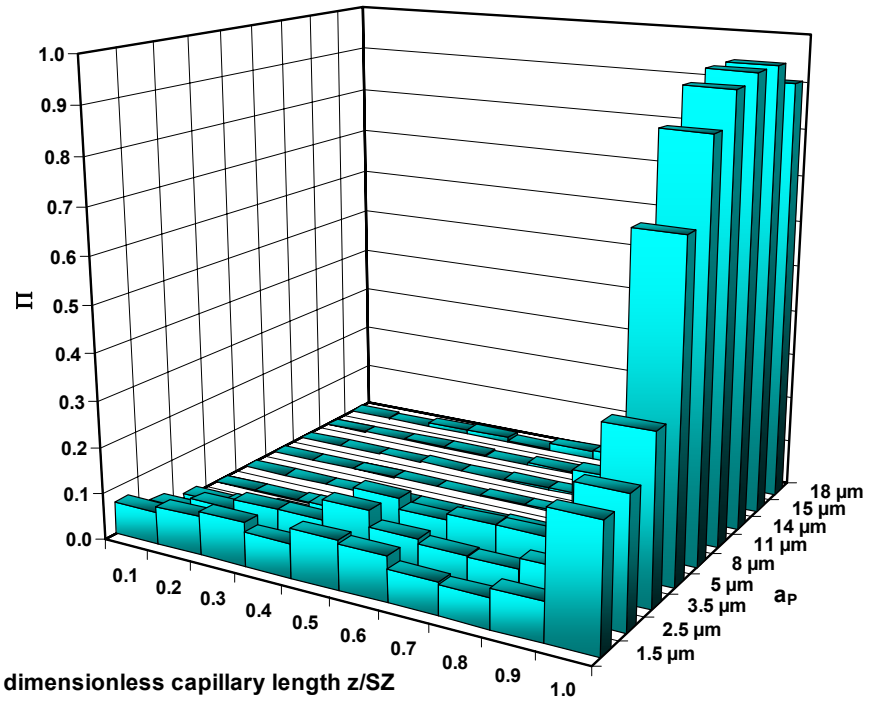

Figure 4.14: Fractions of deposited primary particles after filtration (TMP = 0.7 bar, average flux of approx. 179 L/m²/h) as coagulated suspension vs. dimensionless capillary length z/SZ and primary particle radius a_P

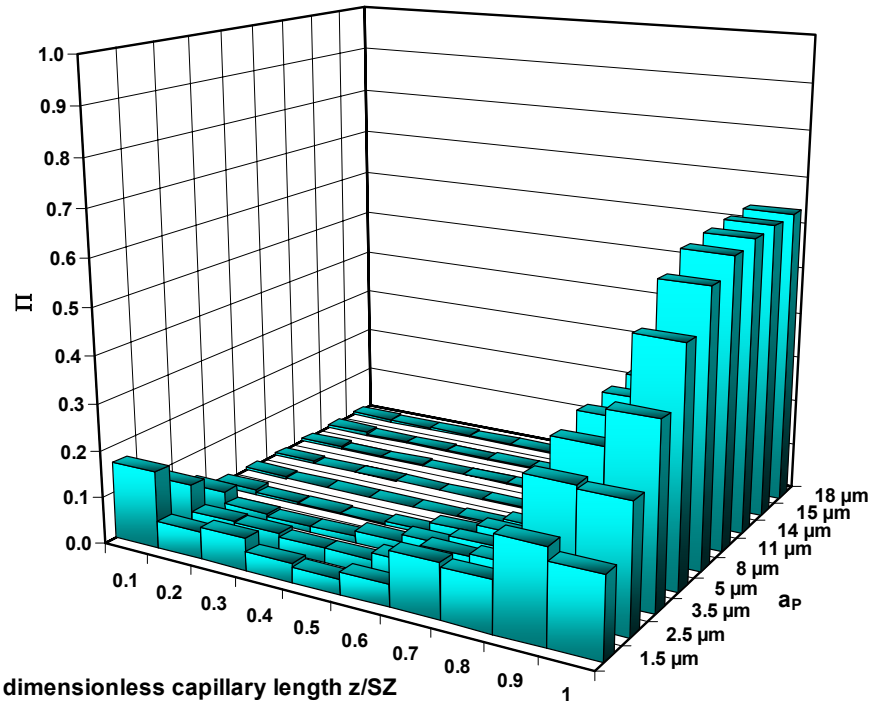

Figure 4.15: Fractions of deposited primary particles after filtration (TMP = 0.7 bar, average flux of approx. 250 L/m²/h) as coagulated suspension vs. dimensionless capillary length z/SZ and primary particle radius a_P

5 Engineering and scientific relevance

The removal of NOM is an important objective at many treatment plants because of its effect on finished water quality and on treatment processes, as e. g. its impact on membrane filtration performance due to severe fouling. Coagulation is an established technology for the removal of NOM and can be combined with membrane filtration processes into the hybrid process coagulation / UF for instance, as discussed briefly in chapter 2.2. Here, most researchers showed that membrane performance will be usually stabilised and flux will often be enhanced compared to filtration performance of raw waters not coagulated prior the membrane. This is, because then NOM will be bared from being irreversibly adsorbed on the membrane surface. Hence, coagulation has to be optimised to account for optimal NOM removal efficiencies first and then to account for optimal membrane performance. As discussed in chapter 2.2, the more effective NOM removal by coagulation, the better flux stabilisation will be. And the more porous the coating layer formation by porous floc aggregates, the higher flux improvement will be. Though, stable operation requires constant membrane permeability, i. e. limited TMP increase over time at constant flux operation or limited flux decrease over time at constant pressure operation. Of course, beside the high finished water quality this will be one of the primary objectives when installing a membrane system for the treatment of all kind of waters. Thus, the hybrid process coagulation and UF might be one process of choice for the direct treatment of surface waters achieving this objective.

But, due to the fact that mass is retained at the membrane wall and that formation of fouling layers will therefore always occur, it will come to permeability declines to some extent. Therefore, backwashing performance becomes important to recover permeability after each filtration cycle. Due to the outcomes of this work and others, e. g. PANGLISCH (2001), it can be derived that it will be of advantage having a homogenously distributed and formed fouling layer along the membrane surface. The resulting contribution to total membrane resistance will then be likewise constant and independent of the capillary length coordinate. This will be advantageous not only during filtration but also during backwashing, where homogenous coating layers will enable uniform backwashing efficiencies over the complete length of the capillary. If

the coating layer is not homogeneous and offers different resistances to flow, then the water will enter the membrane during backwashing at areas of lowest resistance most. Hence, the fouled membrane surface will be cleaned best where it is initially least fouled and worst where it is needed most. This can lead to uncleaned areas of membrane surface if the resistance against backwashing of the fouling layer is high enough. Furthermore, those areas may hamper the discharge of already detached parts of the former fouling layer out of the capillary. In addition, if those areas are not cleaned efficiently during several backwashing cycles this may lead to an increase of bonding forces between the fouling layer and the membrane surface (GIMBEL (1989) cited in PANGLISCH (2001)). Generally, only little is presently known about the detachment characteristics and mechanisms of fouling layers of different composition during backwashing, which should be suspect of additional research.

Considering the above, one easily finds the contradiction within this process combination. On the one hand coagulation leads to a significantly decreased number of colloids and smaller particles by embedding them into larger floc aggregates. On the other hand, larger floc aggregates themselves will contribute to inhomogeneous fouling layer formation, caused by their transport behaviour depending on their size, enhanced by additional floc growth while being transported. This can be reasonably assumed by the outcomes of this work, see chapters 3.5.2 and 3.5.3. However, it may contribute to lowered membrane performance, especially if flocs will be transported to the rear end and clog the capillary, which was found to take place theoretically from the end towards the inlet and from the bottom to the top in a horizontal aligned capillary. As a result, membrane surface area available for filtration can be dramatically reduced over time, especially at high floc volume concentrations within filtration cycles (LERCH ET AL. (2005B)) and, considering long term operation, by decreased cleaning efficiency (HEIJMAN ET AL. (2007)). But clogging of the capillary may also occur somewhere in the beginning or middle of the capillary, especially if the flocs entering are initially large and grow further while being transported (GITIS ET AL. (2005). Hence, flocs entering the capillary should not be too large, limiting the risk of immediate formation of plugs and clogging of the capillary.

If clogging occurs, which may be detected as rapidly increased pressure drop or decreased flux during operation, filtration cycles should be shortened to avoid

compression of the plugged areas and to facilitate backwashing. Further, floc and fouling layer porosity should be kept preferably high, because then the effect of inhomogeneous formed layers on resistance to flow and therefore on achievable performance is low, whereas high porosity will be further supported by larger flocs. If a porous fouling layer will be compressed, then the resistance to flow will be increased due to a lowered porosity and the performance will drop during operation, noticed as pressure drop increase or flux decrease. Hence, large, incompressible and porous flocs and filtration at low TMP will be favourable as discussed in chapter 3.5, but plugging of the capillaries, which is more likely for larger floc aggregates, should be avoided. It has to be mentioned that the statements above are restricted to flocs only; the influence of NOM or other components for instance were not considered.

As suggested by PANGLISCH (2001) for filtration of uncoagulated raw waters, clogging might be avoided by introducing a slow cross-flow velocity at the end of the capillary. The concentrate flow might be further treated in a second membrane stage, adapted in geometry and operation parameters on the better defined, i. e. more tighten particle size distribution. Cross-flow operation in this respect would just be used to transport and push larger flocs out of the capillary which otherwise would be deposited at the dead-end. The flow profile within the capillary lumen will still be laminar. Please note that this is different to commonly known cross-flow operation, where flow along the membrane is often kept turbulent to minimise deposition and where the extracted water volume is mostly governed by the critical flow concept (BACCHIN ET AL. (2006A)). In the following, chosen results of models with different average outlet velocities at boundary 3 and 6 are shown to proof effects of an introduced slow cross-flow. The average velocities at the capillary outlet were chosen to be 1 %, 5 % and 20 % of the inlet average velocity, whereas all other previously used parameters were kept constant. Figure 5.1 shows floc trajectories of different sized flocs for models with 5 % (left) and 20 % (right) average cross-flow velocity at the capillary outlet, whereas just the inner- and outermost floc trajectories and resulting equilibrium trajectories within the capillary for flocs of radius a_F = 29.47 µm and a_F = 60 µm are illustrated. It can be seen that in case of slow cross-flow operation smaller flocs entering the capillary in the neighbouring area of its axis at the inlet will leave the capillary at the end. The faster the chosen cross-flow velocity

the larger this neighbouring area and the more flocs are able to be transported out of the capillary lumen without being deposited. For flocs of radius a_F = 5 µm and 1 % average cross-flow outlet velocity it was found that all flocs entering between the capillary axis and a dimensionless capillary radius r/SR = 0.03 will be transported out of the system. Applying an outlet velocity of 5 % will deliver r/SR = 0.11 and at 20 % will deliver r/SR = 0.273. Hence, assuming an evenly distributed floc suspension entering the capillary, about 0.09 %, 1.23 % or 7.67 %, respectively, of all entering flocs will leave the capillary. This amount will be higher for smaller flocs and lower for larger flocs. For example, the values for flocs of radius a_F = 12.25 µm at 20 % outlet velocity were calculated to be 0.02 % and for 5 % and slower velocities no floc will leave the capillary just as well for flocs even larger. For flocs of those sizes, the front contact point, see chapter 3.5.2, is shifted very slightly towards the inlet for increasing outlet velocities.

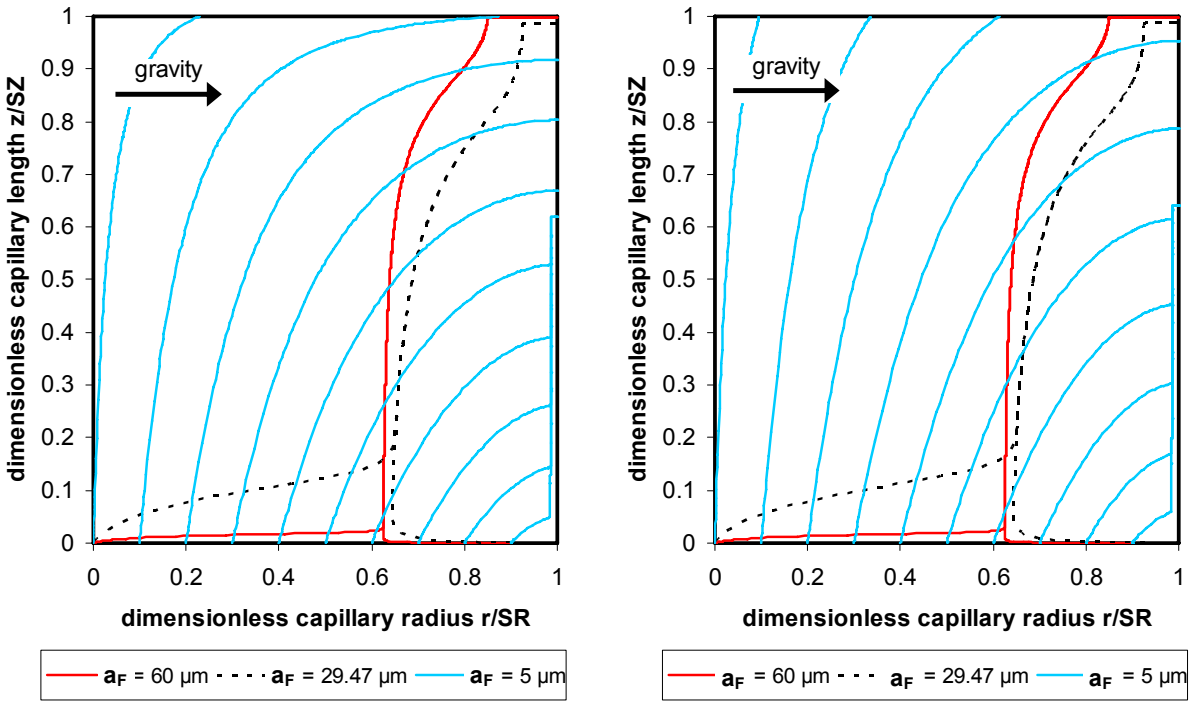

Figure 5.1: Floc trajectories for models with 5 % (left) and 20 % (right) average cross-flow velocity at the capillary outlet

Even at high flux operation, for instance 200 L/m²/h, larger flocs will not be driven out of the system to great extent as indicated in Figure 5.2. Just flocs from the very upper part might be able to escape deposition and leave the capillary. Here, the flow is from the rear to the front and gravity acts from top to bottom. The diameter of the

trajectories was scaled to the modelled floc radius a_F/SR and the colour bar at the right hand side of each plot indicates the magnitude of floc velocity. Larger flocs will not be able to be significantly transported out of the capillary lumen only by introducing slow cross-flow velocities at the capillaries outlet. This shows, clogging caused by larger floc aggregates cannot be avoided unless the flux is dramatically increased.

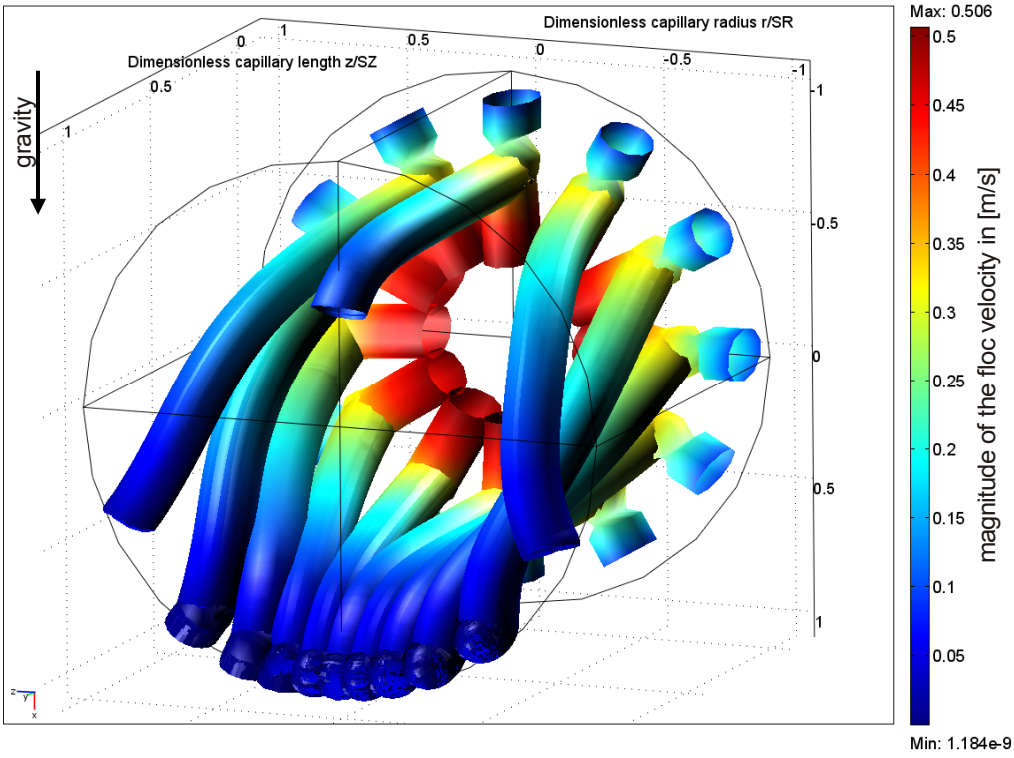

Figure 5.2: Floc trajectories of flocs with radius a_F = 29.47 µm. Capillary operated at 200 L/m²/h and 20 % average cross-flow velocity at the capillary outlet

However, these are the findings just on the basis of the developed theoretical model, which does not claim being complete yet. For instance, the model presumes a stagnant, neither compressible nor expandable fouling layer. If a floc is once deposited it will not be moved to another position. Further, no tangential flow through the fouling layer is included in the model so far. However, in real operation the composition of the fouling layer will be much more multifaceted. For instance, it was shown by MARSELINA ET AL. (2007) using direct observation techniques, that the upper part of a fouling layer is fluidised by the passing fluid during operation. This viscous flow of the upper part of the fouling layer, tangential along the membrane, could be probably used to avoid clogging at slow cross-flow velocities at the capillary outlet.

A possibility to achieve homogeneous distribution of flocs along the membrane surface will be the adaptation of the capillaries geometry in combination with adapted fluxes. This will have a significant effect on the limiting radius, which subdivides the flocs in flocs being deposited over the complete length of the capillary, if small enough, and, if larger, in flocs being deposited at the earliest after certain distances to the capillary inlet, see chapter 3.5.2. This adaptation of the cylindrical geometry of the capillary and operation condition will shift the limiting radius to smaller or larger radii as desired. For instance, the limiting radius for a capillary 1 m in length, 2.5 mm in radius, driven at a flux of 80 L/m²/h with 5 % average outlet velocity was calculated to be a_F = 20.27 µm. For the same properties but with different flux of 150 L/m²/h it was calculated to be smaller with 16.29 µm. For the same properties but different capillary radius of r_C = 1 mm it was calculated to be a_F = 7.94 µm. The same was found for dead-end operation. When modelling a capillary 1 m in length, 1 mm in radius, driven at a flux of 80 L/m²/h, the limiting radius was found to be a_F = 8 µm, just a bit larger than operated with 5 % cross-flow velocity at the capillary outlet. Decreasing the capillary length will lead to an additional increase up to a_F = 11.48 µm if the other parameters are kept constant. Hence, low flux operation applied in capillaries with larger diameters and shorter length will generally lead to increased limiting radii and therefore enabling homogenous floc deposition along the membrane surface for somewhat larger floc aggregates. The above may be utilised in the hybrid process coagulation and MF/UF to target-oriented adaptation and optimisation of the coagulation process with respect to filtration performance. Hence, process limitations can be identified and operational malfunction or faulty utilisation may be avoided too.

This knowledge may be further utilised in other hybrid membrane processes too, where some kind of precoating of the membrane surface is applied. Here, the precoating material like powdered activated carbon or silica dust is used to cover the surface, where one objective among possibly others is fouling protection, see chapter 2.2. Generally, precoating layers have to be evenly distributed and formed along the surface and should be easily detachable during backwashing too. Both, particle size distribution of the material, which should be ideally tight for this purpose, as well as geometry and properties of the capillaries to be used can be adjusted to each other to achieve best performance of the process and to reduce operating costs.

Another interesting and promising approach to enhance operating performance within the hybrid process coagulation and membrane filtration was found in this work when discussing the influence of sedimentation on floc transport, see chapter 3.5.2.2. It was shown that vertical aligned membrane capillaries may be of advantage if the fluid enters the membrane at the top, i. e. operation is driven in top-down mode. For smaller flocs, transport is comparable as in bottom-up operation of vertical aligned capillaries and as in horizontal aligned capillaries. But, after exceeding a certain limiting size, which was found to be a_F = 83.9 µm for flocs with a relative density of 1.05, the flocs will be collected on an equilibrium trajectory and eventually transported towards the capillary axis and not towards the membrane wall. Finally, they will be retained at the dead-end of the capillary. Please note, the floc size lies within the size distribution of the flocs used in the experimental part of this work. The same behaviour was found for flocs of size a_F = 29.47 µm with higher densities as illustrated in Figure 5.3.

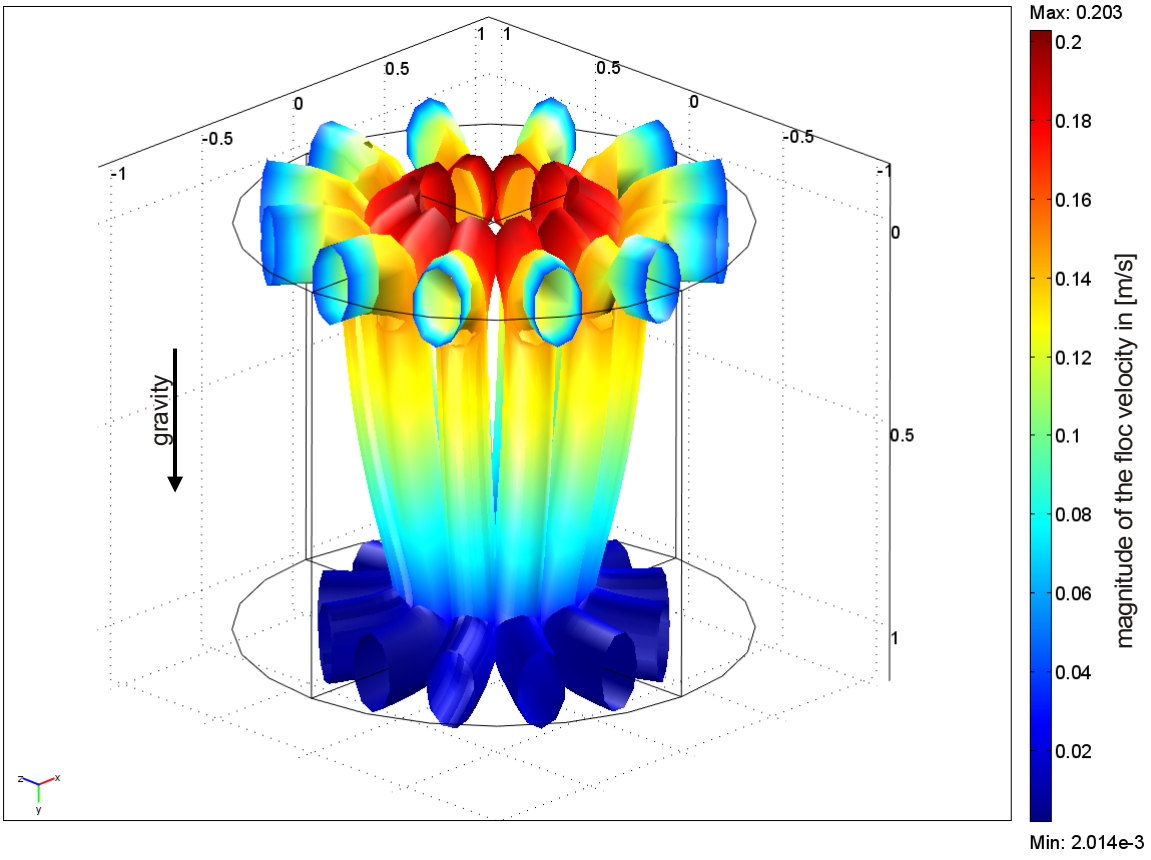

Figure 5.3: Floc trajectories of flocs with radius a_F = 29.47 µm, ballasted with micro sand (relative density of 1.72) within a vertical aligned capillary, operated at 80 L/m²/h in top-down dead-end mode

The flocs will merge to equilibrium trajectories but not being transported towards the membrane wall for relative densities larger than approximately 1.72. An increased density of the floc aggregates can be achieved within the hybrid process in similar way as in the ACTIFLO® process (Krüger A/S, Denmark) which utilises micro sand as a seed for floc formation, providing surface area that enhances coagulation and acting as ballast in the formed flocs. To avoid clogging of the membrane at the dead-end, a slight cross-flow of 1 % may be of high advantage. However, this theoretical approach needs to be further investigated for practical applications in membrane systems in future research.

Generally, the chosen approach of modelling floc transport and resulting fouling layer formation in dead-end capillaries with CFD/FEM delivered some advantages. The model can be easily used as tool to calculate floc, or generally particle transport in arbitrary cylindrical capillary geometries, due to its scaled dimensionless form, at arbitrary alignments, due to its universal layout. This may not only be utilised for modelling the floc transport and fouling layer formation as done in this work, but can be used for evaluation and optimisation of technical designs and processes in practical as well as scientific problems. For instance, after some minor adaptations of the membrane wall boundary for risk analysis in membrane integrity problems too.

Numerical difficulties occurred when modelling the fouling layer formation over time, especially for larger floc aggregates, as described in chapter 3.5.3. This was because of locally arising very high floc volume concentrations along the equilibrium trajectory compared to areas in the vicinity. Resolution of the applied mesh could not be adapted to resolve the sharp gradients to deliver acceptable results. Additionally, it was found that the description of floc volume was generally problematic within the used FEM software modes. This problem is based on the chosen, so called Euler-Lagrange approach, i. e. one continuous phase (the fluid) related to a fixed coordinate system and one dispersed phase (the flocs) related to a system moving with the fluid (compare PASCHEDAG (2004) for instance), used to describe floc transport and fouling layer formation. The approach considers flocs as single mass points in the continuous phase only, not as flocs requiring a certain volume. Moving flocs are therefore numerically calculated along the node points on the mesh. Hence, calculation and limitation of the floc volume concentration to a fixed value was not

directly possible, but might be assessable by additionally codes to be programmed in future work. Relief may be also found in other commercially available software products, using finite volume methods (FVM) instead. This enables the direct use of the so called Euler-Euler approach, i. e. two continuous phases (the fluid and the floc suspension) related to a fixed coordinate system (compare PASCHEDAG (2004) for instance). FVM considers a certain volume around its node points on a mesh for numerical calculation, enabling to consider flocs as spheres rather than points during numerical calculation.

Future work on the model should also account for size distributions rather than single sizes and enlarge the model to include additional phases in suspension or solution respectively, such as dissolved species like dissolved NOM and its components or salts to include the effect of direct adsorption onto the membrane for instance. To account for floc agglomeration during transport within the membrane capillary, population balances might be further implemented into the existing model. This new approach in numerical modelling accounts for changes of particle or floc properties, usually size distribution, and simulates the interaction of agglomeration and breakage of one phase in multi phase flow, SCHÜTZ ET AL. (2007).

Another aspect to be included into future modelling should be the implementation of the mass fractal dimension d_F into the used equations to consider the impact on transport and deposition behaviour of more realistic floc structures. Considering the formed fouling layer, it should be done additional modelling work on floc and layer compressibility as well as the detachment behaviour of deposited flocs.

6 Summary

The interest in low pressure membrane filtration, i. e. micro- and ultrafiltration (MF and UF) increased rapidly in recent years, especially due to the extremely high requirements for potable water quality with respect to hygiene aspects. With UF, the filtrate quality is quite independent of the raw water quality with respect to larger colloidal and particulate water components. Further advantages are the possibility of fully automatic operation, compact system design, high space utilisation and provided flexibility in system enlargements, modernisations and new installations. But beside those advantages some limiting or even adversarial factors exist, especially when applying MF or UF for the direct treatment of surface. One of these is fouling, another one the inadequate retention efficiency of disinfection by products (DBP) precursors. Particularly dissolved organic matter (DOM) can be very problematic due to the formation of hardly reversible and/or irreversible fouling layers and due to its general contribution in formation of DBP. To get these problems under control, different pretreatment processes are conceivable and available, whereas this work is focused on the hybrid process coagulation and UF. Coagulation is an established technology for the removal of DOM and, from an engineering perspective, can easily be combined with membrane processes, still offering the advantages of the membrane as mentioned above.

Nevertheless, it is necessary to understand what the limiting factors are, when they are of importance and how their effects may be avoided. The most important point in this respect is to understand how fouling layers are formed within this process combination, because these layers will limit the efficiency of the entire process. Formation of layers of brownian and non-brownian particles and colloids in inside-out driven capillary membranes is quite well understood but yet the knowledge is not developed far enough to cope for the formation of larger and porous floc aggregates. Therefore, the objective of this work was to contribute to the understanding of formation of fouling layers by porous floc aggregates during filtration of coagulated raw waters in inside-out driven capillary membranes.

A computational fluid dynamics (CFD) model was developed, using the software COMSOL Multiphysics (COMSOL AB, Sweden) for the description of the complete

flow field in inside-out driven UF capillaries of arbitrary cylindrical geometry, alignment, i. e. vertical or horizontal, and operation condition, i. e. cross-flow or dead-end. This was done by numerical calculations of the Navier-Stokes and continuity equations first for stationary and second for transient flows, including the effects of dynamic fouling layer formation. Based on the modelled flow field, floc velocities and trajectories were derived by balancing the forces and torques acting on the flocs in the flow field. The forces and torques considered arose from sedimentation, shear induced and Brownian diffusion, double layer repulsion and van der Waals attraction, drag by filtration, virtual mass and lateral migration. Floc agglomerates were considered being ideally spherical, rigid and of constant shape, consisting of primary particles embedded in iron or aluminium hydroxide, revealing an inner porosity, low density and low zeta potential. To account for the inner porosity of the flocs an equivalent hydrodynamic floc radius was introduced. The effect of the porous aggregates on floc suspension viscosity was considered by introducing a correction factor. The derived floc velocities were further used to model stationary floc volume concentration distributions by numerical calculations of the convection and diffusion equation. In the first step, the models were used to describe initial and stationary floc transport and deposition behaviour. Deposition of flocs along the membrane surface will be classed by floc size. Flocs of size smaller than a certain limiting radius will be deposited widely homogeneous over the total capillary length. Larger flocs occupy preferential places on the membrane surface and do not deposit until they are at a certain distance to the capillary inlet. The larger the particle size, the longer this distance. However, flocs of certain size entering the capillary at its axis or direct vicinity will not be transported to the rear end of the capillary. They will be deposited at so called rear contact points, some distance away from the dead-end. The distance between the dead-end and the rear contact point increases with increasing floc radius until all incoming flocs are forced to merge an equilibrium trajectory, independent of their radial starting position at the inlet. All flocs on this trajectory are deposited theoretically at one single point, ring or ring section at the membrane wall and will be shifted back towards the dead-end with further increasing floc sizes.

However, in contrast to solid particle suspensions, it could be shown that the more widely homogeneous distribution and preferential deposition of smaller and mid sized particles was reduced. Thus, it still comes to the formation of zones with different

composition, porosity and thickness, but the majority of particles embedded in generally larger flocs will be transported towards the dead-end which may cause clogging of the capillary. It was further found that this inhomogeneous fouling layer formation will be enhanced by additional floc growth during transport as can be reasonably assumed by the outcome of this work.

In a second step the models were coupled and eventually used to account for the growing layer height and its influence on the flow field, the floc volume distribution and resulting floc trajectories, predicting fouling layer formation over time. The height of the layer was calculated by integrating the mass flux of flocs onto the membrane surface, whereas the porosity of the fouling layer was calculated based on the Happel model for bulk permeabilities. The increased resistance against the filtrate flow according to the resistance in series model was then used to derive the new fluid flow field over time. However, it came to major convergence problems during the numerical calculation of the floc volume distribution over time, especially if larger flocs were modelled. But convergence could eventually be achieved for smaller floc sizes. Though, the results were not satisfying and only imprecise statements could be made concerning calculability of the permeability decline due to fouling layer formation, but nevertheless qualitative aspects were concluded. It was shown that the local resistance increases at surface areas of preferential deposition, whereupon the fluid rather flows through uncoated or less coated areas. Accordingly, different floc trajectories are developed over time and transport of flocs is shifted towards the capillary inlet, i. e. towards areas less fouled. It was further shown that clogging of the capillaries dead-end takes place over time and theoretically from the end towards the inlet and from the bottom to the top of a horizontal aligned capillary. Setting the modelled results in contrast to experimental investigations showed satisfactory results for both, the modelled flow field and conditionally the fouling layer formation.

New aspects could be derived qualitatively to understand the formation of fouling layers by porous floc aggregates in inside-out driven capillary membranes on which recommendations for appropriate operation conditions were concluded. Under these are e. g. top-down dead-end or cross-flow operation for the filtration of flocs, ballasted with micro sand.

References

ALTENA, F. W.; BELFORT, G.:
Lateral migration of spherical particles in porous flow channels: Application to membrane filtration.
Chem. Eng. Sci. 39 (1984), Nr. 2, pp. 343-355

ALTMANN, J.; RIPPERGER, S.:
Particle deposition and layer formation at the crossflow microfiltration.
J. Membr. Sci. 124 (1997), pp. 119-128

AMY, G.:
Fundamental understanding of organic matter fouling of membranes In: IWA SPECIALISED CONFERENCE ON MEMBRANES, Conference Proceedings (Ed.) Bd. CD-ROM. Harrogate: IWA, 2007

ANDERSON, J. D.; DEGREZ, G.; DICK, E.; GRUNDMANN, R.:
Computational fluid dynamics; An introduction. In: WENDT, J. F. (Ed.): *Computational fluid dynamics; An introduction*. Berlin: Springer-Verlag, 1992. - ISBN 3-540-53460-1

BACCHIN, P.; AIMAR, P.; SANCHEZ, V.:
Model for colloidal fouling of ultrafiltration membranes.
AIChE Journal 41 (1995), Nr. 2, pp. 368-376

BACCHIN, P.; ESPINASSE, B.; BESSIERE, Y.; FLETCHER, D. F.; AIMAR, P.:
Numerical simulation of colloidal dispersion filtration: description of critical flux and comparison with experimental results.
Desalination 192 (2006), pp. 74-81

BACCHIN, P.; AIMAR, P.; FIELD, R. W.:
Critical and sustainable fluxes: Theory, experiments and applications.
J. Membr. Sci. 281 (2006), pp. 42-69

BEAVERS, G. S.; JOSEPH, D. D.:
Boundary conditions at a naturally permeable wall.
J. Fluid Mech. 30 (1967), Nr. 1, pp. 197-207

BEHRENS, S. H.; BORKOVEC, M.:
Electrostatic interaction of colloidal surfaces with variable charge.
J. Phys. Chem. B 103 (1999), pp. 2918-2928

BELFORT, G.; NAGATA, N.:
Fluid mechanics and cross-flow filtration: Some thoughts.
Desalination 53 (1985), pp. 57-79

BENKHALA, Y. K.; OULD-DRIS, A.; JAFFRIN, M. Y.; SI-HASSEN, D.:
Cake growth mechanism in cross-flow microfiltration of mineral suspensions.
J. Membr. Sci. 98 (1995), Nr. 1, pp. 107-117

BERGSTRÖM, L.:
Hamaker constants of inorganic materials.
Adv. Coll. Inter. Sci. 70 (1997), pp. 125-169

BERMAN, A. S.:
Laminar flow in channels with porous walls.
J. Appl. Phys. 24 (1953), Nr. 9, pp. 1232-1235

BIRD, R. B.; STEWART, W. E.; LIGHTFOOT, E. N.:
Transport Phenomena. 2. Edition New York: Wiley, 2002. - 0-471-36474-6

BLUME, I.; KOENHEN, D. M.; ROESINK, H. D. W.:
The XIGA-Concept; The first full-scale applications using a new module system for ultrafiltration. In: MELIN, T.; RAUTENBACH, R. und DOHMANN, M. (Eds.): *Möglichkeiten und Perspektiven der Membrantechnik bei der kommunalen Abwasserbehandlung und Trinkwasseraufbereitung: Begleitbuch zur 1. Aachener Tagung Siedlungswasserwirtschaft und Verfahrenstechnik 30.06.-01.07.97*. Aachen, 1997, pp. B7-1 - B7-13

BOERLAGE, S. F. E.:
Scaling and particulate fouling in membrane filtration systems. In: WAGENINGEN UNIVERSITY (Ed.): *PhD dissertation at the Wageningen University: Scaling and particulate fouling in membrane filtration systems*. Lisse: Swets & Zeitlinger Publishers b.v., 2001. - 90-5809-2429

CARROLL, T.; KING, S.; GRAY, S. R.; BOLTO, B. A.; BOOKER, N. A.:
The fouling of microfiltration membranes by NOM after coagulation treatment.
Water Res. 34 (2000), Nr. 11, pp. 2861-2868

CHELLAM, S.; WIESNER, M. R.:
Particle transport in clean membrane filters in laminar flow.
Environ. Sci. Technol. 26 (1992), Nr. 26, pp. 1611-1621

CHELLAM, S.; WIESNER, M. R.; DAWSON, C.:
Laminar flow in porous ducts.
Reviews in Chemical Engineering 11 (1995), pp. 53-99

CHEN, Y.; DONG, B. Z.; GAO, N. Y.; FAN, J. C.:
Effect of coagulation pretreatment on fouling of an ultrafiltration membrane.
Desalination 204 (2007), pp. 181-188

CHERYAN, M.:
Ultrafiltration and microfiltration handbook. In: CHERYAN, M. (Ed.): *Ultrafiltration and microfiltration handbook*. Lancaster: Technomic Publishing Company, Inc., 1998

References

CHO, J.; SOHN, J.; CHOI, H.; KIM, I. S.; AMY, G.:
Effects of molecular weight cutoff, f/k ratio (a hydrodynamic condition), and hydrophobic interactions on natural organic matter rejection and fouling in membranes.
J. Water Supp. Res. Technol. - AQUA 51 (2002), Nr. 2, pp. 109-123

CHO, M.-H.; LEE, C.-H.; LEE, S.:
Effect of flocculation conditions on membrane permeability in coagulation-microfiltration.
Desalination 191 (2006), pp. 386 396

COMSOL AB:
In: COMSOL AB (Ed.): *Multiphysics User's Guide*. Bd. Version 3.3a. Stockholm: 2006

COMSOL AB:
In: COMSOL AB (Ed.): *Chemical Engineering Module User's Guide*. Bd. Version 3.3a. Stockholm: 2006

COX, R. G.; BRENNER, H.:
The lateral migration of solid particles in Poiseuille flow - I Theory.
Chem. Eng. Sci. 23 (1968), pp. 147-173

CRAUN, C. F.; HUBBS, S. A.; FROST, F.; CALDERON, R. L.; VIA, S. H.:
Waterborne outbreaks of cryptosporidiosis.
AWWA Journal 90 (1998), Nr. 9, pp. 81-91

CRAUN, G. F.:
Waterborne outbreaks in Giardiasis. In: JAKUBOWSKI, W. und HOFF, J. C. (Eds.): *Waterborne transmission of Giardiasis*. Ohio: U.S. Environmental Protection Agency, 1979, pp. 127-149

DAVIS, R. H.; LEIGHTON, D. T.:
Shear-induced transport of a particle layer along a porous wall.
Chem. Eng. Sci. 42 (1987), Nr. 2, pp. 275-281

DIN ISO 9276-1 AND 9276-2:
Darstellung der Ergebnisse von Partikelgrößenanalysen;
Teil 1: Grafische Darstellung;
Teil 2: Berechnung von mittleren Partikelgrößen/-durchmessern und Momenten aus Partikelgrößenverteilungen. In: DEUTSCHES INSTITUT FÜR NORMUNG E.V (Ed.): *DIN ISO 9276-1 und 2*. Bd. 9276-1. Berlin: Beuth Verlag, 2004

DO-QUANG, Z.; COCKX, A.; LAINÉ, J.-M.; ROUSTAN, M.:
Applying CFD modelling to enhance water treatment. *1st World Water Congress of the International Water Association (IWA) in Paris, Conference Preprint, Drinking Water Treatment*. Bd. Book 2. Paris:, 2000, pp. 50-55

DREW, D. A.; SCHONBERG, J. A.; BELFORT, G.:
Lateral inertial migration of small sphere in fast laminar flow through a membrane duct.
Chem. Eng. Sci. 46 (1991), Nr. 12, pp. 3219-3224

DVGW-ARBEITSBLATT W 218:
Flockung in der Wasseraufbereitung - Flockungstestverfahren. In: DVGW DEUTSCHE VEREINIGUNG DES GAS- UND WASSERFACHES E.V. (Ed.): *DVGW Regelwerk; Technische Mitteilung; Arbeitsblatt W 218*. Bd. W 218. Bonn:, 1997. - ISSN 0176 - ISSN 0176-3490

ECKSTEIN, E. C.; BAILEY, D. G.; SHAPIRO, A. H.:
Self-diffusion of particles in shear flow of a suspension.
J. Fluid Mech. 79 (1977), pp. 191-208

EINSTEIN, A.:
Über die von der molekularkinetischen Theorie der Wärme geforderte Bewegung von in ruhenden Flüssigkeiten suspendierten Teilchen.
Ann. d. Phys. 323 (1905), Nr. 4 / 18, pp. 549-560

ELIMELECH, M.; GREGORY, J.; JIA, X.; WILLIAMS, R.:
Particle Deposition & Aggregation - Measurement, Modelling and Simulation. *Particle Deposition & Aggregation*. Oxford:, 1995. - 0 7506 0743 2

FACHGRUPPE WASSERCHEMIE IN DER GESELLSCHAFT DEUTSCHER CHEMIKER:
Anwendung statistischer Methoden zur Beurteilung von Analysenergebnissen in der Wasseranalytik. In: ARBEITSGRUPPE "STATISTIK IN DER WASSERANALYTIK" IN DER FACHGRUPPE WASSERCHEMIE, Fachgruppe Wasserchemie in der Gesellschaft Deutscher Chemiker in Gemeinschaft mit dem Normenausschuss Wasserwesen im DIN Deutsches Institut für Normung (Ed.): *Deutsche Einheitsverfahren zur Wasser-, Abwasser- und Schlammuntersuchung*. Bd. 1. Weinheim: VCH, 1997. - 3-527-28872-4

FAN, L.; HARRIS, J. L.; RODDICK, F.; BOOKER, N. A.:
Influence of the characteristics of natural organic matter on the fouling of microfiltration membranes.
Water Res. 35 (2001), Nr. 18, pp. 4455-4463

FANE, A. G.:
Ultrafiltration of suspensions.
J. Membr. Sci. 20 (1984), Nr. 3, pp. 249-259

FANE, A. G.; FELL, C. J. D.; NOR, M. T.:
Ultrafiltration of colloidal suspensions and macromolecular solutions in an unstirred batch cell.
Ind. Eng. Chem. Fundam. 73 (1982), C1

References

FENG, J; HU, H. H.; JOSEPH, D. D.:
Direct simulation of initial value problems for the motion of solid bodies in a Newtownian fluid. Part 2. Couette and Poiseuille flows.
J. Fluid Mech. 277 (1994), pp. 271-301

FINLAYSON, B. A.:
Introduction to chemical engineering computing Hoboken: Wiley, 2006. - 978-0-471-74062-9

FUTSELAAR, H.; WEIJENBERG, D. C.:
System design for large-scale ultrafiltration applications.
Desalination 119 (1998), pp. 217-224

FUTSELAAR, H.; WILDEBOER, E.; WEIJENBERG, D. C.:
The AquaFlex System; New developments in module and system design for water treatment. In: MELIN, T.; RAUTENBACH, R. und DOHMANN, M. (Eds.): *Membrantechnik in der öffentlichen Wasseraufbereitung und Abwasserbehandlung - Bemessung, Umsetzung, Kosten; Begleitbuch zur 2. Aachener Tagung Siedlungswasserwirtschaft und Verfahrenstechnik, 15.09.98 - 16.09.98*. Melin, T.; Rautenbach, Aachen:, 1998

GIMBEL, R.:
Abscheidung von Trübstoffen aus Flüssigkeiten in Tiefenfiltern Habilitationsschrift. In: BEREICH WASSERCHEMIE AM ENGLER-BUNTE-INSTITUT DER UNIVERSITÄT KARLSRUHE (Ed.): *Veröffentlichungen des Bereichs und des Lehrstuhls für Wasserchemie und der DVGW-Forschungsstelle am Engler-Bunte-Institut der Universität Karlsruhe*. Bd. 25. Frankfurt: ZfGW-Verlag, 1984. - 3-922671-10-1

GIMBEL, R.:
The dynamic particle adhesion process and its effect on particle aggregation.
Aqua 38 (1989), pp. 156-164

GIMBEL, R.; HAGMEYER, G.:
Anforderungen an die Membrantechnik in der Trinkwasseraufbereitung. In: MELIN, T. und Dohmann, M. (Ed.): *Membrantechnik in der Wasseraufbereitung und Abwasserbehandlung -Perspektiven, Neuentwicklungen und Betriebserfahrungen im In- und Ausland- 5. Aachener Tagung Siedlungswasserwirtschaft und Verfahrenstechnik*. Bd. 5. Aachen:, 2003. - 3-921955-28-9, pp. Ü3-1 - Ü3-26

GIMBEL, R.; PANGLISCH, S.; HAGMEYER, G.:
Abschlußbericht für das Forschungsvorhaben 02WT9411/8 -Ultrafiltration zur Abtrennung von Algen und algenbürtigen Substanzen mit verschiedenen Vorbehandlungen In: GERHARD MERCATOR UNIVERSITÄT -GH DUISBURG (Ed.) Duisburg: Eigenverlag, 1996

GITIS, V.; LERCH, A.; GIMBEL, R.:
Retention of humic acid by ultrafiltration with polyaluminium coagulant.
J. Water Supp. Res. Technol. - AQUA 54 (2005), Nr. 4, pp. 213-223

GOLDMAN, A. J.; COX, R. G.; BRENNER, H.:
Slow viscous motion of a sphere parallel to a plane wall-II. Couette flow.
Chem. Eng. Sci. 22 (1967), pp. 653-660

GOLDMAN, A. J.; COX, R. G.; BRENNER, H.:
Slow viscous motion of a sphere parallel to a plane wall-I. Motion through a quiescent fluid.
Chem. Eng. Sci. 22 (1967), pp. 637-651

GOREN, S. L.:
The hydrodynamic force resisting the approach of a sphere to a plane permeable wall.
J. Colloid Interface Sci. 69 (1979), Nr. 1, pp. 78-85

GOREN, S. L.; O'NEILL, M. E.:
On the hydrodynamic resistance to a particle of a dilute suspension when in the neighbourhood of a large obstacle.
Chem. Eng. Sci. 26 (1971), pp. 325-338

GRAY, S. R.; RITCHIE, C. B.; BOLTO, B. A.:
Effect of fractionated NOM on low-pressure membrane flux declines.
Water Sci. Technol.: Water Supply 4 (2004), Nr. 4, pp. 189-196

GREEN, G.; BELFORT, G.:
Fouling of ultrafiltration membranes: Lateral migration and the particle Trajectory model.
Desalination 35 (1980), pp. 129-147

GREGORY, J.:
Interfacial Phenomena. In: IVES, K. (Ed.): *The Scientific Basis of Filtration*. Leyden: Noordhoff, 1975, pp. 53-90

GREGORY, J.:
Approximate expressions for retarded van der Waals interaction.
J. Colloid Interface Sci. 83 (1981), Nr. 1, pp. 138-145

GREGORY, J.:
Fundamentals of flocculation.
J. Crit. Rev. Environ. Control 19 (1989), pp. 185 230

GRUBBS, F.; BECK, G.:
Extension of Sample Sizes and Percentage Points for Significance Tests of Outlying Observations.
Technometrics 14 (1972), Nr. 4, pp. 847-853

GRUBBS, F. E.:
Sample criteria for testing outlying observations.
Ann. Math. Statist. 21 (1950), Nr. 1, pp. 27-58

References

GRUBBS, F. E.:
Procedures for detecting outlying observations in samples.
Technometrics 11 (1969), Nr. 1, pp. 1-21

GUIGUI, C.; ROUCH, J. C.; DURAND-BOURLIER, L.; BONNELYE, V.; APTEL, P.:
Impact of coagulation conditions on the in-line coagulation/UF process for drinking water production.
Desalination 147 (2002), pp. 95-100

HAGMEYER, G.; GIMBEL, R.; KIEPKE, O.; DAUTZENBERG, W.:
Flocculation/ Ultrafiltration for drinking water treatment of reservoir water. In: AMERICAN WATER WORKS ASSOCIATION (Ed.): *Proceedings of the AWWA Membrane Technology Conference, San Antonio*. Bd. CD-ROM. San Antonio: Eigenverlag, 2001. - 1-58321-096-2

HAGMEYER, G.; GIMBEL, G.; DAUTZENBERG, W.:
Requirements for flocculation followed by ultrafiltration for direct treatment of reservoir water. In: AMERICAN WATER WORKS ASSOCIATION (Ed.): *Membrane Technology Conference Proceedings, Atlanta, 02. - 05.03.03*. Bd. CD-ROM. Atlanta: Eigenverlag, 2003. - 1-58321-275-2

HÄNEL, D.:
In: INSTITUT FÜR VERBRENNUNG UND GASDYNAMIK (Ed.): *Strömungslehre I - Eine Einführung in die Mechanik der Fluide*. Duisburg: Eigenverlag, 1992

HARMANT, P.; AIMAR, P.:
Coagulation of colloids retained by porous walls.
AIChE Journal 42 (1996), Nr. 12, pp. 3523-3532

HEIJMAN, S. G. J.; VANTIEGHEM, M.; RAKTOEA, S.; VERBERK, J. Q. J. C.; VAN DIJK, J. C.:
Blocking of capillaries as fouling mechanism for dead-end operated ultrafiltration membranes.
J. Membr. Sci. 287 (2007), pp. 119-125

HO, B. P.; LEAL, L. G.:
Inertial migration of rigid spheres in two-dimensional unidirectional flows.
J. Fluid Mech. 65 (1974), Nr. part 2, pp. 365-400

HOEK, E. M. V.; AGARWAL, G. K.:
Extended DLVO interactions between spherical particles and rough surfaces.
Colloid Interface Sci. 298 (2006), pp. 50-58

HOEK, E. M. V.; ELIMELECH, M.:
Cake-enhanced concentration polarization: A new fouling mechanism for salt-rejecting membranes.
Environ. Sci. Technol. 37 (2003), pp. 5581-5588

HOWE, K. J.:
Effect of coagulation pretreatment on membrane filtration performance. *Dissertation thesis at the university of Illinois at Urbana-Champaign*. Urbana:, 2001

HOWE, K. J.; CLARK, M. M.:
Fouling of microfiltration and ultrafiltration membranes by natural organic matter. *Environ. Sci. Technol.* 36 (2002), pp. 3571-3576

HOWE, K. J.; ISHIDA, K. P.; CLARK, M. M.:
Use of ATR/FTIR spectrometry to study fouling of microfiltration membranes by natural waters.
Desalination 147 (2002), pp. 251-255

HUANG, P. Y; FENG, J; HU, H. H.; JOSEPH, D. D.:
Direct simulation of the motion of solid particles in Couette and Poiseuille flows of viscoelastic fluids.
J. Fluid Mech. 343 (1997), pp. 73-94

HUCK, P. M.; PAYMENT, P.; HRUDEY, S. E.; ANDERSON, W. B.:
A severe waterborne disease outbreak in Walkerton, Ontario: Issues relating to treatment and distribution. In: AMERICAN WATER WORKS ASSOCIATION (Ed.): *Conference Proceedings AWWA Water Quality Technology Conference, November 11 - 15, 2001, Nashville, Tennessee*. Bd. CD-ROM. Nashville: Eigenverlag, 2001, p. M8-2

HUNG, C.-C.; TIEN, C.:
Effect of particle deposition on the reduction of water flux in reverse osmosis.
Desalination 18 (1976), pp. 173-187

IVES, K. J.:
Rate theories. In: IVES, K.J. (Ed.): *The scientific basis of flocculation*. Bd. E No. 27. 1. Edition Netherlands: Sijthoff & Noordhoff International Publishers B.V., 1978. - 9028607587, pp. 37-61

JANSON, A.; O'TOOLE, G.; LEE, M.-F.:
The 273,000 m^3/d immersed membrane system at Chestnut Avenue Water Works: its novel design and first year of operation.
J. Water Supp. Res. Technol. - AQUA 6 (2006), Nr. 2, pp. 19-24

JUNG, C.-W.; SON, H.-J.; KANG, L. S.:
Effects of membrane material and pretreatment coagulation on membrane fouling: fouling mechanism and NOM removal.
Desalination 197 (2006), pp. 154-164

KABSCH-KORBUTOWICZ, M.:
Impact of pre-coagulation on ultrafiltration process performance.
Desalination 194 (2006), pp. 232-238

References

KARNIS, A.; GOLDSMITH, H. L.; MASON, S. G.:
The flow of supsensions through tubes
V. Inertial effects.
Can. J. Chem. Eng. (1966), Nr. August, pp. 181-193

KENNEDY, M. D.; ZHIZHONG, L.; FEBRINA, E.; VAN HOOF, S.; SCHIPPERS, J.:
Affects of coagulation on filtration mechanisms in dead-end ultrafiltration. In: IWW RHEINISCH-WESTFÄLISCHES INSTITUT FÜR WASSERFORSCHUNG GGMBH (Ed.): *Berichte aus dem IWW Rheinisch-Westfälisches Institut für Wasserforschung gGmbH*. Bd. 37a. Mülheim an der Ruhr: Eigenverlag, 2002. - 0941 - 0961, pp. 185-210

KIM, A. S.; HOEK, E. M. V.:
Cake structure in dead-end membrane filtration: Monte Carlo Simulation.
Environ. Eng. Sci. 19 (2002), Nr. 6

KOLLBACH, J.-S.; HAESKE, J.; SCHILLING, S.:
Planerische Aspekte bei Membrananlagen zur Wasser- und Abwasseraufbereitung. In: MELIN, T.; RAUTENBACH, R. und DOHMANN, M. (Eds.): *Möglichkeiten und Perspektiven der Membrantechnik bei der kommunalen Abwasserbehandlung und Trinkwasseraufbereitung; Begleitbuch zur 1. Aachener Tagung Siedlungswasserwirtschaft und Verfahrenstechnik, 30.06.97 - 01.07.97*. Aachen:, 1997

KOUTSOU, C. P.; YIANTSIOS, S. G.; KARABELAS, A. J.:
Direct numerical simulation of flow in spacer-filled channels: Effect of spacer geometrical characteristics.
J. Membr. Sci. 291 (2007), pp. 53-69

KROMKAMP, J.; BASTIAANSE, A.; SWARTS, J.; BRANS G.; VAN DER SMAN, R. G. M.; BOOM, R. M.:
A suspension flow model for hydrodynamics and concentration polarisation in crossflow microfiltration.
J. Membr. Sci. 253 (2005), pp. 67-79

LAHOUSSINE-TURCAUD, V.; WIESNER, M. R.; BOTTERO, J.-Y.:
Fouling in tangential-flow ultrafiltration: The effect of colloid size and coagulation pretreatment.
J. Membr. Sci. 52 (1990), pp. 173-190

LAHOUSSINE-TURCAUD, V.; WIESNER, M. R.; BOTTERO, J.-Y.; MALLEVIALLE, J.:
Coagulation-Flocculation with aluminium salts: Influence on the filtration efficacy with microporous membranes.
Water Res. 26 (1992), Nr. 5, pp. 695-702

LEE, J.-D.; LEE, S.-H.; JO, M.-H.; PARK, P.-K.; LEE, C.-H.; KWAK, J.-W.:
Effect of coagulation conditions on membrane filtration characteristics in coagulation-microfiltration process for water treatment.
Environ. Sci. Technol. 34 (2000), pp. 3780-3788

LEE, S. A.; FANE, A. G.; AMAL, R.; WAITE, T. D.:
The effect of floc size and structure on specific cake resistance and compressibility in dead-end microfiltration.
Sep. Sci. Technol. 38 (2003), Nr. 4, pp. 869-887

LEEUWEN, van, J.; CHOW, C.; FABRIS, R.; WITHERS, N.; PAGE, D.; DRIKAS, M.:
Application of a fractionation technique for the better understanding of the removal of NOM by alum coagulation.
Water Sci. Technol.: Water Supply 2 (2002), Nr. 5 - 6, pp. 427-433

LEIGHTON, D.; ACRIVOS, A.:
Viscous resuspension.
Chem. Eng. Sci. 41 (1986), Nr. 6, pp. 1377-1384

LEIGHTON, D.; ACRIVOS, A.:
The shear-induced migration of particles in concentrated suspensions .
J. Fluid Mech. 181 (1987), pp. 415-439

LERCH, A.; PANGLISCH, S.; HAGMEYER, G.; SCHÖN, M.; FEHN, J.; GIMBEL, R.:
Direct Potable Water Treatment of River Waters by Flocculation/Ultrafiltration. In: INTERNATIONAL WATER ASSOCIATION (Ed.): *Proceedings of the 3rd IWA World Water Congress, Melbourne, Australia, 7.-12.04.02*. Bd. CD-ROM. Melbourne, 2002

LERCH, A.; HAGMEYER, G.; GIMBEL, R.; FEHN, J.:
A comparison of laboratory and pilot plant experiments on the combination of flocculation / ultrafiltration for direct potable water treatment of river water.
Water Sci. Technol.: Water Supply 3 (2003), Nr. 5-6, pp. 345-352

LERCH, A.; PANGLISCH, S.; NAHRSTEDT, A.; GIMBEL, R.:
The influence of temperature on size and structure of flocs in the hybrid process coagulation / ultrafiltration. In*: Chemical Water and Wastewater Treatment; Proceedings of the 11th Gothenburg Symposium 2004, Orlando, Florida, USA*, H.H. HAHN; E. HOFFMANN; H. ODEGAARD (Eds.), 1. Edition, Vol. 1, London: IWA Publishing, 2004, pp. 265-273 - ISBN/ISSN 1 84339 068 X

LERCH, A.; PANGLISCH, S.; GIMBEL, R.:
Research experiences in direct potable water treatment using coagulation/ultrafiltration.
Water Sci. Technol. 51 (2005), Nr. 6-7, pp. 221-229

References

LERCH, A.; LOI-BRÜGGER, A.; GIMBEL, R.:
Teilprojekt C1: Ultra- und Mikrofiltration zur direkten und vorbehandlungsminimierten Aufbereitung von stark belasteten Rohwässern
Exportorientierte F&E auf dem Gebiet der Wasserver- und -entsorgung Teil I: Trinkwasser
Schlussbericht zum Projektverbund unter Förderung des BMBF 02WT0282. In: DVGW - TECHNOLOGIEZENTRUM WASSER KARLSRUHE (Ed.): *Exportorientierte Forschung und Entwicklung auf dem Gebiet der Wasserver- und -entsorgung Teil I: Trinkwasser*. Bd. 2 Leitfaden. Karlsruhe: Eigenverlag, 2005. - 3-00-015478-7

LIU, S.:
Particle dispersion for suspension flow.
Chem. Eng. Sci. 54 (1999), Nr. 7, pp. 873-891

LIU, S.; MASLIYAH, J. H.:
Rheology of suspensions. In: SCHRAMM, L. L. (Ed.): *Suspensions: fundamentals and applications in the petroleum industry; Advances in chemistry series*. Bd. 251. Washington DC : American Chemical Society, 1996. - 0-8412-3136-2, pp. 107-176

LYKLEMA, J.:
Fundamentals. *Fundamentals of interface and colloid science*. Bd. 1. London: Academic Press Ltd., 1991. - 0-12-460525-7

MARSELINA, Y.; LE-CLECH, P.; STUETZ, R. M.; CHEN, V.:
Detailed characterization of fouling deposition and removal on hollow fibre membrane by direct observation technique In: IWA SPECIALISED CONFERENCE ON MEMBRANES, Conference Proceedings (Ed.) Bd. CD-ROM. Harrogate: IWA, 2007

MASLIYAH, J. H.; NEALE, G.; MALYSA, K.; VAN DEN VEN, T. G. M.:
Creeping flow over a composite sphere: Solid core with porous shell.
Chem. Eng. Sci. 42 (1987), Nr. 2, pp. 245-253

MATAS, J. P.; MORRIS, J. F.; GUAZELLI, E.:
Lateral forces on a sphere.
Oil & Gas Sci. Tech. 59 (2004), Nr. 1, pp. 59-70

MELIN, T.; RAUTENBACH, R.:
Membranverfahren: Grundlagen der Modul- und Anlagenauslegung.
Membranverfahren: Grundlagen der Modul- und Anlagenauslegung. 2. Edition Berlin Heidelberg: Springer- Verlag, 2004. - 3-540-61573-3

MULDER, M.:
Basic principles of membrane technology. *Basic principles of membrane technology*. Dordrecht: Kluwer Academic Publishers, 1991. - 0-7923-0978-2

MULDER, T.:
Untersuchungen zur Entwicklung permeabler Hohlkörperkollektoren zur Trübstoffabscheidung aus wäßrigen Lösungen in Schüttbettfiltern. *Dissertation, Universität - GH - Duisburg*. Duisburg:, 1990

NAHRSTEDT, A.:
Zum dynamischen Filtrationsverhalten von Schüttschichten aus Permeablen Synthetischen Kollektoren bei der Trübstoffabscheidung aus wäßrigen Suspensionen Dissertation, Universität - GH - Duisburg. In: IWW RHEINISCH-WESTFÄLISCHES INSTITUT FÜR WASSERFORSCHUNG GEMEINNÜTZIGE GMBH (Ed.): *Berichte aus dem IWW Rheinisch-Westfälischen Institut für Wasserforschung gemeinnützige GmbH*. Bd. 25. Mülheim a.d.R.: Eigenverlag, 1999. - 0941-0961

NGUYEN, M. T.:
Deckschichtbildung in Kapillarmembranen bei der Querstrom-Mikrofiltration und ihre Beeinflussung durch polymere Flockungsmittel. *Dissertation an der TU Dresden*. Dresden:, 2004

NGUYEN, M.-T.; RIPPERGER, S.:
Investigation on the effect of flocculants on the filtration behaviour in microfiltration of fine particles.
Desalination 147 (2002), pp. 37-42

OSEEN, C. W.:
Über die Stokes'sche Formel und über die verwandte Aufgabe in der Hydrodynamik. *Arkiv. Mat. Astron.* 6 (1910), pp. 75

OTIS, J. R.; ALTENA, F. W.; MAHAR, J. T.; BELFORT, G.:
Measurements of single spherical particle trajectories with lateral migration in a slit with one porous wall under laminar flow conditions.
Exp. Fluids 4 (1986), Nr. 1, pp. 1-10

PANGLISCH, S.:
Zur Bildung und Vermeidung schwer entfernbarer Partikelablagerungen in Kapillarmembranen bei der Dead-End Filtration
Dissertation, Gerhard Mercartor Universität Duisburg. In: IWW RHEINISCH-WESTFÄLISCHES INSTITUT FÜR WASSERFORSCHUNG GGMBH (Ed.): *Berichte aus dem IWW Rheinisch-Westfälischen Institut für Wasserforschung gemeinnützige GmbH*. Bd. 34. Mülheim an der Ruhr: Eigenverlag, 2001. - 0941-0961

PANGLISCH, S.; KIEPKE, O.; DAUTZENBERG, W.; GIMBEL, R.:
Optimisation of operation and cleaning of membranes - Results on ultra- and microfiltration pilot plant investigation to treat reservoir water.
Desalination 113 (1997), pp. 247-249

PANGLISCH, S.; BRÜGGER, A.; GIMBEL, R.; LERCH, A.:
Entwicklungen im Bereich der Membranfiltration zur Trinkwasserproduktion.
Energie Wasser-praxis. 55 (2004), Nr. 10, pp. 36-43

PARK, P. K.; LEE, S. H.; LEE, C. H.:
Permeability of cake layers formed by chemical flocs in coagulation-membrane processes. In: SEOUL NATIONAL UNIVERSITY AND IWA (Ed.): *Proceedings of the IWA Specialty Conference; Water Environment - Membrane Technology [WEMT]*. Bd. CD-ROM. Seoul: Eigenverlag, 2004

PASCHEDAG, A. R.:
In: WILEY-VCH VERLAG GMBH & CO.KGAA (Ed.): *CFD in der Verfahrenstechnik - Allgemeine Grundlagen und mehrphasige Anwendungen*., 2004. - 3-527-30994-2

PERRY, R. H.; GREEN, D. W.; MALONEY, J. O.:
In: PERRY, R. H.; GREEN, D. W. und MALONEY, J. O. (Eds.): *Perry's Chemical Engineers' Handbook*. 6. Edition New York: McGraw-Hill Companies, Inc., 1984. - 0070494797

PIKKARAINEN, A. T.; JUDD, S. J.; JOKELA, J.; GILLBERG, L.:
Pre-coagulation for microfiltration of an upland surface water.
Water Res. 38 (2004), pp. 455-465

PORTER, M. C.:
Concentration polarization with membrane ultrafiltration.
Ind. Eng. Chem. Process Res. Dev. 11 (1972), Nr. 3, pp. 234-248

PORTER, M. C.:
Ultrafiltration of colloidal suspensions.
AIChE Symposium Series 68 (1972), Nr. 120, pp. 21-30

POSPÍSIL, P.; WAKEMAN, R. J.; HODGSON, I. O. A.; MIKULÁSEK, P.:
Shear stress-based modelling of steady state permeate flux in microfiltration enhanced by two-phase flows.
Chem. Eng. J. 97 (2004), Nr. 2-3, pp. 257-263

RAHIMI, M.; MADAENI, S. S.; ABBASI, K.:
CFD modeling of permeate flux in cross-flow microfiltration membrane.
J. Membr. Sci. 255 (2005), pp. 23-31

RANADE, V. V.; KUMAR, A.:
Fluid dynamics of spacer filled rectangular and curvilinear channels.
J. Membr. Sci. 271 (2006), pp. 1-15

SCHÄFER, A. I.:
Natural organics removal using membranes. *Dissertation at the UNESCO Centre for Membrane Science and Technology*. Sydney: 1999. - 0-7337-0652-1

SCHLICHTING, H.:
Boundary layer theory. *Boundary layer theory*. New York: McGraw-Hill Book Co. Inc., 1955

SCHÜTZ, S.; PIESCHE, M.; GORBACH, G.; SCHILLING, M.; SEYFERT, C.; KOPF, P.; DEUSCHLE, T.; SAUTTER, N.; POPP E.; WARTH, T.:
CFD in der mechanischen Trenntechnik
Chem.-Ing.-Tech., 79 (2007), No. 11, pp. 1777-1796

SCHWINGE, J.; NEAL, P. R.; WILEY, D. E.; FLETCHER, D. F.; FANE, A. G.:
Spiral wound modules and spacers
Review and analysis.
J. Membr. Sci. 242 (2004), pp. 129-153

SEARS, K; ALLEMAN, J. E.; BARNARD, J. L.; OLESZKIEWICZ, J. A.:
Density and activity characterization of activated sludge flocs.
J. Environ. Eng. 132 (2006), Nr. 10, pp. 1235-1242

SEGRÉ, G.; SILBERBERG, A.:
Behaviour of macroscopic rigid spheres in Poiseuille flow
Part I: Determination of local concentration by statistical analysis of particle passages through crossed light beams .
J. Fluid Mech. 14 (1962), pp. 115-135

SEGRÉ, G.; SILBERBERG, A.:
Behaviour of macroscopic rigid spheres in Poiseuille flow
Part II: Experimental results and interpretation.
J. Fluid Mech. 14 (1962), pp. 136-157

SMITH, S. R.:
Hydrodynamcis and mass transfer in slug enhanced ultrafiltration using hollow fibre membranes. *Dissertation at the Keble College, University of Oxford*. Oxford:, 2003

SOFFER, Y.; BEN AIM, R.; ADIN, A.:
Membrane fouling and selectivity mechanisms in effluent ultrafiltration coupled with flocculation.
Water Sci. Technol. 51 (2005), Nr. 6 - 7, pp. 123-134

SONG, L.:
Flux decline in crossflow microfiltration and ultrafiltration: mechanisms and modeling of membrane fouling.
J. Membr. Sci. 139 (1998), pp. 183-200

SONG, L.; ELIMELECH, M.:
Particle deposition onto a permeable surface in laminar flow.
J. Colloid Interface Sci. 173 (1995), pp. 165-180

STIRLING, R.; ARAMINI, J.; ELLIS, A.; LIM, G.; MEYERS, R.; FLEURY, M.; WERKER, D.:
Waterborne Cryptosporidiosis Outbreak
North Battleford, Saskatchewan, Spring, 2001 In: HEALTH CANADA (Ed.) Eigenverlag, 2001

References

STRENGE, K.:
Structure formation in disperse systems. In: DOBIÁŠ, Bohuslav (Ed.): *Coagulation and Flocculation - Theory and Applications*. Bd. 47. New York: Dekker, 1993. - 0-8247-8797-8, pp. 265-320

STUMM, W.; MORGAN, J. J.:
In: SCHNOOR, J. L. und ZEHNDER, A. (Eds.): *Aquatic chemistry*
Chemical equilibria and rates in natural waters. 3. Edition New York: John Wiley & Sons, Inc., 1996. - 0-471-51184-6

SUBRAMANIA, A.; KIMB, S.; HOEK, E. M. V.:
Pressure, flow and concentration profiles in open and spacer-filled membrane channels.
J. Membr. Sci. 277 (2006), pp. 7-17

UHL, W.:
Einfluss von Schüttungsmaterial und Prozessparametern auf die Leistung von Bioreaktoren bei der Trinkwasseraufbereitung
Dissertation, Gerhard Mercartor Universität Duisburg. In: IWW RHEINISCH-WESTFÄLISCHES INSTITUT FÜR WASSERFORSCHUNG GGMBH (Ed.): *Berichte aus dem IWW Rheinisch-Westfälischen Institut für Wasserforschung gemeinnützige GmbH*. Bd. 31. Mülheim a.d.R.: Eigenverlag, 2000. - 0941-0961

USEPA:
Membrane Filtration Guidance Manual. In: UNITED STATES ENVIRONMENTAL PROTECTION AGENCY (USEPA) (Ed.): *Membrane Filtration Guidance Manual - Proposal Draft* -. USA: Eigenverlag, 2003. - EPA 815-D-03-008

USEPA - DBPR:
Enhanced coagulation and enhanced precipitative softening guidance manual. In: UNITED STATES ENVIRONMENTAL PROTECTION AGENCY (USEPA) (Ed.): *Stage 1 Disinfactants and Disinfection Byorducts rule (DBPR)*. Eigenverlag, 1999. - EPA 815-R-99-012

VAINSHTEIN, P.; SHAPIRO, M.:
Porous agglomerates in the general linear flow field.
Colloid Interface Sci. (2006), Nr. 298, pp. 183-191

VAN LEEUWEN, J.; DALY, R.; HOLMES, M.:
Modeling the treatment of drinking water to maximize dissolved organic matter removal and minimize disinfection by-product formation.
Desalination 176 (2005), pp. 81-89

VASSEUR, P.; COX, R. G.:
The lateral migration of a spherical particle in two-dimensional shear flows.
J. Fluid Mech. 78 (1976), Nr. 2, pp. 385-413

VEERAPANENI, S.; WIESNER, M.R.:
Hydrodynamics of fractal aggregates with radially varying permeability.
J. Colloid Interface Sci. 177 (1996), Nr. 1, pp. 45-57

VERBERK, J. Q. J. C.:
Application of air in membrane filtration. *Dissertation at the Technical University of Delft*. Delft:, 2005. - 90-9019344-8

VEREIN DEUTSCHER INGENIEURE:
In: VDI-GESELLSCHAFT VERFAHRENSTECHNIK UND CHEMIEINGENIEURWESEN (GVC) (Ed.):
VDI-Wärmeatlas. 5. Edition Berlin: Springer, 1988. - 3184008509

VISSER, J.:
On Hamaker constants: A comparison between Hamaker constants and Lifshitz-Van der Waals constants.
Adv. Coll. Inter. Sci. 3 (1972), pp. 331-363

WIESNER, M. R.; CLARK, M. M.; MALLEVIALLE, J.:
Membrane filtration of coagulated suspensions.
J. Environ. Eng. 115 (1989), Nr. 1, pp. 20-40

WILEY, D. E.; FLETCHER, D. F.:
Computational fluid dynamics modelling of flow and permeation for pressure-driven membrane processes.
Desalination 145 (2002), pp. 183-186

WILEY, D. E.; FLETCHER, D. F.:
Techniques for computational fluid dynamics modelling of flow in membrane channels.
J. Membr. Sci. 211 (2003), pp. 127-137

WONG, S.; HANNA, J. V.; KING, S.; CARROLL, T.; ELDRIDGE, R. J.; DIXON, D. R.; BOLTO, B. A.; HESSE, S.; ABBT-BRAUN, G.; FRIMMEL, F.H.:
Fractionation of natural organic matter in drinking water and characterization by ^{13}C Cross-Polarization Magic-Angle Spinning NMR Spectroscopy and Size Exclusion Chromatography.
Environ. Sci. Technol. 36 (2002), Nr. 16, pp. 3497-3503

YUAN, S. W.; FINKELSTEIN, A. B.:
Laminar pipe flow with injection and suction through a porous wall.
Trans. ASME 78 (1956), pp. 719-724

ZHAO, Y.; SHARP, M. K.:
Finite element analysis of the lift on a slightly deformable and freely rotating and translating cylinder in two-dimensional channel flow.
J. Biomech. Eng. 121 (1999), Nr. 2, pp. 148-152

References

ZHAO, Z.; WANG, Z.; YE, N.; WANG, S.:
A novel N, O-carboxymethyl amphoteric chitosan/poly(ethersulfone) composite MF membrane and its charged characteristics.
Desalination 144 (2002), pp. 35-39

ZULARISAMA, A. W.; ISMAIL, A. F.; SALIM, R.:
Behaviours of natural organic matter in membrane filtration for surface water treatment — a review.
Desalination 194 (2006), pp. 211-231

ZYDNEY, A. L.; COLTON, C. K.:
A concentration polarization model for the filtrate flux in cross-flow microfiltration of particulate suspensions.
Chem. Eng. Commun. 47 (1986), pp. 1-21

Nomenclature

Roman symbols

a	Panglisch parameter	1/m
a_{eff}	effective radius	m
a_F	floc radius	m
a_{F1}	radius of floc 1	m
a_{F2}	radius of floc 2	m
a_{hF}	hydrodynamic floc radius	m
a_P	primary particle radius	m
a_{QP}	quartz particle radius	m
A	phenomenological coefficient	-
A	system area	m²
A_M	membrane area	m²
B	calculation parameter	-
B_0	calculation parameter	-
B_1	calculation parameter	-
c	concentration	mol/m³
c_β	correction function for the effective viscosity of floc suspensions	-
c_j	concentration of species j	mol/m³
c_{mF}	mass concentration of a floc	kg/m³
D	diffusion coefficient	m²/s
D_{BD}	diffusion coefficient used for Brownian diffusion	m²/s
d_C	capillary diameter	m
d_F	mass fractal dimension	-
D_j	diffusion coefficient of species j	m²/s

D_{SiD}	diffusion coefficient used for shear induced diffusion	m²/s
dX	gradient of the driving force X (c, p, T or E)	div.
E	chemical or electro-chemical potential	J/mol
f	correction function for forces	-
$\vec{F}$	external force vector	N
$F_{BD,r}$	acting force due to Brownian diffusion	N
$\vec{F}_D$	drag force vector	N
$F_{DL,r}$	acting force due to electrical double layer forces	N
f_i	calculation function	-
f	dimensionless inertia induced velocity	-
$F_{SiD,r}$	acting force due to shear induced diffusion	N
$F_{vdW,r}$	acting force due to London-van der Waals forces	N
F_z	force component in z-direction	N
F_φ	force component in φ-direction	N
g	correction function for torques	-
g	gravitational acceleration constant	m/s²
g_r	gravitational acceleration constant in radial direction	m/s²
g_z	gravitational acceleration constant in longitudinal direction	m/s²
G	shear velocity gradient	1/s
H_{121}	Hamaker constant between materials 1 across material 2	J
H_{123}	Hamaker constant between material 1 and material 3 across material 2	J
H_i	Hamaker constant of material i	J
J	flux	m³/m²/s
J_W	water flux	m³/m²/s
k*	dimensionless floc radius	-

k_F	floc permeability coefficient	m²
k_{FL}	fouling layer permeability coefficient	m²
k_M	membrane permeability coefficient	m²
$\vec{K}$	viscous boundary force	N
l_C	capillary length	m
L_P	permeability coefficient	kg/m²/bar/s
l_{su}	start up length	m
n	number concentration of ions per unit volume	No/m³
$\vec{n}$	outward normal vector on a boundary	-
$\vec{N}_i$	mass concentration flux vector of species i=1, 2	m³/m²/s
N_0	imposed mass concentration flux at boundary	m³/m²/s
P	permeability	m³/m²/s/bar
P	Safety	-
P	pressure	bar
p_0	pressure at boundary	bar
$p_{Filtrate}$	filtrate or back pressure	bar
p_{in}	inlet pressure	bar
P_M	membrane permeability	m³/m²/s/bar
p_{out}	outlet pressure	bar
r	radial distance coordinate	m
r_C	capillary radius	m
R	resistance	1/m
R_{CP}	concentration polarisation resistance	1/m
R_{FL}	fouling layer resistance	1/m
R_M	membrane resistance	1/m
R_j	reaction term of species j	mol/m³/s

R_{Tot}	total resistance	1/m
t	time	s
$\vec{t}$	tangential vector on a boundary	-
T	temperature	°C or K
T	Confidence interval	div.
TMP	transmembrane pressure	bar
$\vec{T}_B$	total boundary force	N
u	fluid velocity component in r-direction	m/s
u_{3D}	3D fluid velocity component in x-direction	m/s
U_{3D}	3D fluid velocity magnitude	m/s
u_0	imposed fluid velocity component in r-direction at boundary	m/s
$\vec{u}$	fluid velocity vector	m/s
u_{BD}	lateral velocity	m/s
u_F	floc velocity component in r-direction	m/s
$\vec{u}_F$	floc velocity vector	m/s
u_φ	fluid velocity component in φ-direction	m/s
$\vec{u}_P$	particle velocity vector	m/s
u_r	fluid velocity component in r-direction	m/s
$\vec{u}_{Slip}$	slip velocity vector	m/s
u_z	fluid velocity component in z-direction	m/s
v	fluid velocity component in z-direction	m/s
v_0	imposed fluid velocity component in z-direction at boundary	m/s
v_{3D}	3D fluid velocity component in y-direction	m/s
$\dot{V}$	volume flow	m^3/s
$\bar{v}$	mean axial fluid velocity at the capillary centre	m/s
v_F	floc velocity component in z-direction	m/s

v_{max}	axial fluid velocity at the capillary centre	m/s
v_S	sedimentation velocity	m/s
w_{3D}	3D fluid velocity component in z-direction	m/s
w_F	floc velocity component in φ-direction	m/s
X	coordinate perpendicular to the transport barrier	m
x	value	-
z	longitudinal distance coordinate	m
z	valency of ion	-

Greek symbols

α	calculation parameter	-
β	Brinkman parameter	-
χ	Debye-Hückel parameter	1/m
δ	finite distance between a floc and a collector	m
δ_{FM}	finite distance between a moving floc (surface) and the membrane wall	m
δ_{FM}^{*}	dimensionless distance between a moving floc (surface) and the membrane wall	-
δ_{FM}^{C}	finite distance between a moving floc (centre) and the membrane wall	m
δ_{FM}^{C*}	dimensionless distance between a moving floc (centre) and the membrane wall	-
δ_S	Stern layer thickness	m
Δ_1	calculation parameter	-
Δ_2	calculation parameter	-
Δc	calculation parameter	-
Δp	pressure difference	bar

Nomenclature

ε_0	electrical permittivity	As/V/m
ε_F	floc porosity	-
ϕ	volume concentration	m³/m³
ϕ_F	floc volume concentration	m³/m³
$\phi_{F,\,max}$	maximum floc volume concentration	m³/m³
ϕ_{max}	maximum volume concentration	m³/m³
Φ	rotation axis	°
γ	calculation parameter	-
$\dot{\gamma}$	local shear velocity	1/s
Γ	calculation parameter used for the surface potential	m
η	dynamic fluid viscosity	kg/m/s
$\eta^{20°C}$	dynamic fluid viscosity at 20°C	kg/m/s
η_{FC}	fluid collection efficiency	-
η_S	dynamic suspension viscosity	kg/m/s
I	identity matrix	m
φ	angular coordinate	-
K	viscous boundary force	N
λ	dimensionless correction factor	-
λ_C	characteristic wavelength of interaction	m
μ_x	expected value	div.
ν	kinematic fluid viscosity	m²/s
ρ	fluid density	kg/m³
ρ_F	floc density	kg/m³
σ	total stress tensor	kg/s²
τ	viscous stress tensor	kg/s²

T_B	total boundary force	N
ω	angular velocity	1/s
Ω_h	homogeneous drag coefficient	-
ξ	friction coefficient	kg/s
Ψ	potential	V
Ψ_G	Galvani potential	V
Ψ_O	surface or Volta potential	V
Ψ_S	Stern potential	V
ζ	Zeta potential	V

Superscripts

*	dimensionless
C	centre
m	motion
r	rotation
t	translation
20°C	variable value at T=20°C

Subscripts

0	initial condition at boundary or t = 0
BD	Brownian diffusion
BS	buoyancy and sedimentation
C	capillary
D	drag
DL	double layer
eff	effective
F	floc

FL	fouling or coating layer
FM	floc membrane
hF	hydrodynamic floc
i=1, 2, 3	indication of species, material or function i
j=1, 2, 3	indication of species, material or function j
LM	lateral migration
M	membrane
max	maximum value
P	primary particle
QP	quartz particle
r	radial direction
S	suspension
SiD	shear induced diffusion
vdW	van der Waals
VM	virtual mass
z	longitudinal direction
Φ	rotation axis of a spherical floc
φ	angular direction

Constants

e	electron charge	$-1{,}6 \cdot 10^{-19}$ As
e	Euler's number	2.71828
g	gravitational acceleration	9.81 m/s²
k_B	Boltzman constant	$1{,}3807 \cdot 10^{-23}$ J/K
k_E	Einstein constant	2.5
k_H	Huggins constant	7.1
N_A	Avogadro constant	$6.0221 \cdot 10^{23}$ 1/mol

δ_0	minimum adhesion distance	$1 \cdot 10^{-9}$ m
ε_r	permittivity (relative electric constant)	78
π	Archimedes constant	3.14159

Dimensionless numbers

Re_C	capillary Reynolds number	-
Re_F	floc Reynolds number	-
Pe	Péclet number	-
Sc	Schmidt number	-

Abbreviations

2D	Two dimensional
3D	Three dimensional
CA	Cellulose Acetate
CEB	Chemical Enhanced Backwash
CFD	Computational Fluid Dynamics
CIP	Clean In Place
DBP	Disinfection By-Product
DOM	Dissolved Organic Matter
FEM	Finite Elements Method
FVM	Finite Volume Method
MF	Microfiltration
NF	Nanofiltration
NOM	Natural Organic Matter
PA	Polyamide
PAN	Polyacrylonitrile
PC	Polycarbonate

PES	Polyethersulfone
PI	Polyimide
PP	Polypropylene
PS	Polysulphone
PTFE	Polytetrafluoroethylene
PVDF	Polyvinylidene fluoride
RO	Reverse Osmosis
TMP	Transmembrane Pressure
TOC	Total Organic Carbon
UF	Ultrafiltration
UV	Ultraviolet

Tables

Figures

Figures

Figures

Figures

Appendix

A.1 Properties of different MF and UF membranes

Table A.1: Properties of different MF and UF membranes (adapted from CHERYAN (1998), MELIN AND RAUTENBACH (2004) and MULDER (1991))

Active layer	Hydrophilicity	Range of pH-value	T_{Max} [°C]	MWCO [kD]	Oxidant tolerance
Organic membranes					
PS	hydrophilic	pH 1 – pH 13	90	1 – 500	Medium – high
PES	hydrophilic	pH 1 – pH 14	95	1 - 300	Medium – high
PAN	hydrophilic	pH 2 – pH 10	45	10 – 400	High
PP	highly hydrophobic	pH 4 – pH 10	60	1 – 500	Low
CA	highly hydrophilic	pH 3 – pH 7	30	1 – 50	High
PI	hydrophilic			1 – 100	
PA	hydrophilic	pH 2 – pH 10	60		Very low
PC	hydrophilic				
PTFE	highly hydrophobic		260	MF size only	High
PVDF	hydrophobic	pH 2 – pH 11	70	50 – 200	High
Inorganic membranes					
Al_2O_3 / TiO_2	hydrophilic	pH 0 – pH 14	350	10 – 300	Very high
ZrO_2	hydrophilic	pH 0 – pH 14	400	10 – 300	Very high

A.2 Flow characteristics

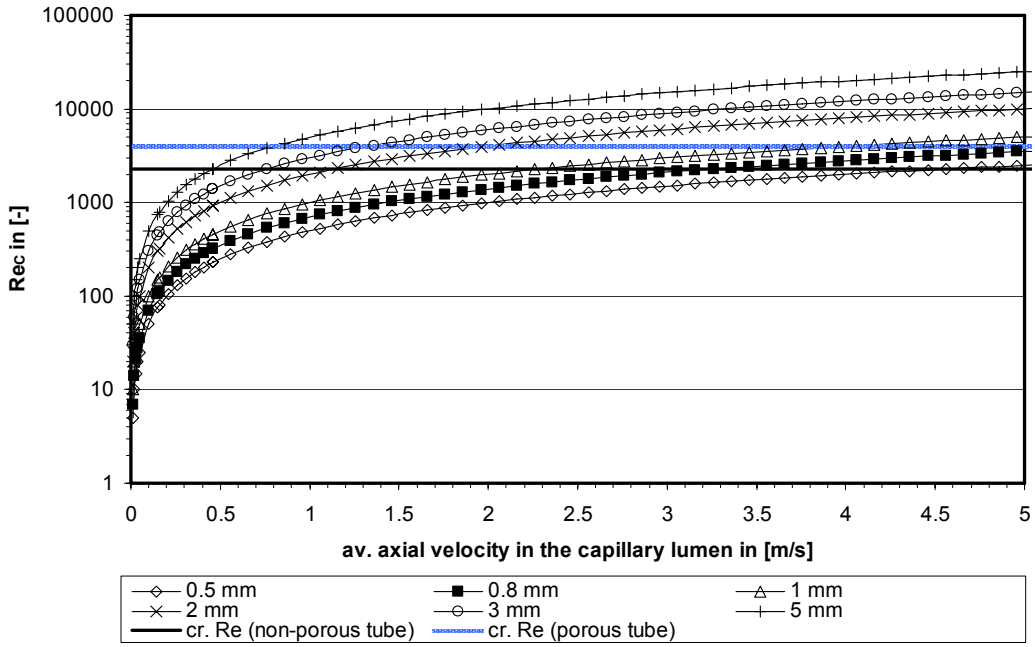

Figure A.1: **Re_C number vs. average axial flow velocity in the capillary lumen at T = 20°C for different capillary diameters and indication of the critical Re for non-porous tube flow and porous tube flow in half logarithmic scale**

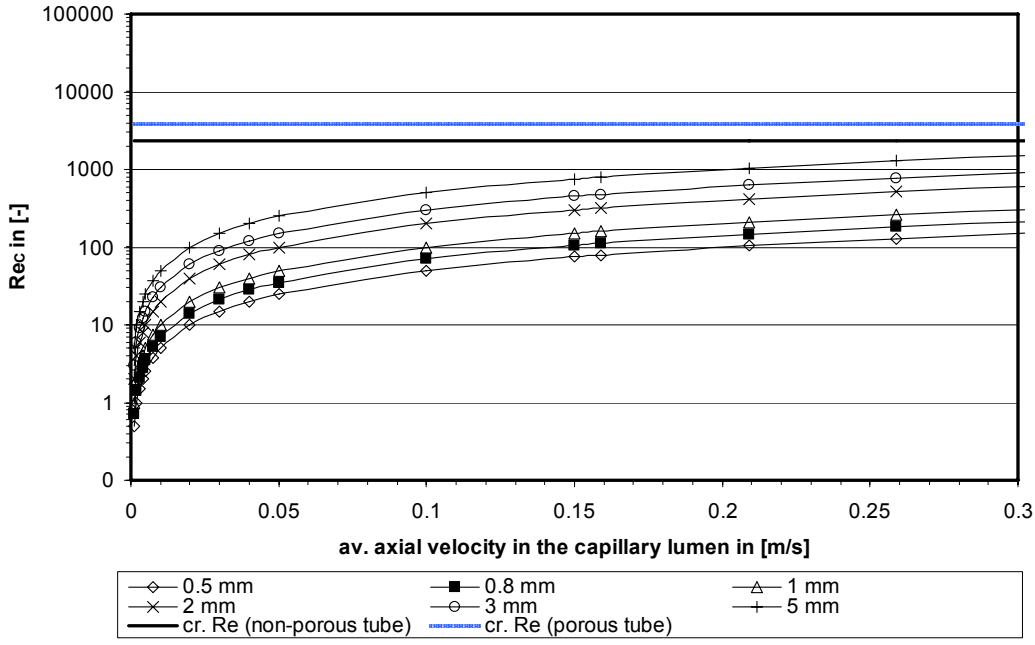

Figure A.2: **Re_C numbers vs. average axial flow velocity, typical for fluxes up to 100 L/m²/h, for different capillary diameters at T = 20°C and indication of the critical Re for non-porous tube flow and porous tube flow in half logarithmic scale**

A.3 The Navier- Stokes equation for an incompressible fluid of constant viscosity in cylindrical coordinates

This is in r-direction:

$$\frac{\partial u_r}{\partial t}+u_r\frac{\partial u_r}{\partial r}+\frac{u_\varphi}{r}\frac{\partial u_r}{\partial \varphi}+u_z\frac{\partial u_r}{\partial z}-\frac{u_\varphi^2}{r}= \qquad \textbf{Equation A.1}$$

$$F_r-\frac{1}{\rho}\frac{\partial p}{\partial r}+\nu\left[\frac{\partial}{r\,\partial r}\left(\frac{r\,\partial u_r}{\partial r}\right)+\frac{\partial^2 u_r}{r^2\partial\varphi^2}+\frac{\partial^2 u_r}{\partial z^2}-\frac{u_r}{r^2}-\frac{2}{r^2}\frac{\partial u_\varphi}{\partial\varphi}\right],$$

in φ-direction:

$$\frac{\partial u_\varphi}{\partial t}+u_r\frac{\partial u_\varphi}{\partial r}+\frac{u_\varphi}{r}\frac{\partial u_\varphi}{\partial \varphi}+u_z\frac{\partial u_\varphi}{\partial z}+\frac{u_r\,u_\varphi}{r}= \qquad \textbf{Equation A.2}$$

$$F_\varphi-\frac{1}{\rho\,r\,\partial\varphi}\frac{\partial p}{}+\nu\left[\frac{\partial}{r\,\partial r}\left(\frac{r\,\partial u_\varphi}{\partial r}\right)+\frac{\partial^2 u_\varphi}{r^2\partial\varphi^2}+\frac{\partial^2 u_\varphi}{\partial z^2}-\frac{u_\varphi}{r^2}+\frac{2}{r^2}\frac{\partial u_r}{\partial\varphi}\right]$$

and in z-direction:

$$\frac{\partial u_z}{\partial t}+u_r\frac{\partial u_z}{\partial r}+\frac{u_\varphi}{r}\frac{\partial u_z}{\partial \varphi}+u_z\frac{\partial u_z}{\partial z}= \qquad \textbf{Equation A.3}$$

$$F_z-\frac{1}{\rho}\frac{\partial p}{\partial z}+\nu\left[\frac{\partial}{r\,\partial r}\left(\frac{r\,\partial u_z}{\partial r}\right)+\frac{\partial^2 u_z}{r^2\partial\varphi^2}+\frac{\partial^2 u_z}{\partial z^2}\right].$$

The equation of continuity can be expressed in cylindrical coordinates as:

$$\frac{\partial u_r}{\partial r}+\frac{u_r}{r}+\frac{\partial u_\varphi}{r\,\partial\varphi}+\frac{\partial u_z}{\partial z}=0\,. \qquad \textbf{Equation A.4}$$

Together with some simplifications due to symmetry of the flow inside the capillary (u_φ , $\frac{\partial}{\partial\varphi}$ and $\frac{\partial^2}{\partial\varphi^2}$ equals zero) the following set of equations can be used for the complete description of the isothermal fluid motion in the capillary:

$$\frac{\partial u_r}{\partial t}+u_r\frac{\partial u_r}{\partial r}+u_z\frac{\partial u_r}{\partial z}=F_r-\frac{1}{\rho}\frac{\partial p}{\partial r}+\nu\left[\frac{\partial}{r\,\partial r}\left(\frac{r\,\partial u_r}{\partial r}\right)+\frac{\partial^2 u_r}{\partial z^2}-\frac{u_r}{r^2}\right], \qquad \textbf{Equation A.5}$$

$$\frac{\partial u_z}{\partial t}+u_r\frac{\partial u_z}{\partial r}+u_z\frac{\partial u_z}{\partial z}=F_z-\frac{1}{\rho}\frac{\partial p}{\partial z}+\nu\left[\frac{\partial}{r\,\partial r}\left(\frac{r\,\partial u_z}{\partial r}\right)+\frac{\partial^2 u_z}{\partial z^2}\right], \qquad \textbf{Equation A.6}$$

$$\frac{\partial u_r}{\partial r}+\frac{u_r}{r}+\frac{\partial u_z}{\partial z}=0. \qquad \textbf{Equation A.7}$$

A.4 Equations for the calculation of the correction factor $c_\beta(\beta)$ to account for the viscosity of porous aggregates suspensions

VAINSHTEIN AND SHAPIRO (2006) presented extended equations for the calculation of the correction function $c_\beta(\beta)$ with:

$$c_\beta(\beta)=\frac{2\cdot\Delta c}{5\cdot\Delta_1}, \qquad \textbf{Equation A.8}$$

$$\beta=\frac{a_F}{\sqrt{k}}, \qquad \textbf{Equation A.9}$$

$$\Delta_1=\left(1+\frac{4}{\beta^2}\right)\cdot\left(\frac{2}{\beta}-\frac{10\cdot f_2(\beta)}{\beta^2\cdot f_1(\beta)}\right)+\frac{12}{\beta^3}\left(1+\frac{10\cdot f_3(\beta)}{\beta^2\cdot f_1(\beta)}\right), \qquad \textbf{Equation A.10}$$

$$\Delta c=\left(\frac{2}{\beta}-\frac{10\cdot f_2(\beta)}{\beta^2\cdot f_1(\beta)}\right)+\frac{3}{\beta}\left(1+\frac{10\cdot f_3(\beta)}{\beta^2\cdot f_1(\beta)}\right), \qquad \textbf{Equation A.11}$$

$$f_1(\beta)=\frac{5}{\beta}\left(\frac{6}{\beta^2}+1\right)\cosh\beta-\left(1+\frac{15}{\beta^2}+\frac{30}{\beta^4}\right)\sinh\beta, \qquad \textbf{Equation A.12}$$

$$f_2(\beta)=\left(\frac{6}{\beta^2}+1\right)\cosh\beta-\left(\frac{3}{\beta}+\frac{6}{\beta^3}\right)\sinh\beta, \text{ and} \qquad \textbf{Equation A.13}$$

$$f_3(\beta)=-\frac{3}{\beta}\cosh\beta+\left(1+\frac{3}{\beta^2}\right)\sinh\beta. \qquad \textbf{Equation A.14}$$

The equations given above show that for the limit $\beta\to\infty$, $c_\beta(\beta)$ will become unity corresponding to the flow around an impermeable particle or floc. The correction function $c_\beta(\beta)$ is illustrated in Figure 3.4.

A.5 Permeability models of porous aggregates as functions of the aggregates porosity ε

The following permeability models of porous aggregates as functions of the aggregates porosity ε, as presented by VEERAPANENI AND WIESNER (1996) and PARK ET AL. (2004), were used for the illustration in Figure 3.5. For a more detailed description of the models please refer to VEERAPANENI AND WIESNER (1996) and PARK ET AL. (2004) and references therein.

A.5.1 Brinkman

$$k_{Brinkmann} = \frac{a_P^2}{18}\left(3 + \frac{4}{1-\varepsilon_F} - 3\sqrt{\frac{8}{1-\varepsilon_F} - 3}\right), \qquad \textbf{Equation A.15}$$

where ε_F denotes the floc porosity and a_P denotes the primary particle radius.

A.5.2 Carman-Kozeny

$$k_{Carman-Kozeny} = \frac{a_P^2}{45}\frac{\varepsilon_F^3}{(1-\varepsilon_F)^2}. \qquad \textbf{Equation A.16}$$

A.5.3 Happel

$$k_{Happel} = \frac{\frac{2\cdot a_P^2}{9\cdot\gamma^3}\left(3 - \frac{9\cdot\gamma}{2} + \frac{9\cdot\gamma^5}{2} - 3\cdot\gamma^6\right)}{\left(3 + 2\cdot\gamma^5\right)} \qquad \textbf{Equation A.17}$$

and

$$\gamma = (1-\varepsilon_F)^{1/3}. \qquad \textbf{Equation A.18}$$

A.5.4 Howells, Hinch, Kim and Russel

$$k_{HHKR} = \frac{2\cdot a_P^2}{9\cdot(1-\varepsilon_F)}\left(\begin{array}{l}1 + \frac{3}{\sqrt{2}}\cdot\sqrt{(1-\varepsilon_F)} + \frac{135}{64}\cdot(1-\varepsilon_F)\cdot\ln(1-\varepsilon_F) \\ + 16.456\cdot(1-\varepsilon_F)\end{array}\right) \qquad \textbf{Equation A.19}$$

A.6 Equations for the determination of the drag coefficient Ω

As presented by VEERAPANENI AND WIESNER (1996), the factor B can be calculated with:

$$B = \frac{B_0}{2(\alpha \cdot \sinh\beta - \cosh\alpha)\cdot B_1}, \qquad \textbf{Equation A.20}$$

with:

$$B_0 = 3(\alpha^4 + 2\alpha\beta^3 + 3\alpha^2)\cosh\alpha + 9\alpha^2(\cosh\beta - \beta\sinh\beta - \alpha\sinh\alpha) + 3\cosh\Delta_2\left[\begin{matrix}(\alpha^3 + 2\beta^3 + 3\alpha)\cdot(\alpha\beta\sinh\beta - \alpha\cosh\beta - \beta\cosh\alpha) \\ + 3\alpha^2\beta\sinh\alpha\end{matrix}\right], \qquad \textbf{Equation A.21}$$
$$+ 3\sinh\Delta_2\left[(\alpha^3 + 2\beta^3 + 3\alpha)\cosh\alpha + 3\alpha^2\left(\begin{matrix}\alpha\beta\sinh\beta - \alpha\cosh\beta \\ - \sinh\alpha\end{matrix}\right)\right]$$

$$B_1 = -6\alpha + (3\alpha + 3\beta + \alpha^3 + 2\beta^3)\cosh\Delta_2 + 3(\alpha^2 - 1)\sinh\Delta_2 \text{ and} \qquad \textbf{Equation A.22}$$

$$\alpha = \frac{a_P}{\sqrt{k_{homogenous}}}. \qquad \textbf{Equation A.23}$$

Herein, the homogeneous permeability coefficient $k_{homogeneous}$ of the floc equals k as calculated with Equation A.17 and β can be calculated with Equation 3.13. Further Δ_2 can be calculated with:

$$\Delta_2 = \beta - \alpha. \qquad \textbf{Equation A.24}$$

A.7 Equations for the calculation of the correction functions $f(\delta_{FM}^*)$ and $g(\delta_{FM}^*)$ to account for hydrodynamic effects on the fluid flow due to the presence of permeable walls

A.7.1 Translation of a spherical particle in stationary fluid

A.7.1.1 Radial direction

$$f_r^t(\delta_{FM}^*) = \text{MIN}\left(f_r^t(\delta_{FM}^*) \text{ given by Mulder}, \sqrt{\frac{2}{3} R_M \cdot a_F} \right)$$

where $f_r^t(\delta_{FM}^*)$ denotes (MULDER (1990)):

$$f_r^t(\delta_{FM}^*) = 1 + 0.99720 \cdot \delta_{FM}^{*\,-1.00014} + 0.13192 \cdot \delta_{FM}^{*\,-0.46139} \qquad \text{for } \delta_{FM}^* < 1.05$$

$$f_r^t(\delta_{FM}^*) = 1 + 1.12992 \cdot \delta_{FM}^{*\,-0.99252} + 0.00047 \cdot \delta_{FM}^{*\,-0.01113} \qquad \text{for } \delta_{FM}^* \geq 1.05$$

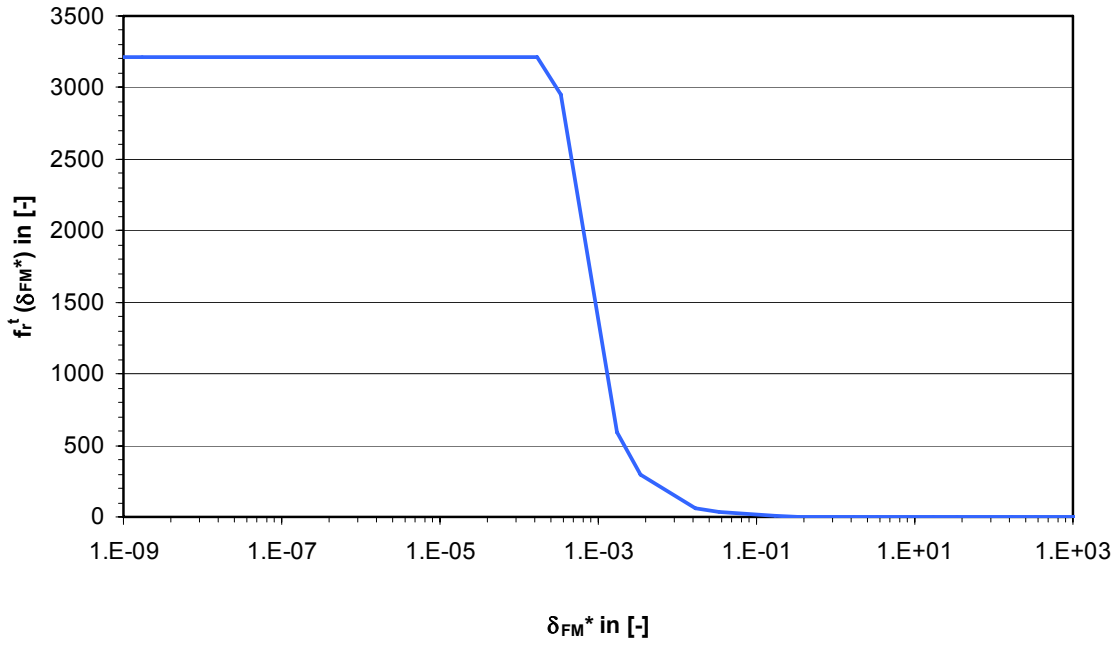

Figure A.3: Approximation of the hydrodynamic wall effect (translation of a spherical rigid floc in r-direction) as a function of the dimensionless floc distance for a floc with radius a_F = 29.47 µm and a membrane resistance $R_M = 5.24 \cdot 10^{11}$ 1/m

A.7.1.2 Longitudinal direction

$$f_z^t(\delta_{FM}^*) = 0.9588 - \frac{8}{15}\cdot \ln\left(\delta_{FM}^*\right) \qquad \text{for } \delta_{FM}^* < 0.018$$

$$f_z^t(\delta_{FM}^*) = -5.55595 - 0.67502\cdot \ln\left(\delta_{FM}^*\right) + 6.16045\cdot \delta_{FM}^{*\,0.01689} + 0.79053\cdot \delta_{FM}^{*\,0.35461} \qquad \text{for } 0.018 \le \delta_{FM}^* \le 0.43$$

$$f_z^t(\delta_{FM}^*) = \left(1 - 9\,\frac{\alpha}{16} + \frac{\alpha^3}{8} - 45\,\frac{\alpha^4}{256} - \frac{\alpha^5}{16}\right)^{-1} \qquad \text{for } \delta_{FM}^* > 0{,}43$$

$$\text{where : } \alpha = \left(\delta_{FM}^* + 1\right)^{-1}$$

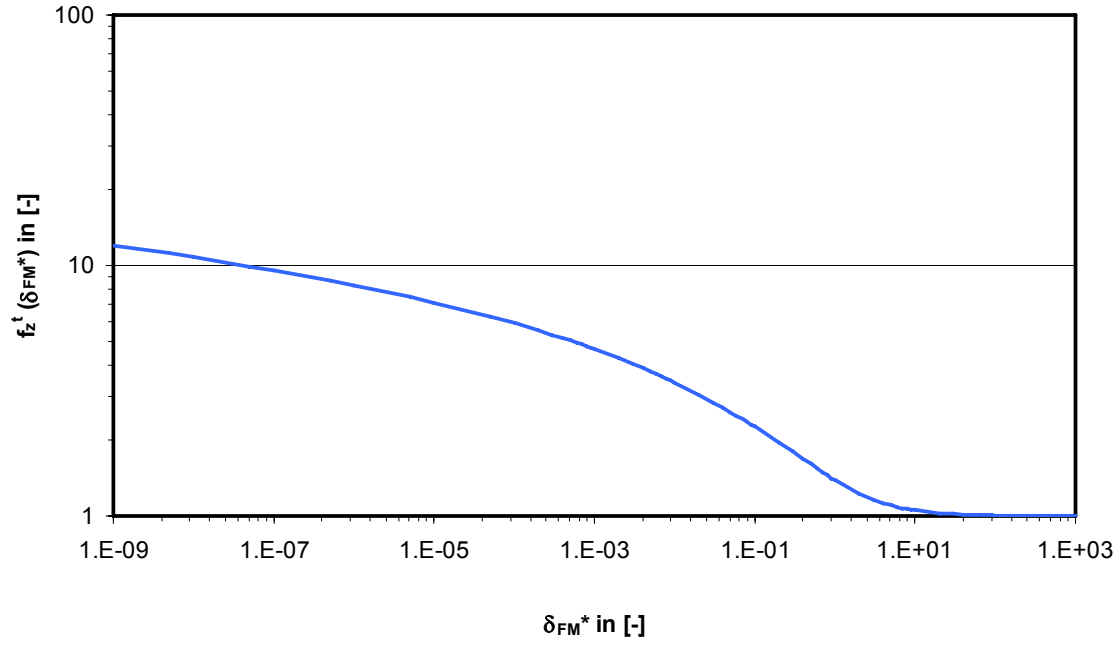

Figure A.4: Hydrodynamic wall effect (translation of a spherical, rigid floc in z-direction) as a function of the dimensionless floc distance

A.7.1.3 Angular direction

$$g_{\Phi}^{t}(\delta_{FM}^{*}) = -0.1895 - \frac{1}{10}\cdot \ln\left(\delta_{FM}^{*}\right) \qquad \text{for } \delta_{FM}^{*} < 0.0079$$

$$g_{\Phi}^{t}(\delta_{FM}^{*}) = 0.34067 - 0.10023\cdot \ln\left(\delta_{FM}^{*}\right) - 0.63769\cdot \delta_{FM}^{*\,0.01599} + 0.29474\cdot \delta_{FM}^{*\,0.33147} \qquad \text{for } 0.0079 \le \delta_{FM}^{*} \le 0.4944$$

$$g_{\Phi}^{t}(\delta_{FM}^{*}) = 3\frac{\alpha^{4}}{32}\cdot\left(1 - 3\frac{\alpha}{8}\right) \qquad \text{for } \delta_{FM}^{*} > 0.4944$$

$$\text{where : } \alpha = \left(\delta_{FM}^{*} + 1\right)^{-1}$$

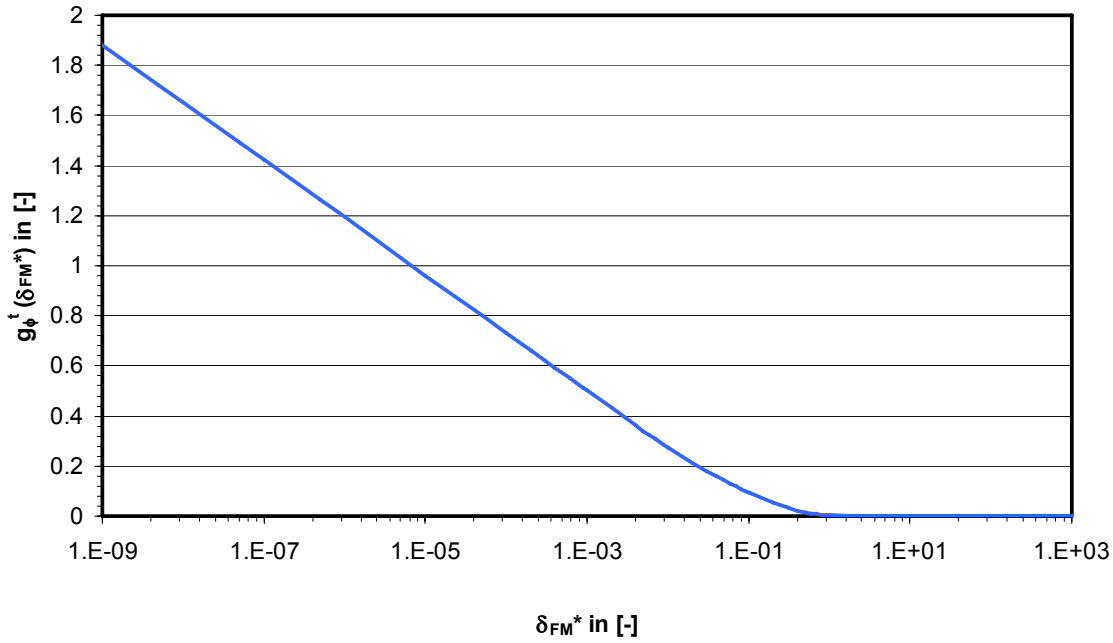

Figure A.5: Hydrodynamic wall effect (translation of a spherical, rigid floc in φ-direction) as a function of the dimensionless floc distance

A.7.2 Rotation of a stationary, spherical particle in stationary fluid

A.7.2.1 Longitudinal direction

$$f_z^r(\delta_{FM}^*) = -0.25260 - \frac{2}{15}\cdot\ln\left(\delta_{FM}^*\right) \qquad \text{for } \delta_{FM}^* < 0.007$$

$$f_z^r(\delta_{FM}^*) = -1.76242 - 0.20706\cdot\ln\left(\delta_{FM}^*\right) + 1.01864\cdot{\delta_{FM}^*}^{0.19263} + 0.74827\cdot{\delta_{FM}^*}^{0.00226} \qquad \text{for } 0.007 \le \delta_{FM}^* \le 0.665$$

$$f_z^r(\delta_{FM}^*) = \frac{\alpha^4}{8}\cdot\left(1 - 3\,\frac{\alpha}{8}\right) \qquad \text{for } \delta_{FM}^* > 0.665$$

$$\text{where : } \alpha = \left(\delta_{FM}^* + 1\right)^{-1}$$

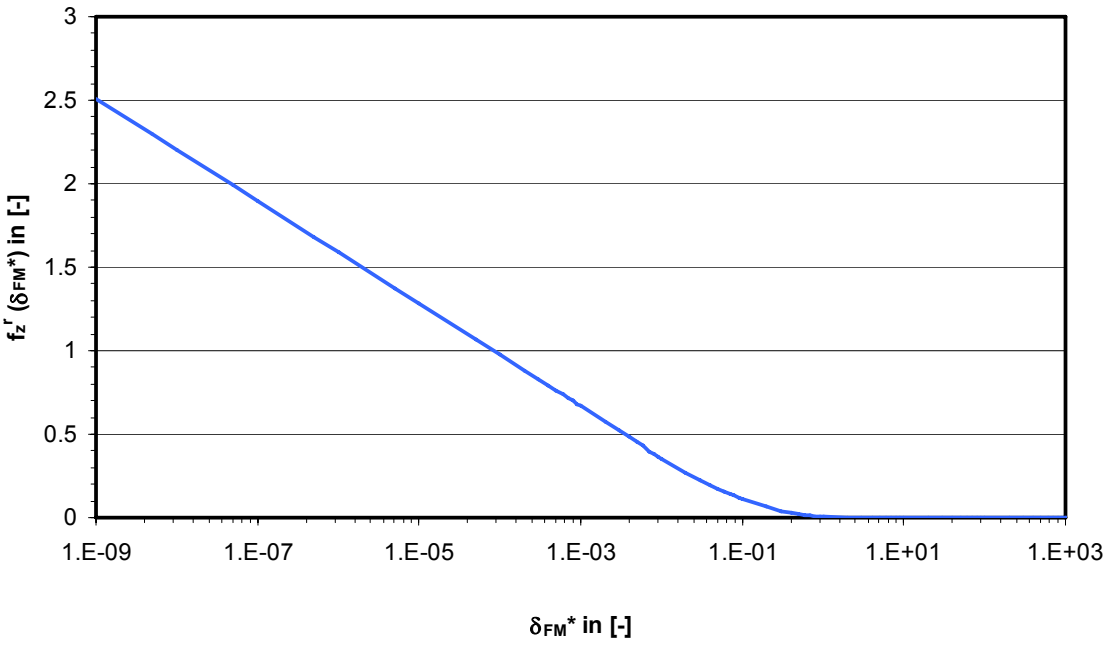

Figure A.6: Hydrodynamic wall effect (rotation of a stationary, spherical and rigid floc in stationary fluid in z-direction) as a function of the dimensionless floc distance

A.7.2.2 Angular direction

$$g_{\Phi}^{r}(\delta_{FM}^{*}) = 0.38171 - \frac{2}{5}\cdot\ln\left(\delta_{FM}^{*}\right) \qquad \text{for } \delta_{w}^{*} < 0.003$$

$$g_{\Phi}^{r}(\delta_{FM}^{*}) = -5.98237 - 0.64327\cdot\ln\left(\delta_{FM}^{*}\right) + 5.91097\cdot\delta_{FM}^{*\,0.03697} + 1.10032\cdot\delta_{FM}^{*\,0.30998} \qquad \text{for } 0.003 \le \delta_{FM}^{*} \le 0.75$$

$$g_{\Phi}^{r}(\delta_{FM}^{*}) = 1 + 5\,\frac{\alpha^{3}}{16} \qquad \text{for } \delta_{FM}^{*} > 0.75$$

$$\text{where}: \alpha = \left(\delta_{FM}^{*} + 1\right)^{-1}$$

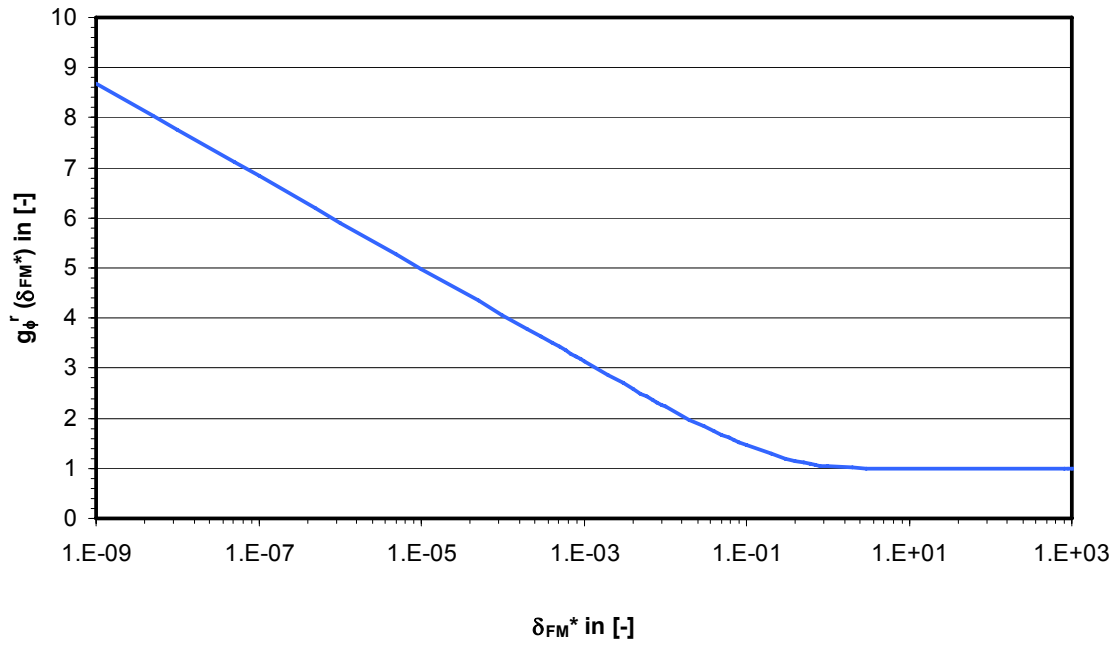

Figure A.7: Hydrodynamic wall effect (rotation of a stationary, spherical and rigid floc in stationary fluid in φ-direction) as a function of the dimensionless floc distance

A.7.3 Fluid flow around a stationary, spherical particle

A.7.3.1 Longitudinal direction

$$f_z^m(\delta_{FM}^*) = 1 + 0.32336 \cdot \exp\left(-0.23981 \cdot \delta_{FM}^*\right) + 0.37612 \cdot \exp\left(-1.62000 \cdot \delta_{FM}^*\right) \qquad \text{for } \delta_{FM}^* < 5.493$$

$$f_z^m(\delta_{FM}^*) = 1 + 9\,\frac{\alpha}{16} \qquad \text{for } \delta_{FM}^* \geq 5.493$$

$$\text{where : } \alpha = \left(\delta_{FM}^* + 1\right)^{-1}$$

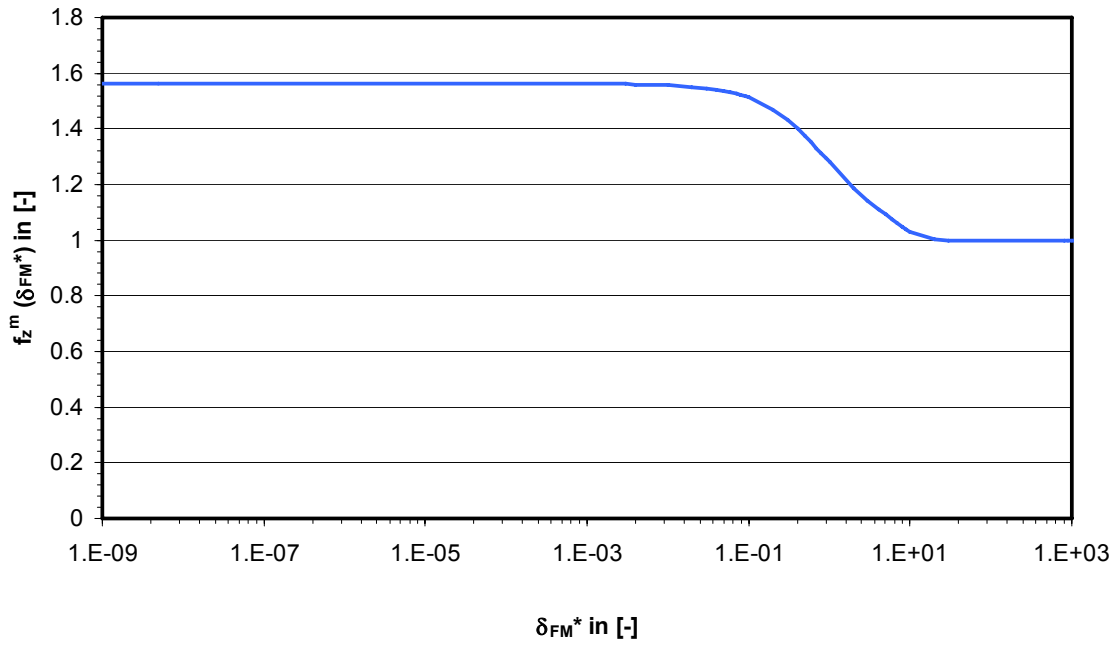

Figure A.8: Hydrodynamic wall effect (fluid flow around a stationary, spherical and rigid floc in z-direction) as a function of the dimensionless floc distance

A.7.3.2 Radial direction

$$f_r^m(\delta_{FM}^*) = -5.44505 + 7.26026 \cdot \exp\left(-0.02131 \cdot \delta_{FM}^*\right) + 1.41100 \cdot \exp\left(-1.91406 \cdot \delta_{FM}^*\right) \quad \text{for } \delta_{FM}^* < 2.871$$

$$f_r^m(\delta_{FM}^*) = -4.00512 + 1.85369 \cdot \delta_{FM}^{*\,-0.37655} + 3.99281 \cdot \delta_{FM}^{*\,0.03640} \quad \text{for } 2.871 \le \delta_{FM}^* \le 40$$

$$f_r^m(\delta_{FM}^*) = 1 \quad \text{for } \delta_{FM}^* > 40$$

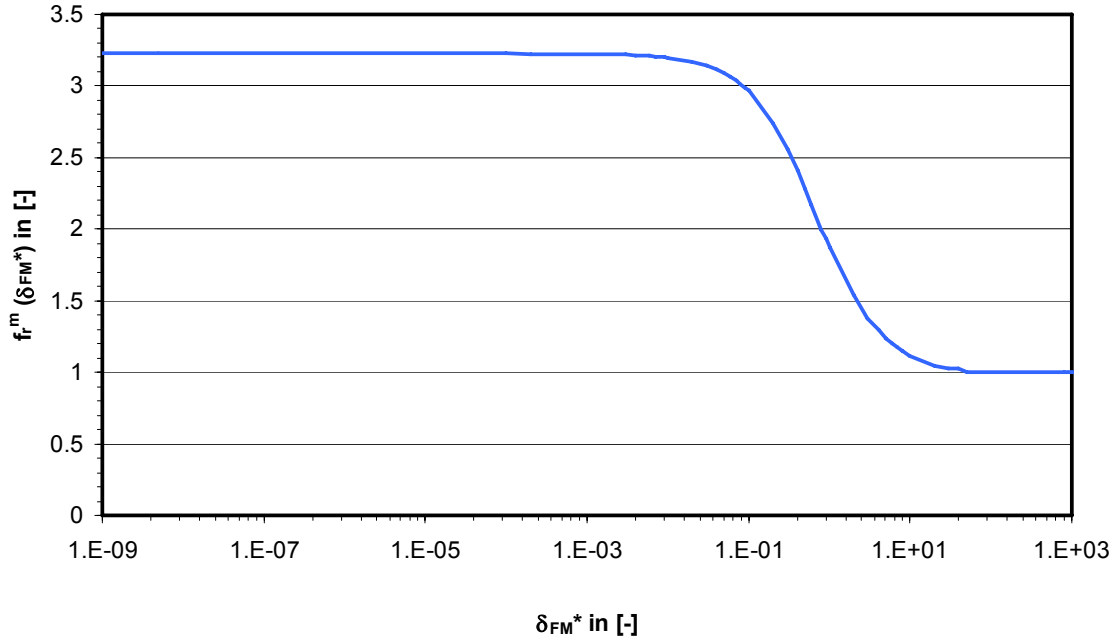

Figure A.9: Hydrodynamic wall effect (fluid flow around a stationary, spherical and rigid floc in r-direction) as a function of the dimensionless floc distance

A.7.3.3 Angular direction

$$g_{\Phi}^{m}(\delta_{FM}^{*}) = 0.30976 + 0.64780 \cdot \exp\left(-1.20356 \cdot \delta_{FM}^{*}\right) - 0.01538 \cdot \exp\left(0.00543 \cdot \delta_{FM}^{*}\right) \quad \text{for } \delta_{FM}^{*} < 1$$

$$g_{\Phi}^{m}(\delta_{FM}^{*}) = \alpha - 3\frac{\alpha^{4}}{16} \quad \text{for } \delta_{FM}^{*} \geq 1$$

$$\text{where : } \alpha = \left(\delta_{FM}^{*} + 1\right)^{-1}$$

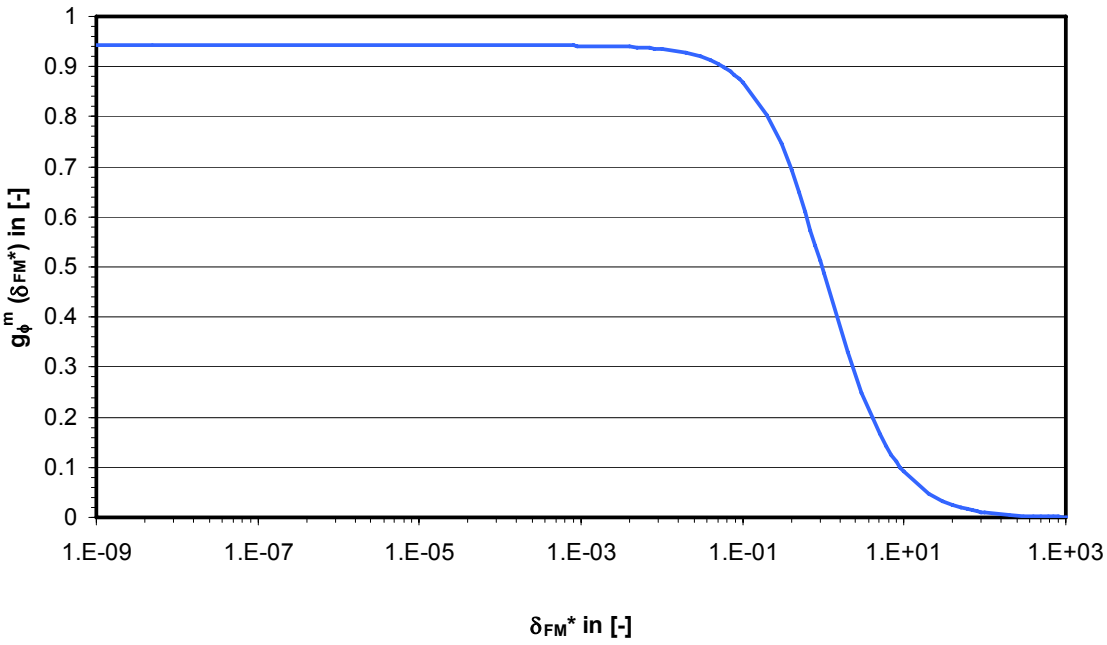

Figure A.10: Hydrodynamic wall effect (fluid flow around a stationary, spherical and rigid floc in φ-direction) as a function of the dimensionless floc distance

A.8 Dimensionless inertia induced velocities

The functions $f_2(\delta_{FM}^{C*})$ and $f_3(\delta_{FM}^{C*})$ used for the determination of he lateral migration as described in chapter 3.3.7 are functions of the dimensionless distance of the floc centre from the wall, given by:

$$\delta_{FM}^{C*} = \frac{\delta_{FM}^{C}}{r_C}$$ **Equation A.25**

and can be considered as dimensionless inertia induced velocities. They were not presented by VASSEUR AND COX (1976) as numerical equations but as figures. For the case of nonneutrally buoyant spherical flocs a sixth-order polynomial approximation could be derived graphically from VASSEUR AND COX (1976) for $f_2(\delta_{FM}^{C^*})$ with:

$$f_2\left(\delta_{FM}^{C^*}\right) = 6\cdot 10^{-5} - 0.6089\cdot\left(\delta_{FM}^{C^*}\right) + 3.0573\cdot\left(\delta_{FM}^{C^*}\right)^2 - 6.3347\cdot\left(\delta_{FM}^{C^*}\right)^3 + 6.969\cdot\left(\delta_{FM}^{C^*}\right)^4 - 3.5474\cdot\left(\delta_{FM}^{C^*}\right)^5 + 0.4647\cdot\left(\delta_{FM}^{C^*}\right)^6. \quad \textbf{Equation A.26}$$

A numerical fit of $f_3(\delta_{FM}^{C^*})$ was presented by OTIS ET AL. (1986), cited in CHELLAM AND WIESNER (1992), with the following sixth-order polynomial approximation:

$$f_3\left(\delta_{FM}^{C^*}\right) = 1.532139 - 12.182786\cdot\left(\delta_{FM}^{C^*}\right) + 21.652283\cdot\left(\delta_{FM}^{C^*}\right)^2 + 4.495068\cdot\left(\delta_{FM}^{C^*}\right)^3 - 28.176666\cdot\left(\delta_{FM}^{C^*}\right)^4 + 10.950694\cdot\left(\delta_{FM}^{C^*}\right)^5 + 0.198042\cdot\left(\delta_{FM}^{C^*}\right)^6. \quad \textbf{Equation A.27}$$

PANGLISCH (2001) mentioned that the dimensionless inertia induced velocity only has one radial component, being constant for all φ in a capillary or pipe flow respectively. Hence, the solution for a plane Poiseuille flow in a slit equals the solution for a Poiseuille pipe flow and the dimensionless particle distance from the wall, $\delta_{FM}^{C^*}$ can be substituted with the dimensionless radial particle distance r* as follows:

$$r^* = \frac{r}{r_C} = \frac{2\delta_{FM}^{C^*} - 1}{\cos\varphi}. \quad \textbf{Equation A.28}$$

Here, r denotes the radial coordinate and r_C denotes the capillary radius. After substitution Equation A.27 will match the fifth-order polynomial approximation presented by PANGLISCH (2001) as illustrated in Figure A.11. The inertia induced lift velocity of a rigid, neutrally buoyant spherical particle or floc, allowed to rotate, is directed into the direction of the membrane wall at $|r^* \cos\varphi| = 1$ for all $|r^* \cos\varphi| < 0.62$ and directed into the direction of the flow axis for all $|r^* \cos\varphi| > 0.62$. At $r^* \cos\varphi = 0.62$ and $r^* \cos\varphi = 0$ a migration equilibrium exists.

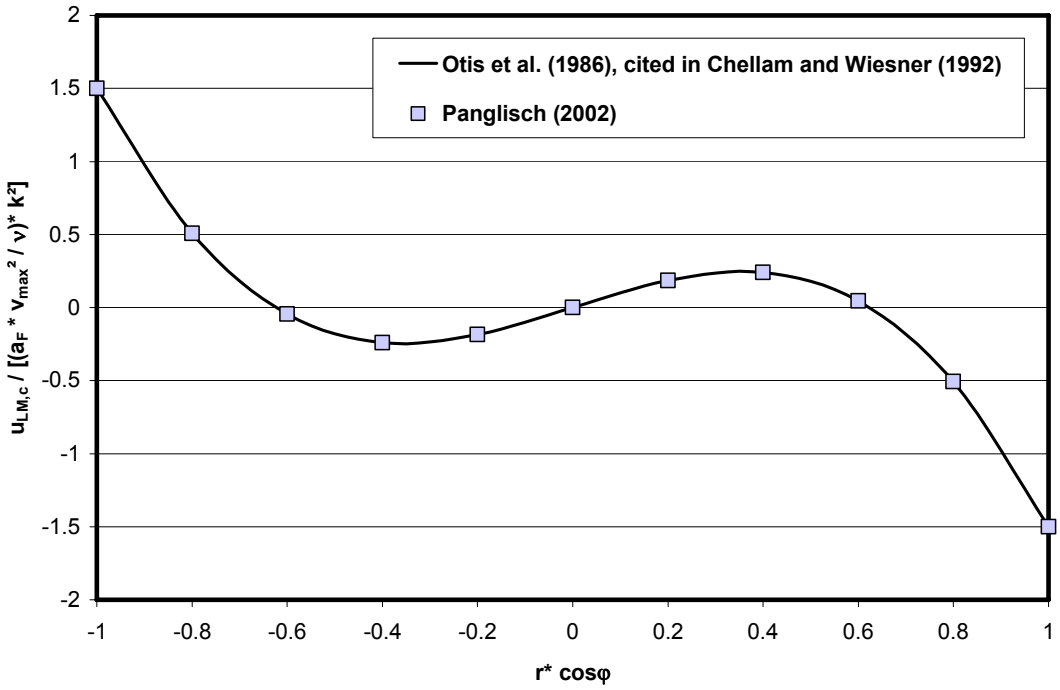

Figure A.11: Polynomial fit of the lift velocity experienced by a neutrally buoyant spherical particle or floc in a Poiseuille pipe flow as presented by PANGLISCH (2001) and OTIS ET AL. (1986), cited in CHELLAM AND WIESNER (1992)

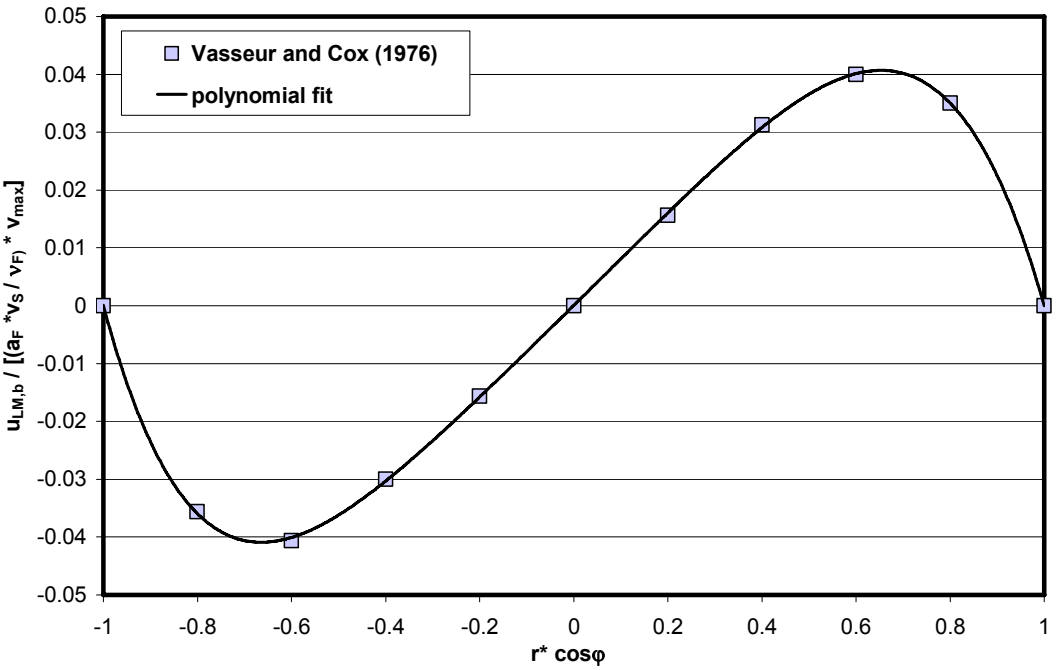

Figure A.12: Polynomial fit of the lift velocity experienced by a nonneutrally buoyant spherical floc in a Poiseuille pipe flow adapted from VASSEUR AND COX (1976)

Compared to Figure A.11, the equilibrium position for nonneutrally buoyant spherical flocs may be moved either towards the axis if the floc lags the flow, i. e. for flocs heavier than the fluid, thus going slower, or towards the wall at $|r^* \cos \varphi| = 1$ if the floc leads the flow, i. e. for flocs lighter than the fluid.

A.9 Surface charge and configuration of the electric double layer

The development of an electric charge at the surface of particles can arise in three principle ways (STUMM AND MORGAN (1996)): Firstly, the charge may arise from chemical reactions at the surface of solids if the surface contains ionisable groups, i. e. –OH, –COOH, $–OPO_3H_2$ and –SH. The surface charge then depends on the degree of ionisation, i. e. proton transfer and consequently depending on pH value of the medium. At low pH values a positively charged surface prevails and at high pH values a negatively charged surface is formed. At some intermediate pH values, the so called isoelectric point, the surface charge will be zero. Secondly, the surface charge at the phase boundary may be caused by latice imperfections at the solid surface and by isomorphous replacements, i. e. atomic substitution with atoms having differentially numbers of electrons. This permanent structural charge is usually for a mineral. Thirdly, a surface charge may be established by adsorption of a hydrophobic species or a surfactant ion. Ionic species carrying a hydrophobic moiety may bind inner-spherically or outer spherically depending on whether the surface-coordinative or the hydrophobic interaction prevails. Thus different types of surface charge density contribute to the net total particle charge on a particle.

The surface charge of solids suspended in water will be neutralised by contrary charged ions, the so called counterions, which concentrate in the close vicinity of the surface. Ions of the same charge as the surface charge of the solids, the so called co-ions, will be displaced. This leads to a more or less diffusively distribution of the ions in the liquid in contact with the solid, usually idealised as an electric double layer as illustrated in Figure A.13. The electric double layer consists of two layers around the solid surface, the Stern layer and the diffusive double layer. The Stern layer is directly attached to the negatively charged surface with Galvani potential Ψ_G and can be further subdivided into the inner and outer Helmholtz layer, see Figure A.13. The inner Helmholtz layer is built by specifically adsorbed unhydrated ions and water

molecules of the hydration hull of the solid which are directly in contact with the solid surface. Depending on the charge of the specifically adsorbed unhydrated ions, the Galvani potential Ψ_G is increased or decreased linearly to the Volta potential, or surface potential respectively Ψ_o. The region where only hydrated counterions are located is called the outer Helmholtz layer in which the potential is decreasing to the Stern potential Ψ_S at the Stern plane. The Stern layer can be assumed as a layer of fixed molecules and counterions with a thickness of about δ_S = 0.5 nm, corresponding to the diameter of a hydrated ion. Hence, a minimum adhesion distance of 1 nm can be supposed for two suspended surfaces. Outside the Stern layer is the diffusive layer which extends outwards into the bulk solution. Here, the potential in the diffusive double layer, in which dissolved co-ions and counterions are freely mobile, is decreasing exponentially until a balance of electrostatic and thermal forces is attained. At a distance $1/\kappa$ the Stern potential has dropped by a factor 1/e. This distance can be used as a measure of thickness of the double layer, often referred to as the Debye-Hückel length where the free bulk solution starts.

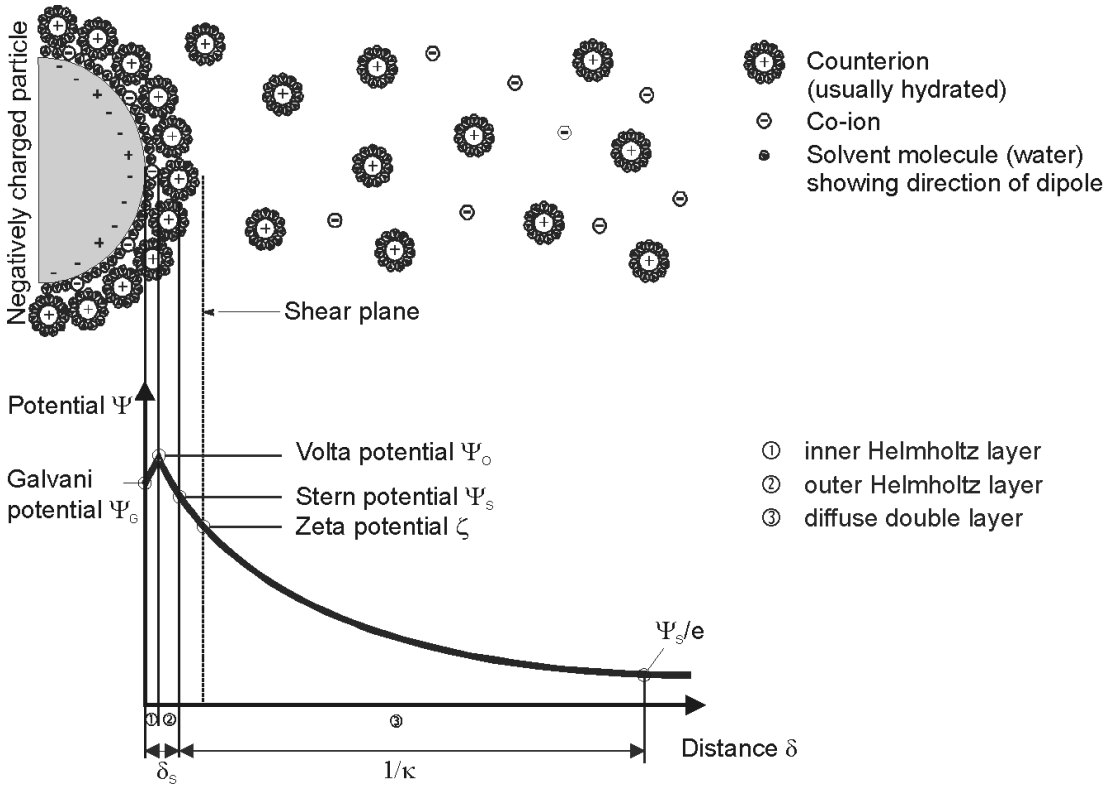

Figure A.13: Configuration of the electric double layer at a suspended negatively charged particle and resulting distribution of the charge potential as function of distance (adapted from NAHRSTEDT (1999))

The shear plane, as illustrated in Figure A.13, separates the ‘fixed’ from the ‘mobile’ parts of the electrical double layer. The electrical potential at the shear plane is the electrokinetic potential, or the zeta potential, which can be derived with the help of electrophoretic mobility or streaming potential measurements. It is usually assumed that the shear plane lies outside but fairly close to the Stern plane, so that essentially the zeta potential can be used with good agreement as a measure of the real Stern potential.

A.10 Calculated DLVO forces

According to the DLVO theory, the attractive London-van der Waals and repulsive double layer forces acting between adjacent surfaces are superposed. The calculations are based on Equation 3.67 to Equation 3.73 and the general data set given in Table A.2. The values are those of the experimental setup as introduced in chapter 4 or taken from literature, i. e. NAHRSTEDT (1999), PANGLISCH (2001), VISSER (1972), SOFFER ET AL. (2005) and ZHAO ET AL. (2002). The closest calculated distance was set to 1 nm, representing the minimum adhesion distance δ_0 between two particles/flocs or a particle/floc and the membrane wall respectively.

Table A.2: General data set used for the calculation of the DLVO forces

Description	Parameter	COMSOL	Value	Unit
Stern potential approx. Zeta potential of iron hydroxide flocs ζ_F)	$\Psi_{S,F}$	Psi_1	-12^{-3}	V
Stern potential (approx. Zeta potential of PES membrane ζ_M)	$\Psi_{S,M}$	Psi_2	-15^{-3}	V
Stern potential (approx. Zeta potential of latex primary particle ζ_P)	$\Psi_{S,P}$	Psi_1	-60^{-3}	V
Hamaker constant between iron hydroxide floc and PES membrane across water	$H132_{FM}$	H_132_FM	$2.63 \cdot 10^{-19}$	J
Hamaker constant between primary particle and PES membrane across water	$H132_{PM}$	H_132_PM	$1.54 \cdot 10^{-20}$	J
Characteristic wavelength of interaction	λ_C	lambda_c	$100 \cdot 10^{-9}$	m
Avogadro constant	N_A	N_A	$6.0221 \cdot 10^{23}$	1/mol
Boltzmann constant	k_B	k_B	$1.3807 \cdot 10^{-23}$	J/K
Electrical permittivity	ε_0	eps_0	$8.8542 \cdot 10^{-12}$	As/V/m
Hardness	c_0	c_0	2	mol/m³
Valency ($z = z_i$)	z	z	2.00	-
Temperature	T	T	293.15	K
Permittivity (relative dielectric constant)	ε_r	eps_r	78.00	-
Minimum adhesion distance	δ_0	d_0	$1.0 \cdot 10^{-9}$	m
Electron charge	e	e	$-1.60 \cdot 10^{-19}$	As

The Stern potentials were presented in chapter 4.1.1 (membrane), chapter 4.1.2 (particle) and chapter 4.2 (floc). For all other values please refer to chapter 3.3.8.

For instance, the resulting force will be usually repulsive at larger distances of two surfaces. For a decreasing distance between the two surfaces, repulsion will increase up to a certain maximum at some nanometer in distance at first. When the surfaces approach each other further, attractive forces will increase and dominate at very close distances, see Figure A.14.

For coagulated particles, embedded in iron hydroxide flocs, the DLVO sum accounts to mainly attractive forces even for larger distances as illustrated in Figure A.15.

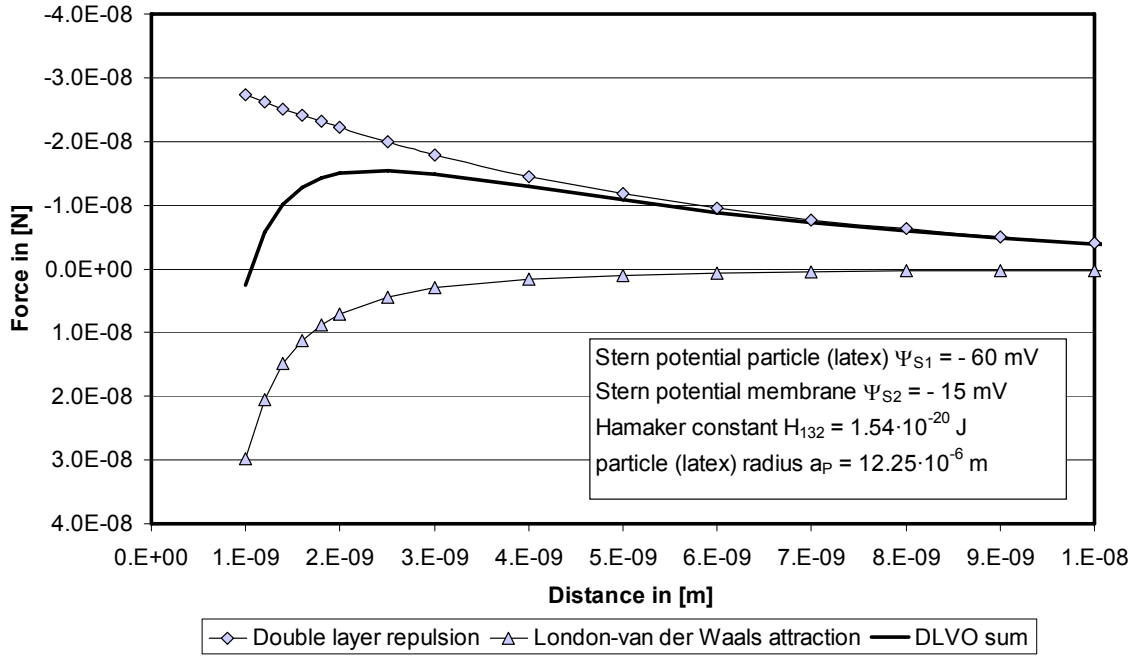

Figure A.14: DLVO sum, London–van der Waals and electric double layer forces between a primary particle of radius a_P = 12.25 µm and the membrane wall

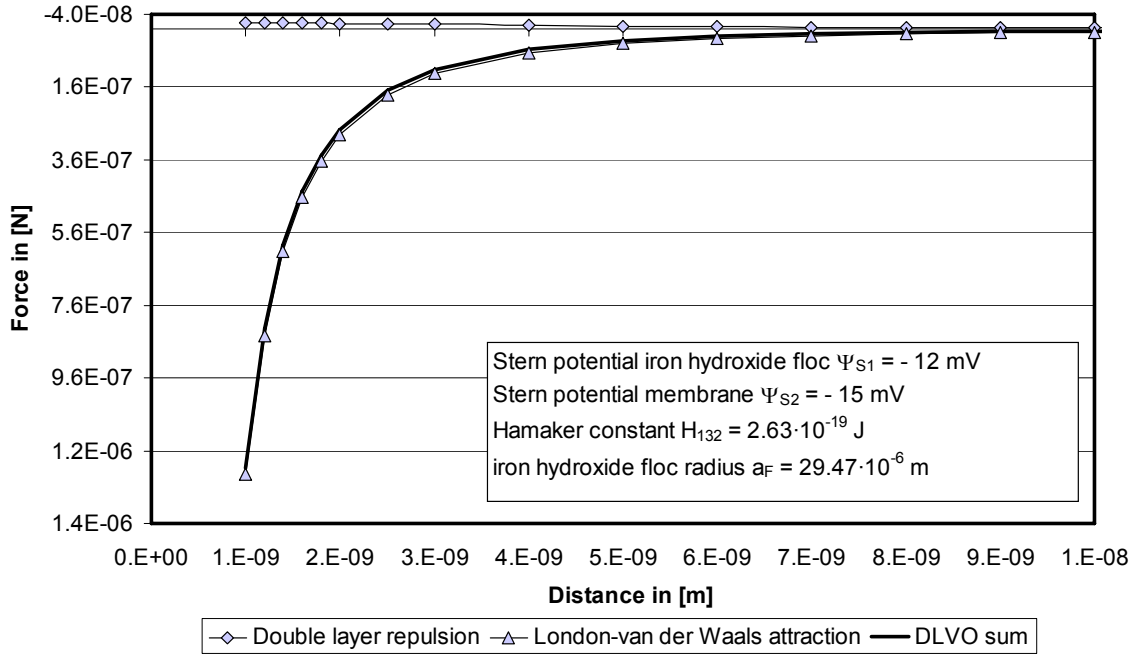

Figure A.15: DLVO sum, London–van der Waals and electric double layer forces between an iron hydroxide floc of radius a_F = 29.47 µm and the membrane wall

A.11 Model constants and parameters

Constants were used for modelling the flow field, the concentration distribution in the membrane capillary and floc trajectories as given in Table A.3. For further information please refer to chapters 3.2, 3.3 and 3.4. The expressions used in the column 'COMSOL' denotes the name of the parameter used in the software.

Table A.3: Constant parameters used in the model

Description	Parameter	COMSOL	Value	Unit
Capillary length	l_C	cap_l	1	m
Capillary radius	r_C	cap_r	0.0004	m
Membrane resistance	R_M	mem_R	$5.24 \cdot 10^{11}$	1/m
Flux	J	flux	$2.22 \cdot 10^{-5}$	$m^3/m^2/s$
Gravitational acceleration in x direction in	g_r	g_r	9.81	m/s^2
Gravitational acceleration in y direction	g_z	g_z	0	m/s^2
Fluid temperature	T	fluid_T	293.15	K
Relative floc or particle density	ρ_{rel}	rho_rel	1.05	-
Floc radius	a_F	a_F	$29.47 \cdot 10^{-6}$	m
Floc density	ρ_F	floc_rho	1050	kg/m^3
Floc mass concentration	c_{mF}	m_c_F	1	kg/m^3
(Minimum) Floc porosity	ε_F	eps_F	0.26	-
Maximum floc volume concentration	$\phi_{F,max}$	phi_max	0.74	m^3/m^3
Primary particle radius	a_P	a_P	$12.25 \cdot 10^{-6}$	m

The determined values for different initial parameters at time $t_0 = 0$ are listed in Table A.4.

Table A.4: Calculated initial parameters using the constants given in Table A.3

Description	Parameter	COMSOL	Value	Unit
Initial fluid inlet velocity in radial direction	u_0	fluid_u0	0	m/s
Initial fluid inlet velocity in longitudinal direction	v_0	fluid_v0	0.111	m/s
Initial fluid inlet pressure	p_0	fluid_p0	$1.348 \cdot 10^{4}$	Pa
Panglisch parameter	a	a	0.691	1/m
Membrane filtration area	A_M	mem_A	$2.513 \cdot 10^{-3}$	m²
Inlet volume flow	$\dot{V}_0$	fluid_V_flow0	$5.585 \cdot 10^{-8}$	m³/s
Initial dynamic fluid viscosity at 20°C	η_0	fluid_eta0	$1.003 \cdot 10^{-3}$	Pa·s
Initial fluid density at 20°C	ρ_0	fluid_rho0	998.204	kg/m³
floc mass	m_F	floc_mass	$6.689 \cdot 10^{-15}$	kg
Initial floc volume concentration in the bulk flow	$\phi_{F,0}$	phi_0	$9.524 \cdot 10^{-4}$	m³/m³
Gravitational force in radial direction	F_r	g_r·fluid_rho0	9792.383	N/m³
Gravitational force in longitudinal direction	F_z	g_z·fluid_rho0	0	N/m³

The gravitational forces F_r and F_z were defined to account for gravitation in a horizontal orientated capillary as given in the experimental setup, see chapter 4.

A.12 CFD modelled start-up length

The start up length for the development was found to be smaller than 0.5 % of the total capillary length as shown in Figure A.16, approximately 6 times smaller than predicted by Equation 3.2. For this reason it was decided to model the flow into the capillary with a laminar flow profile in the following, giving the numerical model more robustness.

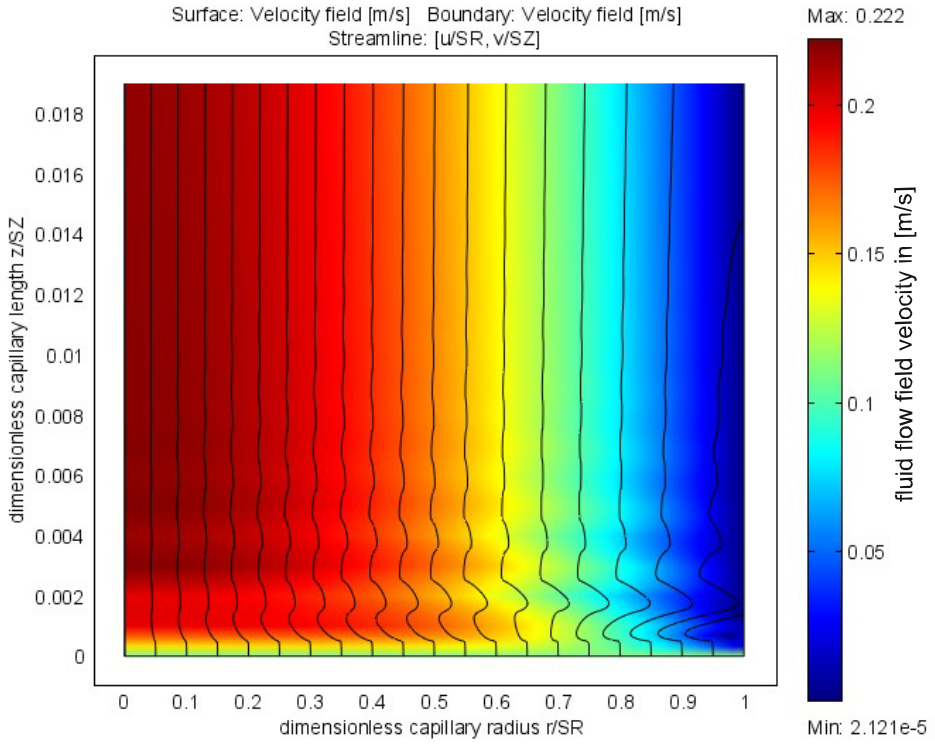

Figure A.16: Axial symmetric velocity field and fluid flow streamlines at capillary inlet, display detail of Figure 3.18

A.13 Model mesh

As mentioned in chapter 3.4.1 and 3.4.2, the software is able to work with triangular, quadrilateral, tetrahedral, brick, and prism meshes using fully automatic and adaptive mesh generation. For using mapped meshes the geometry needs to be fairly regular and the shape of each subdomain must not differ too much from a rectangular shape. When using the mapping technique, a logical quad mesh is defined on the unit square for each subdomain and is then mapped onto the real geometry by transfinite interpolation. For the mapping technique to work properly, the following conditions needs to be satisfied: each subdomain must be bounded by at least four boundary segments; each subdomain must be bounded by one connected boundary component only and the geometry must not contain isolated vertices or isolated boundary segments.

The overall mesh density is determined from the distribution of edge elements on the boundary segments and can be adapted to areas or boundary segments of special interest by using constrained edge element distributions. It is possible to choose

between specifying the number of equally distributed edge elements or the distribution of mesh vertices along the boundary segment. The latter, which gives full control of the edge element distribution, is specified by vector valued expressions of strictly increasing values starting with zero, specifying the relative arc length values of the mesh vertices along the edge. However, for the mapping technique to work, the opposite sides of each logical unit square need to be discretised by the same number of edge elements. The vector valued expressions were applied to account for a sufficient high resolution of the mesh especially at the capillary entrance, where the laminar flow profile is established and at the membrane wall, where the interacting forces between fluid flow, moving flocs and membrane wall will be likely highest and where the cake layer build-up will occur.

The 2D mesh as given in chapter 3.4.2 can be transformed into 3D by using extrusion coupling variables, which maps values from the source domain, here in 2D, to the destination domain in 3D. Because the destination domain has higher dimension than the source domain, the mapping is done by extruding point-wise values to the higher dimensions. This transformation between the source and destination is performed by the so called general transformation. Here, the source transformation is a one-to-one mapping that maps the mesh of the physical source domain to an intermediate mesh embedded in a space of the same dimension as the source. The destination transformation is a mapping from the destination domain, where the value of the variable is defined, to the same space that contains the intermediate mesh. When the value of the coupling variable is requested somewhere in the destination domain, the software transforms the destination points using the destination transformation. It compares the resulting coordinates to the elements in the intermediate mesh in order to find corresponding locations in the physical source domain. To avoid the need to solve a nonlinear system of equations for every destination point, the software assumes that the source transformation is linear on each element of the intermediate mesh. In practice, the transformation is often trivial and leaves the coordinates unchanged, but it can also rescale, stretch, bend, or reflect the mesh. For more detailed information about the applied transformation refer to COMSOL AB (2006A). While transforming the 2D model into 3D, the applied mesh is generated automatically with tetrahedral mesh elements. The mesh was always refined and adjusted to account for a sufficient high resolution at the areas of interest.

Nevertheless, the mesh has to be adapted for each model. For example, one chosen mesh as illustrated in Figure A.17 consists of 333.173 elements over the whole modelled capillary, with 44.052 elements directly at the boundaries, delivering 1.644.941 degrees of freedom.

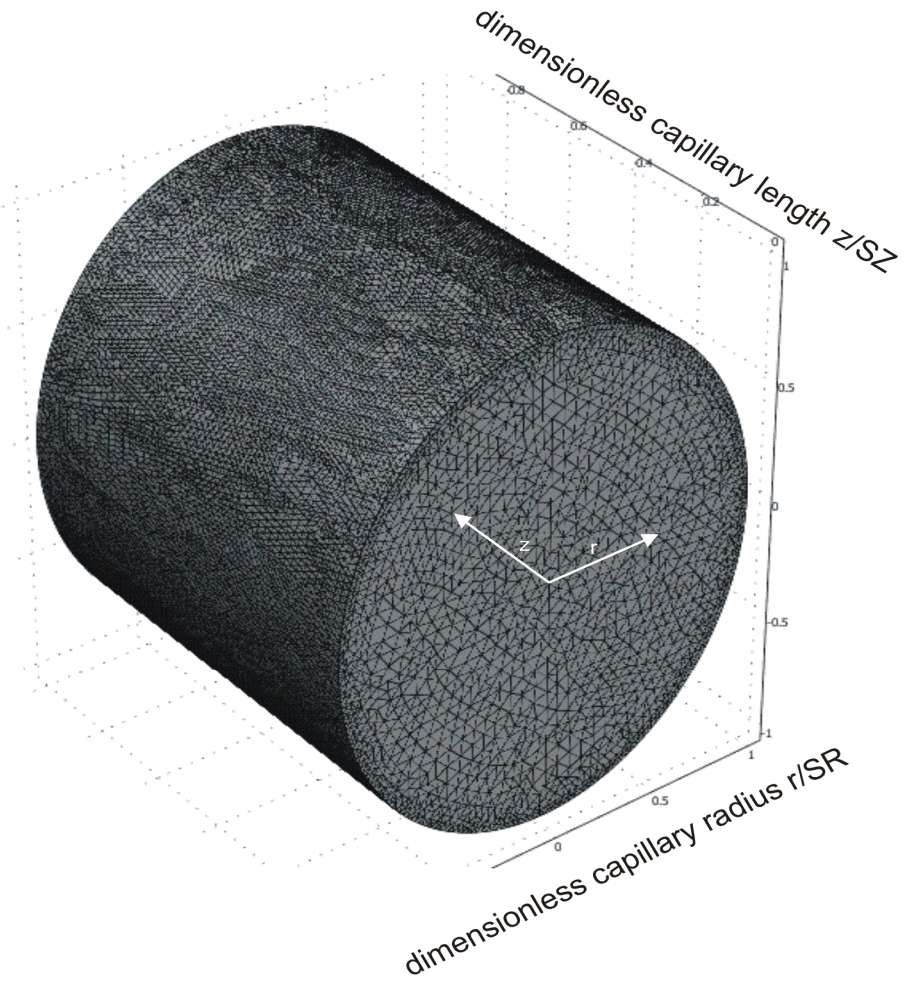

Figure A.17: Unstructured mesh of the dimensionless model in 3D

A.14 Transformation from 2D to 3D

For the transformation of the 2D model geometry into 3D, the coordinates and the velocity components have to be adapted to the 3D model geometry. The coordinates of the 2D model geometry r and z were set to x as radial and y as longitudinal coordinate respectively in the 3D model geometry. Additionally, a second radial coordinate z is introduced. Hence the radial coordinate can be now calculated with:

$$r = \sqrt{x^2 + z^2}\ .$$ **Equation A.29**

The angle φ can be calculated using the so called four-quadrant inverse tangent function 'atan2 (x, z)' of the software COMSOL. This function is used to derive the angle φ directly in the correct quadrant when transferring cartesian coordinates into polar coordinates. It computes the point wise arctan of the two scalars x and z, such that $\tan(\varphi) = z/x$. For more details please refer to COMSOL AB (2006B). Following velocity components could than be derived, using the four-quadrant inverse tangent of the coordinates x and z, the origin velocity components u and v of the 2D model and trigonometric functions. For instance, the radial velocity component in x-direction accounts to:

$$u_{3D} = u \cdot \sin(\text{atan2}(x,z)),$$ **Equation A.30**

the axial velocity component in y-direction to:

$$v_{3D} = v\ ,$$ **Equation A.31**

and the radial velocity component in z-direction to:

$$w_{3D} = u \cdot \cos(\text{atan2}(y,z)).$$ **Equation A.32**

The magnitude of the velocity could be derived as:

$$U_{3D} = \sqrt{u_{3D}^2 + v_{3D}^2 + w_{3D}^2}\ .$$ **Equation A.33**

According to this example of transformation of the fluid flow velocities, all necessary values can be transformed from 2D to 3D, except floc velocities due to the influence of gravity, acting only into one direction. Hence, floc velocities were calculated directly in 3D, using the transformed 3D fluid flow velocities and all other functions as described in this work.

A.15 Statistical methods

6.1.1 Grubbs outlier test

There is a scatter in the results of the measured data due to statistical and systematic influences. Systematically influenced individual values are considered as faulty, i. e. as outliers. To assess whether an extreme value is to be designated as an outlier, test values are calculated by various methods which have to be compared with tabulated numerical values of different levels of significance. The choice of a definite level of significance includes the risk to reject an extreme value as outlier when in fact there is no outlier (type 1 risk). At the same time this choice includes also a risk of failing to reject an actual outlier (type 2 risk). Since incorrect results may falsify the result of the measured data, outliers have to be traced and rejected. All data sets used in this work were tested according to the outlier r_m- test as presented by Grubbs (GRUBBS AND BECK (1972), GRUBBS (1969), GRUBBS (1950) all cited in UHL (2000)). In statistics, a result is significant if it is unlikely to have occurred by chance, given that a presumed null hypothesis H_0 is true (type 1 risk). The level of significance was chosen to be highly significant with α = 1 %. The Grubbs r_m- test compares each individual value x* with the mean value $\bar{x}$ and the standard deviation s of the measured data set. The null hypothesis H_0 is chosen to be that the individual value x* out of n values is no outlier. This null hypothesis was accepted on the level of significance if

$$\hat{f}_m = \frac{\left|\bar{x} - x^*\right|}{s} \leq r_m(\alpha, n) \qquad \textbf{Equation A.34}$$

was true, otherwise rejected. If an individual value was tested to be an outlier it was eliminated and the test repeated for all remaining values of the data set. This was done for all individual values until all remaining values were accepted and indicated to be no outlier.

The experimental investigations presented in this work are often time series in which each individual value has to be evaluated in comparison to the value measured chronologically before. UHL (2000) presented a method which adapts Grubbs r_m- test to time series. This method is comparable to the moving average method,

consequently it was called the moving outlier test. Each individual value in a time series was compared to (n-1) chronological values, whereas (n-1)/2 were before and (n-1)/2 after the investigated individual value. The test was then performed according to Equation A.34 and the procedure described above.

6.1.2 Confidence intervals

The experimental values illustrated in the figures in this work are often presented with corresponding confidence intervals if possible. The confidence interval T(x*, P) of each measured value x* or of the mean value of n-fold replied measurements was than calculated according to FACHGRUPPE WASSERCHEMIE IN DER GESELLSCHAFT DEUTSCHER CHEMIKER (1997) with:

$$T(x,P) = \frac{s}{\sqrt{n}} \cdot t(\alpha, n-1), \qquad \textbf{Equation A.35}$$

where the interval

$$x - T(x,P) < \mu_x > x + T(x,P) \qquad \textbf{Equation A.36}$$

contains the expected value μ_x with safety $P = (1-\alpha)$, whereas the expected value can be regarded as an estimation value of the real value.

A.16 Geometrical data of the used capillaries in the experiments

Table A.5: Lengths of the used capillaries and intersections in the experiments

	Cap. A	Cap. B	Cap. C
Inlet potting	19	14	19
membrane section I	321	311	309
Potting I	7	14	19
membrane section II	321	312	317
Potting II	9	16	13
membrane section III	321	310	307
Potting III	9	17	23

A.17 Particle count experiments

The considerably reduction of deposited small and mid sized primary particles along the capillary in relation to the pure solid primary particle suspensions was also found in other particle count experiments as mentioned in chapter 4.5. The results are given in the following, whereas both, fractions of deposited primary particles after filtration as uncoagulated and as coagulated suspension vs. dimensionless capillary length z/SZ and primary particle radius a_P are shown for comparison. Figure A.18 indicates that smaller and mid sized primary particles were not transported up to the end of the capillary, being deposited after shorter distances to the capillary inlet, which is in good accordance to the theoretical considerations, see chapter 3.5.2.

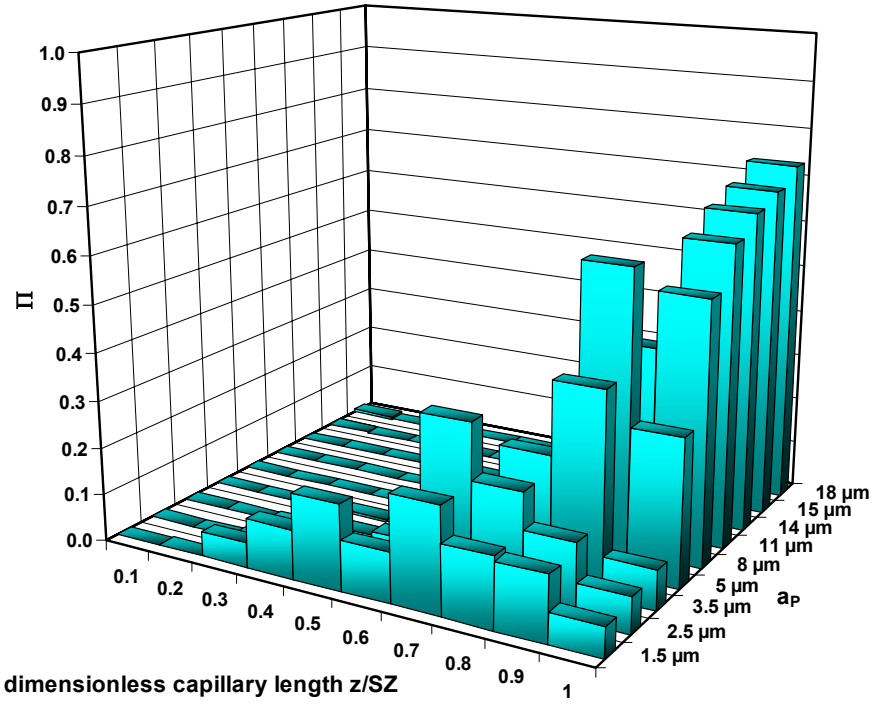

Figure A.18: Fractions of deposited primary particles after filtration (TMP = 0.4 bar, average flux unknown) as uncoagulated suspension vs. dimensionless capillary length z/SZ and primary particle radius a_P

Figure A.19 to Figure A.22 show the measured results for deposited primary particles after filtration at constant TMP of 0.4 bar as coagulated suspension vs. dimensionless capillary length z/SZ and primary particle radius a_P.

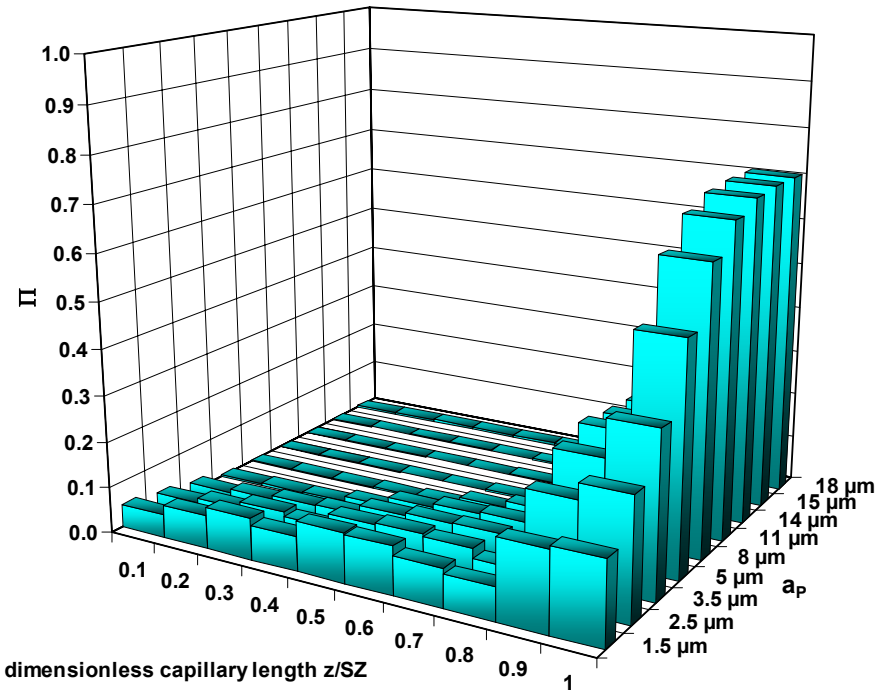

Figure A.19: Fractions of deposited primary particles after filtration (TMP = 0.4 bar, average flux of approx. 151 L/m²/h) as coagulated suspension vs. dimensionless capillary length z/SZ and primary particle radius a_P

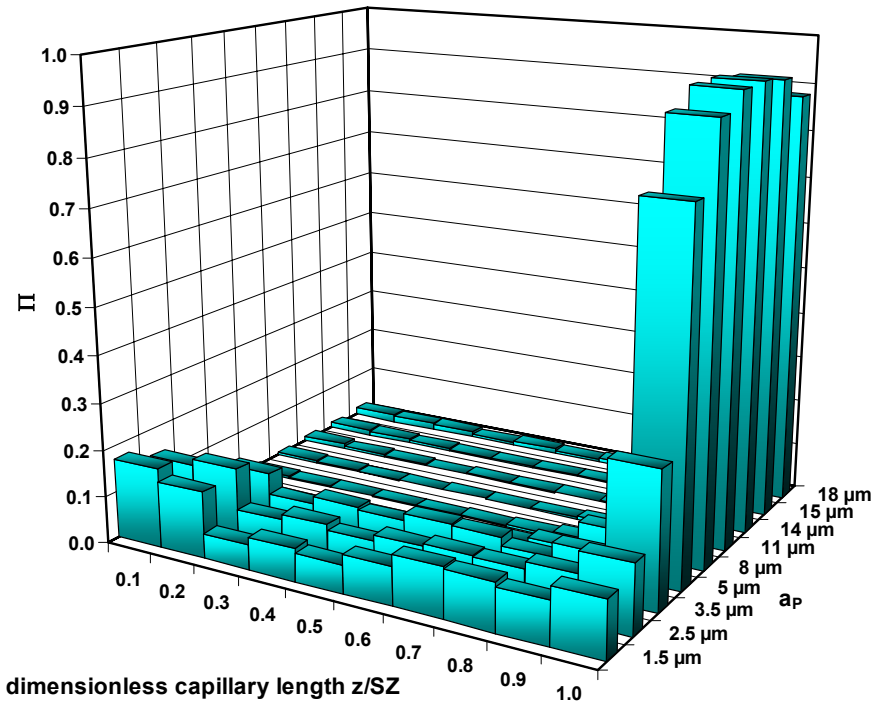

Figure A.20: Fractions of deposited primary particles after filtration (TMP = 0.4 bar, average flux of approx. 186 L/m²/h) as coagulated suspension vs. dimensionless capillary length z/SZ and primary particle radius a_P

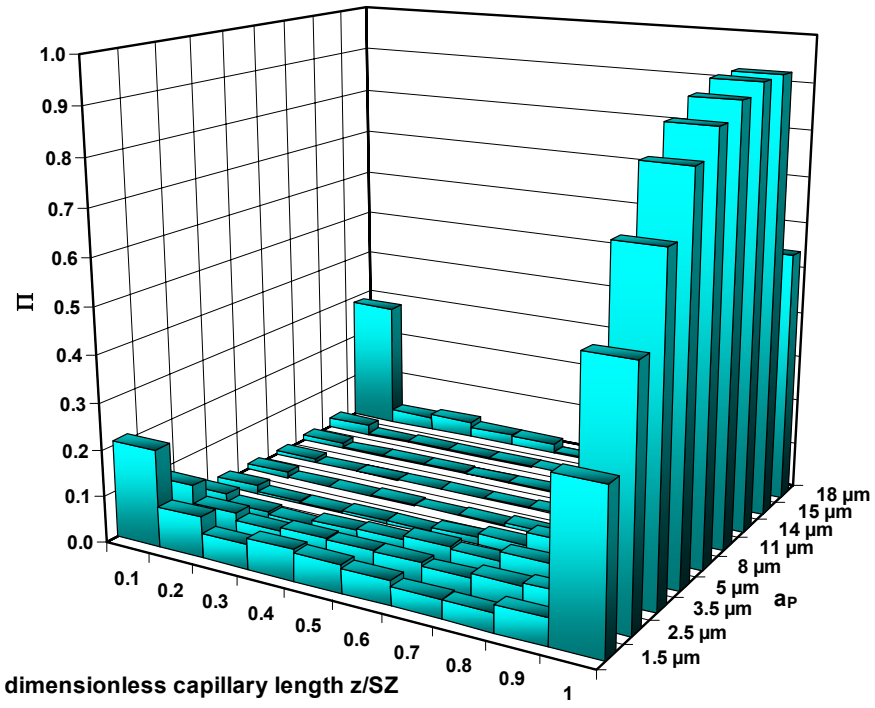

Figure A.21: Fractions of deposited primary particles after filtration (TMP = 0.4 bar, average flux of approx. 156 L/m²/h) as coagulated suspension vs. dimensionless capillary length z/SZ and primary particle radius a_P

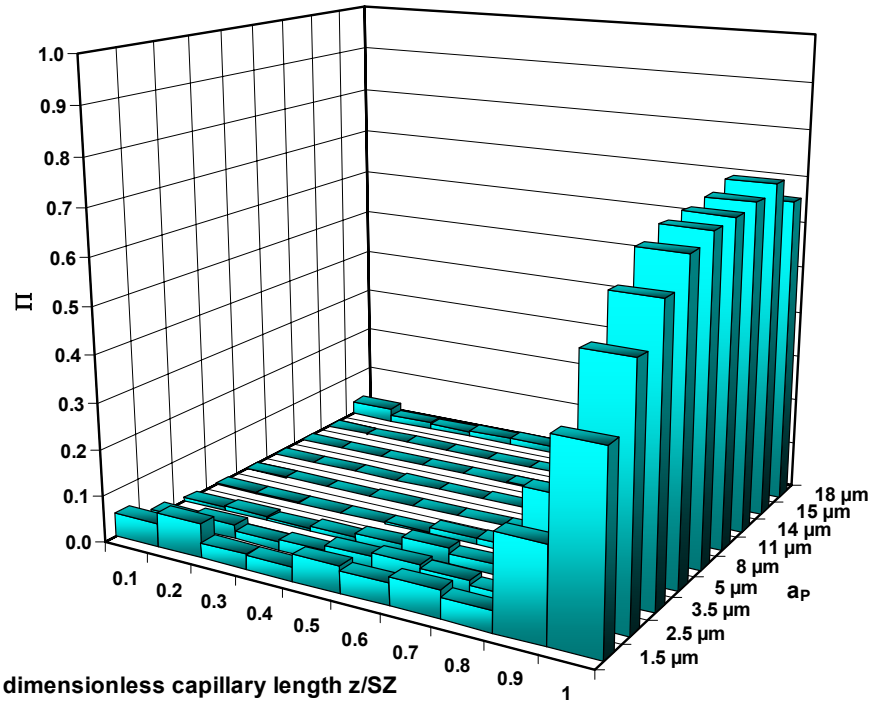

Figure A.22: Fractions of deposited primary particles after filtration (TMP = 0.4 bar, average flux of approx. 198 L/m²/h) as coagulated suspension vs. dimensionless capillary length z/SZ and primary particle radius a_P

The comparison of Figure A.18 to Figure A.22 delivers similar results as described in chapter 4.5. The fractions of small and mid sized primary particles in the range from a_P = 1.5 µm to about a_P = 14 µm was increased in the last two capillary length sections at z/SZ = 0.9 and z/SZ = 1, hence at the end of the capillary for the coagulated suspensions. Accordingly, the fraction of primary particles of the same size range decreased in the middle and the third quarter of the capillary length at z/SZ = 0.5 to z/SZ = 1. This clearly indicates that smaller and mid size particles were transported as floc agglomerate more deeply into the capillary as they would have actually done due to their own size.

CURRICULUM VITAE

André Paul Lerch

born 10th of April 1969 in Düsseldorf, Germany
married, one child

Professional Experience

since 2005	Research Associate at the Institute for Urban Water Management, Water Supply Engineering Group, Technische Universität Dresden, Germany
1999 - 2005	Research Assistant at the Department of Process Engineering / Water Technology, Universität Duisburg-Essen, Germany

Academic Education

1999	M. Sc. (Diplom Hauptprüfung)
1993	B. Sc (Diplom-Vorprüfung)
1990	Enrolment at the Universität – GH- Duisburg , Germany, Studies of Mechanical Engineering

Military service

1989 - 1990	Military service at a technical maintenance company (InstKP 30)

School Education

1989	Abitur (A-level / High School Certificate)
1979 - 1989	städt. Meerbusch Gymnasium (High School) in Meerbusch, Germany
1975 - 1979	St. Martinus Grundschule (Primary School) in Meerbusch, Germany

Dresden, 28th of February 2008